NONLINEAR VIBRATION ANALYSIS AND OPTIMAL DAMPING DESIGN OF SANDWICH CYLINDRICAL SHELLS WITH VISCOELASTIC AND ER-FLUID TREATMENTS

Farough Mohammadi

A thesis

In the Department of

Mechanical and Industrial Engineering

Presented in Partial Fulfillment of the Requirements

for the Degree of Doctor of Philosophy at

Concordia University

Montreal, Quebec, Canada

June 2012

© Farough Mohammadi, 2012

CONCORDIA UNIVERSITY

SCHOOL OF GRADUATE STUDIES

This is to certify that the thesis prepared

By: **Farough Mohammadi**

Entitled: **Nonlinear Vibration Analysis and Optimal Damping Design of Sandwich Cylindrical Shells with Viscoelastic and ER-Fluid Treatment**

and submitted in partial fulfillment of the requirements for the degree of

DOCTOR OF PHILOSOPHY (Mechanical Engineering)

complies with the regulations of the University and meets the accepted standards with respect to originality and quality.

Signed by the final examining committee:

_____ Chair
Dr. C. Mulligan

_____ External Examiner
Dr. N. Wereley

_____ External to Program
Dr. F. Haghighat

_____ Examiner
Dr. S. Rakheja

_____ Examiner
Dr. I. Stiharu

_____ Thesis Supervisor
Dr. R. Sedaghati

Approved by

Dr. A. Dolatabadi, Graduate Program Director

June 4, 2012

_____
Dr. Robin A.L. Drew, Dean
Faculty of Engineering & Computer Science

ABSTRACT

Nonlinear vibration analysis and optimal damping design of sandwich cylindrical shells with viscoelastic and ER-fluid treatments

Farough Mohammadi, Ph.D.
Concordia University, 2012.

Viscoelastic and smart fluid materials such as electro-rheological (ER) and magneto-rheological fluids have been used in many applications in industry to suppress vibration in sandwich shell structures. The main objective of this dissertation is to investigate and develop analysis models and design optimization strategies to optimally suppress the vibration of cylindrical shell/panel type structures using both passive and semi-active treatments. This dissertation constitutes two major related parts. In the first part, passive treatment using viscoelastic layer is studied for sandwich cylindrical shell using semi-analytical finite element modeling. In order to provide more accuracy a higher order Taylor's expansion of transverse and in-plane displacement fields is developed for the core layer of sandwich cylindrical shell structures including the least number of degrees of freedom. The developed model is then employed to formulate cut and partial treatment modeling which are applied to increase damping and reduce the weight of the structure. The formulations are also modified in order to consider the slippage between layers at the interfaces. A systematic parametric study is presented to investigate the effect of main parameters such as temperature, vibration amplitude, pre-stress components, slippage and etc on vibration damping characteristics of sandwich shell structure. The temperature distribution at each layer is obtained by solving the transient heat transfer equation for axisymmetric cylindrical structure based on the finite difference

method using irregular grid. Finally, by combining the semi-analytical finite element method and the optimization algorithms a design optimization methodology has been formulated to maximize the damping characteristics in sandwich cylindrical shell using the optimal number and location of cuts and partial treatments with the optimal thicknesses of the treating layers.

In the second part of the dissertation, semi-active treatment using smart ER fluid layer is studied. The shear stress response and the dynamic mechanical properties of the ER fluid created by dispersing cornstarch into corn oil are experimentally explored for small/large shear strain amplitude, moderate range of frequencies and different field intensities. A new constitutive model has been also proposed to predict accurately the measured experimental data in both frequency and time domains. Then, the nonlinear vibration analysis of sandwich shell/panel structure with constrained electrorheological (ER) fluid is investigated for different boundary conditions using the finite element method. In order to reduce the computational costs, a new notation referred to as H-notation is also developed over the two well known notations referred to as B and N notations in order to represent the nonlinear equations of motion. Finally, a design optimization methodology has been presented to maximize damping in sandwich cylindrical panel using both unconstrained viscoelastic and constrained ER fluid damping layers. The unconstrained viscoelastic layer is employed in order to practically seal the constrained ER fluid patches and boundaries of the ER based sandwich structure. Then, an optimization problem has been formulated to find simultaneously the optimum number and distribution of unconstrained viscoelastic and constrained ER fluid patches, electric field intensity and thickness ratios of the treating layers.

This thesis is dedicated to

my dear and beloved parents, Tahmineh and Ahmad for their

continuous supports in completion of this work.

ACKNOWLEDGMENT

Foremost, I would like to gratefully acknowledge and thank Prof. Ramin Sedaghati for his great supervision and crucial guidance from the beginning of the thesis as well as providing me continuous support and encouragement throughout the research. I believe that without his advices and suggestions this research would not have been possible.

Also, I would like to thank the technical staff and faculty member of Mechanical and Industrial Engineering Department at Concordia University particularly my committee members.

Finally, I would like to express my sincere thanks and gratitude to my parents, sisters, brothers and friends for their patience and supports during my studies.

TABLE OF CONTENT

Page

NOMENCLATURE

bols	Nomenclature
a	radius of the cylinder
C_p	specific heat
E	Young's modulus
F	the equivalent nodal force
G'	storage modulus
G''	loss modulus
H	rate of internal heat generation
h	coefficient of convection
h_i , i= t,b, c	thickness of the top (i=t), bottom (i=b) and core (i=c) layers
K^*	frequency dependent complex shear stiffness parameter of the adhesive layer
K	stiffness matrix
$k(\omega)$	real part of the frequency dependent complex shear stiffness parameter of the adhesive layer
L	length of the cylinder
M	mass matrix
N_j , j=1,2, 3	Lagrangian shape functions
q	vector of nodal displacements
x	axial coordinate
t,b, c	indices for representing top, bottom and core, respectively.
u, v, w	translational displacement field in axial, circumferential and thickness directions, through the thickness off each layer, respectively
u_0, v_0 , w_0	translational displacement field of the middle plane in axial, circumferential and thickness directions, respectively

Greek letters

$\gamma_{\xi s}$, $\gamma_{\xi s}$, $\gamma_{\xi\theta}$	in-plane shear strain, transverse shear strain in axial direction, transverse shear strain in hoop direction, respectively
$\widetilde{\gamma}$	shear strain amplitude
$\widetilde{\dot{\gamma}}$	shear strain rate amplitude
ε_{ss}, $\varepsilon_{\theta\theta}$, $\varepsilon_{\xi\xi}$	normal strains in axial, hoop and transverse direction, respectively
$\eta(\omega)$	frequency dependent loss factor
η_{eff}	effective loss factor
θ	circumferential coordinate
υ	Poisson's ratio
ξ_1, ξ_2, ξ_3	thickness coordinates located at the middle plane of the top, bottom and core layers, respectively
ρ	density
$\sigma_{ss}, \sigma_{\theta\theta}, \sigma_{\xi\xi}$	normal stresses in axial, hoop and transverse direction, respectively
σ^0	pre-stress components due to the thermal field and internal/external pressure
$\tau_{\xi s}$, $\tau_{\xi s}$, $\tau_{\xi\theta}$	in-plane shear stress, transverse shear stress in axial direction, transverse shear stress in hoop direction respectively
$\widetilde{\tau}$	shear stress amplitude
$\boldsymbol{\varphi}$	eigenvector
$\Phi_1^c, \Phi_2^c, \Phi_3^c, \Theta_1^c, \Theta_2^c, \Theta_3^c, \Psi_1^c, \Psi_2^c$	higher order terms of displacement fields in the Taylor's series expansions in the core layer
ψ_1, ψ_2	rotations of the normals to the middle plane in axial and circumferential directions, respectively
ω	frequency

LIST OF FIGURES

Page

LIST OF TABLES

Page

CHAPTER 1

INTRODUCTION

1.1 Introduction

Suppression of noise and vibration is a major concern in many load-bearing structures such as automotive, aerospace and marine vehicles. Although the vibration can be suppressed using vibration isolator by shifting the natural frequency for certain modes, the sandwich structures with damping layers can be effectively used to overcome this issue for wide frequencies. Amongst these structures, sandwich cylindrical shells or panels are widely used for many applications such as boilers, pressurized gas tanks and aircraft fuselage. There are three different treatment methods in order to suppress the unwanted vibration in continuous elastic structures. In the first method, the base layer is covered by constrained or unconstrained viscoelastic layer to achieve a passive treatment. Due to the ability of viscoelastic material in converting strain energy into heat, they are frequently used in sandwich beam, plate and shell structures where damping is desired for a designed frequency range. This method is simple, economical and easy to implement as no external energy source is required to operate the system. Although passive viscoelastic layers can be designed to reliably suppress vibration in a designed frequency range, the damping performance in viscoelastic materials is typically limited to narrow frequency bands and also highly affected by the environmental disturbances such as temperature.

To overcome this limitation, another method is to cover the base layer with the constrained smart controllable fluid such as Magnetorheological (MR) and Electrorheological (ER) fluids to achieve a semi-active treatment. The rheological properties of these smart fluids are changed when they are exposed to external magnetic

or electric fields. These semi-active configurations may address the limitations of passive viscoelastic treatments by effectively utilizing the motion of the structure to develop the control forces using adaptive smart fluids in order to configure the structural system under different excitation conditions. Considering this, ER or MR treatments can potentially offer the reliability and fail-safe feature of the passive viscoelastic treatments while maintaining the adaptability to be tuned for different frequency ranges without requiring large power sources or expensive hardwares needed by fully active systems.

In the third method, the vibration of the elastic structure may be controlled actively by smart piezoelectric materials in the form of distributed actuators and sensors attached to the main structure. This material can convert mechanical forces to electric charge as sensors and also it can develop elastic normal or shear strain under external electrical field as actuators. Due to the requirement of complex hardware and also large power consumption, the active control systems may not be practically feasible for vibration control of large structural systems. Moreover, as active control systems deliver energy into the system, they must be carefully designed with respect to control stability.

Considering above, the main focus in this research is on passive viscoelastic and semi-active smart fluid treatments and their combinations to damp vibration of multilayer shells. For semi-active treatment, ER fluid has been used as smart controllable fluid due to its low density which can be used to treat the structure without significant increase in the total mass of structure. Also, the electric field can be generated much easier than the magnetic field in sandwich cylindrical shell along the radial direction. In passive treatment, the damping layer in sandwich structures are viscoelastic material which can be used in two different configurations as constrained and unconstrained damping layers.

In the following a systematic literature review on the recent pertinent works regarding vibration damping in viscoelastic and smart fluid based sandwich structures has been presented.

1.2 Viscoelastic based Sandwich Structure

Many polymers exhibit viscoelastic properties which can be effectively used to suppress vibration in different structures in which they are able to dissipate mechanical strain energy into heat. However, their mechanical properties are highly affected by many parameters such as temperature, frequency of the vibration, strain amplitude and pre-stress components due to external pre-loads. Different mathematical models including Voigt, Maxwell, Zenner and fractional derivative models have been previously developed for viscoelastic materials in order to establish the constitutive equation relating the stress and strain components. Using these classical models, the constitutive equation under small harmonic shear loading for a constant temperature can be generally written as:

$$\tilde{\tau} = \left(G'(\omega) + \mathrm{i}\, G''(\omega)\right)\tilde{\gamma} \tag{1.1}$$

where $G'(\omega)$ and $G''(\omega)$ are respectively storage and loss modulus which depends on the frequency, $\tilde{\tau}$ and $\tilde{\gamma}$ are respectively the amplitude of the shear stress and shear strain components. The classical models determine the mathematical expressions for $G'(\omega)$ and $G''(\omega)$. The energy dissipated per each cycle depends on the imaginary part of the complex shear modulus $G^{*}=G'(\omega)+\mathrm{i}G''(\omega)$. Material loss factor is also defined based on the ratio of the loss modulus to storage modulus. The damping layer made of viscoelastic material can be used in the sandwich structure in order to suppress noise and vibration. The following addresses the literature review on the application of the viscoelastic materials in vibration damping of structures.

The analysis of constrained and unconstrained viscoelastic sandwich plate structure was conducted by Ross et al. [1]. In their work, loss factor was defined in terms of strain energy. Loss factor has been considered as an indicator to measure damping characteristic of a sandwich structure which is proportional to the ratio of the dissipated energy due to the damping layer to the maximum potential energy. This definition was examined by Ungar and Kerwin [2] who showed that it is meaningful for massless structure; however it may not be applied for the structure with mass except at the natural frequencies. Mead and Markus [3] presented sixth-order differential equation for three-layered sandwich beam in terms of the transverse deflection. Different boundary conditions were investigated in their studies. Classical theory has been considerably used to model sandwich structures [4-6]. The effects of shear deformation and rotational inertia have been investigated by Rao [7] for short sandwich beam. He also developed an analysis procedure to obtain loss factor and natural frequency for various boundary conditions [8]. Vibration damping analysis of sandwich viscoelastic beam has been investigated by Wang and Wereley [9] using spectral finite element method. The damping behavior of sandwich viscoelastic plate using analytical approach was studied by Wang et al. [10]. Ramesh and Ganesan [11] formulated semi analytical finite element model based on the first order shear deformation theory (FSDT) for obtaining the damping properties of cylindrical and conical shells. Parametric studies were also conducted to investigate the effect of some parameters such as geometry and material properties on the damping properties. Sainsbury and Masti [12] developed a combination of two elements named as FEM_1 (rectangular curved shape with four corner nodes) and FEM_2 (rectangular curved shape with four corner nodes and four mid-side nodes) in the

finite element formulation of partial treatment in sandwich cylindrical shell. Ramesh and Ganesan [13] compared the results from different theories including Wilkins Theory (WT), Khatua's Theory (KT) and Discrete Layer Theory (DLT) in semi-analytical finite element modeling of the sandwich shell structure.

Higher order expansion in displacement fields of the core layer considering slippage at the interfaces in sandwich beam structure was assumed by Bai and Sun [14]. They implemented the physical Lagrange multiplier in order to consider the higher order displacement fields in the core of the beam structure. It was shown that the slippage may increase damping characteristics of the beam structure. The effect of slippage between fiber and matrix on damping characteristics in composite structures was also investigated by McLean and Read [15] and Nelson and Hancock [16]. They experimentally demonstrated that slippage reduces damping properties and therefore it should be avoided. The higher order model of the displacement fields in the core layer of sandwich beam structure was also examined by Babert et al [17]. Using the Green function, they presented an approximate solution by assuming perfect bonding at the interfaces to find the displacement fields at the core layer. By comparing the damping behavior resulted from their analysis to the experimental data, they showed that assuming the higher expansion of displacement field for sandwich beam structure provides more accurate model. Araújoet et al. [18] used the higher order shear deformation theory to represent the displacement field at the viscoelastic core layer in vibration analysis of sandwich composite plate structure. However, there is a lack of the compatibility between the displacement fields at the different layers in which implementing the boundary conditions

does not compatibly give the displacement fields at the core layer in terms of the displacement fields at the top and bottom layers.

Material properties and damping behavior of viscoelastic materials are strongly frequency/ temperature dependent. Jones [19] used "temperature-frequency equivalence" principle to measure complex modulus of damping material in terms of temperature and frequency. Lesieutre et al. [20] implemented anelastic displacement field model with temperature dependence to investigate the heat dissipating effect on elastomeric specimen based on the one-dimensional model of simple shear. Teng and Hu [21] investigated the effect of frequency, temperature and also the dimension of damping material on vibration characteristics of sandwich beam structure. Hao and Rao [22], presented analytical formulation to analyze damping in three layered sandwich beams considering the effect of temperature. Moreira et al. [23] developed the viscoelastic modeling based on isothermal model in order to contribute temperature and frequency effects directly in the model. Gupta and Kumar [24] used the Kelvin model to analyze vibration of non-homogenous viscoelastic rectangular plate under various value of thermal gradient.

Effect of pre-stress components on the buckling and vibration behavior has been also investigated by many researchers. The vibration analysis of pressurized bare cylindrical shell was studied by Ross et al. [25-27]. Sabri and Lakis [28] used classical finite element method and Sanders shell theory to investigate the dynamic stability of partially fluid-filled cylindrical shell under external and internal pressure. Using semi-analytical finite element method and the concept of geometric stiffness matrix, Ganesan and Pradeep [29] analyzed vibration and buckling behavior of a bare cylindrical shell containing hot liquid. The temperature effect on damping behavior of cylindrical sandwich structure was

considered by Xia and Lukasiewicz [30]. Ganesan et al. [31], Pradeep et al. [32] and Pradeep and Ganesan [33] presented comprehensive studies on the damping behavior and vibration analysis of piezothermoelastic composite cylindrical shell, composite sandwich beam and composite sandwich plate under thermal loading. These studies indicate that the damping behavior of sandwich structures is affected by pre-stress components and temperature condition. Due to the damping in the viscoelastic sandwich structure, the dissipated energy related to the hysteresis mechanism will be generated in the core viscoelastic layer as a source of heat. This phenomenon has been reported in some application such as self heating of elastomeric lead–lag dampers used in articulated rotors of helicopters [34, 35].

From the previous studies it can be realized that the vibration damping analysis has been mainly investigated for beam/plate type structures and there are few works reported in the literature for sandwich shell structure. Linear or lower order displacement field has been frequently assumed to represent the displacement in the constrained core layer for sandwich shell structure. However for thick core layer, the lower order expansion of displacement field may not be accurate enough and thus higher order models should be used. This is particularly very important for partial treatment and cut modeling in design optimization which may lead to thick viscoelastic core layer.

1.3 ER and MR based Sandwich Structures

ER and MR fluids have many applications in engineering such as shock absorption, vibration control of structures and flow control of fluids due to their ability to provide reversible and rapid response [36-40]. An ER fluid consists of suspension of solid dielectric particle dispersed in an insulating oil [41]. Similarly, MR fluids can be

prepared by dispersing magnetic particles such as nickel and iron in a carrying fluid such as oil [42]. The rheological properties of the MR and ER fluids are immediately changed when they are subjected to external magnetic and electric field, respectively. ER fluids naturally behave as Newtonian fluid and immediately transform to the plastic (semi-solid) state under electric field due to the formation of polarized particle chains in the direction of electric field. This phenomenon was first reported by Winslow [43]. Compared with the MR fluid, ER fluids have lower yielding strength but relatively lower response time and density [44]. ER and MR fluids can be used in three different modes, namely flow mode, squeeze-flow mode and shear mode in which the mode of operation depends on the applications [45-47]. The flow mode can be used in shock absorber, dampers and servo-valves in which the fluid flow can be tuned by altering the electric or magnetic field. The shear mode can be applied in brakes, clutches and also damping layer of sandwich structure in order to suppress noise and vibration. The squeeze mode is used in impact dampers to control small amplitude vibration with large force.

In this dissertation, it has been focused on ER fluid materials and their application in sandwich structures. However the methodology can be easily extended to MR fluid materials. Various types of ER fluids reported in the literatures were discussed by Block and Kelly [48]. For instance, Winslow [43] used different ER fluids which consist of solid particles such as starch, gypsum, stone, carbon, lime and silica dispersed in insulating oil such as mineral oil and kerosene. Steady shear response of ER fluids has been studied in literatures for different electric field intensities and particle concentrations [49, 50]. Plenty of studies on dynamic characteristics of smart fluids are available in literatures. The material properties and stress response generally depend on

the electric field intensity, frequency and amplitude of the deformation in ER fluid material. In the linear region the properties mainly depend on frequency and external field intensity. Linear viscoelastic properties of alumina dispersed in silicone oil in terms of frequency and electric field was investigated by Parthasarathy et al. [51]. The dynamic behavior under large amplitude oscillatory shear was also investigated by Parthasarathy and Klingenberg [52] using particle-level simulation method. They showed that under very small shear strain amplitude, the fluid exhibits linear viscoelastic behavior. The nonlinear behavior could easily be achieved by slight change of particles localization, instability in external field and large strain amplitude [53]. Consequently, due to the instability in external field regardless the sensibility of the rheometers, there is no assurance that linear properties are obtained in a real experiment [54]. Gamota and Filisco [55-57] investigated ER fluid responses under moderate frequencies (10-50 Hz) and high frequencies (300-400 Hz). They showed that the ER fluid response is mainly affected by shear strain amplitude and electric field strength. Based on the Fourier transformation technique, Gamota et al. [58] discovered that for certain strain amplitude the response is linear under small field intensity, however, with increasing field intensity the ER fluid shows nonlinear behavior since the higher order harmonic terms appear in the Fourier transformation analysis. This indicates that not only large shear strain amplitude leads to nonlinear viscoelastic behavior of the smart fluid, but it can also be resulted from high field intensity. Furthermore, they showed that yielding stress of the smart fluid depends on the field intensity and frequency. Nonlinear viscoelastic properties of MR fluid for different shear strain amplitudes and frequencies were investigated by Li et al. [59]. It was shown that at angular frequency ω=5 rad/s and magnetic field of 340

mT, the nonlinearity in stress response occurs for shear strain amplitudes greater than 0.1 % in which the storage modulus depends on the strain amplitude. They also presented different critical frequencies where the trend of effective complex modulus is changed at these frequencies. It was shown that with increasing shear strain amplitude, the critical frequencies decrease. Therefore, if the amplitude is small enough then the effective complex modulus remains constant over a moderate range of frequency. Choi et al. [60] obtained complex modulus of an ER fluid using free oscillation response of sandwich beam in which the ER fluid was constrained by thin polystyrene faces. They employed ER fluids consisting of zeolite-silicone oil and cornstarch-corn oil with different particle weight fraction. Although their method provides a condition to catch the linear viscoelastic behavior, the properties could be affected by the constraining faces. The complex modulus of the ER fluid consisting of cornstarch suspensions in silicone oil under large amplitude oscillatory shear strain was investigated by Lee and Cheng [61]. They showed that for large strain amplitude, the material properties of the ER fluid can be approximately frequency independent.

In many applications, ER and MR fluids are subjected to oscillatory shear [62]. The dynamic properties of ER and MR fluids under oscillating shear strains in both pre-yielding and post yielding regimes are mathematically investigated by many researchers. Under external field, these smart fluids show linear viscoelastic behavior for small amplitude oscillatory shear strain $\gamma = \tilde{\gamma}\sin(\omega t)$ in which ω is the angular frequency. The shear stress response then can be expresses as:

$$\tau = \tilde{\gamma}\left(G'(\omega, E)\sin(\omega t) + G''(\omega, E)\cos(\omega t)\right) \tag{1.2}$$

where $G'(\omega,E)$ and $G''(\omega,E)$ are respectively storage and loss modulus which depends on the frequency and field intensity. For large amplitude oscillatory shear, dynamic properties of the smart material not only depends on the frequency and the external field, but it also depends on the amplitude. In this case, the Fourier transformation technique is the most common method to quantify the behavior of material [63]. According to this method, the stress response under the harmonic shear strain may be expressed as:

$$\tau = \tilde{\gamma}(G_1'(\omega,E,\tilde{\gamma})\sin(\omega t) + G_1''(\omega,E,\tilde{\gamma})\cos(\omega t)) + \tilde{\gamma}\sum_{n=1}^{\infty}\left[G_{2n+1}'(\omega,E,\tilde{\gamma})\sin\left((2n+1)\omega t\right) + G_{2n+1}''(\omega,E,\tilde{\gamma})\cos\left((2n+1)\omega t\right)\right] \quad (1.3)$$

For small amplitude G'_{2n+1} and G''_{2n+1} are respectively small enough compared to G'_1 and G''_1. Noteworthy, by reversing the coordinate system the stress response does not change [64] which explains why only odd harmonic terms are included in Eq. (1.3). In the nonlinear regime, the behavior of the smart fluid material changes through the cycle (intercycle nonlinearities). The reported experimental data for storage and loss modulus in the literature using the rheometer device are obtained based on the either the lower order terms G'_1 and G''_1 in Fourier transformation or based on the shear stress amplitude and phase behavior at the fundamental frequency as:

$$G'(\omega,E,\tilde{\tau}) = \frac{\tilde{\tau}}{\tilde{\gamma}}\cos(\phi) \qquad G''(\omega,E,\tilde{\tau}) = \frac{\tilde{\tau}}{\tilde{\gamma}}\sin(\phi) \quad (1.4)$$

where $\tilde{\tau}$ and $\tilde{\gamma}$ are respectively shear stress and strain amplitudes and ϕ is the phase difference between shear stress and strain at the fundamental frequency. Linear and nonlinear viscoelastic properties of ER and MR fluids were studied by Weiss et al. [65]. According to their results, at constant amplitude the nonlinearity in storage modulus-frequency relation increases as the external field intensity increases. As mentioned

before, in the linear regime the nonlinear terms in Fourier transformation relation are negligible compared to G'_1 and G''_1. In this region the viscoelasticity can be modeled using classic viscoelastic models such as Voigt, Maxwell, Zenner and fractional derivative models. Although the Fourier transformation technique is suitable to show the nonlinear viscoelastic behavior under large amplitude oscillation shear (LAOS), it does not give the physical interpretation of the material response. Cho et al. [66] proposed a new method to physically interpret the LAOS data by decomposing the nonlinear stress response into the elastic and viscoelastic components using Taylor expansion. However, the coefficients of the polynomial which define the material properties are not unique and depend on the order of the polynomial in the Taylor expansion. To overcome this issue, Ewoldt et al. [67] suggested a framework using Chebyshev polynomials $T_n(x)$ as the basis functions in order to avoid the effect of incorporating the higher order terms in the lower order terms. Also the Chebyshev polynomials can be easily related to the Fourier coefficients using the identities $T_n(\cos(\theta))=\cos(n\theta)$ and $T_n(\sin(\theta))=\sin(n\theta)(-1)^{(n-1)/2}$. Furthermore, they presented different first order modulus of viscoelasticity in nonlinear regime and defined their physical interpretation. They showed that G'_1 and G''_1 in Eq. (1.3) averagely exhibit dynamic properties of the smart fluids for nonlinear viscoelastic behavior.

For large amplitude, the Bingham plastic model or other purely viscous Newtonian fluid models such as Cross model [68], Papanastasiou model [69], Carreau-Yasuda model [64] can be employed in the nonlinear regime. In addition to these models, some studies were presented to show the nonlinear behavior of these materials such as the study reported by Gopalakrishna and Wereley [70] who presented a model using nonlinear

combination of viscoelastic element for pre-yield and simple viscous element for post-yield regimes to capture nonlinear behavior of ER fluid under oscillatory shear loading. Based on the non-parametric identification method, Ehrgott and Masri [71] modeled the force response of the ER fluid (alumino-silicate dispersed in fluorinated liquids) obtained by the experiment using Chebyshev polynomials in terms of displacement and velocity with 64 corresponding coefficients for a single field strength value. Considering different field intensities, the number of the coefficients to be estimated is too numerous. Lee [72] used a nonlinear stress-strain relation to obtain a constitutive model for ER fluids in nonlinear regime. He neglected the effect of frequency on the stress response of the ER fluid. Based on this constitutive model for representing the hysteresis loop and using the energy method proposed by Ungar and Kerwin [2], Lee and Cheng [73] obtained the equivalent linearized storage and loss modulus and then compared the results to the experimental data based on Eq. (1.4). The comparison showed a good agreement between the complex modulus resulted by the simulation and the experiment. However, the stress amplitudes predicted by the model were considerably different from those obtained by the experiment. The reason is that the complex modulus obtained experimentally based on the Eq. (1.4) does not represent the equivalent complex modulus and consequently they should not be compared to each other. Therefore the constitutive model does not represent the true hysteresis loop. The Bingham-Hooke model was used by Laun et al. [74] to describe material properties of MR fluids in the linear and nonlinear regimes for single field intensity and single frequency. The model has been expressed as:

$$\tau = \begin{cases} G_0(\gamma - \gamma_B) & |\tau| \le \tau_y \\ \text{sign}(\gamma)\tau_y + \eta_B \dot{\gamma} - \lambda \dot{\tau} & |\tau| > \tau_y \end{cases} \tag{1.5}$$

in which τ_y is yielding stress, G_0 is elastic modulus, η_B is Bingham viscosity, λ is relaxation time and γ_B is a constant shear deformation. They showed that this model fails to capture loss modulus at small amplitude. Considering this, they added a viscous term $\eta_p\dot{\gamma}$ to the total stress component without changing the Bingham-Hooke model element. The parameters of the model were then adjusted to predict the experimental results. They also improved the results by considering weighted sum of the contributions from different yielding stress into the total shear stress response. According to the results, the complex modulus was not still close to the experimental data in the nonlinear regime.

Using the material properties in small oscillation, some studies have been reported on vibration damping of structures with MR/ER fluid damping layers. Yalcintas and Coulter [75, 76] analytically investigated vibration behavior of sandwich beam with ER fluid core layer. Choi et al. [60] obtained complex modulus of ER fluid using free oscillation response of sandwich beam. They also studied vibration characteristics of a composite sandwich beam structure with constrained ER fluid layer [77]. Jia-Yi [78] studied the vibration and damping characteristics of constrained ER fluid sandwich cylindrical shell using semi-analytical finite element modeling in linear region. Similar study was presented by Kang et al. [79] on ER fluid sandwich beam structure using finite element method. Sun et al. [80] studied vibration analysis of MR fluid sandwich beam structure under small amplitude oscillation Shear. Zhou and Wang [81] analyzed damping characteristics of partially magnetized sandwich beam with MR fluid core layer. Dwivedy et al. [82] also studied instability of MR fluid sandwich beam with MR fluid under oscillating axial load. Vibration damping analysis for constrained fully and partially treated MR fluid beam structure was also presented by Rajamohan et al. [83,

84] . Dynamic behavior of 3D space truss structure including embedded MR fluid damper was studied by Dominguez et al. [85].

As it can be realized, the studies on structural vibration damping using MR/ER semi-active treatment are mainly limited to the linear region of MR/ER fluids where the complex modulus is independent from amplitude of the shear strain. Due to the small linear region in ER fluid, vibration analysis of the sandwich structure containing ER fluid should be investigated in nonlinear region where the material properties depend on frequency, amplitude and electric field. Currently, there are no available studies on vibration damping in ER/MR based sandwich cylindrical shells/panels subjected to large deformation.

1.4 Nonlinear Vibration Analysis of Sandwich Structures

Nonlinear vibration analysis of shell/plate structures has been widely studied by many researchers. The extensive reviews are reported in references [86-89]. Different frameworks have been employed in these studies in order to define the displacement fields through the shell/plate type structures including classical theory (CT), first order shear deformation theory (FSDT) and higher order shear deformation theory (HSDT). Based on the displacement distribution in the shell/plate structures and also strain-displacement relationships, different nonlinear shell theories have been also developed such as Donnell [90], Flügge-Lur'e-Byrne [91], Novozhilov [92] and Sanders-Koiter [93] shell theories which are extensively reported by Amabili [94]. By employing the Lagrange equations or Hamilton principle, the equations of motion are then established using the total strain and kinetic energies in the shell/plate structures. The nonlinear equations of motion can be solved using numerical methods such as finite element, finite

difference and Rayleigh-Ritz methods. Also it can be solved analytically using the perturbation technique. By employing the finite element method, the partial differential equations of motion are converted to set of ordinary differential equations and techniques such as collocation method, harmonic balance method and Galerkin methods can be used to solve the free nonlinear vibration problem. Xia and Lukaziewicz [95, 96] analyzed nonlinear free vibration damping of sandwich plates and sandwich cylindrical panels using harmonic balance method and the multi-mode Galerkin technique. Nonlinear vibration analysis of viscoelastic sandwich beam was investigated by Daya et al. [97] based on the harmonic balance method coupled with one mode Galerkin technique. Using asymptotic–numerical method and perturbation techniques, Azrar [98] investigated vibration analysis of plate structure. The nonlinearity appeared in the stiffness matrix due to the large deformation can be also solved by the simple iteration technique or Newton-Raphson method. This methodology has been addressed in many studies as follows. Based on the von Karman's hypothesis, Han and Petyt [99] analyzed nonlinear vibration analysis for fundamental mode of thin plate structure using hierarchical finite element method. They employed harmonic balance method considering the first term in the time series in order to establish the nonlinear eigenvalue problem which was solved using the simple iteration technique. Due to nonlinearity in the equations of motion, the displacement in free vibration can be expressed using the higher order terms in the time domain. However, as shown by Prabhakara and Chia [100], small difference exists between the results using the first term and first two terms in the time series. Liu and Huang [101] investigated nonlinear vibration analysis of composite laminated plate based on FSDT and von Karman's hypothesis using finite element modeling and the direct

iteration procedure. Similar study has been reported by Nanda and Bandyopadhyay [102] for laminated composite cylindrical panel. Based on HSDT, Panda and Singh [103, 104] studied nonlinear free vibration analysis of laminated composite cylindrical and spherical shell panels using finite element modeling and the direct iteration technique. Singha and Daripa [105] used finite element method and von Karman's hypothesis to analyze nonlinear free vibration of laminated composite skew plates and the direct iteration technique was used to solve the nonlinear amplitude dependent eigenvalue problem obtained by the Galerkin method.

The nonlinear amplitude dependent stiffness matrices in equations of motion have been expressed by two notations. In B-notation, according to the procedure developed by Mallet and Marcal [106], an asymmetric amplitude dependent stiffness matrix is achieved. However, Rajasekaran and Murray [107] showed that the derivation can be performed in a way that a symmetric form of the nonlinear stiffness matrices in N-notation is resulted. The correlation between these two notations has been also shown by Wood and Schrefler [108]. These two notations are not efficient enough regarding the computational costs associated with integrations repeatedly performed in the direct integration technique.

1.5 Design Optimization of Sandwich Structures

Parametric studies and optimization to investigate the effect of the main parameters such as dimensions of the layers, material properties and partial treatment on the damping characteristics in passive and semi-active treatments have been investigated by many researchers. Ramesh and Ganesan [11, 109] presented the effect of geometry and material properties of viscoelastic layer on loss factor using semi-analytical finite element

modeling based on the first order shear deformation theory (FSDT) for shells of revolution. Plunkett and Lee [110] optimized damping characteristics of a viscoelastic sandwich beam structure using partial treatment by cutting the constraining layer into optimal lengths. Mantena et al. [111], maximized loss factor in constrained viscoelastic sandwich beam structure by optimizing side length of the treatments. Optimal size and dimension of treatments in sandwich layered plate structure was also investigated by Huang et al. [112]. Trompette and Fatemi [113] obtained the best position of one cut considering lack of continuity in longitudinal displacement in cantilever viscoelastic sandwich beam to maximize loss factor. Ajmi and Bourisli [114] maximized loss factor by considering the optimized number of treatments in partial treatment of viscoelastic sandwich beam structure and appropriate thickness ratio of top and core layers. Lepoittevin and Kress [115] optimized the distribution of cuts in constraining and constrained layers of sandwich viscoelastic beam structures. They showed that by embedding the cuts, transverse shear strain at core layer increases and consequently the damping increases. Design optimization of MR based sandwich beam structure has been investigated by Rajamohan et al. [116] in which optimal location of MR fluid treatment patches was found in order to maximize loss factor. Lepik [117] optimized thickness distribution of axisymmetric viscoelastic cylindrical shell layer in order to minimize the deflection under impulsive loading. Zheng et al. [118] minimized vibration response of cylindrical shell using the optimal size and location of viscoelastic treatment patches.

As it can be realized, the design optimization reported in the literature are based on optimizing thicknesses of the damping and constraining layers or optimizing the side length of certain number of treating patches to maximize damping. These studies are

mainly conducted for beam/plate type structures [110-116]. Fewer studies on design optimization of sandwich shell/panel structures are available in literatures which have been presented only for passive damping [117, 118]. Also there is no study available in the literature in which the both viscoelastic and smart fluid materials are used in a way that the configuration of the treatments, the thicknesses of the treating layers and the electric field intensity are simultaneously optimized in order to maximize the damping in sandwich panel structure.

1.6 Motivation and Objectives

In the first part of this dissertation, passive treatment using viscoelastic layer is studied for sandwich cylindrical shell structure using the semi-analytical finite element modeling and the design optimization has been carried out to achieve the maximum damping. In the second part of this dissertation, the semi-active treatment using ER fluid material has been analyzed for the sandwich shell structure using the finite element modeling. Finally, the design optimization has been conducted in order to obtain optimum damping using both viscoelastic and ER fluid treatments.

As mentioned before, damping characteristics of sandwich structure are mainly investigated for plate-beam sandwich structure and there are few works on vibration damping analysis of sandwich shell structure. The lower order expansion has been often used for the displacement field of core layer which may not be accurate enough for the thick core layers.

Compared with viscoelastic material, the ER fluids have much lower yielding stress. Thus for relatively large deformation, these smart fluids enter to the post-yielding region and therefore the vibration damping analysis should be conducted considering the

nonlinear regime. As mentioned before, currently there are no available studies on vibration damping in ER sandwich cylindrical shells/panels considering the nonlinear behavior of the smart fluid material. In the nonlinear regime, material properties depend on frequency, shear strain amplitude and electric field intensity. These properties are required in order to investigate the nonlinear vibration analysis of sandwich panel structure. However, the material properties in post yielding provided in the literatures are not sufficient to be used in nonlinear vibration analysis of sandwich structure. Also a constitutive model is required to accurately predict the experimental data for different shear strain amplitudes, frequencies and electric field intensities.

The nonlinear vibration analysis of sandwich shell structures is computationally very expensive. An efficient finite element modeling is required to model vibration damping in these structures. The two well-known B and N notations used for representing the nonlinear equation of motion are not computationally efficient as they require numerous integrations iteratively performed throughout the direct iteration technique.

Considering the abovementioned limitations in the literature, in the following the objectives accomplished in this dissertation have been summarized:

i. Semi-analytical finite element modeling for vibration damping analysis of passive viscoelastic sandwich cylindrical shell structure and investigating the effect of main parameters on vibration damping characteristics. These parameters include the core rigidity, ambient temperature, internal temperature and the resulted thermal stress components introduced at each layer, heat dissipation, slippage between layers at the interfaces, large deformation, stress components due to internal/external pressure, thickness ratio of the layers,

partial treatment and its distribution, cutting and its distribution at the top and core layers, and the method of treating the viscoelastic layer including the constrained and unconstrained treatment processes.

ii. Developing a higher-order expansion for representing the displacement fields in a thick viscoelastic damping layer with the least number of degrees of freedom. The higher order model provide the compatibility between the displacement fields at different layers so that implementing the boundary conditions provide the displacement fields at the core layer in terms of those at the top and bottom layers. Considering this, the higher order model can be implemented to model cut and partial treatment. The results are also compared with those obtained by the lower order expansion. Although the higher order models include the least number of variable and provide more accuracy than the linear order model, however it results in more complexity in formulations.

iii. Deriving the formulation based on considering slippage between the layers at the interfaces and investigating the effect of slippage on vibration damping characteristics in viscoelastic sandwich shell structures. Also the higher order model has been employed in the finite element modeling of sandwich cylindrical shell under thermal and internal/external pressure loading.

iv. Optimizing damping characteristics in passive viscoelastic treatment using optimum number of cuts/treatments and their distribution as well as the optimum thickness ratios of viscoelastic core and elastic top layers of sandwich cylindrical shell structure.

v. Conducting experimental study to obtain material properties of ER fluid material for different shear strain amplitudes, frequencies and electric field intensities. A constitutive model is also developed to predict the experimental results in both frequency and time domains.

vi. Nonlinear vibration analysis of ER based sandwich shell structure using finite element modeling and developing a new notation (referred to as H-notation) in order to efficiently represent the nonlinear equations of motion. Using this notation leads to considerable reduction in the computational costs caused by the time consuming integrations in the nonlinear vibration analysis of structure using direct iterating technique.

vii. Design optimization in sandwich shell structure with both viscoelastic and smart fluid patches in which simultaneously the configuration of the viscoelastic and ER fluid treatments, the thicknesses of the treating layers and the electric field intensity are optimized to maximize the damping in sandwich shell structure.

1.7 Organization of the Dissertation-Manuscript based Format

The dissertation has been written according to the manuscript-based format based on the requirements described in "Thesis Preparation and Thesis Examination Regulation" booklet of the School of graduate Studies at Concordia University. The dissertation includes eight chapters which addresses the objectives illustrated in the previous sections. Chapter 1 presents the relevant studies reported in the literature regarding the viscoelastic and smart fluid materials and their application in vibration damping of sandwich structure. Six articles extracted from this dissertation have been included in Chapters 2

through 7 stating the abovementioned objectives and the method of accomplishment. These articles are published in peer-reviewed and high ranked journals. These chapters are organized in sequential manner which describe the methodologies to address the objectives of the dissertation. Finally, the main conclusions extracted from the dissertation, recommendation and future work have been summarized and included in the chapter 8. In the following the summary of chapters has been presented. It should be mentioned that some repetitions in the developed formulation and the experimental study in some chapters cannot be avoided since they are required to present the integrity of the articles and to illustrate the entire developed methodology.

Chapter 2 presents the following article published in the “International Journal of Mechanical Sciences”:

F. Mohammadi and R. Sedaghati, "Linear and nonlinear vibration analysis of sandwich cylindrical shell with constrained viscoelastic core layer," *International Journal of Mechanical Sciences,* vol. 54, pp. 156–171, 2011

In this article damping characteristics of three-layered sandwich cylindrical shell for thin and thick core viscoelastic layers are studied using semi-analytical finite element method. Higher order expansion of displacement is developed to represent the displacement field of the core layer. The results are also compared with those using the lower order expansion in both frequency and time domains. The effect of geometric nonlinearity due to the large deformation of the sandwich shell structure has also been considered assuming small strain and moderate rotation. Different assumptions based on the continuity and discontinuity in transverse shear stresses and slope of in-plane displacements are considered in the finite element formulation and their effects have been

investigated for compliant and rigid core layers. This has been followed by investigating the effect of thickness ratios of the damping and constraining layers on damping characteristics. Finally, the effect of imperfect bonding between the layers on vibration behavior has been presented and it is shown that slippage between layers at the interfaces leads to reduction in loss factor at the majority of modes.

Chapter 3 presents the following article published in the "Journal of Sandwich Structures and Materials":

F. Mohammadi, R. Sedaghati, "Damping characteristics of sandwich cylindrical shell under pressure and thermal load," *Journal of Sandwich Structures and Materials,* vol. 14, pp. 157–180, 2012.

In this article, damping characteristics of viscoelastic sandwich cylindrical shell under internal/external pressure and internal temperature is investigated. By implementing finite difference method for irregular grids in the sandwich cylinder, temperature distribution at each layer is determined. Using the higher order model for displacement fields at the viscoelastic core layer described in chapter 2 and considering the effects of temperature and frequency on material properties of damping layer, vibration behavior of a pressurized sandwich cylindrical shell under the temperature variation has been investigated. The thermal stresses introduced at each layer and also the stress components due to internal/external pressure are obtained and then considered in the vibration analysis using the concept of geometric stiffness matrix. Effect of heat dissipation on vibration behavior of a pressurized cylinder under harmonic variation of the pressure has also been investigated

Chapter 4 presents the following article published in the "Journal of sound and vibration":

F. Mohammadi, R. Sedaghati, "Vibration analysis and design optimization of viscoelastic sandwich cylindrical shell," *Journal of Sound and Vibration*, vol. 331, pp. 2729–2752, 2012.

In this article, the developed higher order expansion is formulated to model cut and partial treatment in which the displacement fields at the core layer are compatibly described in terms of the displacement fields at the elastic faces. The developed model includes the least number of degree of freedom in the finite element modeling. The formulation has also been modified to consider the slippage between layers at the interfaces. Finally, by combining the finite element method and the optimization algorithms based on the genetic algorithm and sequential quadratic programming technique, a design optimization methodology has been formulated to maximize the damping characteristics using the optimal number and location of cuts and partial treatments with optimal thicknesses of top and core layers.

Chapter 5 presents the following article published in the "Journal of Intelligent Material Systems and Structures":

F. Mohammadi, R. Sedaghati, "Dynamic mechanical properties of an electrorheological fluid under large amplitude oscillatory shear strain," *Journal of Intelligent Material Systems and Structures*, Accepted to be published, doi: 10.1177/1045389X12442013.

In this article, the shear stress response and the dynamic mechanical properties of an ER fluid are experimentally investigated for small/large shear strain amplitude at moderate range of frequencies and different field intensities. A new efficient constitutive

model has also been also proposed which can accurately predict the measured experimental data. Compared with the Fourier transformation rheology, the proposed model requires less number of parameters in order to predict the stress response and the mechanical properties including storage and loss modulus for different strain amplitudes, frequencies and field intensities. This leads to considerable simplification in parameter identification process using optimization methods.

Chapter 6 presents the following article published in the "Journal of Smart Materials and Structures":

F. Mohammadi, R. Sedaghati. "Nonlinear free vibration analysis of sandwich shell structures with constrained electrorheological fluid layer," *Smart Materials and Structures* 21 (2012) 075035 (18pp).

In this article, nonlinear vibration analysis of sandwich shell structure with constrained ER fluid is investigated for different boundary conditions. To accomplish this, the nonlinear finite element model of a multilayer shell structure with ER fluid layer as the core layer has been developed. A new notation referred to as H-notation is presented over the two well-known notations referred to as B and N notations in order to represent the nonlinear equations of motion. This notation leads to considerable reduction in the computational costs caused by the time consuming integrations in the nonlinear vibration analysis of structure using direct iterating technique. Particularly, this notation is very useful for solving the nonlinear vibration analysis of sandwich layered shell structures in which large numbers of integrations are required to be repeatedly performed throughout the direct iteration method. Finally, for different boundary conditions the effects of small

and large displacements, core thickness ratio and electric field intensity on nonlinear vibration damping behavior of the sandwich shell structure are presented.

Chapter 7 presents the following article published in the "Journal of Intelligent Material Systems and Structures":

F. Mohammadi, R. Sedaghati. "Vibration Analysis and Design Optimization of Sandwich Cylindrical Panels Fully and Partially Treated with Electrorheological Fluid Materials," *Journal of Intelligent Material Systems and Structures*, DOI: 10.1177/1045389X12451195, June 2012.

In this article, vibration analysis and damping characteristics of sandwich cylindrical panel structures using semi-active electrorheological (ER) fluid treatments have been investigated for different boundary conditions. Unconstrained viscoelastic material has been used at boundaries and untreated locations to seal ER fluids. First, an efficient finite element method has been formulated to investigate the effect of electric field intensity and thickness of top constrained elastic layer on the vibration and damping performance of the viscoelastic and ER based sandwich cylindrical panel. Then a design optimization methodology has been developed to simultaneously optimize the number of unconstrained viscoelastic and constrained ER fluid patches and their distributions, thickness ratios of the ER core and constrained elastic layers to base layers and the external electric field intensity. The methodology integrates the finite element model of the sandwich panel with the combined genetic algorithm and sequential quadratic programming to effectively identify the global optimal solutions. The results show that for some boundary conditions the sandwich panel partially treated with ER fluids provides better damping performance compared with that of fully treated.

Chapter 8 includes the highlights and conclusion of the dissertation with some recommendations for further works.

CHAPTER 2

VIBRATION ANALYSIS OF SANDWICH CYLINDRICAL SHELL WITH CONSTRAINED VISCOELASTIC CORE LAYER

2.1 Introduction

Sandwich structures have many applications in industries such as automotive, aerospace and marine vehicles especially where suppression of vibration and noises are required. The sandwich structures are composed of number of layers. Depending on the application, these layers are made of different types of material such as aluminum, steel, composite and viscoelastic material. Vibration analysis of sandwich structures with viscoelastic core layer such as viscoelastic sandwich beam, plate and shell type structures have been studied by many researchers [1-14]. These studies as addressed in Chapter 1 mainly include analytical solution, finite element modeling, experimental works, parametric studies and optimization in order to increase damping properties. Increasing the thickness of the damping layer has basically no significant effect on the total mass of the sandwich cylindrical structure; however it can cause significant increase in the damping properties. A higher order model is then required for analyzing sandwich cylindrical shell with thick core layer.

In this chapter, semi-analytical finite element model is developed to analyze the sandwich cylindrical shell structure and the results including loss factors, natural frequencies and frequency response function (FRF) are obtained using both lower and higher order expansions of the displacement field through the thickness of the core layer. Continuity and discontinuity in transverse shear stresses and slopes of in-plane displacements in axial direction are considered in the finite element formulations and the

results are compared for stiff and compliant core layers. Effect of slippage between the layers is also analyzed and is shown that the imperfect bonding leads to reduction in loss factor for the majority of modes suggesting that the slippage should be prevented. The developed finite element model is then extended to consider the effect of large deflection on natural frequency and loss factor. Loss factor is calculated based on the concept of modal strain energy dissipated in each cycle for the sandwich structure. Transient vibration analysis under impulsive load is also presented using the lower and higher order models to observe the damping behavior of each model.

In the following, first, the formulation for displacement fields through the core layer is determined using the lower order model. Then, the continuity and discontinuity in transverse shear stresses and in-plane displacements (slippage effect) are formulated. This is followed by developing a higher order model for representing displacement distribution through the thickness of core layer in which the slippage between the layers is considered at interfaces. Next, the Lagrange equations are employed to develop the semi-analytical finite element formulation. The effect of large deflection is considered using non-linear Green's Strain Tensor which is based on small strain and moderate rotation. Proper shape functions and the degrees of freedom (DOF) have been chosen to accommodate different configurations considering the continuities and discontinuities in transverse shear stresses and slope of in-plane displacements.

2.2 Linear Distribution of Displacement through Thickness of the Viscoelastic Core Layer

Here, a three-layered sandwich cylindrical shell with core viscoelastic layer shown in Figure 2.1 has been considered. According to the FSDT, the dynamic displacement fields

(in terms of time) for a three layered sandwich cylindrical shell, are defined in terms of the displacements of the middle planes including u_0, v_0 and w_0 and the rotations of the normals to the middle plane in axial and circumferential directions denoted by ψ_1 and ψ_2, respectively. The total displacement field is then given as:

$$\begin{aligned} u_i(x,\theta,\xi_i,t) &= u_o^i(x,\theta,t) + \xi_i \psi_1^i(x,\theta,t) \\ v_i(x,\theta,\xi_i,t) &= v_o^i(x,\theta,t) + \xi_i \psi_2^i(x,\theta,t) \qquad -\frac{h_i}{2} < \xi_i < \frac{h_i}{2} \\ w_i &= w_i(x,\theta,t) \end{aligned} \tag{2.1}$$

The indices i=t, b and c represent respectively top, bottom and core layers and ξ_i is the coordinate in thickness direction at the middle plane of the top, bottom and core layers, respectively and $(\xi_t, \xi_b, \xi_c) = (\xi_1, \xi_2, \xi_3)$. u, v and w are respectively the total displacement in axial (x), circumferential (θ) and thickness directions. The in-plane displacements are linear through the thickness and the transverse deflection is assumed to be constant with respect to the thickness coordinate of the sandwich cylinder. It should be noted that in classical theory, since the transverse shear stresses at the elastic faces are neglected, rotations ψ_1 and ψ_2 for the top and bottom elastic layers can be represented as:

$$\psi_1 = -\frac{\partial w(x,\theta,\mathrm{t})}{\partial x} \qquad \psi_2 = -\frac{\partial w(x,\theta,\mathrm{t})}{a\partial\theta} \tag{2.2}$$

where a is the radius of the cylinder. The results from both theories are different for very thin and very thick layers due to the poor performance of classical theory for thick layers and poor performance of FSDT for very thin layers. However for very thin layers, the FSDT is in very good agreement with the classical theory if sufficient number of higher order elements is employed in the finite element modeling. In the following subsections, the displacement field for the different configurations has been derived based on the lower order expansion of the displacement fields.

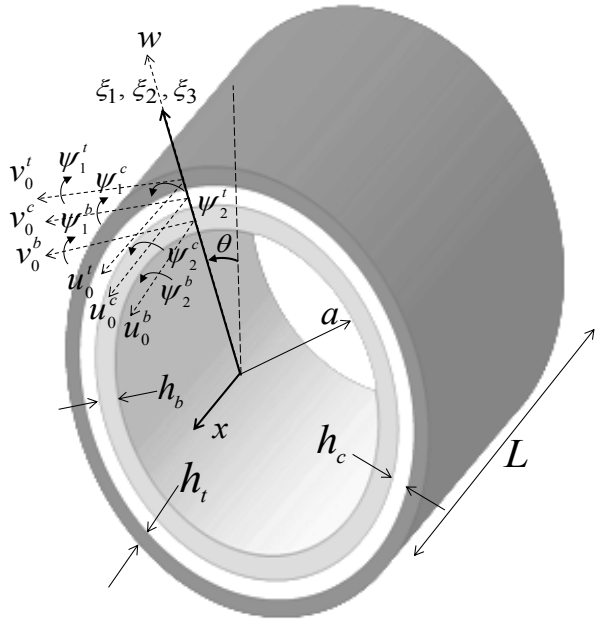

Figure 2.1 Sandwich cylindrical shell; displacements and rotations at each layer

2.2.1 Continuity in displacements and discontinuity in transverse shear stresses at the interfaces

For sandwich viscoelastic structures with compliant core layer, continuity in transverse shear stresses provides a rigid model which cannot correctly show the vibration damping behavior of the sandwich structure. In this section, the continuity is only considered for in-plane displacements and transverse deflection (perfect bonding). By implementing boundary conditions at the interfaces, displacement fields at the top and bottom layers are calculated using the displacement field at the core layer. The boundary conditions for perfect bonding can be described as:

$$\begin{aligned} &\xi_1 = -h_t/2 \text{ and } \xi_3 = h_c/2: && u_t = u_c && v_t = v_c && w_t = w_c \\ &\xi_2 = h_b/2 \text{ and } \xi_3 = -h_c/2: && u_b = u_c && v_b = v_c && w_b = w_c \end{aligned} \tag{2.3}$$

Therefore, the displacement fields of the top and bottom layers are obtained as follows:

$$u_t = u_0^c + \frac{\left(h_t\psi_1^t + h_c\psi_1^c\right)}{2} + \xi_1\psi_1^t \qquad -\frac{h_t}{2} < \xi_1 < \frac{h_t}{2} \tag{2.4}$$

$$v_t = v_0^c + \frac{\left(h_t\psi_2^t + h_c\psi_2^c\right)}{2} + \xi_1\psi_2^t$$

$$u_b = u_0^c - \frac{\left(h_b\psi_1^b + h_c\psi_1^c\right)}{2} + \xi_2\psi_1^b \qquad -\frac{h_b}{2} < \xi_2 < \frac{h_b}{2} \tag{2.5}$$

$$v_b = v_0^c - \frac{\left(h_b\psi_2^b + h_c\psi_2^c\right)}{2} + \xi_2\psi_2^b$$

2.2.2 Continuity in both displacements and transverse shear stresses at the interfaces

For viscoelastic sandwich structure, the continuity in transverse stresses is generally disregarded since the rigidity of the model for sandwich structure increases. In this chapter, the effect of this continuity has been fundamentally investigated for compliant and stiff core layers. The assumption of the continuity in transverse stresses leads to elimination of rotational displacement at the top and bottom layers. Therefore number of DOF is reduced and subsequently more rigidity in the finite element formulation is provided. In sandwich structure in which the core material is stiff enough compared to the constrained layers, this assumption provides more accurate solution. On the other hand, this assumption is not suitable for compliant viscoelastic sandwich structure. To obtain displacement fields in this case, in addition to the continuity of translational displacements, the transverse shear stresses are also equated at the interfaces as follows:

$$\begin{aligned}
&\xi_1 = -\frac{h_t}{2} && \tau_{\xi_1 x} = G_t\left(\psi_1^t + \frac{\partial w}{\partial x}\right) && \tau_{\xi_1\theta} = G_t\left(\psi_2^t + \frac{\partial w}{a\partial\theta}\right)\\
&\xi_3 = \frac{h_c}{2} && \tau_{\xi_3 x} = G_c\left(\psi_1^c + \frac{\partial w}{\partial x}\right) && \tau_{\xi_3\theta} = G_c\left(\psi_2^c + \frac{\partial w}{a\partial\theta}\right)\\
&\xi_2 = \frac{h_b}{2} && \tau_{\xi_2 x} = G_b\left(\psi_1^b + \frac{\partial w}{\partial x}\right) && \tau_{\xi_2\theta} = G_b\left(\psi_2^b + \frac{\partial w}{a\partial\theta}\right)\\
&\xi_3 = -\frac{h_c}{2} && \tau_{\xi_3 x} = G_c\left(\psi_1^c + \frac{\partial w}{\partial x}\right) && \tau_{\xi_3\theta} = G_c\left(\psi_2^c + \frac{\partial w}{a\partial\theta}\right)
\end{aligned} \tag{2.6}$$

$$\tau_{\xi_1 x} = \tau_{\xi_3 x},\ \tau_{\xi_1\theta} = \tau_{\xi_3\theta},\ \tau_{\xi_2 s} = \tau_{\xi_3 x},\ \tau_{\xi_2\theta} = \tau_{\xi_3\theta}$$

in which transverse shear stresses and shear modulus are denoted by τ and G in each layer, respectively. According to the boundary conditions in Eq. (2.6), the rotations at the top and bottom faces are obtained as:

$$\psi_1^t = \frac{G_c}{G_t}\psi_1^c + \left(\frac{G_c - G_t}{G_t}\right)\frac{\partial w}{\partial x} \qquad \psi_2^t = \frac{G_c}{G_t}\psi_2^c + \left(\frac{G_c - G_t}{G_t}\right)\frac{\partial w}{a\partial\theta}$$
$$\psi_1^b = \frac{G_c}{G_b}\psi_1^c + \left(\frac{G_c - G_b}{G_b}\right)\frac{\partial w}{\partial x} \qquad \psi_2^b = \frac{G_c}{G_b}\psi_2^c + \left(\frac{G_c - G_b}{G_b}\right)\frac{\partial w}{a\partial\theta} \tag{2.7}$$

By substituting Eq. (2.7) into Eqs (2.4) and (2.5), the displacement fields at the top and bottom elastic layers can be written in terms of the displacements and rotations of the core layer as:

$$u_t = u_0^c + \frac{h_c\psi_1^c}{2} + \left(\xi_1 + \frac{h_t}{2}\right)\left(\frac{G_c}{G_t}\psi_1^c + \left(\frac{G_c - G_t}{G_t}\right)\frac{\partial w}{\partial x}\right)$$
$$v_t = v_0^c + \frac{h_c\psi_2^c}{2} + \left(\xi_1 + \frac{h_t}{2}\right)\left(\frac{G_c}{G_t}\psi_2^c + \left(\frac{G_c - G_t}{G_t}\right)\frac{\partial w}{a\partial\theta}\right) \qquad -\frac{h_t}{2} < \xi_1 < \frac{h_t}{2} \tag{2.8}$$

and

$$u_b = u_0^c - \frac{h_c\psi_1^c}{2} + \left(\xi_2 - \frac{h_b}{2}\right)\left(\frac{G_c}{G_b}\psi_1^c + \left(\frac{G_c - G_b}{G_b}\right)\frac{\partial w}{\partial x}\right)$$
$$v_b = v_0^c - \frac{h_c\psi_2^c}{2} + \left(\xi_2 - \frac{h_b}{2}\right)\left(\frac{G_c}{G_b}\psi_2^c + \left(\frac{G_c - G_b}{G_b}\right)\frac{\partial w}{a\partial\theta}\right) \qquad -\frac{h_b}{2} < \xi_2 < \frac{h_b}{2} \tag{2.9}$$

2.2.3 Slippage between layers; discontinuity in in-plane displacements and transverse shear stresses at the interfaces

The effect of slippage between fiber and matrix on damping properties of composite structures was investigated by McLean and Read [15] and Nelson and Hancock [16]. They demonstrated that slippage reduces damping properties and should be prevented. However, by implementing complex shear modulus for the adhesive layer at the interfaces, Bai and Sun [14] showed that slippage can increase loss factor in sandwich

beam structure for a certain range of material property for the adhesive layer. In order to consider slippage and therefore discontinuity of displacements between layers, it is assumed that the core layer and the constraining elastic layers are glued by a viscoelastic adhesive layer at the interfaces [14]. Transverse shear stresses at the interfaces are calculated using the difference between in-plane displacements at the interfaces. Therefore, the boundary conditions at the interfaces given in Eq. (2.3) are modified to the following expressions:

$$\begin{aligned}
&\left(\xi_1 = -\frac{h_t}{2}, \xi_3 = \frac{h_c}{2}\right) \rightarrow \tau_{\xi_3 x} = K^*\left(u_t - u_c\right), \tau_{\xi_3 \theta} = K^*\left(v_t - v_c\right) \\
&\left(\xi_2 = \frac{h_b}{2}, \xi_3 = -\frac{h_c}{2}\right) \rightarrow \tau_{\xi_3 x} = K^*\left(u_c - u_b\right), \tau_{\xi_3 \theta} = K^*\left(v_c - v_b\right)
\end{aligned} \tag{2.10}$$

where $K^* = k(\omega)(1+ i\eta(\omega))$ is the complex shear stiffness parameter of the adhesive layer which is a function of frequency. Large values of $k(\omega)$ leads to small slippage between layers. Perfect bonding would be achieved when $k(\omega)$ is very large. By substituting displacements from Eq. (2.1) into the Eq. (2.10), the following relations are obtained:

$$\begin{aligned}
G_c\left(\psi_1^c + \frac{\partial w}{\partial x}\right) &= K^*\left(u_0^t - \frac{h_t}{2}\psi_1^t - u_0^c - \frac{h_c}{2}\psi_1^c\right) \\
G_c\left(\psi_2^c + \frac{\partial w}{a\partial \theta}\right) &= K^*\left(v_0^t - \frac{h_t}{2}\psi_2^t - v_0^c - \frac{h_c}{2}\psi_2^c\right) \\
G_c\left(\psi_1^c + \frac{\partial w}{\partial x}\right) &= K^*\left(u_0^c - \frac{h_c}{2}\psi_1^c - u_0^b - \frac{h_b}{2}\psi_1^b\right) \\
G_c\left(\psi_2^c + \frac{\partial w}{a\partial \theta}\right) &= K^*\left(v_0^c - \frac{h_c}{2}\psi_2^c - v_0^b - \frac{h_b}{2}\psi_2^b\right)
\end{aligned} \tag{2.11}$$

Considering Eq. (2.11), the displacement fields in the elastic faces given in Eq. (2.1) may be rewritten as:

$$u_t = u_0^c + \frac{\left(h_t\psi_1^t + h_c\psi_1^c\right)}{2} + \xi_1\psi_1^t + \frac{G_c}{K^*}\left(\psi_1^c + \frac{\partial w}{\partial x}\right)$$
$$v_t = v_0^c + \frac{\left(h_t\psi_2^t + h_c\psi_2^c\right)}{2} + \xi_1\psi_2^t + \frac{G_c}{K^*}\left(\psi_2^c + \frac{\partial w}{a\partial\theta}\right) \qquad -\frac{h_t}{2} < \xi_1 < \frac{h_t}{2} \qquad (2.12)$$

$$u_b = u_0^c - \frac{\left(h_b\psi_1^b + h_c\psi_1^c\right)}{2} + \xi_2\psi_1^b - \frac{G_c}{K^*}\left(\psi_1^c + \frac{\partial w}{\partial x}\right)$$
$$v_b = v_0^c - \frac{\left(h_b\psi_2^b + h_c\psi_2^c\right)}{2} + \xi_2\psi_2^b - \frac{G_c}{K^*}\left(\psi_2^c + \frac{\partial w}{a\partial\theta}\right) \qquad -\frac{h_b}{2} < \xi_2 < \frac{h_b}{2} \qquad (2.13)$$

2.3 Nonlinear Distribution of Displacements through Thickness of the Viscoelastic Core Layer

In a thick viscoelastic layer with compliant material property, the displacement fields vary through the thickness and therefore the lower order expansion of displacement field through the thickness may not be accurate enough. In this section, a nonlinear model for distribution of the displacement fields through the thickness of the core layer is formulated. Here, it is assumed that the in-plane normal and shear stresses at the core layer are negligible. According to the equilibrium equations, transverse shear stresses are constant with respect to the transfer direction through the thickness of the core layer. The normal stress in thickness direction and the slippage between layers at the interfaces, however, are considered. The following nonlinear polynomial displacement fields for the core layer are assumed:

$$u_c = u_0^c + \xi_3\Phi_1^c + {\xi_3}^2\Phi_2^c + {\xi_3}^3\Phi_3^c$$
$$v_c = v_0^c + \xi_3\Theta_1^c + {\xi_3}^2\Theta_2^c + {\xi_3}^3\Theta_3^c \qquad -\frac{h_c}{2} < \xi_3 < \frac{h_c}{2} \qquad (2.14)$$
$$w_c = w_0^c + \xi_3\,\Psi_1^c + {\xi_3}^2\Psi_2^c$$

Transverse shear strains are related to the constant transverse shear stresses as:

$$\gamma_{\xi_3 x} = \frac{\tau_{\xi_3 x}}{G_c} = \frac{2(1+\upsilon_c)}{E_c}\tau_{\xi_3 x} = 2(1+\upsilon_c)\beta_1$$
$$\gamma_{\xi_3 \theta} = \frac{\tau_{\xi_3 \theta}}{G_c} = \frac{2(1+\upsilon_c)}{E_c}\tau_{\xi_3 \theta} = 2(1+\upsilon_c)\beta_2 \quad (2.15)$$

where

$$\beta_1 = \frac{\tau_{\xi_3 x}}{E_c}\ , \quad \beta_2 = \frac{\tau_{\xi_3 \theta}}{E_c}\ ,$$

E_c and υ_c are respectively Young modules and Poisson's ratio of the core material. Shear strains can be calculated using the displacement distribution stated in Eq. (2.14) as follows:

$$\gamma_{\xi_3 x} = \frac{\partial u_c}{\partial \xi_3} + \frac{\partial w_c}{\partial x} = \Phi_1^c + 2\xi_3 \Phi_2^c + 3{\xi_3}^2 \Phi_3^c + \frac{\partial w_0^c}{\partial x} + \xi_3 \frac{\partial \Psi_1^c}{\partial x} + {\xi_3}^2 \frac{\partial \Psi_2^c}{\partial x}$$
$$\gamma_{\xi_3 \theta} = \frac{\partial v}{\partial \xi_3} + \frac{\partial w}{a\partial \theta} = \Theta_1^c + 2\xi_3 \Theta_2^c + 3{\xi_3}^2 \Theta_3^c + \frac{\partial w_0^c}{a\partial \theta} + \xi_3 \frac{\partial \Psi_1^c}{a\partial \theta} + {\xi_3}^2 \frac{\partial \Psi_2^c}{a\partial \theta} \quad (2.16)$$

Equating the coefficient of ${\xi_3}^0$, ${\xi_3}^1$ and ${\xi_3}^2$ in Eqs (2.15) and (2.16) yields the following relations:

$$\Phi_1^c + \frac{\partial w_0^c}{\partial x} = 2(1+\upsilon_c)\beta_1 \qquad 2\Phi_2^c + \frac{\partial \Psi_1^c}{\partial x} = 0 \qquad 3\Phi_3^c + \frac{\partial \Psi_2^c}{\partial x} = 0$$
$$\Theta_1^c + \frac{\partial w_0^c}{a\partial \theta} = 2(1+\upsilon_c)\beta_2 \qquad 2\Theta_2^c + \frac{\partial \Psi_1^c}{a\partial \theta} = 0 \qquad 3\Theta_3^c + \frac{\partial \Psi_2^c}{a\partial \theta} = 0 \quad (2.17)$$

Now, substituting $\Phi_1^c, \Phi_2^c, \Phi_3^c, \Theta_1^c, \Theta_2^c$ and Θ_3^c from Eq. (2.17) into Eq. (2.14) yields the in-plane displacement fields through the thickness of the core layer as:

$$u_c = u_c^0 + \xi_3\left(2(1+\upsilon_c)\beta_1 - \frac{\partial w_0^c}{\partial x}\right) - \frac{{\xi_3}^2}{2}\frac{\partial \Psi_1^c}{\partial x} - \frac{{\xi_3}^3}{3}\frac{\partial \Psi_2^c}{\partial x}$$
$$v_c = v_c^0 + \xi_3\left(2(1+\upsilon_c)\beta_2 - \frac{\partial w_0^c}{a\partial \theta}\right) - \frac{{\xi_3}^2}{2}\frac{\partial \Psi_1^c}{a\partial \theta} - \frac{{\xi_3}^3}{3}\frac{\partial \Psi_2^c}{a\partial \theta} \quad (2.18)$$

The relation between normal stress and normal strain can be expressed as:

$$\sigma_{xx} = \frac{E_c}{(1+\upsilon_c)(1-2\upsilon_c)}\left[(1-\upsilon_c)\varepsilon_{xx} + \upsilon_c\left(\varepsilon_{\theta\theta} + \varepsilon_{\xi_3\xi_3}\right)\right]$$
$$\sigma_{\theta\theta} = \frac{E_c}{(1+\upsilon_c)(1-2\upsilon_c)}\left[(1-\upsilon_c)\varepsilon_{\theta\theta} + \upsilon_c\left(\varepsilon_{\xi_3\xi_3} + \varepsilon_{xx}\right)\right] \quad (2.19)$$
$$\sigma_{\xi_3\xi_3} = \frac{E_c}{(1+\upsilon_c)(1-2\upsilon_c)}\left[(1-\upsilon_c)\varepsilon_{\xi_3\xi_3} + \upsilon_c\left(\varepsilon_{\theta\theta} + \varepsilon_{xx}\right)\right]$$

in which σ_{xx}, $\sigma_{\theta\theta}$ and $\sigma_{\xi 3\xi 3}$ are normal stresses in axial, hoop and transverse direction, respectively, and ε_{xx}, $\varepsilon_{\theta\theta}$ and $\varepsilon_{\xi 3\xi 3}$ are the corresponding normal strains. As mentioned before, the in-plane normal stresses are neglected. This assumption is reasonable since the strain energy related to these stresses is small compared with the strain energy due to the transverse shear stresses. Also the forces in these directions are carried by the elastic faces. Thus $\sigma_{xx} \approx 0$ and $\sigma_{\theta\theta} \approx 0$ and from Eq. (2.19) the in-plane normal strains can be written as:

$$\varepsilon_{xx} = -\frac{\upsilon_c}{1-\upsilon_c}\left(\varepsilon_{\theta\theta} + \varepsilon_{\xi_3\xi_3}\right)$$
$$\varepsilon_{\theta\theta} = -\frac{\upsilon_c}{1-\upsilon_c}\left(\varepsilon_{\xi_3\xi_3} + \varepsilon_{xx}\right) \quad (2.20)$$

In order to define the profile of the displacement field in the core layer, the relative governing equilibrium equation with neglecting the inertia forces is employed which can be written as:

$$\frac{\partial \tau_{\xi_3 x}}{\partial x} + \frac{\partial \tau_{\xi_3 \theta}}{a\partial \theta} + \frac{\partial \sigma_{\xi_3 \xi_3}}{\partial \xi_3} = 0 \quad (2.21)$$

The displacement field is afterward adjusted to fulfill the dynamic motion of the core layer. Substituting $\tau_{\xi 3x}$, $\tau_{\xi 3\theta}$ and $\sigma_{\xi 3\xi 3}$ from Eq. (2.15) and (2.19) into Eq. (2.21) gives the following relation between β_1 and β_2:

$$\frac{\partial \beta_1}{\partial x}+\frac{\partial \beta_2}{a\partial \theta}=-\frac{\frac{\partial}{\partial \xi_3}\left[(1-\upsilon_c)\varepsilon_{\xi_3\xi_3}+\upsilon_C\left(\varepsilon_{\theta\theta}+\varepsilon_{xx}\right)\right]}{(1+\upsilon_c)(1-2\upsilon_c)} \tag{2.22}$$

Using Eq. (2.20) and normal transverse strain-displacement relation ($\varepsilon_{\xi3\xi3} = \partial w/\partial\xi_3$), Eq. (2.22) is simplified to the following equation:

$$\frac{\partial \beta_1}{\partial x}+\frac{\partial \beta_2}{a\partial \theta}=-\frac{\partial^2 w_c}{\partial {\xi_3}^2} \tag{2.23}$$

Now, by substituting w_c from Eq. (2.14) into Eq. (2.23), Ψ_2^c is obtained as:

$$\Psi_2^c=-\frac{\left(\frac{\partial \beta_1}{\partial s}+\frac{\partial \beta_2}{a\partial \theta}\right)}{2} \tag{2.24}$$

Finally, substituting Eq (2.24) into Eq. (2.14) yields the transverse displacement through the thickness of the core layer as follows:

$$w_c=w_c^0+\xi_3\,\Psi_1^c-\frac{{\xi_3}^2}{2}\left(\frac{\partial \beta_1}{\partial x}+\frac{\partial \beta_2}{a\partial \theta}\right) \tag{2.25}$$

The boundary conditions mentioned in Eq. (2.10) which include the slippage effect are implemented in order to obtain the displacement distribution at the elastic faces. If u_0^c, v_0^c, w_0^c, Ψ_1^c, β_1 and β_2 are the translational and rotational displacements at the middle of core layer, then the translational displacements at the middle of top and bottom elastic faces are obtained in terms of the displacements fields at the core layer. Therefore, the displacement fields through the top and bottom layers are determined as follows:

$$
\begin{aligned}
u_t &= u_0^c + \frac{h_c}{2}\left(2(1+\upsilon_c)\beta_1 - \frac{\partial w_0^c}{\partial x}\right) - \frac{h_c^2}{8}\frac{\partial \Psi_1^c}{\partial x} + \frac{h_c^3}{48}\left(\frac{\partial^2 \beta_1}{\partial s^2} + \frac{\partial^2 \beta_2}{a\,\partial\theta\,\partial x}\right) + \frac{h_t}{2}\psi_1^t \\
&\quad + \xi_1 \psi_1^t + 2(1+\upsilon_c)\beta_1 \frac{G_c}{K^*} \\
v_t &= v_0^c + \frac{h_c}{2}\left(2(1+\upsilon_c)\beta_2 - \frac{\partial w_0^c}{a\partial\theta}\right) - \frac{h_c^2}{8}\frac{\partial \Psi_1^c}{a\partial\theta} + \frac{h_c^3}{48}\left(\frac{\partial^2 \beta_1}{a\,\partial\theta\,\partial s} + \frac{\partial^2 \beta_2}{a^2\partial\theta^2}\right) + \frac{h_t}{2}\psi_2^t \\
&\quad + \xi_1 \psi_2^t + 2(1+\upsilon_c)\beta_2 \frac{G_c}{K^*} \\
w_t &= w_0^c + \frac{h_c}{2}\Psi_1^c - \frac{h_c^2}{8}\left(\frac{\partial \beta_1}{\partial x} + \frac{\partial \beta_2}{a\,\partial\theta}\right)
\end{aligned}
\tag{2.26}
$$

$$
\begin{aligned}
u_b &= u_0^c - \frac{h_c}{2}\left(2(1+\upsilon_c)\beta_1 - \frac{\partial w_0^c}{\partial x}\right) - \frac{h_c^2}{8}\frac{\partial \Psi_1^c}{\partial x} - \frac{h_c^3}{48}\left(\frac{\partial^2 \beta_1}{\partial x^2} + \frac{\partial^2 \beta_2}{a\,\partial\theta\,\partial x}\right) - \frac{h_b}{2}\psi_1^b \\
&\quad + \xi_2 \psi_1^b - 2(1+\upsilon_c)\beta_1 \frac{G_c}{K^*} \\
v_b &= v_0^c - \frac{h_c}{2}\left(2(1+\upsilon_c)\beta_2 - \frac{\partial w_0^c}{a\partial\theta}\right) - \frac{h_c^2}{8}\frac{\partial \Psi_1^c}{a\partial\theta} - \frac{h_c^3}{48}\left(\frac{\partial^2 \beta_1}{a\,\partial\theta\,\partial x} + \frac{\partial^2 \beta_2}{a^2\partial\theta^2}\right) - \frac{h_b}{2}\psi_2^b \\
&\quad + \xi_2 \psi_2^b - 2(1+v_c)\beta_2 \frac{G_c}{K^*} \\
w_b &= w_0^c - \frac{h_c}{2}\Psi_1^c - \frac{h_c^2}{8}\left(\frac{\partial \beta_1}{\partial x} + \frac{\partial \beta_2}{a\,\partial\theta}\right)
\end{aligned}
\tag{2.27}
$$

2.4 Semi-Analytical Finite Element Method

In order to drive the equations of motion in the finite element form, the Lagrange's equation is employed. Considering this, the kinetic and potential energies in sandwich cylindrical shell should be determined in terms of the displacements. In this chapter the effect of geometric nonlinearity has been also investigated using von Karman's hypothesis. According to this hypothesis, for infinitesimal in-plane displacements *u* and *v*, the nonlinear terms which only depend on *w* are contributed in the strain-displacement relations. The nonlinear strain–displacement relation using non-linear Green's Strain

Tensor which are based on small strain and moderate rotation for a cylindrical shell element can be expressed as follows [94]:

$$\varepsilon_{xx}^{i}=\left(\frac{\partial u_i}{\partial x}+\frac{1}{2}\left(\frac{\partial w_i}{\partial x}\right)^2\right)\qquad \varepsilon_{\theta\theta}=\frac{1}{1+\xi_i/a}\left(\frac{\partial v_i}{a\partial\theta}+\frac{w_i}{a}+\frac{1}{2}\left(\frac{\partial w_i}{a\partial\theta}\right)^2\right)\qquad \varepsilon_{\xi_i\xi_i}=\frac{\partial w_i}{\partial\xi_i}$$

$$\gamma_{x\theta}^{i}=\left(\frac{\partial v_i}{\partial x}\right)+\frac{1}{1+\xi_i/a}\left(\frac{\partial u_i}{a\partial\theta}\right)+\frac{\partial w_i}{a\partial\theta}\frac{\partial w_i}{\partial x}\qquad \gamma_{\xi_i x}^{i}=\frac{\partial u_i}{\partial\xi_i}+\frac{\partial w_i}{\partial x} \tag{2.28}$$

$$\gamma_{\xi_i\theta}^{i}=\frac{\partial v_i}{\partial\xi_i}+\frac{1}{1+\xi_i/a}\left(\frac{\partial w_i}{a\partial\theta}-\frac{v_i}{a}\right)$$

It should be noted that if the thickness of each layer is small compared to the radius, then the ratio ξ_i/a can be neglected. Kinetic energy T and strain energy U of an element can be expresses as follows:

$$T_i=\int_{-\frac{h_i}{2}}^{\frac{h_i}{2}}\int_0^{2\pi}\int_{-\frac{L_e}{2}}^{\frac{L_e}{2}}\frac{1}{2}\rho_i\left(\dot{u}_i^{\,2}+\dot{v}_i^{\,2}+\dot{w}_i^{\,2}\right)\mathrm{d}V_i \tag{2.29}$$

$$U_i=\int_{-\frac{h_i}{2}}^{\frac{h_i}{2}}\int_0^{2\pi}\int_{-\frac{L_e}{2}}^{\frac{L_e}{2}}\frac{1}{2}\left(\sigma_{ss}^{i}\,\varepsilon_{ss}^{i}+\sigma_{\theta\theta}^{i}\,\varepsilon_{\theta\theta}^{i}+\sigma_{\xi_i\xi_i}^{i}\,\varepsilon_{\xi_i\xi_i}^{i}+\tau_{s\theta}^{i}\,\gamma_{s\theta}^{i}+\tau_{\xi_i s}^{i}\,\gamma_{\xi_i s}^{i}+\tau_{\xi_i\theta}^{i}\,\gamma_{\xi_i\theta}^{i}\right)\mathrm{d}V_i \tag{2.30}$$

where i=t, b and c, $\mathrm{d}V_i=(a+\xi_i)\mathrm{d}\theta\mathrm{d}x\,\mathrm{d}\xi_i$, L_e is the length of cylindrical shell element and ρ is density. Using the constitutive equation and strain-displacement relations, kinetic and strain energies are determined for each layer. The displacements fields derived before for different combinations of assumption including slippage, continuity in transverse shear stress, and nonlinearity in the distribution of displacements through the thickness of core, will be substituted into Eq. (2.28) and subsequently into Eq. (2.29) and (2.30) to obtain the kinetic and strain energies with respect to relative displacement components.

In order to develop the governing differential equations in the finite element form, the displacement fields should be related to the identified nodal displacement components

using the shape functions. Here, the semi-analytical finite element approach has been used in which the displacement fields in circumferential direction has been expressed analytically using Fourier expansion and discretized in the axial direction using appropriate shape functions. Considering this, the displacement fields for the different assumptions discussed before can be presented in the following form:

$$
\begin{aligned}
w_0^c &= \sum_{j=1}^{m}\sum_{n=0}^{\infty} N_j w_j^c \cos(n\theta-\varphi) & v_0^c &= \sum_{j=1}^{m}\sum_{n=0}^{\infty} N_j v_j^c \sin(n\theta-\varphi)\\
u_0^c &= \sum_{j=1}^{m}\sum_{n=0}^{\infty} N_j u_j^c \cos(n\theta-\varphi) & \Psi_1^c &= \sum_{j=1}^{m}\sum_{n=0}^{\infty} N_j \Psi_{1j}^c \cos(n\theta-\varphi)\\
\beta_1 &= \sum_{j=1}^{m}\sum_{n=0}^{\infty} N_j \beta_{j1} \cos(n\theta-\varphi) & \beta_2 &= \sum_{j=1}^{m}\sum_{n=0}^{\infty} N_j \beta_{j2} \sin(n\theta-\varphi)\\
\psi_1^i &= \sum_{j=1}^{m}\sum_{n=0}^{\infty} N_j \psi_{j1}^i \cos(n\theta-\varphi) & \psi_2^i &= \sum_{j=1}^{m}\sum_{n=0}^{\infty} N_j \psi_{j2}^i \sin(n\theta-\varphi)
\end{aligned}
\tag{2.31}
$$

in which $i=t$, b and c, and m is the number of nodes for each cylindrical shell element in axial direction. Since in the cylindrical shell there is no preference for the orientation of circumferential modes, an arbitrary phase angle denoted by φ must be included [119]. The orientations of the modes depend on the distribution of the external forces. In general, $\varphi=\varphi_0$ and $\varphi=\varphi_0+\pi/2$ in which φ_0 is an arbitrary constant.

Table 2.1 Required DOFs for different finite element models based on the different assumptions and theories.

DOF		
Continuity in transverse shear stresses	Continuity in in-plane slopes	Model
$\text{DOF}=[u_0^c\ v_0^c\ w_0^c\ \psi_1^c\ \psi_2^c\ \psi_1^t\ \psi_2^t\ \psi_1^b\ \psi_2^b]$		
Discontinuous	Discontinuous	Lower Order
$\text{DOF}=[u_0^c\ v_0^c\ w_0^c\ \psi_1^c\ \psi_2^c]$		
Continuous	Discontinuous	Lower Order
$\text{DOF}=[u_0^c\ v_0^c\ w_0^c\ \psi_1^c\ \psi_2^c\ \frac{\partial u_0^c}{\partial s}\ \frac{\partial v_0^c}{\partial s}]$		
Continuous	Continuous	Lower Order
$\text{DOF}=[u_0^c\ v_0^c\ w_0^c\ \beta_1^c\ \beta_2^c\ \Psi_1^c\ \psi_1^t\ \psi_2^t\ \psi_1^b\ \psi_2^b]$		
Discontinuous	Discontinuous	Higher Order

The nodal displacements associated with the different assumptions and approaches are summarized in Table 2.1. Considering three-node elements in axial direction, the Lagrangian shape functions N_1, N_2 and N_3 according to FSDT can be expressed as:

$$N_1 = \frac{2x^2}{{L_e}^2} - \frac{x}{L_e} \qquad N_2 = 1 - \frac{4x^2}{{L_e}^2} \qquad N_3 = \frac{2x^2}{{L_e}^2} + \frac{x}{L_e} \tag{2.32}$$

where the coordinate is located at the center of element. The continuity in the slope of in-plane displacements provided in Table 2.1 can also be applied by considering these rotations as a part of the degrees of freedom. Therefore the in-plane displacements u and v at the core layer can be written as:

$$u_0^c = \sum_{n=0}^{\infty} \left(N_4 u_1 + N_5 \left.\frac{\partial u_0^c}{\partial x}\right|_1 + N_6 u_2 + N_7 \left.\frac{\partial u_0^c}{\partial x}\right|_2 + N_8 u_3 + N_9 \left.\frac{\partial u_0^c}{\partial x}\right|_3 \right) \cos(n\theta - \varphi) \tag{2.33}$$

$$v_0^c = \sum_{n=0}^{\infty} \left(N_4 v_1 + N_5 \left.\frac{\partial v_0^c}{\partial x}\right|_1 + N_6 v_2 + N_7 \left.\frac{\partial v_0^c}{\partial x}\right|_2 + N_8 v_3 + N_9 \left.\frac{\partial v_0^c}{\partial x}\right|_3 \right) \sin(n\theta - \varphi) \tag{2.34}$$

where the Lagrangian shape functions N_4 through N_9 are determined as:

$$\begin{aligned}
N_4 &= \frac{2x^2}{{L_e}^2} - \frac{10x^3}{{L_e}^3} - \frac{8x^4}{{L_e}^4} + \frac{24x^5}{{L_e}^5} & N_5 &= \frac{x^2}{2{L_e}^2} - \frac{x^3}{{L_e}^3} - \frac{2x^4}{{L_e}^4} + \frac{4x^5}{{L_e}^5} \\
N_6 &= 1 - \frac{8x^2}{{L_e}^2} + \frac{16x^4}{{L_e}^4} & N_7 &= x - \frac{8x^3}{{L_e}^3} + \frac{16x^5}{{L_e}^5} \\
N_8 &= \frac{4x^2}{{L_e}^2} + \frac{10x^3}{{L_e}^3} - \frac{8x^4}{{L_e}^4} - \frac{24x^5}{{L_e}^5} & N_9 &= -\frac{x^2}{2{L_e}^2} - \frac{x^3}{{L_e}^3} + \frac{2x^4}{{L_e}^4} + \frac{4x^5}{{L_e}^5}
\end{aligned} \tag{2.35}$$

Now the displacement fields for each layer, strain-displacement relation and stress-strain relations are substituted into Eqs (2.29) and (2.30) to obtain the strain and kinetic energies in each layer. Consequently, the kinetic and strain energies in each element can be expressed as:

$$T = T_{\text{top}} + T_{\text{core}} + T_{\text{bottom}}$$
$$U = U_{\text{top}} + U_{\text{core}} + U_{\text{bottom}} \tag{2.36}$$

As mentioned before, Lagrange's equation is used here to establish the governing equations of motion:

$$\frac{\mathrm{d}}{\mathrm{d}t}\left(\frac{\partial T}{\partial \dot{q}_k}\right) - \left(\frac{\partial T}{\partial q_k}\right) + \left(\frac{\partial U}{\partial q_k}\right) = F_k \quad k = 1, \cdots, n \tag{2.37}$$

where n is the total DOF in the sandwich panel structure, q and F are the nodal displacements and applied external force, respectively, and T and U are respectively the kinetic and potential energies in the sandwich shell structure. Substituting Eq. (2.36) into the Lagrange's equation and assembling all the elements in the axial direction will yield the following finite element equation of motions:

$$[M]\{\ddot{q}\} + [K]\{q\} = \{F(t)\} \tag{2.38}$$

where $\{F\}$ is the equivalent nodal force, $[K]=[K'(\omega)+\mathrm{i}K''(\omega)]$ is a complex frequency dependent stiffness matrix, $[M]$ is the mass matrix and $\{q\}$ is the vector of nodal displacements in cylindrical shell. To obtain the modal characteristics of the viscoelastic structures, one can write Eq. (2.38) in the following form:

$$\left(-\omega^2[M] + [K(\omega)]\right)\{q\} = 0 \tag{2.39}$$

It should be noted that two sources of nonlinearity including frequency and large deformation exist in the stiffness matrix. Considering this, one cannot use the direct eigenvalue analysis to identify the natural frequencies and associated mode shapes. To calculate the effect of large deformation, the nonlinear terms in Eq. (2.28) are expressed as follows:

$$\frac{1}{2}\left(\frac{\partial w}{\partial x}\right)^2 = \frac{1}{2} f_1 \left(\frac{\partial w}{\partial x}\right) \qquad \frac{\partial w}{a\partial\theta}\frac{\partial w}{\partial x} = f_2 \frac{\partial w}{\partial x} \qquad \frac{1}{2}\left(\frac{\partial w}{a\partial\theta}\right)^2 = \frac{1}{2} f_2 \left(\frac{\partial w}{a\partial\theta}\right) \tag{2.40}$$

where

$$f_1 = \left(\frac{\partial w}{\partial x}\right) \text{ and } f_2 = \frac{\partial w}{a\partial\theta}$$

Thus, the total stiffness matrix has two distinct linear and nonlinear parts as follows.

$$[K(\omega)] = [K_1(\omega)]^{\mathrm{L}} + [K_2(\omega)]^{\mathrm{NL}} \tag{2.41}$$

For the case of small deflection (ignoring $[K_2(\omega)]^{\mathrm{NL}}$ in Eq. (2.41)), one may use the direct forced harmonic response method for a wide frequency range to obtain the natural frequencies. If the harmonic force function is expressed as $F = F_0 \, e^{i\omega t}$ then the Eq. (2.38) can be written as:

$$\left(-\omega^2[M] + [K(\omega)]\right)\{\tilde{q}\} = \{F_0\} \tag{2.42}$$

where $\tilde{q}$ is the amplitude of the vibration. The natural frequencies associated with transverse vibration can be calculated using the frequency response by solving the set of linear equations solved at different frequencies. Thus the solution strongly depends on the resolution of frequency axis and the computational costs may be expensive. Another method to find the natural frequency and the corresponding mode shapes is iterative process. The eigenvalue problem of Eq. (2.39) is solved iteratively using the evaluated stiffness matrix at the natural frequencies. The starting points for each mode in the iteration can be the evaluated stiffness matrix at the natural frequencies of the bare cylinder. Here an iterative procedure has also been implemented to identify modal characteristics considering large deformation. Therefore, two iterative procedures (one due to dependency on the natural frequencies and another due to large deformation) are

required to evaluate natural frequencies and the corresponding mode shapes for large deflection of sandwich layered structure. The developed algorithm for this iterative process is summarized as follows:

1. By neglecting the nonlinear terms f_1 and f_2, the eigenvalue problem is solved for small deflection.
2. The solution of nonlinear eigenvalue problem is started using the stiffness matrix evaluated at the natural frequency of the bare cylinder for each fundamental mode in circumferential direction. The properties of the viscoelastic material are evaluated at the new natural frequency. New eigenvalue problem is then established using the new properties.
3. The iteration continues until the following defined criteria is achieved:

$$\frac{\left|\omega_{j,i} - \omega_{j,i-1}\right|}{\omega_{j,i-1}} \leq \lambda_1$$

where $\omega_{j,i}$ and $\omega_{j,i\text{-}1}$ are the current and previous states of the real part of the frequency at iteration j related to the nonlinearity in large deformation and λ_1 is tolerance of convergence and is chosen to be 10^{-6}.

4. The corresponding eigenvectors $\{V_0\}$ associated to the eigenvalues are calculated using the standard algorithms for extracting eigenvectors.
5. The obtained eigenvectors should be normalized and scaled up. In nonlinear free vibration, natural frequencies depend on the deformed configuration of the structure. After normalization, in order to scale up the eigenvectors, maximum deflection is assumed to be proportional to the thickness of the cylinder. Therefore an arbitrary configuration can be expressed as follows:

$$\{V\} = Dh\{V_0\}$$

where h is the thickness of the cylinder and D is the coefficient of proportion. Since the effect of the large deformation is investigated assuming linear elastic and viscoelastic properties respectively for the constraining and constrained layers, the maximum transverse displacement should not be large so that the materials enter the nonlinear regime. Consequently the coefficient of the proportion D should not exceed some certain value which depends on the material properties and the dimensions of the layers. For large deformation, the maximum deflection considered in the literatures has been assumed to be of the same order as the thickness. Here, the maximum deflection is chosen to be less than twice of the bare layer thickness ($D \leq 2$) which can be applied for the layers with high enough yielding stress in which they do not enter the nonlinear regime.

6. The nonlinear terms f_1 and f_2 can now be calculated to update the non-linear relation between the strain and displacement.

7. Steps 2-6 are repeated until to reach a frequency which provides the desired convergence as follows:

$$\frac{\left|\omega_{j,i} - \omega_{j-1,i}\right|}{\omega_{j-1,i}} \leq \lambda_2$$

in which λ_2 is the tolerance of convergence and is chosen to be 10^{-5}.

8. The whole procedure is repeated for diffrenet value of D.

Damping property of sandwich structure is related to the imaginary part of stiffness matrix. As mentioned before, the loss factor is defined as the ratio of dissipated energy per radian and maximum potential energy at natural frequency. Thus:

$$\eta_i = \frac{\{\phi_i\}^{\mathrm{T}}[K'']\{\phi_i\}}{\{\phi_i\}^{\mathrm{T}}[K']\{\phi_i\}} \tag{2.43}$$

where η_i is the loss factor related to the i^{th} mode, $\{\phi\}$ is the normalized eigenvector in free vibration, K' and K'' are respectively real and imaginary parts of the stiffness matrix.

2.5 Transient Vibration

In this section, transient response for the lower or higher order models is formulated. The forced vibration of a sandwich structure with viscoelastic layer is given in Eq. (2.38). Since the viscoelastic material properties depend on the frequency, the above equation cannot be solved using direct integration method or modal superposition method as the material property should be expressed in the time domain. Using the Discrete Fourier Transform (DFT) technique, Eq. (2.38) can be solved in frequency domain [120-122]. The time response of the equation subsequently is obtained by using Inverse Discrete Fourier Transform (IDFT). Implementing DFT on Eq. (2.38) yields the following equation in frequency domain as:

$$\left([K(\omega_j)] - \omega_j^2[M]\right)\{\tilde{q}(\omega_j)\} = \{\tilde{F}(\omega_j)\} \tag{2.44}$$

where

$$\{\tilde{F}(\omega_j)\} = \Im\{F(t_k)\} = \sum_{k=1}^{N} F(t_k) e^{\frac{-2\pi i}{N}(j-1)(k-1)}$$

ω_j is a set of discrete frequencies of the frequency response $\tilde{q}(\omega_j)$ and frequency spectra of the force $\tilde{F}(\omega_j)$, t_k is a set of discrete times for the time response $q(t_k)$ and the transient force $F(t_k)$, and N is number of samples. DFT and IDFT are also denoted by $\Im$ and $\Im^{-1}$, respectively.

Eq. (2.44) can be solved for $\tilde{q}(\omega_j)$ as follows:

$$\{\tilde{q}(\omega_j)\} = \frac{\{\tilde{F}(\omega_j)\}}{[K(\omega_j)] - \omega_j^2[M]} \tag{2.45}$$

Time response of the Eq. (2.45) can be obtained using IDFT as:

$$\{q(t_k)\} = \Im^{-1}\{\tilde{q}(\omega_j)\} = \frac{1}{N}\sum_{k=1}^{N}\tilde{q}(\omega_j)e^{\frac{2\pi i}{N}(j-1)(k-1)} \tag{2.46}$$

The choice of N depends on the shape of frequency response, accuracy and the capacity of computation [120]. For the inverse transformation, the interval of frequency $\Delta\omega$ must be the reciprocal of the total time as follows:

$$\Delta\omega = \frac{2\pi}{N\Delta t} \tag{2.47}$$

2.6 Results and Discussion

The finite element model is first validated for a bare cylindrical shell by comparing the natural frequencies presented in this chapter with the results reported in literatures. For sandwich cylindrical structure, the natural frequency and loss factor resulted by different finite element formulations are also compared with those in the literatures. The different finite element formulations are developed based on the different assumptions including the continuity or discontinuity in transverse stress and slopes of in-plane displacements in axial direction. Also, the results based on the lower and higher order expansions of displacement through thickness of the core layer have been compared for different boundary conditions. Furthermore, parametric studies are presented to show the effect of slippage on the loss factors. The effect of large deformation on the natural frequencies and the corresponding loss factors is also investigated and finally, to show the damping

behavior of both lower and higher order models, the transient response of the sandwich structure shell under impulse loading is presented using both models.

2.6.1 Validation of the finite element model

The free vibration characteristics of bare cylindrical shell at different circumferential and axial modes are compared with those presented in literatures. Djoudi and Bahai [123] investigated finite element model of cylindrical shallow shell based on assumed strain fields developed by Ashwel and Sabir [124]. Chung [125] developed analytical method to evaluate natural frequencies in the bare cylindrical shell. The length, thickness and radius of the cylinder are respectively 511.2 mm, 1.5 mm and 216.2 mm.

Table 2.2 Natural frequencies (Hz) of clamped-free bare cylindrical shell

m	*n*	Present study	Reference [123]	Nastran [125]	Analytical [125]
1	1	**857.5**	-	-	-
	2	**405.6**	403.91	410.1	403.72
	3	**225.1**	224.79	232.2	223.34
	4	**174.6**	172.4	180.5	171.77
	5	**203.6**	203.37	206.2	199.16
	6	**274.9**	274.04	275.5	268.86
	7	**369.8**	369.8	370.1	361.92
	8	**482.5**	482.96	483.5	472.54
	9	**611.1**	611.42	614	599.03
	10	**755.4**	755.14	—	740
2	2	**1440.5**	1446.56	—	1437.11
	3	**932.9**	940.2	943.2	928.28
	4	**649.4**	647.25	671.4	644.48
	5	**500.0**	509.11	529.3	494.69
	6	**448.6**	442.16	478	442
	7	**473.1**	477.32	496.9	464.59
	8	**550.0**	542.69	567.2	539.45
	9	**661.2**	656.06	673.2	648.34
	10	**796.5**	788.39	—	781.15
3	2	**2491.3**	2530.79	—	2487.6
	3	**1841.5**	1876.8	—	1834.82
	4	**1376.1**	1412.72	—	1367.64
	5	**1066.3**	1103.56	—	1057.12
	6	**874.7**	875.29	—	864.82
	7	**795.97**	789.5	—	767.65
	8	**763.3**	748.35	—	750.67
	9	**812.9**	809.48	—	798.18
	10	**910.8**	884.6	—	893.6

Also Young modules, Poisson's ratio and density are respectively 1.83×10^{11} N/m^2, 7492 kg/m^3 and 0.3. In Table 2.2, the natural frequencies for clamped-free boundary condition (C-F) are given and compared to these studies. As it can be realized, good agreement exists between the presented results and those reported in References [123, 125].

Comprehensive investigation has been presented to model the sandwich cylindrical shell with viscoelastic core under different assumptions. In axial direction, 15 three-node elements are used. Based on the different types of continuity at the interfaces discussed in Table 2.1, three finite element models using FSDT are developed. FEM (a) is based on the linear distribution of displacement through the thickness of viscoelastic layer and discontinuity in transverse shear stresses at the interfaces. FEM (b) is similar to FEM (a) except that the transverse shear stresses at the interfaces are continuous. For FEM (c), in addition to the continuity in transverse shear stresses, the slopes of in-plane displacements in axial direction are also considered to be continuous. First, the frequency response of these finite element formulations for three-layered sandwich cylindrical shell, in which all three layers are made of the same elastic material and same size, is compared with the frequency response of an equivalent single layer cylinder made of the same elastic material. To have a fair comparison, the thickness of the single-layer cylindrical shell is the same as the entire thickness of the three-layered sandwich cylindrical shell and also the radius and length are the same in both structures. Using this way, the frequency response using different assumptions can be compared to the exact frequency response from the equivalent single elastic layer modeling. The clamped-free boundary condition has been considered.

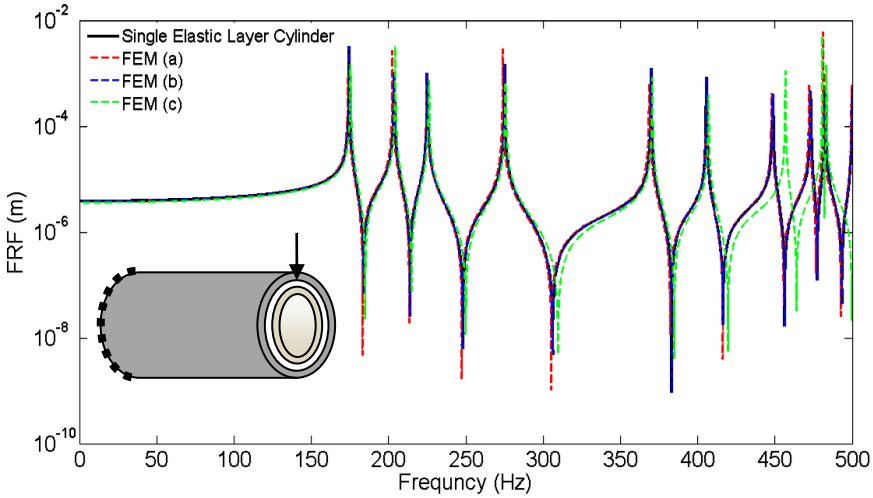

Figure 2.2 Frequency response in clamped free sandwich cylindrical shell with identical properties in each layer; Compression between FEMs (a), (b) and (c)

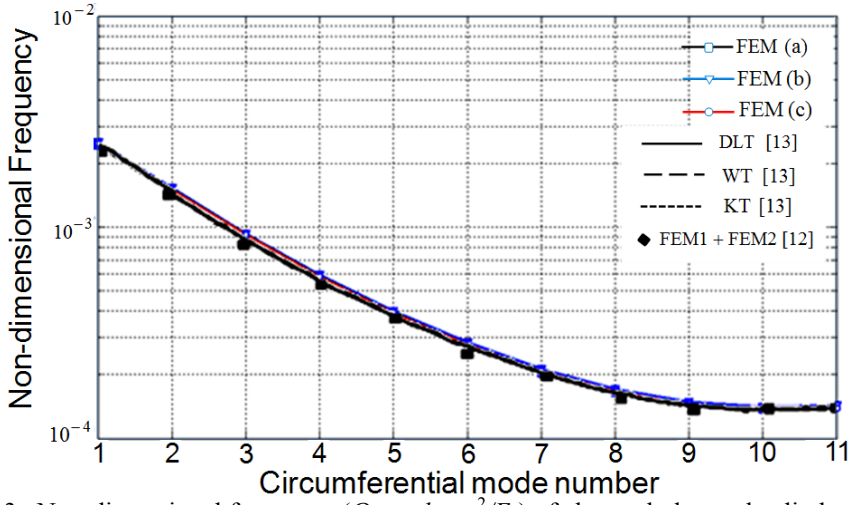

Figure 2.3 . Non-dimensional frequency ($\Omega = \rho_b h_b a\omega^2/E_b$) of clamped-clamped cylinder; comparison between different FEMs

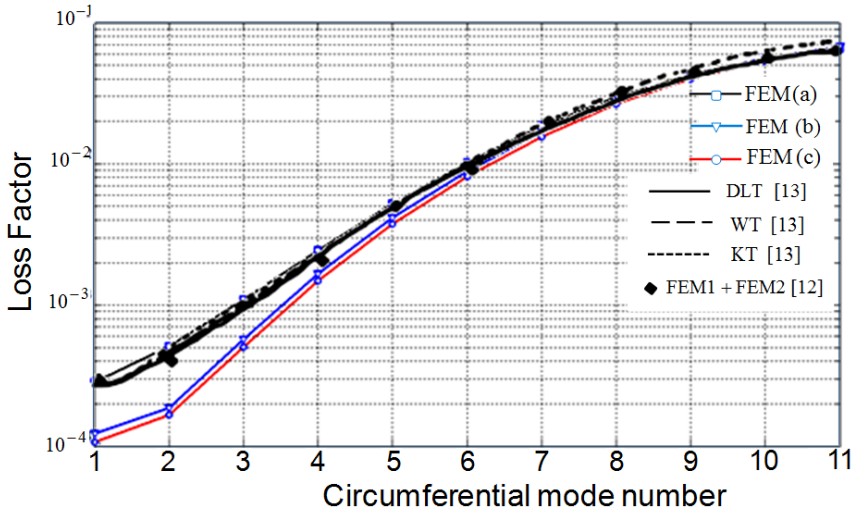

Figure 2.4 Loss Factor of clamped-clamped cylinder, comparison between different FEMs

The frequency response under unit transverse harmonic point load applied at the tip of the cylinder is shown in Figure 2.2. The deflection is measured at the point where the load is exerted. As it can be realized, frequency response of FEM (a) and (b) are generally in agreement with the single elastic layer cylinder at lower frequencies. At high frequencies, the results based on FEM (a) slightly differ from those based on FEM (b). The frequency response of FEM (c), on the other hand, deviates significantly from single elastic layer especially at higher natural frequencies. FEM (c) exhibits more continuity at nodes which leads to more rigid model and consequently larger natural frequencies. FEM (b), perfectly match with single elastic layer cylinder since the continuity in transverse shear stress provide better model for sandwich structures where the material properties of layers are relatively close to each other.

Next, the FEM (a), (b) and (c) are implemented in viscoelastic sandwich cylindrical shell where the viscoelastic core is compliant. The results including natural frequency and loss factor for different circumferential and first axial modes are compared with the results presented by other researchers [12, 13]. Sainsbury and Masti [12] developed a combination of two elements named as FEM1 and FEM2 in the finite element formulation for sandwich cylindrical shell in a way that both top and core layers were discretized by FEM2 and the bottom layer was discretized by FEM1. Ramesh and Ganesan [13] compared three different theories including Discrete Layer Theory (DLT), Wilkins Theory (WT) and Khatua's Theory (KT) in the semi-analytical finite element modeling of sandwich viscoelastic cylindrical shells. The length and radius of the cylinder are 100 mm. The thicknesses of the three layers are equal to 1 mm. Young modules, Poisson's ratio and density of the elastic layer are respectively 2.1×10^{11} N/m^2,

0.3 and 7850 kg/m^3. Young modules, density and Poisson's ratio of the viscoelastic layer are respectively (2.3+0.8i) × 10^7 N/m^2, 1340 kg/m^3 and 0.34. In this case, the material property of the core layer is independent of frequency. The natural frequencies and corresponding loss factors for different circumferential and first axial modes are shown in Figures 2.3 and 2.4, respectively. Results show a good agreement between the natural frequencies obtained by the FEM (a), (b) and (c) and those reported in the references. The loss factor resulted by FEM (b) and (c), on the other hand deviate from the results by FEM (a) and other theories at higher modes meaning that the FEM (a) is a suitable model for the compliant viscoelastic sandwich cylindrical shells. As mentioned before, where the core layer is stiff, the FEM (b) provides more precise results. FEM (c) is not accurate for sandwich structures due to the high rigidity in the model.

2.6.2 Comparison between lower and higher order models for damping analysis of sandwich cylindrical shell

The results based on lower and higher order models are developed for thick and thin core viscoelastic layers. The core layer material is assumed to be frequency dependent. The length, thickness and radius of the cylinder are respectively 511.2 mm 1.5 mm and 216.2 mm. Also Young modules, density and Poisson's ratio of the elastic layer are respectively 1.83 × 10^{11} N/m^2, 7492 kg/m^3 and 0.3. Shear modules, density and Poisson's ratio of the viscoelastic layer are respectively 0.142 $(\omega/2\pi)^{0.475}$(1+1.46i) N/m^2, 1140 kg/m^3 and 0.34. In the case of thin core layer, loss factor and natural frequencies for different circumferential and axial modes of clamped-clamped and clamped-free sandwich cylindrical shells are presented in Tables 2.3 and 2.4, respectively. The results show that the loss factor and natural frequency for both models are close for thin core layer. Only at higher modes (n = 1and 2) in which the loss factor is small, the results are

different. It can be observed that the higher order model, generally exhibits higher damping properties and the natural frequencies are nearly similar for both models.

Table 2.3 Loss factor of sandwich cylindrical shell for different circumferential and axial modes; h_b=1.5 mm, h_c=h_t=0.3 mm

		C-F			C-C		
		m			*m*		
n	Model	1	2	3	1	2	3
1	Lower order	4.621E-05	7.87E-05	0.00029	0.00010421	0.000287	0.000826
	Higher order	0.000416	0.001189	0.002395	0.001312	0.003578	0.004996
2	Lower order	0.00069996	0.0004	0.000579	0.000382	0.000681	0.001338
	Higher order	0.0099458	0.001312	0.00303	0.001224	0.002697	0.004325
3	Lower order	0.019287	0.002298	0.001797	0.002302	0.001942	0.002589
	Higher order	0.01974	0.002941	0.003325	0.003074	0.003206	0.004749
4	Lower order	0.098567	0.012651	0.005575	0.012392	0.005923	0.005419
	Higher order	0.09967	0.012828	0.006492	0.013414	0.006922	0.00709
5	Lower order	0.16073	0.041707	0.015202	0.041095	0.015952	0.011145
	Higher order	0.1612	0.0419	0.01584	0.042076	0.017051	0.012666
6	Lower order	0.17091	0.085623	0.034256	0.085064	0.036346	0.022214
	Higher order	0.1713	0.085828	0.034693	0.086327	0.03668	0.023151
7	Lower order	0.16408	0.1202	0.061683	0.12023	0.063793	0.038271
	Higher order	0.1644	0.1203	0.061381	0.1218	0.063846	0.039161
8	Lower order	0.15393	0.13381	0.087161	0.13455	0.089033	0.058572
	Higher order	0.1542	0.1339	0.087713	0.13548	0.090113	0.058769
9	Lower order	0.14375	0.1343	0.10511	0.13523	0.1078	0.077222
	Higher order	0.1441	0.1343	0.10532	0.13565	0.1073	0.077417
10	Lower order	0.13431	0.1294	0.11198	0.13029	0.11402	0.09121
	Higher order	0.1346	0.1295	0.11271	0.13051	0.11403	0.09126

Table 2.4 Natural frequencies of sandwich cylindrical shell for different circumferential and axial modes; h_b=1.5 mm, h_c=h_t=0.3 mm

		C-F			C-C		
		m			*m*		
n	Model	1	2	3	1	2	3
1	Lower order	844.9	2286.2	3036.1	1912.1	3011.7	3348.4
	Higher order	844.8	2286.0	3033.8	1911.3	3008.3	3343.6
2	Lower order	400.2	1420.1	2456.6	1198.8	2185.5	2818.2
	Higher order	400.1	1419.5	2454.5	1198.5	2183.5	2815.1
3	Lower order	225.1	921.1	1816.8	807.8	1588.9	2269.0
	Higher order	225.1	921.0	1815.8	807.6	1588.2	2267.3
4	Lower order	179.0	644.5	1360.1	584.9	1201.8	1822.7
	Higher order	179.0	644.4	1359.6	584.8	1201.5	1821.7
5	Lower order	208.6	500.0	1057.1	466.1	952.0	1491.1
	Higher order	208.6	499. 9	1056.8	466	951.9	1490.6
6	Lower order	277. 5	449. 4	869.2	426.8	798.8	1257.0
	Higher order	277. 5	449. 3	869.1	426.8	798.8	1256.7
7	Lower order	367.9	470.4	773.0	452.3	723.6	1104.3
	Higher order	367.9	470.4	772.9	452.3	723.6	1104.2
8	Lower order	474.3	541.2	753.1	524.6	715.7	1023.1
	Higher order	474.3	541.2	753	524.6	715.7	1023.1
9	Lower order	595.3	644.2	794.6	628.4	763.7	1006.1
	Higher order	595.3	644.2	794.6	628.4	763.7	1006.1
10	Lower order	730.2	769.9	882.3	754.6	854.5	1044.7
	Higher order	730.2	769.9	882.3	754.6	854.5	1044.7

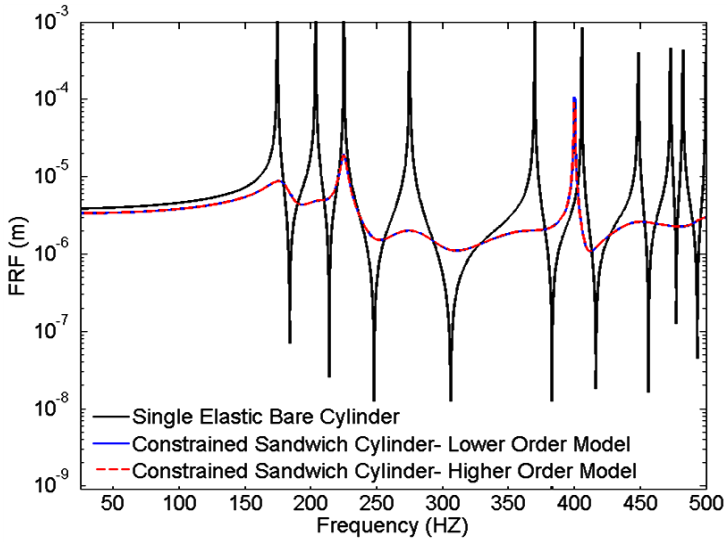

Figure 2.5 Frequency response of clamped-free sandwich cylindrical shell (h_b=1.5 mm, h_t= h_c= 0.3 mm)- comparison between the nonlinear and linear models for thin core layer

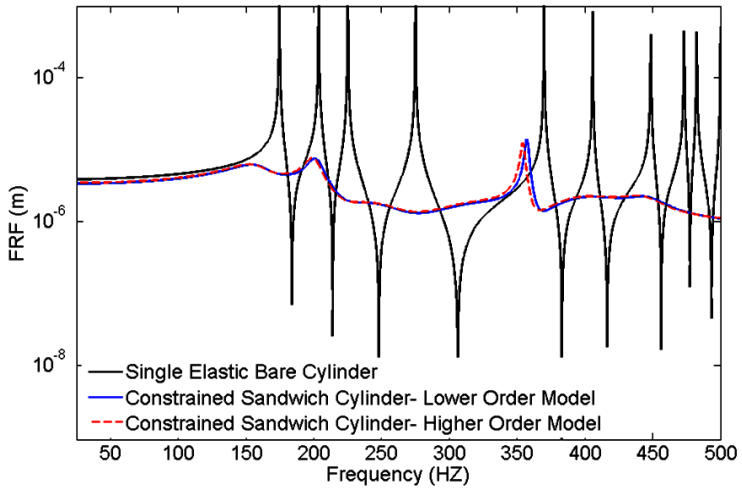

Figure 2.6 Frequency response of clamped-free sandwich cylindrical shell (h_b=1.5 mm, h_t=0.3 mm, h_c=3 mm)- comparison between nonlinear and linear models for tick core

Frequency responses for thin (h_c= 0.3 mm) and thick (h_c=3 mm) viscoelastic layers in clamped–free sandwich shell is also shown in Figures 2.5 and 2.6, respectively. Compared to the lower order model, the higher order model shows smaller deflection at the natural frequencies. As it can be realized, the results from the lower and higher order models deviate for thick viscoelastic core layer considerably at higher natural frequencies. Parametric study is also conducted to demonstrate the effect of the constraining layer and the core layer thicknesses on the loss factor associated with the

first four circumferential and first axial modes. The results are shown in Figures 2.7 and 2.8 for clamped-free and clamped-clamped boundary conditions, respectively. R_t and R_c represent the ratio of constraining layer and core layer thicknesses to the base layer thickness, respectively. According to the results, in order to achieve higher damping in the case of the thin core, thickness of constraining layer should increase. However the effect is more significant up to certain ranges of R_t. After these ranges, the increase in R_t slightly increase the loss factor in the expense of increasing the mass of the structure. In the case of the thick viscoelastic core layer, increasing R_t leads to decrease in loss factor. When the constraining layer is thin, thick core layer show higher damping property than the thin core. On the other hand, for thick constraining layer, by increasing the thickness of core layer, loss factor first decreases and then increases. Optimization study may be conducted in order to find the best set of R_t and R_c in order to achieve a light structure with high damping property.

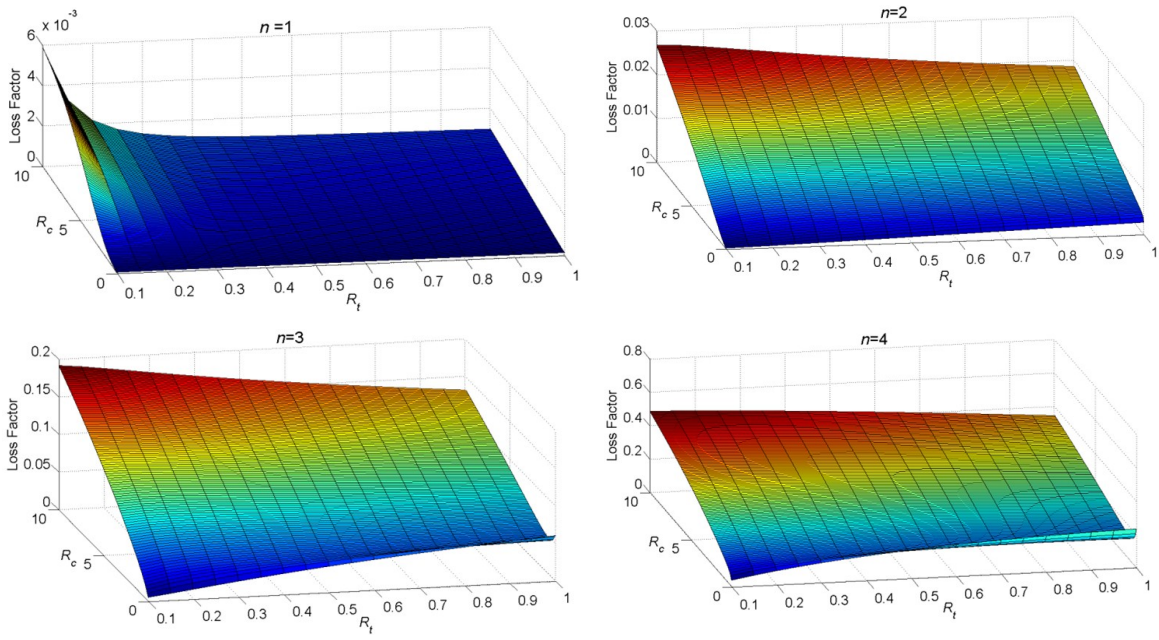

Figure 2.7 Variation of loss factor at different circumferential and first axial modes versus R_t and R_c for clamped-free sandwich cylinder

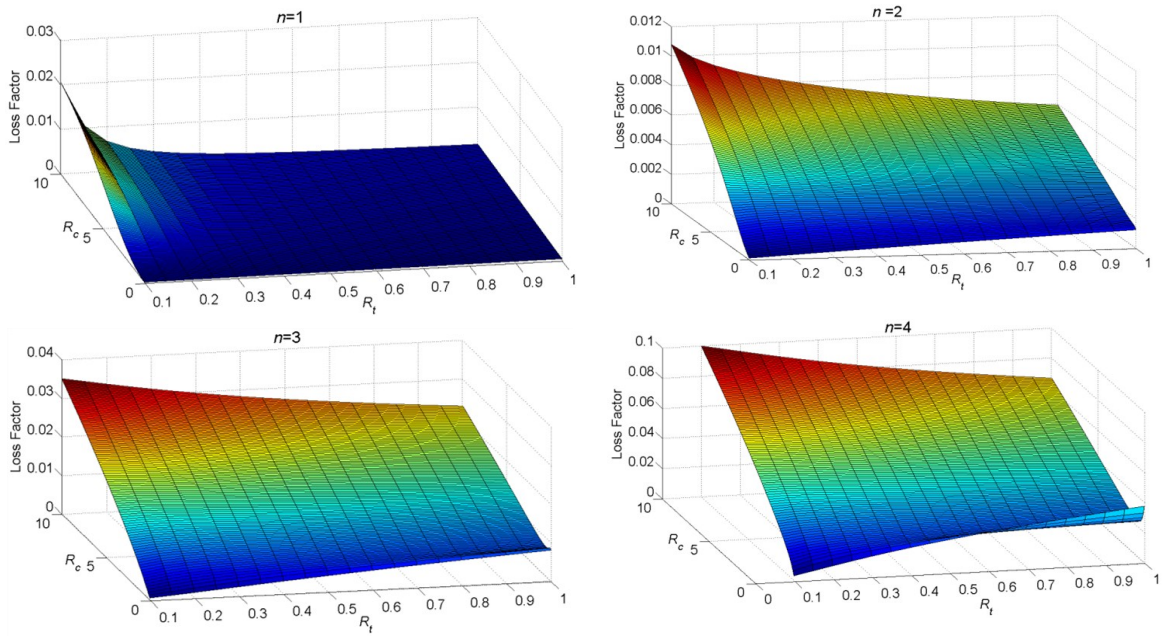

Figure 2.8 Variation of loss factor at different circumferential and first axial modes versus R_t and R_c for clamped-clamped sandwich cylinder

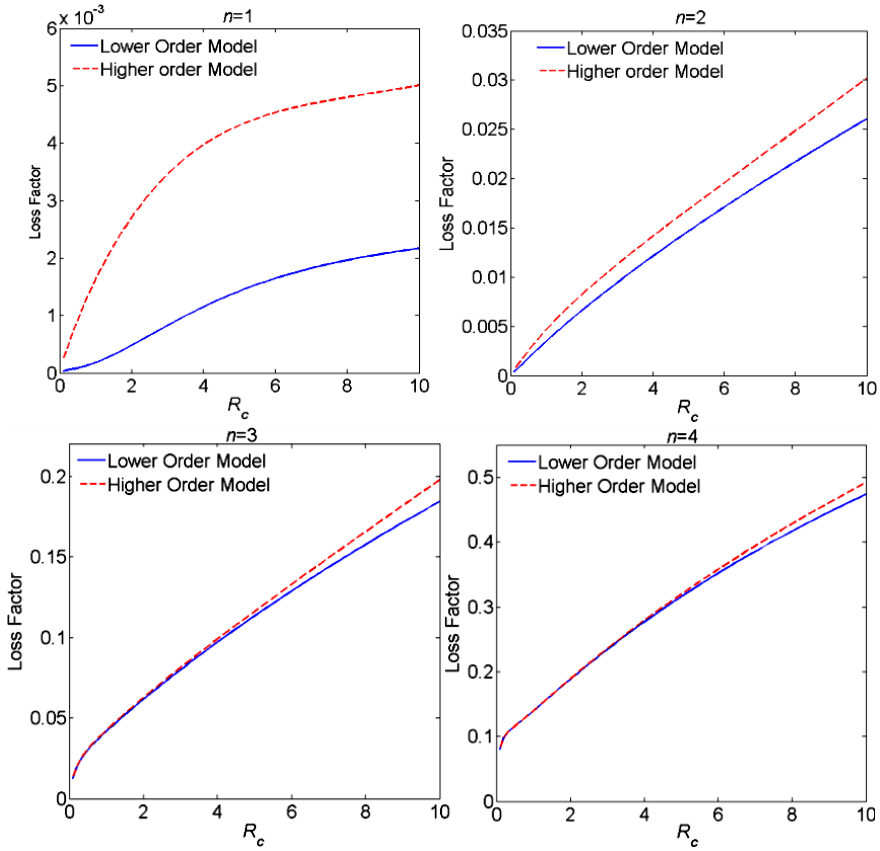

Figure 2.9 Comparison between the results from the linear and nonlinear models at different circumferential and first axial modes for clamped-free boundary condition, $R_t = 0.2$

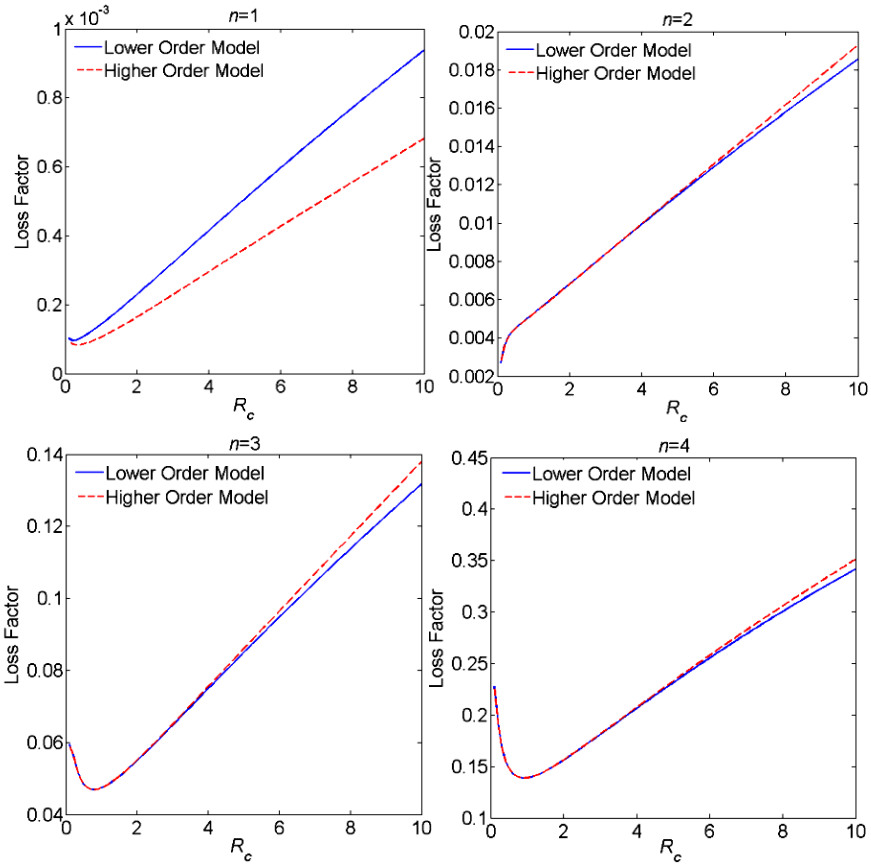

Figure 2.10 Comparison between the results from the linear and nonlinear models at different circumferential and first axial modes for clamped-free boundary condition, $R_t = 1$

Figures 2.9 and 2.10 show the behavior of the loss factor versus R_c for thin (R_t =0.2) and thick (R_t =1) constraining layers in clamped-free sandwich cylindrical shell. As it can be observed, the results from the linear and nonlinear models deviate for thick cores. Also as mentioned before, at higher frequencies these models result in different loss factors.

2.6.3 Effect of slippage at the interfaces

The shear stiffness parameter K^* of the adhesive layer can be related to the shear modulus of the core layer as $K^* h_c = CG_c$ in which C is a non-dimensional parameter which determine the bonding at the interfaces. It should be noted that in order to achieve a perfect bonding, large value of C should be assigned.

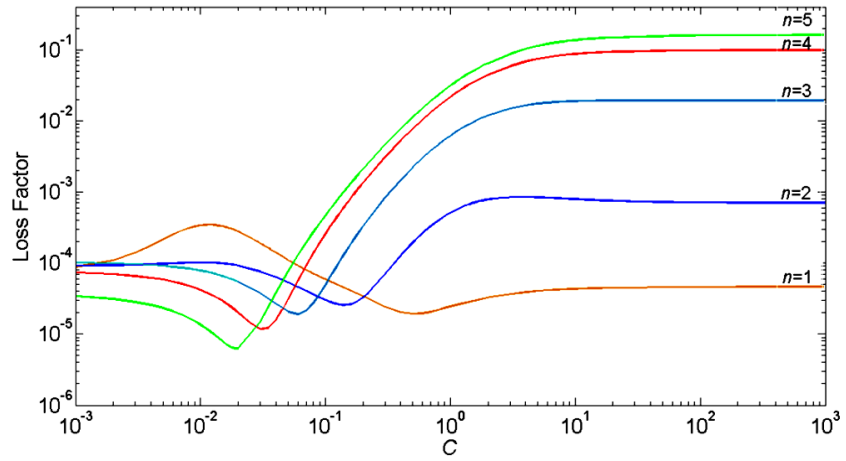

Figure 2.11 Loss factor versus shear rigidity of adhesive layer in clamped-free boundary condition at first axial mode and different circumferential modes, h_b=1.5 mm, $R_c = R_t$ =0.2

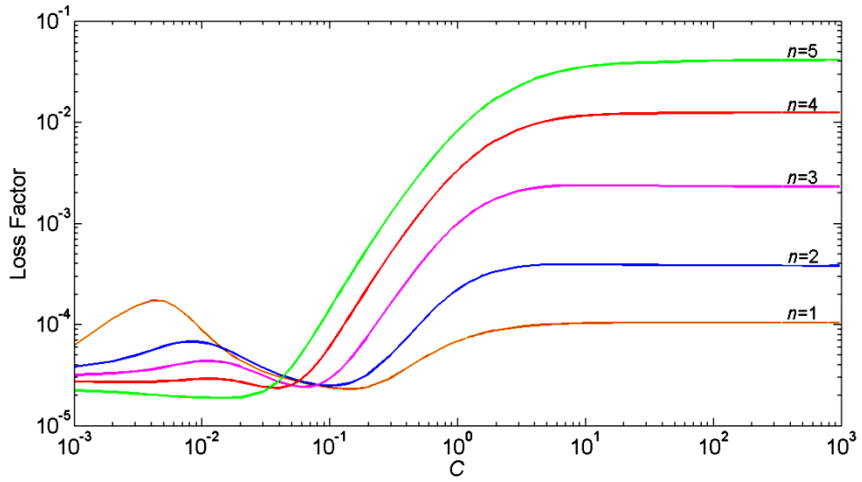

Figure 2.12 Loss factor versus shear rigidity of adhesive layer in clamped- clamped boundary condition at first axial mode and different circumferential modes, h_b=1.5 mm, $R_c = R_t$ =0.2

The results are developed based on the lower order model of displacement distribution through the thickness of the core layer. Figures 2.11 and 2.12 show the loss factor at first five circumferential and first axial modes for clamped-clamped and clamped-free boundary conditions, respectively. It can be realized that the loss factor decreases as the bonding at the interfaces becomes weaker except at the first circumferential mode in both clamped-free and clamped-clamped boundary conditions. Also, small amount of the slippage leads to increase in loss factor at the second circumferential mode (n=2). One can observe that as C increases, the loss factors approaches to the results from perfect

bonding model. Consequently, in order to achieve more conservative design it is better to provide perfect bonding between the layers.

2.6.4 Effect of large deflection

In this section the effect of large deflection on the loss factors and natural frequencies is presented. It has been assumed that the top and bottom layers remain in elastic region and the material property of the viscoelastic layer is linear. First, the effect of large deflection on the natural frequency is presented for bare cylindrical shell and the results are compared to the works done by other researchers. The maximum deflection is considered to be proportional to the thickness as $W_{\max}=Dh$ in which D is the proportional factor. Table 2.5 shows the linear period of oscillation T_{L} and also the ratio of nonlinear period T_{NL} to the linear value associated with the forth circumferential and first axial mode for simply supported boundary condition. In Table 2.6, another comparison is presented for different boundary condition (v = 0 on edges) at different modes. The results are in good agreement with those presented in References [126, 127]. The material property and dimensions are also given in caption of the Tables 2.5 and 2.6. After the validation of the procedure, the developed iterative processes mentioned before are used to extract natural frequencies and the loss factors of the sandwich structure. The material property and geometrical dimensions given for sandwich shell structure with frequency dependent viscoelastic damping layer mentioned before has been used and h_c=0.3mm is chosen for the core thickness. Since the thickness of the core is small, linear distribution model for displacement fields is considered for the core layer. The results including loss factors and natural frequencies for clamped-clamped and clamped-free boundary conditions are shown in Tables 2.7 and 2.8, respectively. The results show that

consideration of geometrical nonlinearity condition leads to larger natural frequency and consequently smaller amount of loss factor.

Table 2.5 T_{NL}/T_L in bare cylindrical shell, $E = 2.96 \times 10^7$ lb/in^2, $\upsilon = 0.3$, $\rho = 7.33 \times 10^4$ lb-s^2/in^4, $h_b = 0.01$ in, $L=\pi/2$ in, a =1 in, boundary conditions: $w = u = v = 0$ on edges; n =4, m=1

		T_{NL}/T_L		
	$T_L \times 10^{-5}$(s)	D=1	D=2	D=3
Ref [126]	1.8898	0.98	0.94	0.89
Ref [127]	1.8607	0.9777	0.9182	0.8382
Present study	**1.9031**	**0.9711**	**0.8968**	**0.8022**

Table 2.6 T_{NL}/T_L in bare cylindrical shell, $E = 2.96 \times 10^7$ lb/in^2, $\upsilon = 0.3$, $\rho = 7.33 \times 10^4$ lb-s^2/in^4, $h_b = 0.01$ in, $L=\pi/2$ in, a =1 in, boundary conditions: $v = 0$ on the edges

			T_{NL}/T_L					
	$T_L \times 10^{-5}$(s)		D=1		D=2		D=3	
	Ref [126]	Present study	Ref. [127]	Present study	Ref. [127]	Present study	Ref.[127]	Present study
n=2, m=1	1.0844	**1.0851**	0.9992	**0.9989**	0.9971	**0.9958**	0.9937	**0.9910**
n=3, m=1	1.6967	**1.7074**	0.9940	**0.9916**	0.977	**0.9678**	0.9509	**0.9321**
n=4, m=1	2.4761	**2.5728**	0.9617	**0.9011**	0.8684	**0.8322**	0.7588	**0.7063**

Table 2.7 Large deformation effects on the loss factors of clamped-clamped and clamped-free sandwich cylindrical shell; h_b=1.5 mm, $R_c = R_t$ =0.2

n	m=1	Small Deformation	Large Deformation D=0.5	Large Deformation D=1	Large Deformation D=2
1	C-F	0.00004621	0.000046205	0.00004619	0.00004613
	C-C	0.00010421	0.00010417	0.00010403	0.00010321
2	C-F	0.00069996	0.00069872	0.00069503	0.00068072
	C-C	0.000382	0.0003818	0.0003812	0.00037881
3	C-F	0.019287	0.01866	0.016998	0.012508
	C-C	0.002302	0.0022961	0.0022772	0.0022046
4	C-F	0.098567	0.084697	0.059766	0.027392
	C-C	0.012392	0.012199	0.011652	0.0098645
5	C-F	0.16073	0.12452	0.074435	0.051457
	C-C	0.041095	0.025497	0.033346	0.021192
6	C-F	0.17091	0.12708	0.092086	0.089926
	C-C	0.085064	0.074564	0.054506	0.025497
7	C-F	0.16408	0.11572	0.1262	0.1187
	C-C	0.12023	0.097581	0.062181	0.039765
8	C-F	0.15393	0.13839	0.13403	0.12599
	C-C	0.13455	0.10369	0.060684	0.061101
9	C-F	0.14375	0.13585	0.13474	0.1294
	C-C	0.13523	0.10067	0.0833515	0.0770855
10	C-F	0.13431	0.13004	0.127705	0.12508
	C-C	0.13029	0.09287	0.092203	0.088498

Table 2.8 Large deformation effects on the natural frequencies of clamped-clamped and clamped-free sandwich cylindrical shell; h_b=1.5 mm, $R_c = R_t$ =0.2 mm

n	m=1	Small Deformation	Large Deformation D=0.5	Large Deformation D=1	Large Deformation D=2
1	C-F	844.9	844.9	844.93	845.03
	C-C	1912.1	1912.2	1912.3	1912.8
2	C-F	400.2	400.6	401.7	407.5
	C-C	1198.8	1220	1220.6	1220.8
3	C-F	225.0	228.8	239.5	278.7
	C-C	808.8	830.9	813.2	826.5
4	C-F	179.0	195.1	235.2	354.5
	C-C	584.9	589.6	603.7	657.4
5	C-F	208.6	240.7	320.4	418.2
	C-C	466.1	490.1	522.6	666.7
6	C-F	277. 5	329.3	429.5	520.8
	C-C	426.8	460.2	550.6	833.6
7	C-F	367.9	454.1	446.5	456.3
	C-C	452.3	511.3	663.8	1008.5
8	C-F	474.3	526.8	527.8	554.4
	C-C	524.6	615.6	842.5	906.0
9	C-F	595.3	630.9	631.1	653.7
	C-C	628.4	751.3	956.2	958.3
10	C-F	730.2	757.6	768.0	781.1
	C-C	754.6	919.8	967.8	1032.0

The deviation of the results considering large deflection effect from those based on the small deflection is more considerable for the modes with the lower natural frequencies.

2.6.5 Time response under impulsive loading

Transient response has been developed here for both lower and higher order models under impulse loading using DFT/IDFT method. First, the methodology is validated by implementing it on the single degree of freedom model of viscoelastic structure and comparing the obtained results with the analytical approach presented by Nashif et al. [128]. For the sake of comparison, the material properties are directly extracted from reference [128]. First the viscoelastic material is considered to be frequency independent in which the real part of the modulus is 2910 N/m^2, the loss factor is 1.4 and the mass is given to be 0.007382 kg. For the frequency dependent property, the real part of the modulus is $1158(1+100(\omega/2\pi))^{0.1}$ N/m^2 and the loss factor is 0.15.

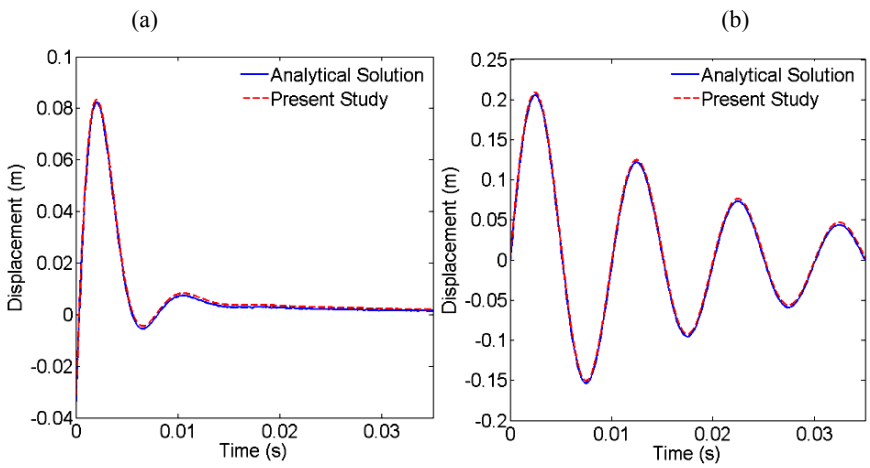

Figure 2.13 Transient response of the single degree of freedom; (a) constant complex modulus (b) frequency dependent complex modulus

The maximum frequency is considered to be 2500 Hz. The time interval Δt is assumed to be 0.0001 resulting the sampling frequency of f_s=10000 which according to the Nyquist theorem should be greater than twice of the considered maximum frequency. Number of samples is assumed to be 10000 and therefore the frequency domain which is [-5000, 5000] is discretized using frequency interval of Δf=1 Hz. Figures 2.13 (a) and (b) compares the time response of the single degree of freedom using the DFT/IDFT approach and the analytical solution under unit impulsive point load for the constant and frequency dependent modulus, respectively. It can be observed that the presented results are in excellent agreement with the analytical results. For the viscoelastic cylindrical sandwich shell, the time response under unit impulse point loading at the tip point of the sandwich cylinder is obtained using the same parameters except that the number of samples is now assumed to be 100000 which result in Δf=0.1 Hz. The thickness of the core is chosen here to be h_c=1.5 mm. Deflection is calculated at the point where the load is exerted. The displacement response at first four circumferential modes for the lower and higher models is shown in Figure 2.14.

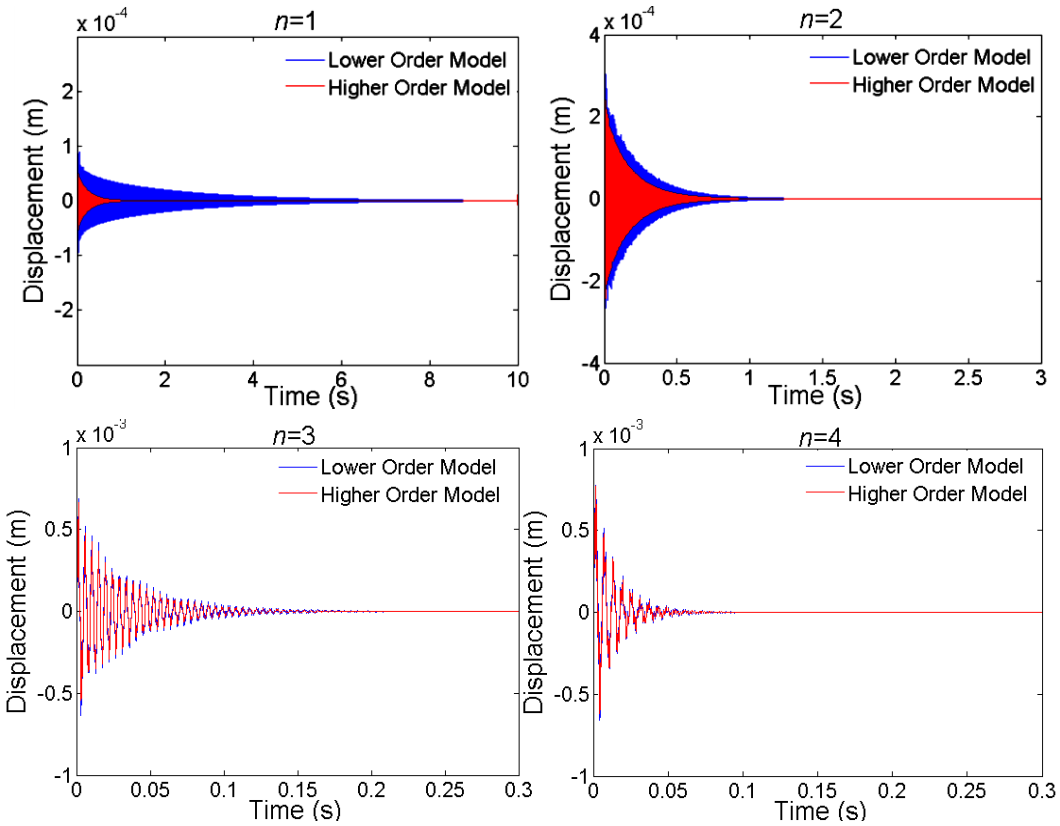

Figure 2.14 Time response for different circumferential modes (n=1,2,3,4)

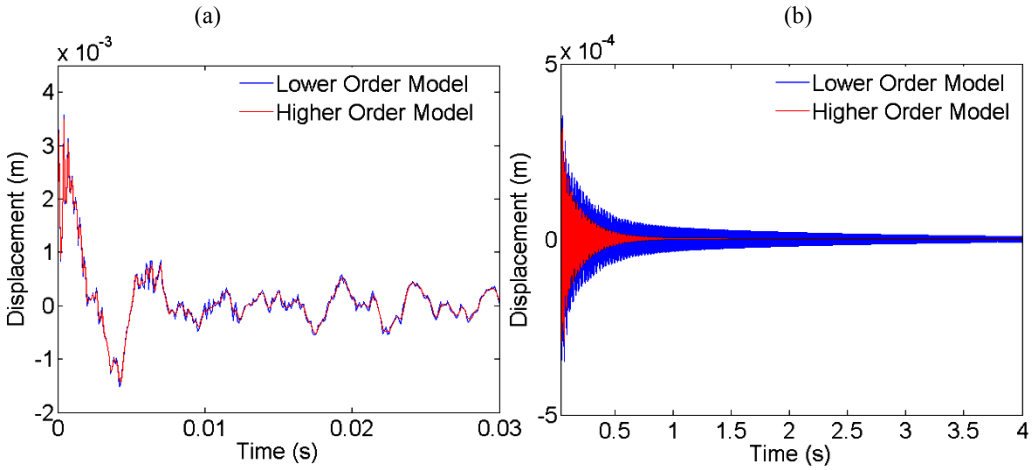

Figure 2.15 Time response obtained by superimposing all circumferential (n=1,...,10) and axial modes; (a) $0 \leq t < 0.03$ and (b) $0.03 \leq t < 4$

The time response based on the summation of all the circumferential and axial modes is also shown in Figure 2.15 (a) and (b) in which Figure 2.15 (a) shows the transient part in the first 0.03 (s). As concluded before, it can be noticed that the higher order model

exhibits more damping property than the lower order model. Therefore, for the higher order model the displacement is expected to reach its initial value faster than the lower order model as is shown in Figures 2.14 and 2.15.

2.7 Conclusion

Different finite element models have been developed for sandwich viscoelastic structures. According to the results, the finite element model in which considers the continuity in transverse shear stresses at the interfaces, gives more accurate results for the three-layered structure with stiff core layer. For viscoelastic sandwich structures in which the material of the core layer is compliant, the continuity in transverse shear stresses should not be considered. Lower and higher order models for representing displacement distribution through the thickness of the core layer in sandwich viscoelastic cylindrical shell were developed. According to the results, the higher order model exhibits more damping properties than the lower order model which leads to less time required to reach the steady state response in the transient vibration. Both models almost result in identical natural frequencies. Effects of slippage were also considered in this chapter. The results showed that slippage must be prevented in order to achieve higher damping behavior. In large deformation, natural frequency increases which leads to the smaller amount of loss factor. The nonlinearity problem due to large deflection and frequency dependent complex modulus has been solved using two iterative procedures. The presented analysis can be extended to the other types of shell of revolution.

CHAPTER 3

EFFECT OF PRESSURE AND TEMPERATURE ON VIBRATION BEHAVIOR OF SANDWICH CYLINDRICAL SHELLS

3.1 Introduction

Cylindrical shell structures are widely used for many applications in industries such as boilers, pressurized gas tanks and aircraft fuselage. Vibration suppression can be achieved in these structures using passive damping treatment. Due to ability of viscoelastic materials in converting strain energy into heat for a designed range of frequency, they have been successfully used in the damping layers of the sandwich structures. However, the damping characteristics of viscoelastic materials are strongly affected by the ambient temperature and the excitation frequency [19-24].

In this chapter, the higher order model for displacement field at the core layer presented in the chapter 2 has been employed to achieve better approximation of damping behavior of sandwich structure with thick/thin core layers. Based on the energy balance and using irregular grid, finite difference method is formulated to obtain temperature distribution at each layer due to the temperature inside the sandwich cylindrical shell and heat dissipation caused by cyclic loading. Considering the effects of temperature and frequency on material properties of damping layer, vibration behavior of a pressurized sandwich cylindrical shell under the temperature variation has been investigated. The thermal stresses introduced at each layer and also the stress components due to internal/external pressure are obtained to be considered in the vibration analysis using the concept of geometric stiffness matrix in the semi-analytical finite element modeling. Then parametric studies have been presented to show the effect of all the above

mentioned parameters on frequency response and damping characteristics of sandwich cylindrical shell. The generated heat raised by dissipated energy not only changes the material properties of the viscoelastic layer, it can also introduce additional thermal stress at each layer. An illustrative example is presented to observe this phenomena for a pressurized sandwich cylinder in which the internal pressure varies periodically between certain ranges of amplitudes.

3.2 Displacement Field

In this section the higher order displacement field derived in the previous chapter has been briefly explained. Displacement field through the thickness of sandwich cylindrical can be expressed in terms of the displacements of the middle plane including u_0, v_0 and w_0 and the rotations of the normals to the middle plane in axial and circumferential directions which are respectively denoted by ψ_1 and ψ_2. The translational and rotational displacements at each layer are shown in Figure 2.1. According to the first order shear deformation theory, the total displacement field can be expressed as:

$$\begin{aligned} u_i(x,\theta,\xi_i,t) &= u_o^i(x,\theta,t) + \xi_i \psi_1^i(x,\theta,t) \\ v_i(x,\theta,\xi_i,t) &= v_o^i(x,\theta,t) + \xi_i \psi_2^i(x,\theta,t) \qquad -\frac{h_i}{2} < \xi_i < \frac{h_i}{2} \\ w_i &= w_i(x,\theta,\mathrm{t}) \end{aligned} \tag{3.1}$$

The bottom, top and core layers are labeled by the indices i=b, t and c, respectively. ξ_i is the coordinate in thickness direction at the middle of each layer and $(\xi_t,\xi_b,\xi_c)=(\xi_1,\xi_2,\xi_3)$. u, v and w are the displacement in axial (x), circumferential (θ) and thickness direction through the thickness of each layer, respectively. Based on the boundary conditions at the interfaces, displacements at bottom and top elastic layers are

calculated using the displacement field at core. The boundary conditions considering perfect bonding at the interfaces can be described as:

$$\begin{aligned} &\xi_1 = -h_t/2 \text{ and } \xi_3 = h_c/2: && u_t = u_c && v_t = v_c && w_t = w_c \\ &\xi_2 = h_b/2 \text{ and } \xi_3 = -h_c/2: && u_b = u_c && v_b = v_c && w_b = w_c \end{aligned} \tag{3.2}$$

Using the above boundary conditions, the displacement fields at the top and bottom elastic layers are determined as:

$$\begin{aligned} u_t &= u_0^c + \frac{\left(h_t\psi_1^t + h_c\psi_1^c\right)}{2} + \xi_1\psi_1^t \\ v_t &= v_0^c + \frac{\left(h_t\psi_2^t + h_c\psi_2^c\right)}{2} + \xi_1\psi_2^t \end{aligned} \qquad -\frac{h_t}{2} < \xi_1 < \frac{h_t}{2} \tag{3.3}$$

$$\begin{aligned} u_b &= u_0^c - \frac{\left(h_b\psi_1^b + h_c\psi_1^c\right)}{2} + \xi_2\psi_1^b \\ v_b &= v_0^c - \frac{\left(h_b\psi_2^b + h_c\psi_2^c\right)}{2} + \xi_2\psi_2^b \end{aligned} \qquad -\frac{h_b}{2} < \xi_2 < \frac{h_b}{2} \tag{3.4}$$

In sandwich structures where the core layer is thick, the linear displacement distribution through the compliant core layer is not accurate enough. Thus, the following nonlinear distribution of displacements is considered at the viscoelastic core layer:

$$\begin{aligned} u_c &= u_0^c + \xi_3\,\Phi_1^c + {\xi_3}^2\Phi_2^c + {\xi_3}^3\Phi_3^c \\ v_c &= v_0^c + \xi_3\,\Theta_1^c + {\xi_3}^2\Theta_2^c + {\xi_3}^3\Theta_3^c \\ w_c &= w_0^c + \xi_3\,\Psi_1^c + {\xi_3}^2\Psi_2^c \end{aligned} \qquad -\frac{h_c}{2} < \xi_3 < \frac{h_c}{2} \tag{3.5}$$

Here it is assumed that in-plane normal and shear stresses are negligible in viscoelastic structures due to the corresponding small energies. However normal stress in thickness direction of viscoelastic layer is considered. The relation between transverse shear stresses and strains can be written as

$$\gamma_{\xi_3 x} = \frac{\tau_{\xi_3 x}}{G_c} = \frac{2\left(1+\upsilon_c\right)}{E_c}\tau_{\xi_3 x} = 2\left(1+\upsilon_c\right)\beta_1 \tag{3.6}$$

$$\gamma_{\xi_3\theta} = \frac{\tau_{\xi_3\theta}}{G_c} = \frac{2(1+\upsilon_c)}{E_c}\tau_{\xi_3\theta} = 2(1+\upsilon_c)\beta_2$$

where

$$\beta_1 = \frac{\tau_{\xi_3 x}}{E_c} \text{ and } \beta_2 = \frac{\tau_{\xi_3\theta}}{E_c}$$

and E_c and υ_c are respectively Young modules and Poisson's ratio of elasticity. Considering the mentioned assumptions and also using constitutive relations and equilibrium equation, the displacement fields at the core layer are obtained as:

$$\begin{aligned} u_c &= u_c^0 + \xi_3\left(2(1+\upsilon_c)\beta_1 - \frac{\partial w_0^c}{\partial x}\right) - \frac{{\xi_3}^2}{2}\frac{\partial \Psi_1^c}{\partial x} - \frac{{\xi_3}^3}{3}\frac{\partial \Psi_2^c}{\partial x} \\ v_c &= v_c^0 + \xi_3\left(2(1+\upsilon_c)\beta_2 - \frac{\partial w_0^c}{a\partial\theta}\right) - \frac{{\xi_3}^2}{2}\frac{\partial \Psi_1^c}{a\partial\theta} - \frac{{\xi_3}^3}{3}\frac{\partial \Psi_2^c}{a\partial\theta} \\ w_c &= w_c^0 + \xi_3\,\Psi_1^c - \frac{{\xi_3}^2}{2}\left(\frac{\partial\beta_1}{\partial x} + \frac{\partial\beta_2}{a\partial\theta}\right) \end{aligned} \tag{3.7}$$

where

$$\Psi_2^c = -\frac{\left(\frac{\partial\beta_1}{\partial x} + \frac{\partial\beta_2}{a\partial\theta}\right)}{2}$$

According to the boundary condition in Eq. (3.2), the translational displacements at the top and bottom elastic layers are obtained in terms of translational displacements u_0^c, v_0^c, w_0^c and rotational displacement Ψ_1^c, β_1 and β_2 as follows:

$$
\begin{aligned}
u_t &= u_0^c + \frac{h_c}{2}\left(2(1+\upsilon_c)\beta_1 - \frac{\partial w_0^c}{\partial x}\right) - \frac{h_c^2}{8}\frac{\partial \Psi_1^c}{\partial x} + \frac{h_c^3}{48}\left(\frac{\partial^2 \beta_1}{\partial x^2} + \frac{\partial^2 \beta_2}{a\,\partial\theta\,\partial x}\right) + \frac{h_t}{2}\psi_1^t + \xi_1\psi_1^t \\
v_t &= v_0^c + \frac{h_c}{2}\left(2(1+\upsilon_c)\beta_2 - \frac{\partial w_0^c}{a\partial\theta}\right) - \frac{h_c^2}{8}\frac{\partial \Psi_1^c}{a\partial\theta} + \frac{h_c^3}{48}\left(\frac{\partial^2 \beta_1}{a\,\partial\theta\,\partial x} + \frac{\partial^2 \beta_2}{a^2\partial\theta^2}\right) + \frac{h_t}{2}\psi_2^t + \xi_1\psi_2^t \\
w_t &= w_0^c + \frac{h_c}{2}\Psi_1^c - \frac{h_c^2}{8}\left(\frac{\partial \beta_1}{\partial x} + \frac{\partial \beta_2}{a\,\partial\theta}\right) \\
u_b &= u_0^c - \frac{h_c}{2}\left(2(1+\upsilon_c)\beta_1 - \frac{\partial w_0^c}{\partial x}\right) - \frac{h_c^2}{8}\frac{\partial \Psi_1^c}{\partial x} - \frac{h_c^3}{48}\left(\frac{\partial^2 \beta_1}{\partial x^2} + \frac{\partial^2 \beta_2}{a\,\partial\theta\,\partial x}\right) - \frac{h_b}{2}\psi_1^b + \xi_2\psi_1^b \\
v_b &= v_0^c - \frac{h_c}{2}\left(2(1+\upsilon_c)\beta_2 - \frac{\partial w_0^c}{a\partial\theta}\right) - \frac{h_c^2}{8}\frac{\partial \Psi_1^c}{a\partial\theta} - \frac{h_c^3}{48}\left(\frac{\partial^2 \beta_1}{a\,\partial\theta\,\partial x} + \frac{\partial^2 \beta_2}{a^2\partial\theta^2}\right) - \frac{h_b}{2}\psi_2^b + \xi_2\psi_2^b \\
w_b &= w_0^c - \frac{h_c}{2}\Psi_1^c - \frac{h_c^2}{8}\left(\frac{\partial \beta_1}{\partial x} + \frac{\partial \beta_2}{a\,\partial\theta}\right)
\end{aligned}
\tag{3.8}
$$

$$
\begin{aligned}
u_b &= u_0^c - \frac{h_c}{2}\left(2(1+\upsilon_c)\beta_1 - \frac{\partial w_0^c}{\partial x}\right) - \frac{h_c^2}{8}\frac{\partial \Psi_1^c}{\partial x} - \frac{h_c^3}{48}\left(\frac{\partial^2 \beta_1}{\partial x^2} + \frac{\partial^2 \beta_2}{a\,\partial\theta\,\partial x}\right) - \frac{h_b}{2}\psi_1^b + \xi_2\psi_1^b \\
v_b &= v_0^c - \frac{h_c}{2}\left(2(1+\upsilon_c)\beta_2 - \frac{\partial w_0^c}{a\partial\theta}\right) - \frac{h_c^2}{8}\frac{\partial \Psi_1^c}{a\partial\theta} - \frac{h_c^3}{48}\left(\frac{\partial^2 \beta_1}{a\,\partial\theta\,\partial x} + \frac{\partial^2 \beta_2}{a^2\partial\theta^2}\right) - \frac{h_b}{2}\psi_2^b + \xi_2\psi_2^b \\
w_b &= w_0^c - \frac{h_c}{2}\Psi_1^c - \frac{h_c^2}{8}\left(\frac{\partial \beta_1}{\partial x} + \frac{\partial \beta_2}{a\,\partial\theta}\right)
\end{aligned}
\tag{3.9}
$$

3.3 Semi-Analytical Finite Element Method

Semi-analytical finite element approach has been used so that the displacement fields in circumferential direction is expressed analytically using Fourier expansion and also is discretized in the axial direction using appropriate shape functions. Considering this, the displacement fields can be presented in the following form:

$$
\begin{aligned}
w_0^c &= \sum_{j=1}^{m}\sum_{n=0}^{\infty} N_j w_j^c \cos(n\theta - \varphi) & v_0^c &= \sum_{j=1}^{m}\sum_{n=0}^{\infty} N_j v_j^c \sin(n\theta - \varphi) \\
u_0^c &= \sum_{j=1}^{m}\sum_{n=0}^{\infty} N_j u_j^c \cos(n\theta - \varphi) & \Psi_1^c &= \sum_{j=1}^{m}\sum_{n=0}^{\infty} N_j \Psi_{1j}^c \cos(n\theta - \varphi) \\
\beta_1 &= \sum_{j=1}^{m}\sum_{n=0}^{\infty} N_j \beta_{j1} \cos(n\theta - \varphi) & \beta_2 &= \sum_{j=1}^{m}\sum_{n=0}^{\infty} N_j \beta_{j2} \sin(n\theta - \varphi) \\
\psi_1^i &= \sum_{j=1}^{m}\sum_{n=0}^{\infty} N_j \psi_{j1}^i \cos(n\theta - \varphi) & \psi_2^i &= \sum_{j=1}^{m}\sum_{n=0}^{\infty} N_j \psi_{j2}^i \sin(n\theta - \varphi)
\end{aligned}
\tag{3.10}
$$

in which m is the number of nodes in axial direction, $i=b$ and t, and N_j are the Lagrangian shape functions. Since there is no preference for the orientation of circumferential modes, thus an arbitrary phase angle φ must be included [119]. The mode

orientations depend on the distribution of the external loading. In general, $\varphi=\varphi_0$ and $\varphi=\varphi_0+\pi/2$ in which φ_0 is an arbitrary constant. For three nodes along the axial direction, the shape functions N_1, N_2 and N_3 in FSDT are given as:

$$N_1 = \frac{2x^2}{{L_e}^2} - \frac{x}{L_e} \qquad N_2 = 1 - \frac{4x^2}{{L_e}^2} \qquad N_3 = \frac{2x^2}{{L_e}^2} + \frac{x}{L_e} \tag{3.11}$$

The displacement fields in each layer can now be used to obtain kinetic and potential energies for that layer. For the core layer, either lower or higher order expansions of displacement fields as discussed before can be implemented. The kinetic and strain energies for each cylindrical shell layer can be obtained using:

$$UT_i = \int_{-\frac{h_i}{2}}^{\frac{h_i}{2}} \int_0^{2\pi} \int_{-\frac{L_e}{2}}^{\frac{L_e}{2}} \frac{1}{2} \rho_i \left({\dot{u}_i}^2 + {\dot{v}_i}^2 + {\dot{w}_i}^2 \right) \mathrm{d}V_i \tag{3.12}$$

$$UE_i = \int_{-\frac{h_i}{2}}^{\frac{h_i}{2}} \int_0^{2\pi} \int_{-\frac{L_e}{2}}^{\frac{L_e}{2}} \frac{1}{2} \left(\sigma^i_{xx}\, \varepsilon^i_{xx} + \sigma^i_{\theta\theta}\, \varepsilon^i_{\theta\theta} + \sigma^i_{\xi_i\xi_i}\, \varepsilon^i_{\xi_i\xi_i} + \tau^i_{x\theta}\, \gamma^i_{x\theta} + \tau^i_{\xi_i x}\, \gamma^i_{\xi_i x} + \tau^i_{\xi_i\theta}\, \gamma^i_{\xi_i\theta} \right) \mathrm{d}V_i \tag{3.13}$$

in which $\mathrm{d}V_i = (a + \xi_i)\mathrm{d}\theta \mathrm{d}s\, \mathrm{d}\xi_i$, ρ is density, a is the radius of the cylinder and L_e is the length of cylindrical shell element. To obtain the strain energy in Eq. (3.13), constitutive equation and strain-displacement relation should be employed. Strain–displacement relation using linear Green's Strain for cylindrical shell element can be expressed as follows [94]:

$$\varepsilon^i_{xx} = \frac{\partial u_i}{\partial x} \quad \varepsilon^i_{\theta\theta} = \frac{1}{1 + \xi_i / a} \left(\frac{\partial v_i}{a \partial \theta} + \frac{w_i}{a} \right) \quad \varepsilon^c_{\xi_3\xi_3} = \frac{\partial w_c}{\partial \xi_i} \qquad \gamma^i_{x\theta} = \left(\frac{\partial v_i}{\partial x} \right) + \frac{1}{1 + \xi_i / a} \left(\frac{\partial u_i}{a \partial \theta} \right)$$

$$\gamma^i_{\xi_i\theta} = \frac{\partial v_i}{\partial \xi_i} + \frac{1}{1 + \xi_i / a} \left(\frac{\partial w_i}{a \partial \theta} - \frac{v_i}{a} \right) \qquad \gamma^i_{\xi_i s} = \frac{\partial u_i}{\partial \xi_i} + \frac{\partial w_i}{\partial x} \tag{3.14}$$

To develop the governing differential equations in the finite element form, displacement fields should be related to the identified nodal displacement components using the shape functions. After substituting stress and strain and also the displacement fields into the Eqs (3.12) and (3.13), the energy of each layer is determined. The total kinetic and strain energies are then:

$$\begin{aligned} U_T &= U_T^{\text{top}} + U_T^{\text{core}} + U_T^{\text{bottom}} \\ U_E &= U_E^{\text{top}} + U_E^{\text{core}} + U_E^{\text{bottom}} \end{aligned} \tag{3.15}$$

Eq. (3.15) can be rewritten for each element in the matrix form:

$$\begin{aligned} U_T &= \frac{1}{2}\left\{\dot{q}^e\right\}^T\left[M^e\right]\left\{\dot{q}^e\right\} \\ U_E &= \int_{-\frac{h}{2}}^{\frac{h}{2}}\int_0^{2\pi}\int_{-\frac{L_e}{2}}^{\frac{L_e}{2}} \frac{1}{2}\{\sigma\}^T\{\varepsilon\}dV = \frac{1}{2}\left\{q^e\right\}^T\left[K^e\right]\left\{q^e\right\} \end{aligned} \tag{3.16}$$

where $\{\sigma\}$ and $\{\varepsilon\}$ are respectively stress and strain components, $\{q^e\}$ is the nodal displacement at each element, $[M^e]$ and $[K^e]$ are elemental mass and stiffness matrices which can be found by summing the kinetic and strain energies of each layer as:

$$\begin{aligned} \left[M^e\right] &= \left[M^e\right]^{\text{top}} + \left[M^e\right]^{\text{core}} + \left[M^e\right]^{\text{bottom}} \\ \left[K^e\right] &= \left[K^e\right]^{\text{top}} + \left[K^e\right]^{\text{core}} + \left[K^e\right]^{\text{bottom}} \end{aligned} \tag{3.17}$$

Pre-stress components due to the thermal field and internal/external pressure in sandwich cylindrical shell can be expressed as:

$$\left\{\sigma^0\right\} = \left\{\sigma_{0xx}^{\text{top}} \quad \sigma_{0\theta\theta}^{\text{top}} \quad \sigma_{0xx}^{\text{bottom}} \quad \sigma_{0\theta\theta}^{\text{bottom}} \quad \sigma_{0\xi_3\xi_3}^{\text{core}}\right\} \tag{3.18}$$

The energies of these stresses are contributing in the total strain energy by implementing the nonlinear strain components which are expressed as follows [94]:

$$\varepsilon_{xx}^{i\ \mathrm{NL}} = \frac{1}{2}\left\{\left(\frac{\partial u_i}{\partial x}\right)^2 + \left(\frac{\partial v_i}{\partial x}\right)^2 + \left(\frac{\partial w_i}{\partial x}\right)^2\right\}$$
$$\varepsilon_{\theta\theta}^{i\ \mathrm{NL}} = \frac{1}{2}\left\{\left(\frac{\partial u_i}{a\partial \theta}\right)^2 + \left(\frac{\partial v_i}{a\partial \theta} + \frac{w_i}{a}\right)^2 + \left(\frac{\partial w_i}{a\partial \theta} - \frac{v_i}{a}\right)^2\right\} \tag{3.19}$$

in which $i = t$ and b is the index for the elastic top and bottom layers. Since the initial normal stress in viscoelastic material for the higher order model is the stress in thickness direction, therefore the corresponding nonlinear terms of normal strain in thickness direction should be considered which is given as:

$$\varepsilon_{\xi_3\xi_3}^{c\ \mathrm{NL}} = \frac{1}{2}\left\{\left(\frac{\partial u_c}{\partial \xi_3}\right)^2 + \left(\frac{\partial v_c}{\partial \xi_3}\right)^2 + \left(\frac{\partial w_c}{\partial \xi_3}\right)^2\right\} \tag{3.20}$$

The works done by initial stresses (U_G) at each layer is then calculated and stored in the total strain energy:

$$U_G = \int_{-\frac{h}{2}}^{\frac{h}{2}} \int_0^{2\pi} \int_{-\frac{L_e}{2}}^{\frac{L_e}{2}} \left\{\sigma^0\right\}^T \left\{\varepsilon^{\mathrm{NL}}\right\} dV = \frac{1}{2}\left\{\delta^e\right\}^T \left[K_G^e\right] \left\{\delta^e\right\} \tag{3.21}$$

in which:

$$\left[K_G^e\right] = \left[K_G^e\right]^{\mathrm{top}} + \left[K_G^e\right]^{\mathrm{core}} + \left[K_G^e\right]^{\mathrm{bottom}}$$

Considering all the energies mentioned before, the Hamilton's principle is employed to establish the equations of motion:

$$\delta \int_{t_0}^{t_1} \left(U - U_T - W\right) = 0 \tag{3.22}$$

where W is the work done by the external forces, U_T is the total kinetic energy, U is the total strain energy ($U=U_E+U_G$) and times t_1 and t_2 are arbitrary times in which at

those times all variation are zero [129]. Substituting all energies into Eq. (3.22) and assembling the elemental stiffness and mass matrices yields the equations of motion as:

$$[M]\{\ddot{q}\}+[K]\{q\}=\{F(t)\} \tag{3.23}$$

in which $\{F(t)\}$ is equivalent nodal forces of the system, $[K]=[K_G]+[K_E]$ and $[M]$ are, respectively, the system stiffness and mass matrices.

It should be noted that the initial stresses in Eq. (3.18) can be obtained considering static deformation under thermal field and internal/external pressure. The constitutive equation for each layer considering temperature distributions can be written as:

$$\begin{aligned}
\sigma_{xx}^{i} &= \frac{E_i}{\left(1-\upsilon_i^2\right)}\left[\left(\varepsilon_{xx}^{i}-\alpha_i\Delta T_i\right)+\upsilon_i\left(\varepsilon_{\theta\theta}^{i}-\alpha_i\Delta T_i\right)\right] \\
\sigma_{\theta\theta}^{i} &= \frac{E_i}{\left(1-\upsilon_i^2\right)}\left[\left(\varepsilon_{\theta\theta}^{i}-\alpha_i\Delta T_i\right)+\upsilon_i\left(\varepsilon_{xx}^{i}-\alpha_i\Delta T_i\right)\right] \\
\sigma_{\xi_3\xi_3}^{c} &= E_c\left(\varepsilon_{\xi_3\xi_3}^{c}-\alpha_c\Delta T_c\right)
\end{aligned} \tag{3.24}$$

where i= t, b. The strain energy is determined with substituting Eq. (3.24) into Equation (3.13) as follows:

$$\begin{aligned}
U_s = \sum_{i}^{t,b}\frac{1}{2}\Bigg(&\int_{-\frac{h_i}{2}}^{\frac{h_i}{2}}\int_0^{2\pi}\int_{-\frac{L_e}{2}}^{\frac{L_e}{2}}\left(\sigma_{xx}^{i}\left(\varepsilon_{xx}^{i}-\alpha_i\Delta T_i\right)+\sigma_{\theta\theta}^{i}\left(\varepsilon_{\theta\theta}^{i}-\alpha_i\Delta T_i\right)+G_i\left(\gamma_{x\theta}^{i\,2}+\gamma_{\xi_i x}^{i\,2}+\gamma_{\xi_i\theta}^{i\,2}\right)\right)dV_i\Bigg) \\
+\frac{1}{2}\Bigg(&\int_{-\frac{h_c}{2}}^{\frac{h_c}{2}}\int_0^{2\pi}\int_{-\frac{L_e}{2}}^{\frac{L_e}{2}}\left(\sigma_{\xi_3\xi_3}^{c}\left(\varepsilon_{\xi_3\xi_3}^{c}-\alpha_c\Delta T_c\right)+G_c\left(\gamma_{\xi_3 x}^{c\,2}+\gamma_{\xi_3\theta}^{c\,2}\right)\right)dV\Bigg)
\end{aligned} \tag{3.25}$$

Using Hamilton's principle for static case, the variation of strain energy is equated to the energy variation introduced into the cylindrical shell by internal/external pressure ($\delta U_s = \delta W_p$). After substituting the energies, the thermal terms in U_S are appeared as the thermal forces:

$$\left[K_s^e\right]\left\{q_s^e\right\}-\left\{F^{\mathrm{Th}}\right\}=\left\{F^P\right\} \tag{3.26}$$

in which F^{Th} and F^P are, respectively, the thermal and external forces, $[K_s]$ is elemental static stiffness matrix and q_s is static deflection. After assembling, the displacement field and subsequently the stress components in each layer are determined as the initial stresses. Considering these pre-stress components, the dynamic response is determined using Eq. (3.23). In the case of free vibration analysis, the Eq. (3.23) becomes:

$$\left(-\omega^2[M]+[K(\omega)]\right)\{q\}=0 \tag{3.27}$$

in which $[K]=\left[K'(\omega)+\mathrm{i}K''(\omega)\right]$ is a complex frequency dependent stiffness matrix due to frequency dependent properties of the damping layer and therefore the eigenvalue problem cannot be directly solved. One method to calculate natural frequencies is developing frequency response of the structure under harmonic loading for wide range of frequencies. This method is expensive since it strongly depends on the resolution of frequency. Alternatively the eigenvalue problem of Eq. (3.27) can be iteratively solved using the evaluated stiffness matrix at the natural frequencies. The best point to start the iteration process could be the natural frequency of bare cylinder. The iteration must be continued until a desired convergence is provided as follows:

$$\frac{\left|\omega_i-\omega_{i-1}\right|}{\omega_{i-1}}\le\lambda_1$$

in which λ_1 is the tolerance of convergence and it is chosen to be 10^{-5}. The energy per volume dissipated in each cycle under displacement $q(t)$ with amplitude q_0 is given by:

$$W_d=\pi K''(\omega)q_0^2 \tag{3.28}$$

For a lossless structure including mass which is vibrating at steady state, the total energy including potential and kinetic energies throughout a cycle can be easily expressed as:

$$U = \frac{1}{2} K'(\omega) \left[\frac{\omega^2}{\omega_n^2} q_0^2 + \left(1 - \frac{\omega^2}{\omega_n^2} \right) q^2(t) \right] \tag{3.29}$$

The loss factor can be defined as the ratio of dissipated energy per radian and maximum potential energy. According to the Eq. (3.29), energy remain constant at natural frequency ($\omega^2 = \omega_n^2$). Therefore, a meaningful definition for the loss factor is obtained only at natural frequencies. The dissipated energy (W_d) and the maximum potential equation (U) for the sandwich structure which is discretized into number of elements can be expressed in the following form:

$$W_d = \pi \{\phi\}^{\mathrm{T}} [K''] \{\phi\} \qquad U = \frac{1}{2} \{\phi\}^{\mathrm{T}} \{K'\} \{\phi\}$$

in which $\{\phi\}$ is the normalized eigenvector in free vibration. Thus, the loss factor η at each mode i can be defined as:

$$\eta_i = \frac{W_d}{2\pi U} = \frac{\{\phi_i\}^{\mathrm{T}} [K''] \{\phi_i\}}{\{\phi_i\}^{\mathrm{T}} \{K'\} \{\phi_i\}} \tag{3.30}$$

3.4 Transient Heat Transfer

Transient heat transfer equation for axisymmetric cylindrical structure shown in Figure 3.1 can be expressed as

$$\frac{\partial^2 T}{\partial \xi^2} + \frac{1}{\xi} \frac{\partial T}{\partial \xi} + \frac{\partial^2 T}{\partial x^2} + \frac{H}{K} = \frac{\rho C_p}{K} \frac{\partial T}{\partial t} \tag{3.31}$$

in which H is the rate of internal heat generation, C_p is the specific heat, ρ is the density and T is the time-dependent distribution of temperature.

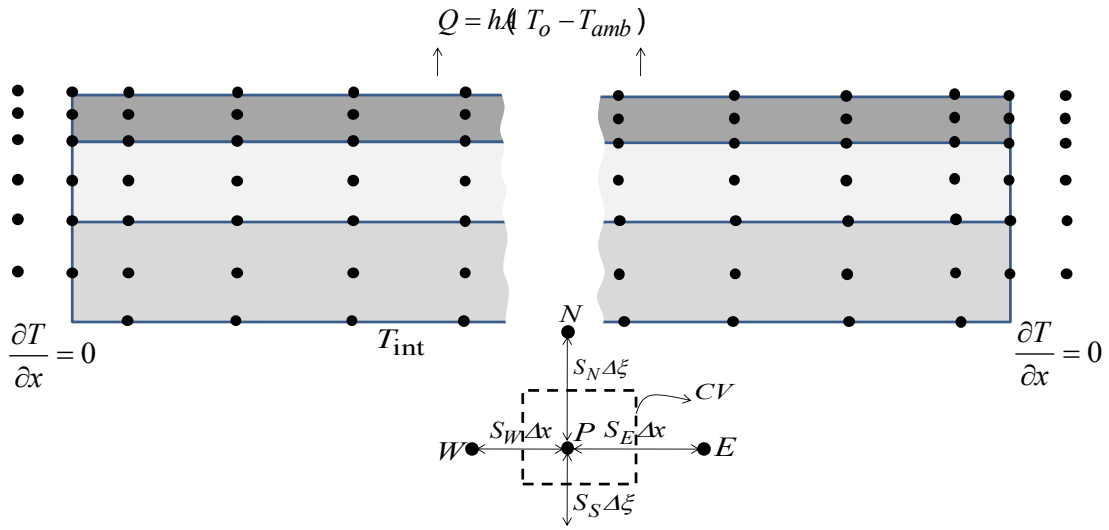

Figure 3.1 Irregular gridding in finite difference model and the boundary conditions

Using finite difference method for irregular grid [130] based on the energy balance for the control volume shown in Figure 3.1, the finite difference equation for point P is formulated in this dissertation as:

$$\begin{aligned}
&\left(\frac{2K_{NP}}{S_N(S_S+S_N)\Delta\xi^2}+\frac{K_{NP}}{S_N(S_S+S_N)a_P\Delta\xi}\right)(T_N-T_P)\\
&+\left(\frac{2K_{SP}}{S_S(S_S+S_N)\Delta\xi^2}-\frac{K_{SP}}{S_S(S_S+S_N)a_P\Delta\xi}\right)(T_S-T_P)\\
&+\frac{2K_{EP}}{S_E(S_E+S_W)\Delta x^2}(T_E-T_P)+\frac{2K_{WP}}{S_W(S_E+S_W)\Delta x^2}(T_W-T_P)+H=\left(\rho C_p\right)_{eff}\frac{\left(T'_P-T_p\right)}{\Delta t}
\end{aligned} \tag{3.32}$$

where a_P, is radial distance between point P and central axis of the sandwich cylinder, T'_P and T_P are respectively current and next state of temperature for a time step Δt (implicit method), K_{ij} (i =S, N, E, W and j=P) is the effective thermal conductivity through the thickness and axial direction of the cylinder. According to grid shown in Figure 3.1, in radial direction only one material contributes in the effective conductivity for each point. However for the nodes at the interfaces the effective conductivity along the axial direction is obtained as:

$$K_{EP} = K_{WP} = \frac{S_N}{(S_S + S_N)} K_N + \frac{S_S}{(S_S + S_N)} K_S \tag{3.33}$$

where K_N and K_S are respectively conductivity at points N and S. Temperature at the inner side of the sandwich cylinder is T_{int} and heat is transferred from the outer side to surrounding environment by convection as:

$$Q = hA(T_o - T_{\text{amb}})$$

in which Q is the rate of heat transfer, h is coefficient of convection, A is the area of contact between sandwich cylinder and environment, T_o is the outer side temperature of each element and T_{amb} is the ambient temperature. Also the temperature gradient in axial direction at the end sides of the sandwich cylinder is assumed to be zero (isolated) and therefore extra column of points at the outer sides of boundary points at the ends of the cylinder are considered in order to equate their temperature to the temperature of the points at the inner side of the boundary points (Figure 3.1).

3.5 Material Property of the Layers

The material properties of the top and bottom elastic layers (Steel AISI 304) and core viscoelastic layer (Viton_B) are given in Table 3.1. The material loss factor and shear modulus of the damping core layer highly depend on temperature and frequency as shown in Figure 3.2.

Table 3.1 Material property of elastic and viscoelastic layers

	Shear modules (N/m^2)	Density (kg/m^3)	Poisson's ratio	Loss Factor	Specific heat (J/Kg °C)	Conductivity (W/m°C)	Thermal expansion coefficients (10^{-6}/°C)
Steel AISI 304	74.2×10^9	7830	0.3	-	503	80.5	17
Viton_B	Figure 3.2	1050	0.4	Figure 3.2	1360	0.2	100

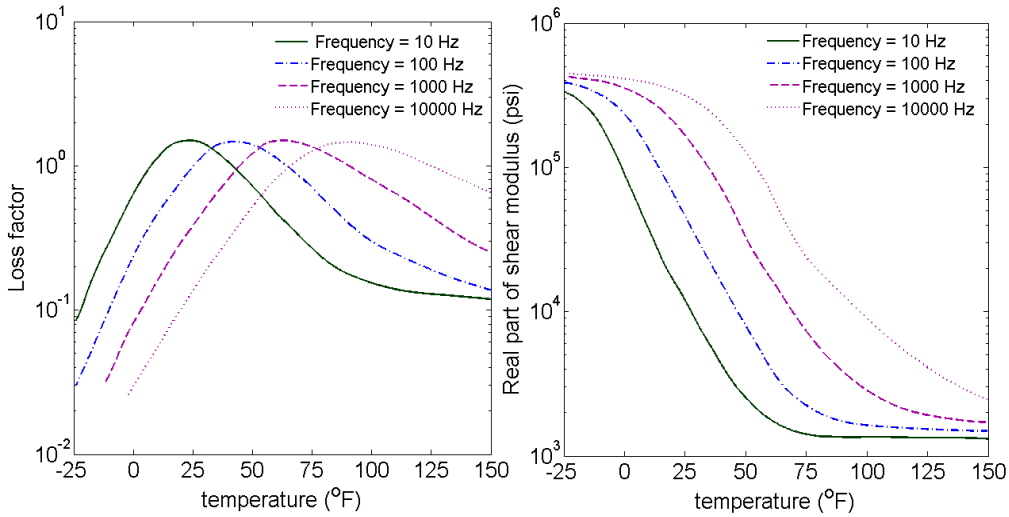

Figure 3.2 Loss Factor and real part of shear modulus versus temperature for Viton-B

These data are directly extracted from Nashif et al. [128] in which the temperature-frequency superposition principle was employed to relate viscoelastic properties at different temperature to the so-called reduced frequency parameter $\alpha_T\omega$ in which α_T is the temperature-dependent shift factor and ω is the actual frequency. Thus, the material properties can be expressed as

$$G(\omega,T) = G(\alpha_T\omega, T_0)$$
$$\eta(\omega,T) = \eta(\alpha_T\omega, T_0) \tag{3.34}$$

where T_0 is the reference temperature. Since there is no available explicit formulation to express the properties in terms of temperature and frequencies, all the points in those nomogram are read and digitized with high resolution. According to the data, changing of the material properties with respect to frequencies can be formulated using linear interpolations between each frequency in logarithmic scale. Considering this, an artificial neural network available in MATLAB has been trained to interpolate the shear modulus and loss factor versus temperature and frequency. The effect of temperature rise $T\text{core}(t)$ within the damping layer due to heat dissipation can be accounted by replacing T in Eq. (3.34) by $T + T\text{core}(t)$ [131]. It should be noted that, the rate of dissipated energy per unit

volume in each element is determined using Eq. (3.28) and then substituted in Eq. (3.32) as H to obtain the temperature distribution at each layer in terms of time.

3.6 Results and Discussion

In the following, first the developed finite element modeling for a simply-supported cylinder under internal/external pressure has been validated by comparing the results with other studies. The temperature distribution using finite difference method for irregular grid is validated by comparing the results to those obtained from finite element method. The natural frequencies and the corresponding loss factors resulted from the lower and higher order models are also compared. Using the nonlinear model, the parametric studies are presented to show the effect of temperature variation, the resulted thermal stress and pressure on damping characteristics of clamped-clamped sandwich cylindrical shell.

3.6.1 Validations

The natural frequency under internal and external pressure for simply supported cylinder is shown in Figure 3.3. The results are compared to the results presented by Sabri and Lakis [28]. The length, radius and thickness of the cylinder are, respectively, 231 mm, 77.25 mm and 1.5 mm. The Poisson's ratio, Young modules and density of the material are 0.3, 200 GPa and 7800 Kg/m^3, respectively. As it can be seen, excellent agreements between the results are observed.

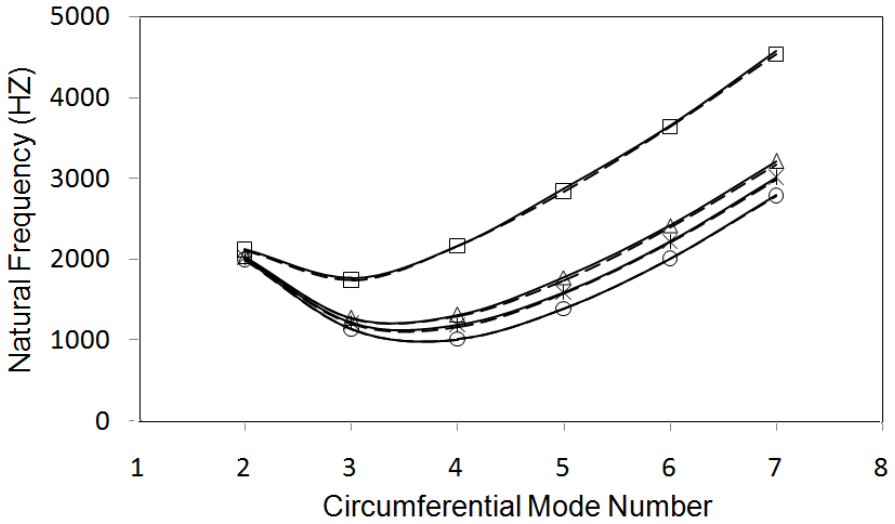

Figure 3.3 Natural frequency of simply supported shell under external/internal pressure; ------Present study, _____ Reference [28]; □, P_{int} = 9 MPa; Δ, P_{int} = 0. 9 MPa; ◊, P_{int} =0.0 MPa; O, P_{ext} = 0.9 MPa

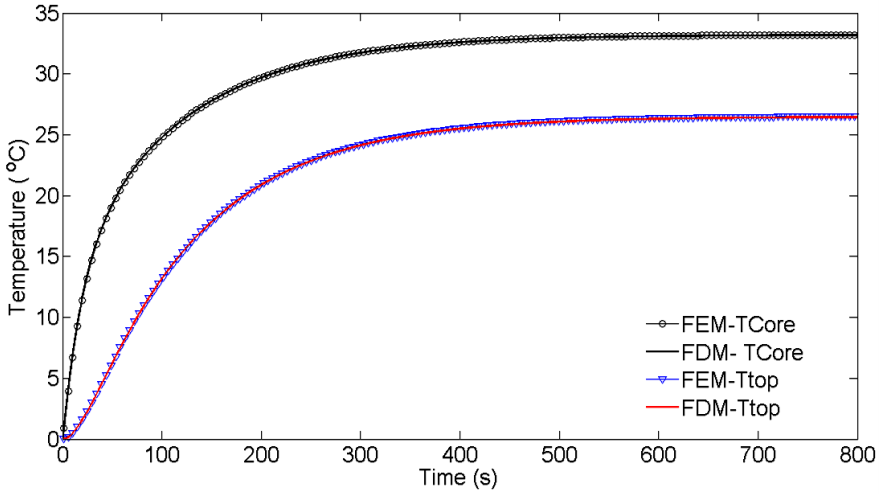

Figure 3.4 Transient temperature relative to the ambient temperature at the middle point of the core and top layers subjected to internal temperature $T_{int}^{realative}$=40 °C (T_{int}=60 °C); comparison between results obtained by FEM and FDM.

Table 3.2 Comparison between linear and nonlinear models for different circumferential mode number *n*

	n	1	2	3	4	5	6	7	8	9	10
Loss factor	Linear Model	0.0004	0.035	0.184	0.256	0.262	0.249	0.232	0.215	0.198	0.192
	Nonlinear Model	0.0012	0.036	0.184	0.256	0.262	0.250	0.233	0.215	0.199	0.194
Natural Frequency (Hz)	Linear Model	335	158	137	211	324	460	619	799	1001	1236
	Nonlinear Model	335	157	137	211	324	460	619	799	1001	1236

Table 3.2 shows comparison between the lower and higher order models at different natural frequencies and corresponding loss factors for a clamped-clamped sandwich cylinder. The material properties of the elastic and viscoelastic layers are given in Table 3.1. In this case the length of the clamped-clamped cylinder is assumed to be L = 2.52 m, the radius is a = 0.3 m and the thickness of bottom, core and top layers are, respectively, 5 mm, 5 mm and 1 mm. The comparison shows that higher order model exhibits more damping characteristics than the lower order model. Both models almost result in same natural frequencies. For these dimensions and the material properties given in Table 3.1, transient temperature at the middle point of viscoelastic core and elastic top layers is shown in Figure 3.4. The results are compared with the results obtained by finite element modeling in ANSYS. The ambient temperature is assumed to be 20 °C and the heat at the top layer is transferred to the environment where h = 20 W/m^{2}K. The temperature inside the cylinder relative to the ambient temperature is 40 °C and the ends of the cylinder are isolated. As it can be realized, excellent agreement exists between the results.

3.6.2 Effect of temperature and internal/external pressure on frequency response and loss factor

Increase in external pressure leads to increase in the flexibility. Consequently, as shown in Figure 3.5, the natural frequencies decrease and the corresponding loss factors increase. Similar results are presented to show the effect of internal pressure on damping and the natural frequencies. According to the results shown in Figure 3.6, the natural frequencies increase and accordingly the corresponding loss factors decrease because of higher stiffness introduced in the sandwich cylinder under internal pressure. Although external pressure provides more damping but due to decrease in stiffness of the sandwich cylinder, larger deflection is expected which is illustrated in Figure 3.7.

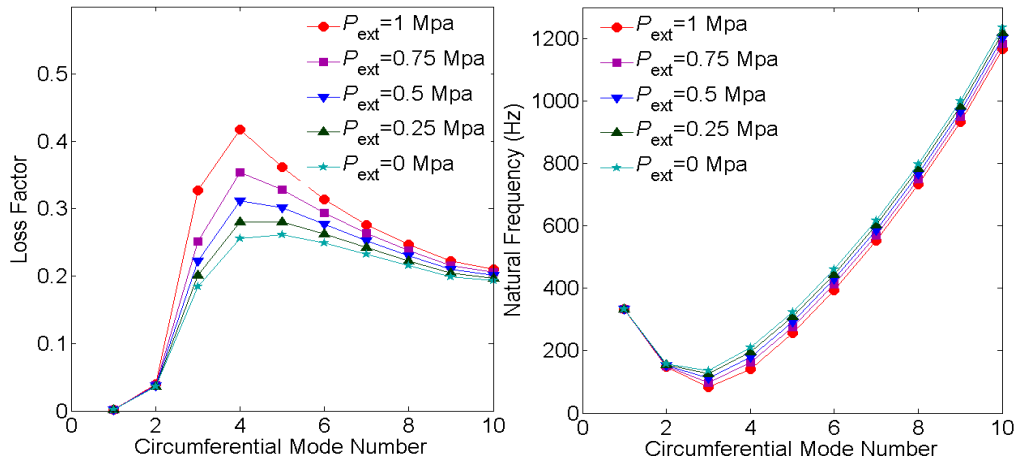

Figure 3.5 Effect of external pressure on loss factor and natural frequency at different circumferential mode

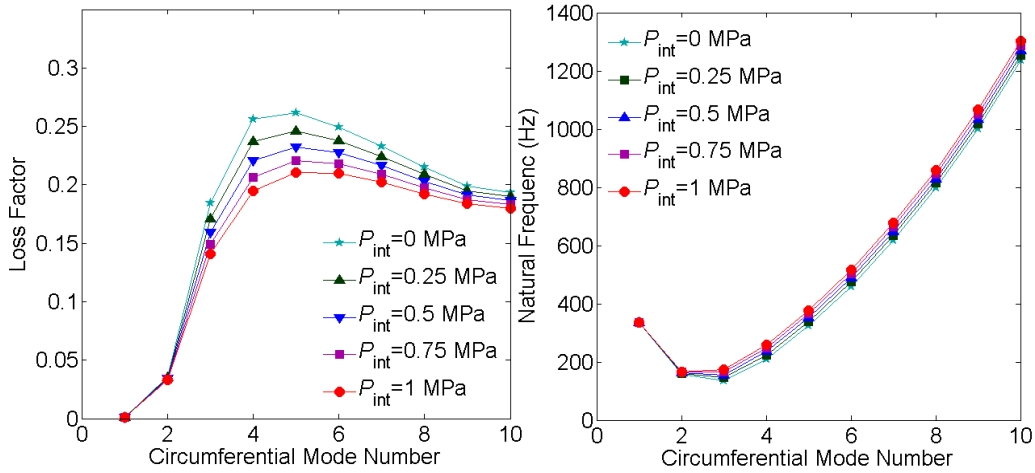

Figure 3.6 Effect of internal pressure on loss factor and natural frequency at different circumferential mode

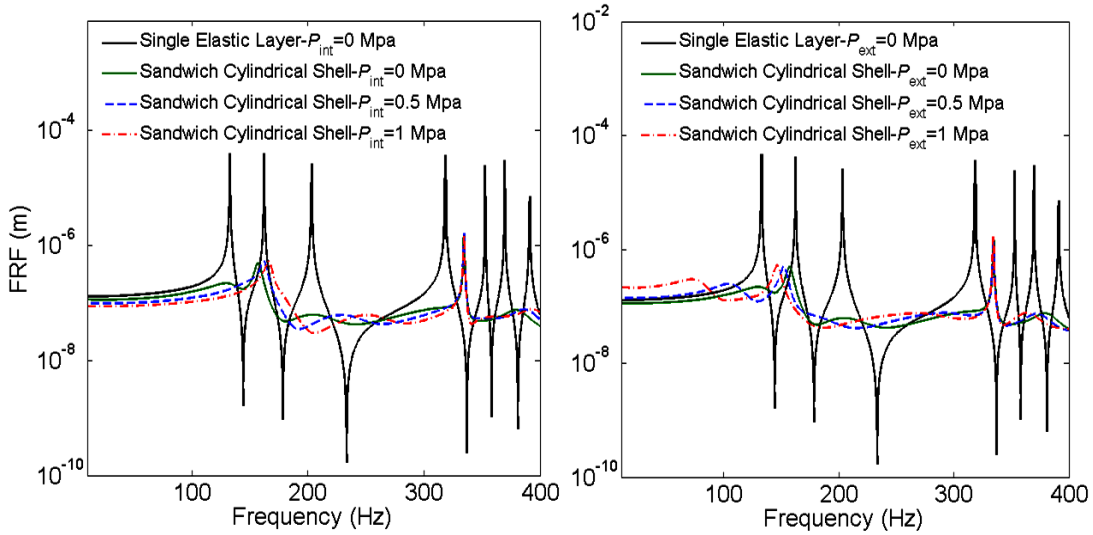

Figure 3.7 Frequency response functions at the middle point of pressurized clamped-clamped sandwich cylinder

However, more decrease in relative displacement at the natural frequencies is observed. On the other hand, the static displacement is decreased under internal pressure compared with that in unpressurized sandwich cylinder. Due to less damping under internal pressure, more increase in relative displacements at the natural frequencies is resulted. Effect of temperature on structural loss factor and frequency response is also investigated. Figure 3.8 shows frequency response for different ambient temperatures. The results indicate that decrease in loss factor and shear modulus of the damping layer caused by environmental temperature leads to decrease in damping characteristics of the viscoelastic layer. In practice, internal temperature of a cylinder differs from ambient temperature. The effect of internal temperature on the natural frequencies and loss factors at the steady state is shown in Figure 3.9. This figure also includes the temperature distribution at the mid section of each layer in the sandwich cylinder. Internal temperature affects the material properties of the core layer and also introduces thermal stresses at each layer. According to Figure 3.2 loss factor and real part of the viscoelastic layer decrease. This leads to decrease in damping behavior and natural frequencies. However the resulted pre-stresses due to the thermal loads increase the stiffness of the structure. Consequently the natural frequencies almost remain unchanged except at higher natural frequencies. However, decline in damping performance of the viscoelastic material and the developed thermal stresses considerably decrease the loss factor of the structure. These can be also observed from the frequency response shown in Figure 3.10.

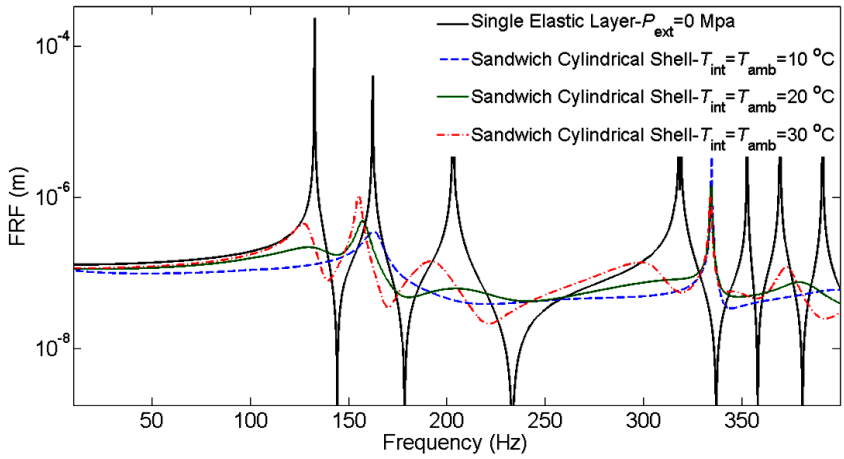

Figure 3.8 Ambient temperature effect on frequency response of empty clamped-clamped sandwich cylindrical shell

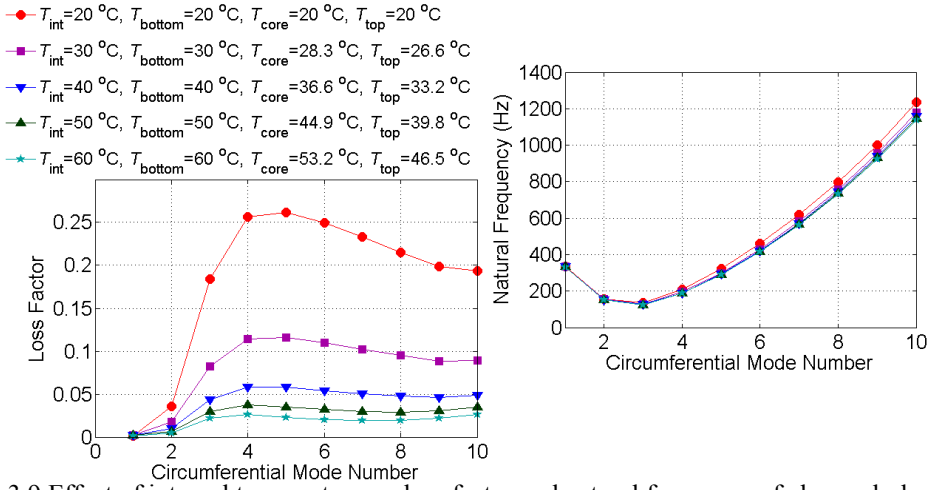

Figure 3.9 Effect of internal temperature on loss factor and natural frequency of clamped-clamped sandwich cylinder

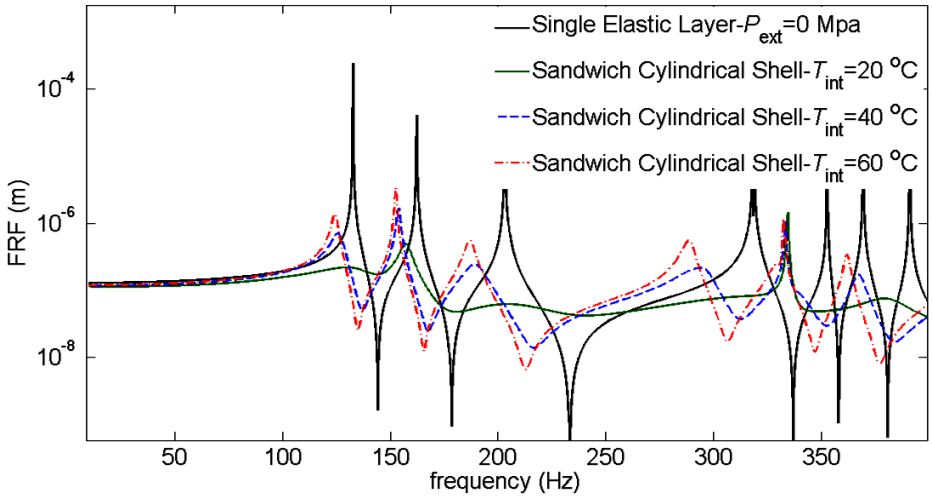

Figure 3.10 Frequency response function at the middle point of sandwich cylinder under internal temperature

3.6.3 Heat dissipation effect of viscoelastic layer

For a pressurized sandwich cylinder in which the pressure is periodically oscillating during time, according to the Eq. (3.28) the mechanical strain energy will be dissipated after each cycle. The internal pressure is assumed to be P_{int} =3 MPa and the amplitude of oscillation is 1 MPa. The rate of dissipated energy for unit volume should be substituted into the Eq. (3.32) as H. This energy will be accumulated inside the viscoelastic layer. Since the conductivity of the viscoelastic material is low, the generated heat will be transferred to constraining layer after long time. The heat then is transformed to the environment through convection. Therefore the temperature keeps on increasing at the viscoelastic layer which leads to decrease in loss factor and shear modulus, and consequently larger amplitude of displacement is resulted. This behavior is shown in Figure 3.11 at frequency of f=100 Hz. For low frequencies small amount of heat is generated with time comparing to the high frequencies. Figure 3.12 shows the temperature distribution along the axial coordinate of the cylinder at the center axis of core layer for high frequency (f = 400 Hz) after 20 s. Figure 3.13 also shows the variation of amplitude at the midpoint of core layer for different convection coefficient. As it can be realized, the amplitude reaches its steady state faster under forced convection. From the results one can conclude that the definition of loss factor is not unique even at natural frequencies. The heat dissipation changes the material properties and also introduces thermal loads in the structure and consequently the structural loss factor changes. Figure 3.14 shows the hysteresis loops after every 10 s under cyclic loading for free convection. According to the shapes and slopes of the trajectories, the area of the ellipse that represents dissipated energy (and consequently loss factor) is changing during time. Thus, in the definition of loss factor the number of cycles should also be considered.

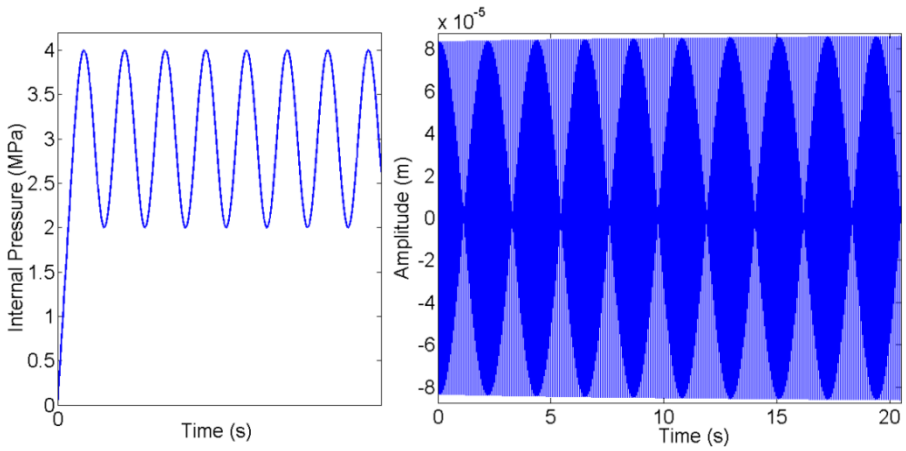

Figure 3.11 Heat dissipation effect on harmonic response of the middle point due to cyclic internal pressure f= 100 Hz

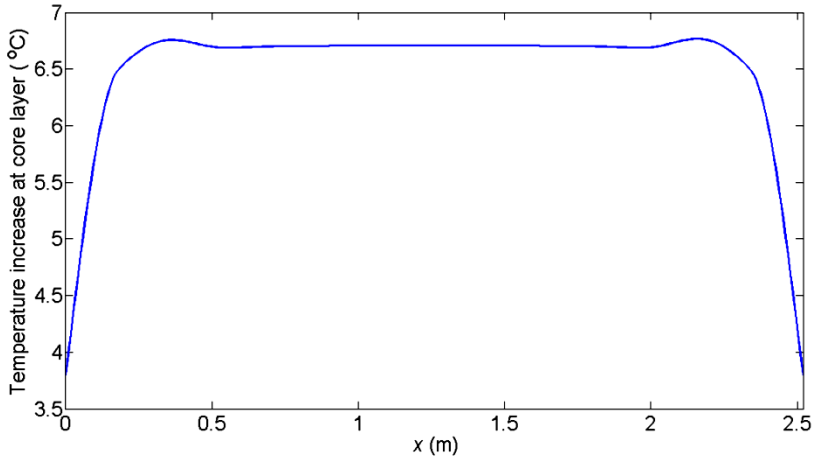

Figure 3.12 Increase in temperature distribution at the core layer along the axial direction of sandwich cylinder due to cyclic internal pressure after 20 (s), f=400 Hz

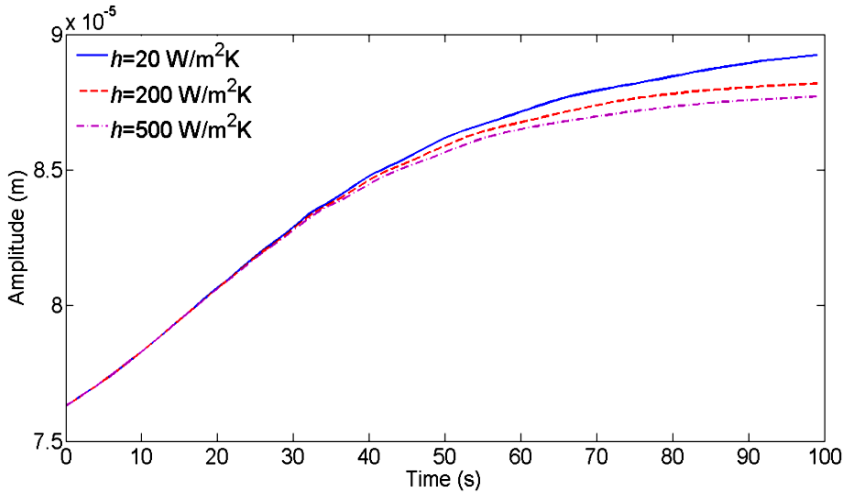

Figure 3.13 Steady state amplitude under convection effect of environment

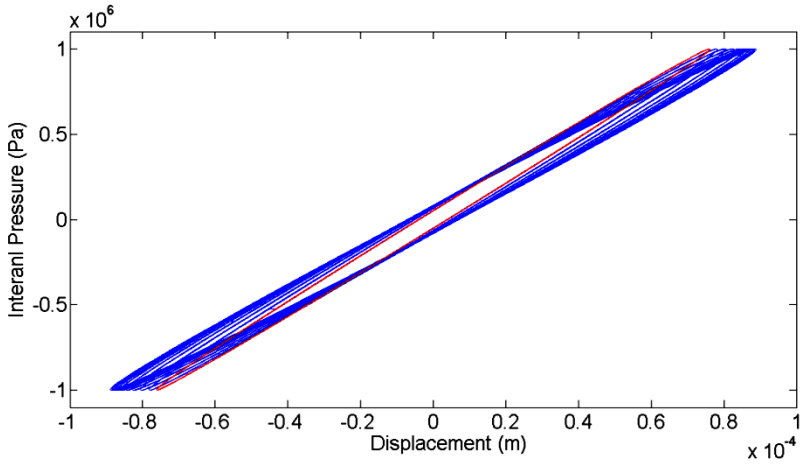

Figure 3.14 Hysteresis loops after every 10 (s) under cyclic loading (f = 400 Hz)

3.7 Conclusion

The frequency response function and vibration characteristics of a pressurized sandwich cylindrical shell under thermal loading were investigated. Not only pre-stress components (resulted from pressure and temperature) affect the damping properties, change in the material properties of the damping layer due to temperature variation can change the frequency response and vibration characteristics. The internal temperature introduces different temperature distribution and consequently different stress distribution at each layer. The heat dissipation from damping layer releases energy which can be considered as a heat source in the heat transfer equation. It was shown that, the thermal load and change in material properties due to the heat generated change the amplitude of response. Therefore, not only the temperature and frequency affect the damping behavior, number of cycles of the harmonic loading can affect the damping characteristics of a sandwich structure.

CHAPTER 4

VIBRATION ANALYSIS AND DESIGN OPTIMIZATION OF VISCOELASTIC SANDWICH CYLINDRICAL SHELL

4.1 Introduction

Damping properties of viscoelastic sandwich structure can be improved by changing some parameters such as thickness of the layers, distribution of partial treatments, slippage between layers at the interfaces, cutting and its distribution at the top and core layers. The optimization problem in literature has been studied to obtain maximum damping in sandwich structures [103-111] which has been addressed in chapter 1. Since the optimization problem may result in a thick core layer, for achieving more accuracy a higher order Taylor's expansion of transverse and in-plane displacement fields should be considered for the core layer as discussed in chapter 2. As shown in chapter 2, this higher order model differs from the lower order at higher frequencies for the thick core layer. Considering this, the higher order model should be employed where the design optimization is desired for higher frequencies. This higher order model is now formulated to model cut and partial treatment in sandwich viscoelastic cylindrical shell.

Two different methods can be used to determine the displacement fields through the thickness of viscoelastic sandwich structures. In the first method, named method_1, the translational displacements at the top and bottom elastic layers are determined using the displacement fields at the core layer by implementing the boundary conditions at the interfaces which was discussed in chapter 2. As shown in this chapter, this method facilitates determination of the displacement fields considering higher order expansion of displacements through the thick core layer but fails to model the cuts and partial

treatment in the sandwich structure. In the second method, named method_2, the displacement fields at the core layer are obtained in terms of the displacements at the bottom and top elastic layers. In spite of the fact that this method brings intricacy into the formulations particularly where the higher order expansion of the core displacement fields is considered, it can effectively model the cuts and partial treatments in the sandwich structure. Both methods should give identical results for fully treated sandwich cylindrical shell.

The main limitation in the previously developed higher order displacement fields in the core layer such as the higher order model considered by Araújoet al. [10] is lack of the compatibility between the displacement fields at the different layers in which implementing the boundary conditions does not compatibly give the displacement fields at the core layer in terms of the displacement fields at the top and bottom layers. Here, based on the profile of displacement fields of the core layer in static deformation, the higher order expansion of transverse and in-plane displacement fields in the thickness direction of the core layer are developed to analyze the vibration damping of the sandwich cylindrical shell with thin or thick core layer. Using this way, not only a good approximation for the shape of the displacement profile in the thickness coordinate can be obtained, but also it is possible to drive the higher order expansion in which the displacement field of the core layer can be represented by those of the elastic faces (i.e. the least number of variable). As explained further, the partial treatment and cut can be then modeled using the developed higher order expansion. By combining the finite element model with the optimization algorithms based on the genetic algorithm (GA) and sequential quadratic programming (SQP) technique, the optimal number, distribution and

thicknesses of the elastic top and core layers in the partial treatments are simultaneously optimized to improve damping of the structure. The results show that damping can significantly improve while the total mass of the structure decreases. In order to improve damping, cuts can be embedded in the sandwich structure to increase transverse shear strains in the core layer at the cut locations. Considering this, cutting in this study has been modeled using the discontinuity at the nodal displacements in the elements at the top and core layers. Here, distribution and the total number of cuts are simultaneously optimized to improve the damping behavior in the sandwich cylindrical shell considering different boundary conditions. The objective function is considered to be an effective loss factor defined based on combinations of loss factor in different circumferential and axial directions and also their contributions in the forced vibration.

4.2 Lower Order Expansion of Displacement Fields through the Thickness of Viscoelastic Core Layer

First order shear deformation theory (FSDT) can be used to define the displacement distribution through the thickness of elastic and viscoelastic layers. As shown in Figure. 2.1, displacement fields for a three layered sandwich shell of revolution are defined in terms of the displacements of the middle plane including u_0, v_0 and w_0 and the rotations of the normals to the middle plane in axial and circumferential directions denoted by ψ_1 and ψ_2, respectively. Considering lower order expansion of displacement fields, the total displacement fields for each layer can be written as:

$$\begin{aligned} u_t(x,\theta,\xi_1,t) &= u_o^t(x,\theta,t) + \xi_1\psi_1^t(x,\theta,t) \\ v_t(x,\theta,\xi_1,t) &= v_o^t(x,\theta,t) + \xi_1\psi_2^t(x,\theta,t) \qquad -\frac{h_t}{2} < \xi_1 < \frac{h_t}{2} \\ w_t &= w_t(x,\theta,t) \end{aligned} \tag{4.1}$$

$$
\begin{aligned}
u_b(x,\theta,\xi_2,t) &= u_o^b(x,\theta,t) + \xi_2\psi_1^b(x,\theta,t) \\
v_b(x,\theta,\xi_2,t) &= v_o^b(x,\theta,t) + \xi_2\psi_2^b(x,\theta,t) \qquad -\frac{h_b}{2} < \xi_2 < \frac{h_b}{2} \\
w_b &= w_b(x,\theta,\mathrm{t})
\end{aligned} \tag{4.2}
$$

$$
\begin{aligned}
u_c(x,\theta,\xi_3,t) &= u_o^c(x,\theta,t) + \xi_3\psi_1^c(x,\theta,t) \\
v_c(x,\theta,\xi_3,t) &= v_o^c(x,\theta,t) + \xi_3\psi_2^c(x,\theta,t) \qquad -\frac{h_c}{2} < \xi_3 < \frac{h_c}{2} \\
w_c &= w_0^c(x,\theta,t)
\end{aligned} \tag{4.3}
$$

Here, slippage between layers at the interface has been considered in the formulations. Based on the methodology presented by Bai and Sun [14], for demonstrating the effect of slippage, it can be assumed that a very thin adhesive layer glues the top and bottom layers to the core layer. Considering this, at the interfaces the in-plane displacements are discontinuous. Using the displacement variation at the interfaces and the viscoelastic property of the adhesive layers, transverse shear stresses at the interfaces are obtained. Therefore the boundary conditions at the interfaces can be expressed as follows:

$$
\begin{aligned}
&\xi_1 = -\frac{h_t}{2} \quad \xi_3 = \frac{h_c}{2} && \tau_{\xi_3 x} = K^*\left(u_t - u_c\right) && \tau_{\xi_3\theta} = K^*\left(v_t - v_c\right) \\
&\xi_2 = \frac{h_b}{2} \quad \xi_3 = -\frac{h_c}{2} && \tau_{\xi_3 x} = K^*\left(u_c - u_b\right) && \tau_{\xi_3\theta} = K^*\left(v_c - v_b\right)
\end{aligned} \tag{4.4}
$$

in which $\tau_{\xi_3 s}$ and $\tau_{\xi_3\theta}$ are respectively transverse shear stresses in axial and circumferential directions and $K^*=k(\omega)(1+i\eta(\omega))$ is a complex shear stiffness parameter of the adhesive layer representing the bonding at the interfaces which is assumed to be frequency dependent. The adhesive layer is assumed to be completely in contact with the core and faces. If a large value is assigned to $k(\omega)$ then:

$$
\frac{\tau_{\xi_3 x}}{K^*} \approx 0 \text{ and } \frac{\tau_{\xi_3\theta}}{K^*} \approx 0
$$

and consequently the in-plane displacements are equal at the interfaces which means that the perfect bonding is provided. Substituting displacements from Eqs (4.1)-(4.3) into Eq. (4.4) and shear stress-strain relationship yields:

$$
\begin{aligned}
G_c\left(\psi_1^c+\frac{\partial w}{\partial x}\right)&=K^*\left(u_0^t-\frac{h_t}{2}\psi_1^t-u_0^c-\frac{h_c}{2}\psi_1^c\right)\\
G_c\left(\psi_1^c+\frac{\partial w}{\partial x}\right)&=K^*\left(u_0^c-\frac{h_c}{2}\psi_1^c-u_0^b-\frac{h_b}{2}\psi_1^b\right)\\
G_c\left(\psi_2^c+\frac{\partial w}{a\partial \theta}\right)&=K^*\left(v_0^t-\frac{h_t}{2}\psi_2^t-v_0^c-\frac{h_c}{2}\psi_2^c\right)\\
G_c\left(\psi_2^c+\frac{\partial w}{a\partial \theta}\right)&=K^*\left(v_0^c-\frac{h_c}{2}\psi_2^c-v_0^b-\frac{h_b}{2}\psi_2^b\right)
\end{aligned}
\tag{4.5}
$$

According to the method_1, by obtaining the translational displacement field at the top and bottom layers from Eq. (4.5) and then substituting into Eqs (4.1)-(4.3), the total displacements at the elastic faces are obtained as:

$$
\begin{aligned}
u_t&=u_0^c+\frac{\left(h_t\psi_1^t+h_c\psi_1^c\right)}{2}+\xi_1\psi_1^t+\frac{G_c}{K^*}\left(\psi_1^c+\frac{\partial w}{\partial x}\right)\\
v_t&=v_0^c+\frac{\left(h_t\psi_2^t+h_c\psi_2^c\right)}{2}+\xi_1\psi_2^t+\frac{G_c}{K^*}\left(\psi_2^c+\frac{\partial w}{a\partial \theta}\right)
\end{aligned}
\qquad -\frac{h_t}{2}<\xi_1<\frac{h_t}{2} \tag{4.6}
$$

$$
\begin{aligned}
u_b&=u_0^c-\frac{\left(h_b\psi_1^b+h_c\psi_1^c\right)}{2}+\xi_2\psi_1^b-\frac{G_c}{K^*}\left(\psi_1^c+\frac{\partial w}{\partial x}\right)\\
v_b&=v_0^c-\frac{\left(h_b\psi_2^b+h_c\psi_2^c\right)}{2}+\xi_2\psi_2^b-\frac{G_c}{K^*}\left(\psi_2^c+\frac{\partial w}{a\partial \theta}\right)
\end{aligned}
\qquad -\frac{h_b}{2}<\xi_2<\frac{h_b}{2} \tag{4.7}
$$

According to the method_2, the in-plane displacements (u_c and v_c) are related to the displacement fields at the elastic top and bottom layers. To implement this, the first two equations in Eq. (4.5) are simultaneously solved for u_0^c and ψ_1^c, and similarly the last two equations in Eq. (4.5) are simultaneously solved for v_0^c and ψ_2^c. These obtained parameters are subsequently substituted into Eq. (4.3) to derive:

$$u_c = \frac{u_0^b + u_0^t}{2} + \frac{\left(h_b\psi_1^b - h_t\psi_1^t\right)}{4} + \xi_3\left(\frac{K^*}{2G_c + K^* h_c}\left(u_0^t - u_0^b\right) - \frac{K^*}{4G_c + 2K^* h_c}\left(h_b\psi_1^b + h_t\psi_1^t\right)\right) - \frac{2G_c\xi_3}{2G_c + K^* h_c}\left(\frac{\partial w}{\partial x}\right) \tag{4.8}$$

$$v_c = \frac{v_0^b + v_0^t}{2} + \frac{\left(h_b\psi_2^b - h_t\psi_2^t\right)}{4} + \xi_3\left(\frac{K^*}{2G_c + K^* h_c}\left(v_0^t - v_0^b\right) - \frac{K^*}{4G_c + 2K^* h_c}\left(h_b\psi_2^b + h_t\psi_2^t\right)\right) - \frac{2G_c\xi_3}{2G_c + K^* h_c}\left(\frac{\partial w}{a\partial\theta}\right) \tag{4.9}$$

where $-h_c/2 < \xi_3 < h_c/2$. For the lower order model, deflection w is considered to be constant through thickness of the sandwich cylinder.

4.3 Higher Order Expansion of Displacement Fields through the Thickness of Viscoelastic Core Layer

The lower order model can satisfy the compatibility in the displacement fields through the thickness of the sandwich structure in which according to the method_2 the in-plane displacements and the rotations are obtained in terms of the displacements at the top and bottom layers as shown in section 4.2. However, in sandwich structures the lower order expansion of displacement distribution through the thickness of the compliant core layer is not accurate enough particularly where the core layer is thick.

The following distribution of displacements is considered at the core layer of the sandwich cylindrical shell:

$$\begin{aligned} u_c &= u_0^c + \xi_3\Phi_1^c + \xi_3{}^2\Phi_2^c + \xi_3{}^3\Phi_3^c \\ v_c &= v_0^c + \xi_3\Theta_1^c + \xi_3{}^2\Theta_2^c + \xi_3{}^3\Theta_3^c \\ w_c &= w_0^c + \xi_3\Psi_1^c + \xi_3{}^2\Psi_2^c \end{aligned} \qquad -\frac{h_c}{2} < \xi_3 < \frac{h_c}{2} \tag{4.10}$$

In order to achieve the compatibility in the deformation of the layers in the sandwich structure, all displacement fields in the core layer including rotations and translations should be identified in terms of the displacements at the top and bottom layers. Since the

boundary conditions at the two interfaces including the continuity in transverse deflection and slippage (or perfect bonding) give six equations for in-plane and transverse displacements, the following developed approach is considered to reduce the eleven parameters of the displacement fields in Eq. (4.10) to six parameters. The total displacement fields in the core layer for harmonic motion can be expressed as follow:

$$\mathbf{q}_c = \begin{bmatrix} u_c(x,\theta,\xi_3) \\ v_c(x,\theta,\xi_3) \\ w_c(x,\theta,\xi_3) \end{bmatrix} \exp(\mathrm{i}\omega t) \tag{4.11}$$

The profile of displacements with respect to the thickness coordinate of the core layer can be defined based on the static deformation. However, the displacement functions are afterward adjusted to fulfill the dynamic motion of the core layer. Considering this, by neglecting the inertia forces the equilibrium equations are written as:

$$\begin{aligned} &\frac{\partial \sigma_{xx}}{\partial x} + \frac{\partial \tau_{x\theta}}{a\partial \theta} + \frac{\partial \tau_{\xi_3 x}}{\partial \xi_3} = 0 \\ &\frac{\partial \tau_{x\theta}}{\partial x} + \frac{\partial \sigma_{\theta\theta}}{a\partial \theta} + \frac{\partial \tau_{\xi_3 \theta}}{\partial \xi_3} = 0 \\ &\frac{\partial \tau_{\xi_3 x}}{\partial x} + \frac{\partial \tau_{\xi_3 \theta}}{a\partial \theta} + \frac{\partial \sigma_{\xi_3 \xi_3}}{\partial \xi_3} = 0 \end{aligned} \tag{4.12}$$

By neglecting the in-plane normal and in-plane shear stresses, the first and second equations in Eq. (4.12) can be rewritten as:

$$\frac{\partial \tau_{\xi_3 x}}{\partial \xi_3} = 0 \Rightarrow \tau_{\xi_3 x} = f(x,\theta) \qquad \frac{\partial \tau_{\xi_3 \theta}}{\partial \xi_3} = 0 \Rightarrow \tau_{\xi_3 \theta} = g(x,\theta) \tag{4.13}$$

Eq. (4.13) indicates that the transverse shear stresses are constant through the viscoelastic core layer.

The relation between the transverse shear stresses and strains can be written as:

$$\gamma_{\xi_3 x} = \frac{\tau_{\xi_3 x}}{G_c} = \frac{2(1+\upsilon_c)}{E_c}\tau_{\xi_3 x} = 2(1+\upsilon_c)\beta_1$$
$$\gamma_{\xi_3 \theta} = \frac{\tau_{\xi_3 \theta}}{G_c} = \frac{2(1+\upsilon_c)}{E_c}\tau_{\xi_3 \theta} = 2(1+\upsilon_c)\beta_2 \quad (4.14)$$

where

$$\beta_1 = \frac{\tau_{\xi_3 x}}{E_c} \text{ and } \beta_2 = \frac{\tau_{\xi_3 \theta}}{E_c}$$

Shear strains can be also obtained using the displacement fields in Eq. (4.10) as follows:

$$\gamma_{\xi_3 x} = \frac{\partial u_c}{\partial \xi_3} + \frac{\partial w_c}{\partial x} = \Phi_1^c + 2\xi_3 \Phi_2^c + 3\xi_3{}^2 \Phi_3^c + \frac{\partial w_0^c}{\partial x} + \xi_3 \frac{\partial \Psi_1^c}{\partial x} + \xi_3{}^2 \frac{\partial \Psi_2^c}{\partial x}$$
$$\gamma_{\xi_3 \theta} = \frac{\partial v}{\partial \xi_3} + \frac{\partial w}{a\partial \theta} = \Theta_1^c + 2\xi_3 \Theta_2^c + 3\xi_3{}^2 \Theta_3^c + \frac{\partial w_0^c}{a\partial \theta} + \xi_3 \frac{\partial \Psi_1^c}{a\partial \theta} + \xi_3{}^2 \frac{\partial \Psi_2^c}{a\partial \theta} \quad (4.15)$$

Equating the coefficient of $\xi_3{}^0$, $\xi_3{}^1$ and $\xi_3{}^2$ from Eqs (4.14) and (4.15) yields the following relations:

$$\Phi_1^c + \frac{\partial w_0^c}{\partial x} = 2(1+\upsilon_c)\beta_1 \qquad 2\Phi_2^c + \frac{\partial \Psi_1^c}{\partial x} = 0 \qquad 3\Phi_3^c + \frac{\partial \Psi_2^c}{\partial x} = 0$$
$$\Theta_1^c + \frac{\partial w_0^c}{a\partial \theta} = 2(1+\upsilon_c)\beta_2 \qquad 2\Theta_2^c + \frac{\partial \Psi_1^c}{a\partial \theta} = 0 \qquad 3\Theta_3^c + \frac{\partial \Psi_2^c}{a\partial \theta} = 0 \quad (4.16)$$

Now, substituting $\Phi_1^c, \Phi_2^c, \Phi_3^c, \Theta_1^c, \Theta_2^c$ and Θ_3^c from Eq. (4.16) into the first and second equations in Eq. (4.10) yields the in-plane displacement fields through thickness of the core as:

$$u_c = u_0^c + \xi_3\left(2(1+\upsilon_c)\beta_1 - \frac{\partial w_0^c}{\partial x}\right) - \frac{\xi_3{}^2}{2}\frac{\partial \Psi_1^c}{\partial s} - \frac{\xi_3{}^3}{3}\frac{\partial \Psi_2^c}{\partial x}$$
$$v_c = v_0^c + \xi_3\left(2(1+\upsilon_c)\beta_2 - \frac{\partial w_0^c}{a\partial \theta}\right) - \frac{\xi_3{}^2}{2}\frac{\partial \Psi_1^c}{a\partial \theta} - \frac{\xi_3{}^3}{3}\frac{\partial \Psi_2^c}{a\partial \theta} \quad (4.17)$$

By neglecting the in-plane normal stresses, the constitutive equations are written as:

$$\varepsilon_{xx} = -\frac{\upsilon_c}{1-\upsilon_c}\left(\varepsilon_{\theta\theta} + \varepsilon_{\xi_3\xi_3}\right)$$

$$\varepsilon_{\theta\theta} = -\frac{\upsilon_c}{1-\upsilon_c}\left(\varepsilon_{\xi_3\xi_3} + \varepsilon_{xx}\right) \tag{4.18}$$

$$\sigma_{\xi_3\xi_3} = \frac{E_c}{(1+\upsilon_c)(1-2\upsilon_c)}\left[(1-\upsilon_c)\varepsilon_{\xi_3\xi_3} + \upsilon_c\left(\varepsilon_{\theta\theta} + \varepsilon_{xx}\right)\right]$$

Substituting $\tau_{\xi_3 x}$, $\tau_{\xi_3\theta}$ from Eq. (4.14) and $\sigma_{\xi_3\xi_3}$ from Eq. (4.18) into the last equation from Eq. (4.12) gives the following relation between β_1 and β_2:

$$\frac{\partial\beta_1}{\partial x} + \frac{\partial\beta_2}{a\partial\theta} = -\frac{\frac{\partial}{\partial\xi_3}\left[(1-\upsilon_c)\varepsilon_{\xi_3\xi_3} + \upsilon_c\left(\varepsilon_{\theta\theta} + \varepsilon_{xx}\right)\right]}{(1+\upsilon_c)(1-2\upsilon_c)} \tag{4.19}$$

which can be simplified by using the first and second equations from Eq. (4.18) and considering $\varepsilon_{\xi_3\xi_3} = \frac{\partial w_c}{\partial\xi_3}$, as follows:

$$\frac{\partial\beta_1}{\partial x} + \frac{\partial\beta_2}{a\partial\theta} = -\frac{\partial^2 w_c}{\partial{\xi_3}^2} \tag{4.20}$$

Now, by substituting w_c from Eq. (4.10) into Eq. (4.20), Ψ_2^c is obtained as:

$$\Psi_2^c = -\frac{\left(\frac{\partial\beta_1}{\partial x} + \frac{\partial\beta_2}{a\partial\theta}\right)}{2} \tag{4.21}$$

Finally, substituting Eq. (4.21) into Eq. (4.10) yields the transverse displacement through the thickness of the core layer as follows:

$$w_c = w_c^0 + \xi_3\,\Psi_1^c - \frac{{\xi_3}^2}{2}\left(\frac{\partial\beta_1}{\partial x} + \frac{\partial\beta_2}{a\partial\theta}\right) \tag{4.22}$$

Now, the total displacement fields in the core layer are obtained in terms of the three translational displacements u_0^c, v_0^c, w_0^c and three rotational displacements $\Psi_1^c, \beta_1, \beta_2$.

According to the method_1, the boundary conditions from Eq. (4.5) and also the continuity in transverse deflection can be implemented to obtain translational displacements at the top and bottom layers in terms of displacement fields in the core layer. Therefore, the displacement fields through the thickness of top and bottom layers are derived as follows:

$$
\begin{aligned}
u_t &= u_0^c + \frac{h_c}{2}\left(2(1+\upsilon_c)\beta_1 - \frac{\partial w_0^c}{\partial x}\right) - \frac{h_c^2}{8}\frac{\partial \Psi_1^c}{\partial x} + \frac{h_c^3}{48}\left(\frac{\partial^2 \beta_1}{\partial x^2} + \frac{\partial^2 \beta_2}{a\,\partial\theta\,\partial x}\right) + \frac{h_t}{2}\psi_1^t \\
&\quad + \xi_1 \psi_1^t + 2(1+\upsilon_c)\beta_1 \frac{G_c}{K^*} \\
v_t &= v_0^c + \frac{h_c}{2}\left(2(1+\upsilon_c)\beta_2 - \frac{\partial w_0^c}{a\partial\theta}\right) - \frac{h_c^2}{8}\frac{\partial \Psi_1^c}{a\partial\theta} + \frac{h_c^3}{48}\left(\frac{\partial^2 \beta_1}{a\,\partial\theta\,\partial x} + \frac{\partial^2 \beta_2}{a^2\partial\theta^2}\right) + \frac{h_t}{2}\psi_2^t \\
&\quad + \xi_1 \psi_2^t + 2(1+\upsilon_c)\beta_2 \frac{G_c}{K^*} \\
w_t &= w_0^c + \frac{h_c}{2}\Psi_1^c - \frac{h_c^2}{8}\left(\frac{\partial \beta_1}{\partial x} + \frac{\partial \beta_2}{a\,\partial\theta}\right)
\end{aligned}
\tag{4.23}
$$

$$
\begin{aligned}
u_b &= u_0^c - \frac{h_c}{2}\left(2(1+\upsilon_c)\beta_1 - \frac{\partial w_0^c}{\partial x}\right) - \frac{h_c^2}{8}\frac{\partial \Psi_1^c}{\partial x} - \frac{h_c^3}{48}\left(\frac{\partial^2 \beta_1}{\partial x^2} + \frac{\partial^2 \beta_2}{a\,\partial\theta\,\partial x}\right) - \frac{h_b}{2}\psi_1^b \\
&\quad + \xi_2 \psi_1^b - 2(1+\upsilon_c)\beta_1 \frac{G_c}{K^*} \\
v_b &= v_0^c - \frac{h_c}{2}\left(2(1+\upsilon_c)\beta_2 - \frac{\partial w_0^c}{a\partial\theta}\right) - \frac{h_c^2}{8}\frac{\partial \Psi_1^c}{a\partial\theta} - \frac{h_c^3}{48}\left(\frac{\partial^2 \beta_1}{a\,\partial\theta\,\partial x} + \frac{\partial^2 \beta_2}{a^2\partial\theta^2}\right) - \frac{h_b}{2}\psi_2^b \\
&\quad + \xi_2 \psi_2^b - 2(1+\upsilon_c)\beta_2 \frac{G_c}{K^*} \\
w_b &= w_0^c - \frac{h_c}{2}\Psi_1^c - \frac{h_c^2}{8}\left(\frac{\partial \beta_1}{\partial x} + \frac{\partial \beta_2}{a\,\partial\theta}\right)
\end{aligned}
\tag{4.24}
$$

According to the method_2, the displacements distribution through the thickness of the core layer should be obtained in terms of the displacement fields at the top and bottom layers. According to the continuity of transverse displacement either considering

slippage or perfect bonding, the transverse displacements at the top and bottom of the core layer are respectively equal to those at the elastic top and bottom layers as:

$$w_t = w_0^c + \frac{h_c}{2}\Psi_1^c + \frac{{h_c}^2}{4}\Psi_2^c \qquad w_b = w_0^c - \frac{h_c}{2}\Psi_1^c + \frac{{h_c}^2}{4}\Psi_2^c$$

Using Eq. (4.21) and solving the abovementioned equations for Ψ_1^c and w_0^c yields:

$$\Psi_1^c = \frac{w_t - w_b}{h_c} \tag{4.25}$$

$$w_0^c = \frac{w_t + w_b}{h_c} + \frac{h_c^2}{8}\left(\frac{\partial\beta_1}{\partial x} + \frac{\partial\beta_2}{a\,\partial\theta}\right) \tag{4.26}$$

Considering the slippage condition at the interfaces, the in-plane translational displacements u_0^c and v_0^c at the core layer are directly obtained in terms of the displacement fields at the top and bottom layers. However, the rotations β_1 and β_2 are related to the displacement fields in the elastic layers by two coupled partial differential equations. Substituting Eqs (4.1), (4.2) and (4.17) for in-plane displacement into Eq. (4.4), yields the following relations:

$$\begin{aligned}
&K^*\left(u_o^t - \frac{h_t}{2}\psi_1^t - \left(u_c^0 + \frac{h_c}{2}\left(2(1+\upsilon_c)\beta_1 - \frac{\partial w_0^c}{\partial x}\right) - \frac{{h_c}^2}{8}\frac{\partial\Psi_1^c}{\partial x} - \frac{{h_c}^3}{24}\frac{\partial\Psi_2^c}{\partial x}\right)\right) = 2G_c(1+\upsilon_c)\beta_1\\
&K^*\left(v_o^t - \frac{h_t}{2}\psi_2^t - \left(v_c^0 + \frac{h_c}{2}\left(2(1+\upsilon_c)\beta_2 - \frac{\partial w_0^c}{a\partial\theta}\right) - \frac{{h_c}^2}{8}\frac{\partial\Psi_1^c}{a\partial\theta} - \frac{{h_c}^3}{24}\frac{\partial\Psi_2^c}{a\partial\theta}\right)\right) = 2G_c(1+\upsilon_C)\beta_2\\
&K^*\left(u_c^0 - \frac{h_c}{2}\left(2(1+\upsilon_c)\beta_1 - \frac{\partial w_0^c}{\partial x}\right) - \frac{{h_c}^2}{8}\frac{\partial\Psi_1^c}{\partial x} + \frac{{h_c}^3}{24}\frac{\partial\Psi_2^c}{\partial x} - u_o^b - \frac{h_b}{2}\psi_1^b\right) = 2G_c(1+\upsilon_c)\beta_1\\
&K^*\left(v_c^0 - \frac{h_c}{2}\left(2(1+\upsilon_c)\beta_2 - \frac{\partial w_0^c}{a\partial\theta}\right) - \frac{{h_c}^2}{8}\frac{\partial\Psi_1^c}{a\partial\theta} + \frac{{h_c}^3}{24}\frac{\partial\Psi_2^c}{a\partial\theta} - v_o^b - \frac{h_b}{2}\psi_2^b\right) = 2G_c(1+\upsilon_c)\beta_2
\end{aligned} \tag{4.27}$$

After substituting Ψ_2^c from Eq. (4.21) into the abovementioned relations in Eq. (4.27) and solving for u_0^c, v_0^c, β_1 and β_2, one can obtain the following equations:

$$u_0^c = \frac{u_0^b + u_0^t}{2} + \frac{h_b \psi_1^b - h_t \psi_1^t}{4} + \frac{h_c^2}{8} \frac{\partial \Psi_1^c}{\partial x} \tag{4.28}$$

$$v_0^c = \frac{v_0^b + v_0^t}{2} + \frac{h_b \psi_2^b - h_t \psi_2^t}{4} + \frac{h_c^2}{8} \frac{\partial \Psi_1^c}{a \partial \theta} \tag{4.29}$$

$$\begin{aligned} &-\left(2K^*(1+\upsilon_c)h_c + 2E_c\right)\beta_1 + \frac{K^* h_c}{2} \frac{\partial(w_t + w_b)}{\partial x} + \frac{K^* h_c^3}{12}\left(\frac{\partial^2 \beta_1}{\partial x^2} + \frac{\partial^2 \beta_2}{a \partial \theta \partial x}\right) \\ &+ K^*\left(u_0^b - u_0^t - \frac{h_b \psi_1^b + h_t \psi_1^t}{2}\right) = 0 \end{aligned} \tag{4.30}$$

$$\begin{aligned} &-\left(2K^*(1+\upsilon_c)h_c + 2E_c\right)\beta_2 + \frac{K^* h_c}{2} \frac{\partial(w_t + w_b)}{a \partial \theta} + \frac{K^* h_c^3}{12}\left(\frac{\partial^2 \beta_1}{a \partial \theta \partial x} + \frac{\partial^2 \beta_2}{a^2 \partial \theta^2}\right) \\ &+ K^*\left(v_0^t - v_0^b - \frac{h_b \psi_2^b + h_t \psi_2^t}{2}\right) = 0 \end{aligned} \tag{4.31}$$

Now, the only unknown parameters are the rotations β_1 and β_2 which can be obtained by solving Eqs (4.30) and (4.31). The solution is given in the next section.

4.4 Semi-Analytical Finite Element Method

Lagrange's equation is used to establish the equations of motion. The kinetic and potential energies are obtained in each layer using the following equations:

$$T_i = \int_{-\frac{h_i}{2}}^{\frac{h_i}{2}} \int_0^{2\pi} \int_{-\frac{L_e}{2}}^{\frac{L_e}{2}} \frac{1}{2} \rho_i \left(\dot{u}_i^2 + \dot{v}_i^2 + \dot{w}_i^2\right) \mathrm{d}V_i \tag{4.32}$$

$$U_i = \int_{-\frac{h_i}{2}}^{\frac{h_i}{2}} \int_0^{2\pi} \int_{-\frac{L_e}{2}}^{\frac{L_e}{2}} \frac{1}{2}\left(\sigma_{xx}^i \varepsilon_{xx}^i + \sigma_{\theta\theta}^i \varepsilon_{\theta\theta}^i + \sigma_{\xi_i\xi_i}^i \varepsilon_{\xi_i\xi_i}^i + \tau_{x\theta}^i \gamma_{x\theta}^i + \tau_{\xi_i x}^i \gamma_{\xi_i x}^i + \tau_{\xi_i\theta}^i \gamma_{\xi_i\theta}^i\right) \mathrm{d}V_i \tag{4.33}$$

where i=t, b and c, $\mathrm{d}V_i = (a + \xi_i)\mathrm{d}\theta \mathrm{d}x \mathrm{d}\xi_i$ and ξ_i is the coordinate in thickness direction at the middle of each layer and $(\xi_t, \xi_b, \xi_c) = (\xi_1, \xi_2, \xi_3)$. In Eq. (4.33) the energy terms related to the in-plan and normal stresses of the core layer, i.e. $\tau_{x\theta}^c$, $\sigma_{\theta\theta}^c$ and σ_{xx}^c are

neglected due to the much small modulus in the core layer compared to the elastic faces as the normal and in-plane shear stresses are mainly carried by the elastic faces. This approximation is also reported in many literatures such as references [14, 17]. Strain–displacement relation using linear Green's Strain for the cylindrical shell element is [94]:

$$\varepsilon_{xx}^{i}=\frac{\partial u_i}{\partial x}\quad \varepsilon_{\theta\theta}^{i}=\frac{1}{1+\xi_i/a}\left(\frac{\partial v_i}{a\partial\theta}+\frac{w_i}{a}\right)\qquad \gamma_{x\theta}^{i}=\left(\frac{\partial v_i}{\partial x}\right)+\frac{1}{1+\xi_i/a}\left(\frac{\partial u_i}{a\partial\theta}\right)$$
$$\gamma_{\xi_i\theta}^{i}=\frac{\partial v_i}{\partial\xi_i}+\frac{1}{1+\xi_i/a}\left(\frac{\partial w_i}{a\partial\theta}-\frac{v_i}{a}\right)\qquad \gamma_{\xi_i x}^{i}=\frac{\partial u_i}{\partial\xi_i}+\frac{\partial w_i}{\partial x}\qquad \varepsilon_{\xi_3\xi_3}^{c}=\frac{\partial w_c}{\partial\xi_i} \tag{4.34}$$

The ratio ξ_i/a is negligible if the thickness of each layer is small compared to the radius. Using the constitutive equations and substituting displacement fields for each layer into Eqs (4.32) and (4.33), the kinetic and potential energies are obtained in terms of the displacements. Semi-analytical finite element modeling can be used to define the translational and rotational displacement fields at the top, bottom and core layers in which the displacements in the circumferential direction are expressed analytically using the Fourier series and also are discretized in the axial direction using the Lagrangian shape functions. Considering this, the possible displacement fields at the top, bottom and core layers for the lower or higher order model of displacement distribution based on the method_1 or method_2 can be defined as:

$$w_0^i=\sum_{j=1}^{m}\sum_{n=0}^{\infty}N_j w_j^i\cos(n\theta-\varphi)\qquad v_0^i=\sum_{j=1}^{m}\sum_{n=0}^{\infty}N_j v_j^i\sin(n\theta-\varphi)$$
$$u_0^i=\sum_{j=1}^{m}\sum_{n=0}^{\infty}N_j u_j^i\cos(n\theta-\varphi)\qquad \Psi_1^c=\sum_{j=1}^{m}\sum_{n=0}^{\infty}N_j\Psi_{1j}^c\cos(n\theta-\varphi)$$
$$\beta_1=\sum_{j=1}^{m}\sum_{n=0}^{\infty}N_j\beta_{j1}\cos(n\theta-\varphi)\qquad \beta_2=\sum_{i=1}^{m}\sum_{n=0}^{\infty}N_j\beta_{j2}\sin(n\theta-\varphi) \tag{4.35}$$
$$\psi_1^i=\sum_{j=1}^{m}\sum_{n=0}^{\infty}N_j\psi_{j1}^i\cos(n\theta-\varphi)\qquad \psi_2^i=\sum_{j=1}^{m}\sum_{n=0}^{\infty}N_j\psi_{j2}^i\sin(n\theta-\varphi)$$

in which m is the number of nodes for each cylindrical shell element in axial direction and i=b,t and c. Since there is no preference for the orientation of circumferential modes, an arbitrary phase angle φ must be included [119]. Generally, $\varphi = \varphi_0$ and $\varphi = \varphi_0 + \pi/2$ in which φ_0 is an arbitrary constant. For the free vibration φ_0=0 and for the forced vibration φ_0 depends on the distribution of the forces. For example in the case of point loading, if the coordinates are located at the same point where the load is exerted, then φ_0=0. Using the configurations of the mode shapes, the physical intuition of the displacement functions are well explained by Soedel [129]. If three nodes are considered in axial direction, the shape functions N_1, N_2 and N_3 are given as:

$$N_1 = \frac{2x^2}{{L_e}^2} - \frac{x}{L_e} \qquad N_2 = 1 - \frac{4x^2}{{L_e}^2} \qquad N_3 = \frac{2x^2}{{L_e}^2} + \frac{x}{L_e} \tag{4.36}$$

As mentioned before, the rotations β_1 and β_2 are two known rotations in method_1 however, according to the method_2, they should be determined by solving partial differential equations given in Eqs (4.30) and (4.31). Here, briefly the solution of theses equations for β_1 and β_2 has been briefly discussed. The solution consists of homogenous and particular parts. The general solution of the coupled differential equations stated in Eqs (4.30) and (4.31) can be obtained by solving the following differential equations which are obtained after eliminating the nonhomogenous terms in Eqs (4.30) and (4.31) as:

$$-\left(2K^*(1+\upsilon_c)h_c + 2E_c\right)\beta_1 + \frac{K^* h_c^3}{12}\left(\frac{\partial^2\beta_1}{\partial x^2} + \frac{\partial^2\beta_2}{a\,\partial\theta\,\partial x}\right) = 0 \tag{4.37}$$

$$-\left(2K^*(1+\upsilon_c)h_c + 2E_c\right)\beta_2 + \frac{K^* h_c^3}{12}\left(\frac{\partial^2\beta_1}{a\,\partial\theta\,\partial x} + \frac{\partial^2\beta_2}{a^2\partial\theta^2}\right) = 0 \tag{4.38}$$

Equations (4.37) and (4.38) can be rewritten in the following form:

$$(-C_1 + C_2 D_{xx})\beta_1 + C_2 D_{x\theta}\beta_2 = 0 \tag{4.39}$$

$$(-C_1 + C_2 D_{\theta\theta})\beta_2 + C_2 D_{x\theta}\beta_1 = 0 \tag{4.40}$$

where

$$C_1 = \left(2K^*(1+\upsilon_c)h_c + 2E_c\right) \quad C_2 = \frac{K^* h_c^3}{12} \quad D_{xx} = \frac{\partial^2}{\partial x^2} \quad D_{\theta\theta} = \frac{\partial^2}{a^2 \partial \theta^2} \quad D_{x\theta} = \frac{\partial^2}{a\partial\theta\partial x}$$

Multiplying Eq. (4.39) by $(-C_1 + C_2 D_{\theta\theta})$ and Eq. (4.40) by $(C_2 D_{S\theta})$ and subtracting from each other give:

$$\left(C_1{}^2 - C_1 C_2 (D_{xx} + D_{\theta\theta}) + C_2{}^2 D_{xx} D_{\theta\theta} - C_2{}^2 D_{x\theta} D_{x\theta}\right)\beta_1 = 0 \tag{4.41}$$

According to the Clairaut's theorem, for a function which has continuous second derivative with respect to θ and s:

$$\frac{\partial^2}{\partial x^2}\frac{\partial^2}{a^2\partial\theta^2} = \frac{\partial^2}{a\partial\theta\partial x}\frac{\partial^2}{a\partial\theta\partial x} \text{ or } D_{xx}D_{\theta\theta} = D_{x\theta}D_{x\theta}$$

After simplifying Eq. (4.41), using the Clairaut's theorem and then dividing Eq. (4.41) by C_1C_2, one can obtain the following partial differential equation:

$$-\kappa\beta_1 + \left(a^2\frac{\partial^2\beta_1}{\partial x^2} + \frac{\partial^2\beta_1}{\partial\theta^2}\right) = 0 \quad 0 < x < x_0 \quad 0 < \theta < \theta_0 \tag{4.42}$$

where

$$\kappa = 24a^2\left[\frac{1+\upsilon_c}{h_c{}^2} + \frac{E_c}{K^* h_c{}^3}\right]$$

Similarly, one can obtain the following equation:

$$-\kappa\beta_2 + \left(a^2\frac{\partial^2\beta_2}{\partial x^2} + \frac{\partial^2\beta_2}{\partial\theta^2}\right) = 0 \quad 0 < x < x_0 \quad 0 < \theta < \theta_0 \tag{4.43}$$

It can be realized that for a moderate thick core layer, κ is a large non-dimensional value. The solution is now presented for β_1 and the similar results can be concluded for β_2. The boundary conditions may be expressed as follow:

$$\beta_1(x,\theta_0)=E(x) \quad \beta_1(x,0)=H(x) \quad \beta_1(x_0,\theta)=G(\theta) \quad \beta_1(0,\theta)=F(\theta) \tag{4.44}$$

According to the superposition principle, the homogenous solution of β_1 is expressed as:

$$\beta_1=\beta_{11}+\beta_{12}+\beta_{13}+\beta_{14} \tag{4.45}$$

in which the boundary conditions are rewritten as follows:

$$\begin{array}{cccc} \beta_{11}(x,\theta_0)=E(x) & \beta_{11}(x,0)=0 & \beta_{12}(x,\theta_0)=0 & \beta_{12}(x,0)=H(x) \\ \beta_{11}(x_0,\theta)=0 & \beta_{11}(0,\theta)=0 & \beta_{12}(x_0,\theta)=0 & \beta_{12}(0,\theta)=0 \\ \beta_{13}(x\theta_0)=0 & \beta_{13}(x,0)=0 & \beta_{14}(x,\theta_0)=0 & \beta_{14}(x,0)=0 \\ \beta_{13}(x_0,\theta)=G(\theta) & \beta_{13}(0,\theta)=0 & \beta_{14}(x_0,\theta)=0 & \beta_{14}(0,\theta)=F(\theta) \end{array} \tag{4.46}$$

The partial differential equation for β_{11} can be written as

$$-\kappa\beta_{11}+\left(a^2\frac{\partial^2\beta_{11}}{\partial x^2}+\frac{\partial^2\beta_{11}}{\partial\theta^2}\right)=0 \quad 0<x<x_0 \quad 0<\theta<\theta_0 \tag{4.47}$$

Using the separation of variables method, β_{11} is expressed as

$$\beta_{11}=X(x)Y(\theta) \tag{4.48}$$

where by separating the equation and implementing the boundary conditions X and Y are obtained as:

$$X(x)=A1_n\sin\left(\frac{n\pi}{x_0}x\right) \tag{4.49}$$

$$Y(\theta)=A2_n\exp\left(\sqrt{\kappa+\frac{n^2\pi^2a^2}{{x_0}^2}}\theta\right)+A3_n\exp\left(-\sqrt{\kappa+\frac{n^2\pi^2a^2}{{x_0}^2}}\theta\right) \tag{4.50}$$

Considering this fact that κ is a large value, the second term in the Eq. (4.50) is eliminated. Using Eqs (4.49) and (4.50), β_{11} is now obtained as follows:

$$\beta_{11} = \sum_{n=1}^{\infty} A3_n \exp\left(\sqrt{\kappa + \frac{n^2\pi^2 a^2}{x_0^2}}\theta\right)\sin(\frac{n\pi}{x_0}x) \tag{4.51}$$

where $A3_n$=$A1_nA2_n$. Using the boundary condition and the Fourier series, $A3_n$ is obtained as follows:

$$A3_n = \frac{2}{x_0}\exp\left(-\sqrt{\kappa + \frac{n^2\pi^2 a^2}{x_0^2}}\theta_0\right)\left(\int_0^{s_0} E(s)\sin\left(\frac{n\pi}{x_0}x\right)dx\right) \tag{4.52}$$

Substituting $A3_n$ into Eq. (4.51) yields:

$$\beta_{11} = \sum_{n=1}^{\infty}\left[A_n(x)\exp\left(\sqrt{\kappa + \frac{n^2\pi^2 a^2}{x_0^2}}(\theta-\theta_0)\right)\right] \tag{4.53}$$

where

$$A_n(x) = \frac{2}{x_0}\left(\int_0^{x_0} E(x)\sin\left(\frac{n\pi}{x_0}x\right)dx\right)\sin\left(\frac{n\pi}{x_0}x\right)$$

Assuming that A is the maximum value of $A_n(x)$ in the interval $0 < x < x_0$, β_{11} satisfies the following inequality:

$$\beta_{11} \le A\sum_{n=1}^{\infty}\left[\exp\left(\sqrt{\kappa + \frac{n^2\pi^2 a^2}{x_0^2}}(\theta-\theta_0)\right)\right] \tag{4.54}$$

For $0 < \theta < \theta_0$ all exponential terms are negative values. Thus, one can write the following inequalities:

$$\exp\left(\sqrt{\kappa+\frac{n^2\pi^2a^2}{x_0^2}}(\theta-\theta_0)\right)\le\exp\left(\sqrt{\kappa}(\theta-\theta_0)\right)$$
$$\exp\left(\sqrt{\kappa+\frac{n^2\pi^2a^2}{x_0^2}}(\theta-\theta_0)\right)\le\exp\left(\frac{n\pi}{x_0}a(\theta-\theta_0)\right) \tag{4.55}$$

Using Eq. (4.55), Eq. (4.54) is splitted into two segments as:

$$\beta_{11}\le A\left(\sum_{n=1}^{m_1}\left[\exp\left(\sqrt{\kappa}(\theta-\theta_0)\right)\right]+\sum_{n=m_1+1}^{\infty}\exp\left(\frac{n\pi}{x_0}a(\theta-\theta_0)\right)\right) \tag{4.56}$$

where m_1 is an arbitrary finite integer value. By implementing the geometric progression formula, the inequality in Eq. (4.56) can be rewritten as:

$$\beta_{11}\le A\left[m_1\exp\left(\sqrt{\kappa}(\theta-\theta_0)\right)+\frac{\exp\left(\frac{\pi a(m_1+1)(\theta-\theta_0)}{x_0}\right)}{1-\exp\left(\frac{\pi a(\theta-\theta_0)}{x_0}\right)}\right]\approx 0 \tag{4.57}$$

Since the argument of exponential function is a negative value within the interval $0<\theta<\theta_0$ and κ is a large non-dimensional value, the first and second terms in Eq. (4.57) are negligible. The Eq. (4.57) is only violated when θ is sufficiently close to θ_0 in which β_{11} approaches to a finite value within a small interval. Considering this, the kinetic and strain energies associated with β_{11} are negligible after the integrations. Using the same approach, it can be proved that β_{12} and β_{14} are zero and one can obtain an inequality for β_{13} similar to Eq. (4.57). Therefore the homogenous solution can be neglected. The particular solution can be written in the following forms:

$$\beta_1=\sum_{n=0}^{\infty}\left(a_0+a_1x+a_2x^2+\ldots\right)\cos(n\theta-\varphi)$$
$$\beta_2=\sum_{n=0}^{\infty}\left(b_0+b_1x+b_2x^2+\ldots\right)\sin(n\theta-\varphi) \tag{4.58}$$

Three terms of the polynomial in axial direction can be considered for the three nodes along the axial direction of the cylinder. By substituting Eq. (4.58) into Eqs (4.30) and (4.31) and also equating the coefficient of x^0, x^1 and x^2 in both differential equations, six linear equations are obtained which can be solved for a_0, a_1, a_2, b_0, b_1 and b_2. These equations are given in the Appendix. The coefficients are then substituted into the Eq. (4.58) to find the displacement fields at the damping layer.

Degrees of freedom at each node considering the lower and higher order Taylor's expansion in the thickness coordinate based on the method _1 and method _2 are summarized in Table 4.1. The kinetic and strain energy must be calculated for each layer using the described displacement distributions. The total kinetic and strain energies are then obtained by summing of the energies in top, bottom and core layers as:

$$U = U_t + U_c + U_b \qquad T = T_t + T_c + T_b \tag{4.59}$$

Lagrange's equation can be employed to establish the equations of motion which can be written as follows:

$$\frac{\mathrm{d}}{\mathrm{d}t}\left(\frac{\partial T}{\partial \dot{q}_k}\right) - \left(\frac{\partial T}{\partial q_k}\right) + \left(\frac{\partial U}{\partial q_k}\right) = F_k \quad k = 1, \cdots, n \tag{4.60}$$

Table 4.1 DOF required in linear and nonlinear displacement distribution models based on method_1 and method_2.

	Displacement expansion through the core layer	Approach	DOF
FEM (a)	Lower order	method_1	$[u_0^c\ v_0^c\ w_0^c\ \psi_1^c\ \psi_2^c\ \psi_1^t\ \psi_2^t\ \psi_1^b\ \psi_2^b]$
FEM (b)	Lower order	method_2	$[u_0^b\ v_0^b\ w_0\ \psi_1^b\ \psi_2^b\ u_0^t\ v_0^t\ \psi_1^t\ \psi_2^t]$
FEM (c)	Higher order	method_1	$[u_0^c\ v_0^c\ w_0^c\ \beta_1^c\ \beta_2^c\ \Psi_1^c\ \psi_1^t\ \psi_2^t\ \psi_1^b\ \psi_2^b]$
FEM (d)	Higher order	method_2	$[u_0^b\ v_0^b\ w_0^b\ \psi_1^b\ \psi_2^b\ u_0^t\ v_0^t\ w_0^t\ \psi_1^t\ \psi_2^t]$

where n is the total DOF in the sandwich panel structure, q and F are the nodal displacements and applied external force, respectively and T and U are respectively the kinetic and potential energies in the sandwich shell structure.

Substituting Eq. (4.59) into the Eq. (4.60) and assembling for all elements gives the equations of motion in the finite element form as:

$$\mathbf{M}\ddot{\mathbf{q}} + \mathbf{K}\mathbf{q} = \mathbf{F} \tag{4.61}$$

where $\mathbf{K} = \mathbf{K}'(\omega) + \mathrm{i}\,\mathbf{K}''(\omega)$ is a complex frequency dependent stiffness matrix. Due to the frequency dependency of viscoelastic properties of the damping layer, stiffness matrix is nonlinear with respect to frequency. In the case of free vibration, Eq. (4.61) can be written in the following form:

$$\left(-\omega^2\mathbf{M} + \mathbf{K}(\omega)\right)\mathbf{q} = 0 \tag{4.62}$$

Eq. (4.62) can not directly be solved due to the nonlinearity in stiffness matrix. Natural frequencies can be found directly using forced harmonic response method for a certain range of frequency. Under harmonic load $\mathbf{F} = \mathbf{F}_0 e^{\mathrm{i}\omega t}$, the Eq. (4.61) can be expressed as:

$$\left(-\omega^2\mathbf{M} + \mathbf{K}(\omega)\right)\mathbf{q} = \mathbf{F}_0 \tag{4.63}$$

Therefore, the natural frequencies and consequently the corresponding loss factors can be calculated using the frequency response by solving a set of linear equations in Eq. (4.63). This method can be expensive since the solution strongly depends on the resolution of frequency axis. The alternative method is to solve eigenvalue problem of Eq. (4.62) iteratively using the evaluated stiffness matrix at the natural frequencies. The evaluated stiffness matrix at the natural frequency of the bare cylinder could be the best starting point for each mode in the iteration process.

As mentioned before, the modal loss factor is defined as the ratio of dissipated energy per radian and maximum potential energy at natural frequency which can be described as [132]:

$$\eta_i = \frac{\boldsymbol{\varphi}_i^{\mathrm{T}} \mathbf{K}'' \boldsymbol{\varphi}_i}{\boldsymbol{\varphi}_i^{\mathrm{T}} \mathbf{K}' \boldsymbol{\varphi}_i} \tag{4.64}$$

in which $\boldsymbol{\varphi}_i$ is the normalized eigenvector in free vibration and η_i is the loss factor related to the *i*th mode.

4.4.1 Unconstrained treatment

Unconstrained treatment can be modeled by eliminating the constraining elastic layer. Therefore the three-layered structure is substituted by two-layered structure which is simpler but inefficient considering the weight point of view [133]. Due to small shear strain at viscoelastic layer in unconstrained treatment, this configuration is useful when a light structure exhibiting small damping behavior is desired. However, as shown in this chapter, in order to achieve considerable damping in unconstrained sandwich structure, thick viscoelastic layer should be considered which leads to increase in the structural weight. The method_1 can effectively be used to formulate the unconstrained treatment. In order to contribute the strain energy related to the in-plane stresses which are predominant in the damping layer for unconstrained treatment, the lower order model is employed which is more reasonable since both shear stresses and in-plane normal stresses are considered in the model. According to the method_1, the displacement distributions for the bottom and viscoelastic layers given in Eqs (4.3) and (4.7) are used in the finite element modeling.

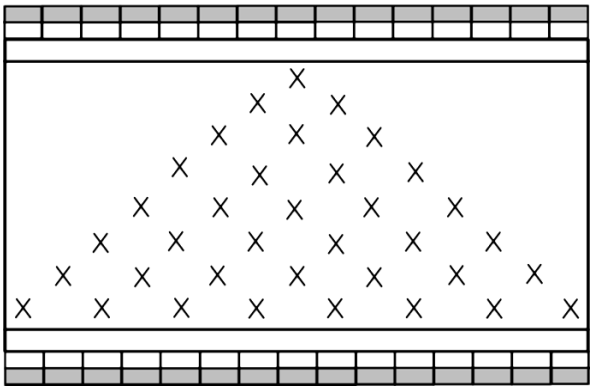

Figure 4.1 Configuration of treatments on the bare cylindrical shell

4.4.2 Partial treatment

Partial treatment leads to reduction of the total weight in sandwich structure and may provide better vibration suppression performance. This can be efficient for the sandwich structures where the objective is reducing the weight while maximizing the damping. Partial treatment in the developed finite element method can be modeled by eliminating the top and core layers for the untreated elements. Considering this, the stiffness and mass matrices of the bare and treated elements are assembled at the base layer during the assembly process. This can be possible by utilizing method_2 that includes the FEMs (b) and (d) shown in Table 4.1 which are describing respectively lower and higher order Taylor's expansion of displacement fields in the thickness coordinate of the core layer. The configuration of treatments (8 configurations) on the bare cylinder for parametric studies presented in this chapter is shown in Figure 4.1 in which fifteen cylindrical shell elements are considered in finite element modeling and the symbol × shows the location of the treatments for each configuration.

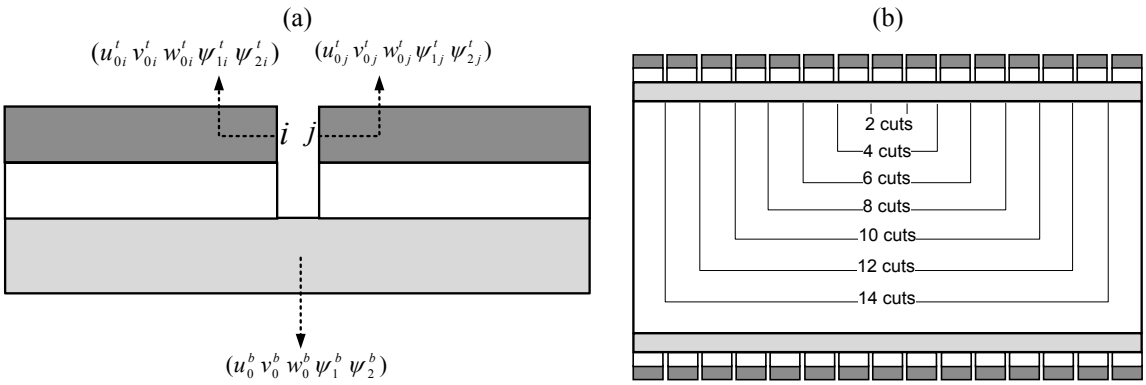

Figure 4.2 (a) Discontinuity of nodal displacements at the cut location. (b) Configuration of cuts on the sandwich cylindrical shell.

4.4.3 Cut modeling

The configuration of one cut is shown in Figure 4.2 (a). Lepoittevin and Kress [20] showed that the cut leads to increase in the transverse shear strain at the core layer and consequently the damping increases. Cuts could be considered as untreated elements in which the size of the elements is very small. Therefore after assembling, the size of stiffness and mass matrices would be too large in which the numerical calculations become too expensive. The cuts here are modeled by considering this fact that the nodal displacement at the elastic top and viscoelastic core layers are discontinuous at the location of the cuts [113] (Figure 4.2 (a)). Considering this, the nodal displacements and the entries of the corresponding mass and stiffness matrices at the cut locations are taken apart in the system stiffness and mass matrices. Although, the effect of damping due to the friction between the elements is not considered in this model but it can show the effect of additional shear strain in the core layer on the damping behavior. As it has been mentioned before, the FEM (b) and (d) which are based on the method_2 can be used to model the cuts since considering the discontinuity in the nodal displacements at the top layer bring about discontinuity of displacement at the core layer so that the displacements at the base layer are still continuous. Discontinuity in the nodal displacements of the core

in the method_1, leads to discontinuity of displacement at top and bottom layers which does not exhibit the behavior and the effect of the cuts in the finite element modeling. Numerical studies show that cutting influences damping properties. The location of cuts is important for different boundary conditions. The best position of the cuts seems to be between the elements of the sandwich structure with higher modal strain energy since the cuts leads to additional shear deformation and consequently more dissipation of energy. In order to observe the effect of the cuts and their distribution, seven configurations of cuts as shown in Figure 4.2 (b) have been used for the parametric studies presented in this chapter in which the discontinuity are considered between different elements according to the number of cuts.

4.5 Optimization Problem

The parametric studies presented in this chapter and chapter 2 show that the damping characteristics are affected by the ratio of the top and core thicknesses to the base layer thickness, slippage between layers, total number and distribution of untreated elements in the partial treatment process and also total number of cuts and their distribution along the axis of the sandwich cylindrical shell. These parameters can be optimized simultaneously or separately in the optimization problem. The objective function can also be the loss factor for each mode or combinations (linear or logarithmic) of all loss factors at different modes. In this study, an effective loss factor is introduced according to combinations of all circumferential and axial modes. As mentioned before, loss factor can be determined at the corresponding natural frequencies in circumferential and axial modes. In practice, the contribution of each mode is different for a particular displacement vector $\mathbf{X}_0$. Therefore, a weighted combination of loss factor is required to be defined as an objective

function. The participation value of each mode can be evaluated in an undamped structure. This value is then considered as a weighting factor for the corresponding loss factor and consequently the weighted combinations of all loss factors related to all modes is considered to be the objective function. For the undamped structure under harmonic loading, the amplitude vector for each circumferential mode can be written as [134]:

$$\mathbf{X}_0^n = \sum_{i=1}^{m} c_i^n \boldsymbol{\varphi}_i^n \tag{4.65}$$

where $\boldsymbol{\varphi}_i^n$ is the normalized eigenvector ($\| \boldsymbol{\varphi}_i^n \| = 1$) for nth circumferential and ith axial mode, c_i^n indicates how much of each axial mode is present in the nth circumferential mode and $\mathbf{X}_0^n$ represents displacement vector through the cylindrical shell due to a particular loading. For each circumferential mode, $\boldsymbol{\varphi}_i^n$ are orthonormal with respect to stiffness and mass matrices as follows:

$$\begin{aligned} &\boldsymbol{\varphi}_i^{n\mathrm{T}} \mathbf{M}^n \boldsymbol{\varphi}_j^n = 0 \quad i \neq j \\ &\boldsymbol{\varphi}_i^{n\mathrm{T}} \mathbf{K}^n \boldsymbol{\varphi}_j^n = 0 \quad i \neq j \end{aligned} \tag{4.66}$$

According to this property, c_i^n can be obtained as:

$$c_i^n = \frac{\boldsymbol{\varphi}_i^{n\mathrm{T}} \mathbf{M}^n \mathbf{X}_0^n}{\boldsymbol{\varphi}_i^{n\mathrm{T}} \mathbf{M}^n \boldsymbol{\varphi}_i^n} \tag{4.67}$$

In order to realize the effect of each particular axial mode on the displacement vector $\mathbf{X}_0^n$, all the eigenvectors should be projected on the $\mathbf{X}_0^n$. Therefore a meaningful relation can be defined to determine the participation of each mode as follows:

$$\alpha_i^n = \frac{\left| c_i^n \mathbf{X}_0^n \cdot \boldsymbol{\varphi}_i^n \right|}{\sum_{i=1}^{m} \left| c_i^n \mathbf{X}_0^n \cdot \boldsymbol{\varphi}_i^n \right|} \tag{4.68}$$

The percentage of each circumferential mode can be directly calculated from the total displacement at each point P in the axial direction:

$$\lambda_n = \frac{\left| \mathbf{X}_0^n(P) \right|}{\sum_{n=1}^{\infty} \left| \mathbf{X}_0^n(P) \right|} \tag{4.69}$$

Therefore the effective loss factor is determined by combining the percentage of all modes in circumferential and axial direction which are participating to form the displacement vector $\mathbf{X}_0$ as follows:

$$\eta_{\text{eff}} = \sum_{n=1}^{\infty} \sum_{i=1}^{m} \lambda_n \alpha_i^n \eta_i^n \tag{4.70}$$

where η_i^n is the loss factor at circumferential mode n and axial mode i and η_{eff} is the effective loss factor. The effective loss factor η_{eff} is now considered as the objective function to be maximized. The constraint of the optimization problem is the total mass of the sandwich structure. The goal here is to suppress the vibration of the base layer. The core and top layers should not have significant impact on the total mass of the structure (mass constraint). Here, first the optimized number of cuts and their distributions are obtained for fully treated sandwich cylinder using the genetic algorithm available in MATLAB. Binary numbers [0 1] are employed to define the location of the cuts in the sandwich cylinder. Therefore the initial populations are created using random binary vectors in a way that 0 is assigned to a place where there is no cut and 1 is assigned to the cut location. For the individuals which include only binary numbers, the useful "Scattered" function is employed for creating the Crossover Children which merges the

parents by choosing randomly from the variables of the first and second parent. The Mutation function has been customized in a way that with probability less than 10% random numbers of the variables are switched from 0 to 1 and vice versa. Another optimization has been conducted to optimize simultaneously total number of treatments, the distribution of the treatment and thickness of the top and core layers. In this case, the total mass of the structure is the constraint of the optimization problem. The genetic algorithm (GA) combined with sequential quadratic programming (SQP) available in MATLAB are used in the optimization process. First all parameters are optimized by employing GA in which the binary vectors, 0 and 1 are assigned to the treated and untreated elements, respectively. Since the thicknesses of the top and bottom layers at the treatments are real value, therefore a crossover function is customized to create the children so that the "Scattered" function is used to create binary vector for the location of the treatments and the "Intermediate" function is used to create the thicknesses of the top and bottom layers in which weighted average of the thicknesses from the parents are evaluated. The same Mutation function mentioned before is used to create mutation children except that for the elements of an individual representing the top and core thicknesses, the Gaussian function is used to add random number to these elements. The optimum thickness can be further improved using SQP subjected to the constraint on total mass. The result obtained by GA is used as the starting point for SQP solution.

4.6 Results and Discussion

First, the finite element models based on the lower and higher order of Taylor's expansion of displacement fields in the thickness coordinate of the core layer using method_1 and method_2 are compared with each other.

Parametric studies are also presented to observe the effect of the partial treatment and the distribution of treated elements on the loss factor of constrained sandwich cylindrical shell. Similar results are presented for the effects of cuts and their distribution on damping behavior. The optimization problem is first solved to find the optimum number and distribution of cuts in a fully treated sandwich cylinder and, finally, the optimization problem is solved to decrease the weight of the sandwich structure using partial treatments in a way that a light structure with maximum effective loss factor is achieved. The results from the parametric study are presented for clamped-free boundary conditions and the optimization results are presented for clamped-free, simply supported and clamped-clamped boundary conditions.

4.6.1 Comparison between lower and higher order models

The properties of the sandwich cylindrical shell structure and the dimensions are given in Table 4.2. Using method_1, the frequency response under point load at the end of the clamped-free cylinder is obtained at the point where the load is exerted. Figure 4.3 shows that for a relatively thin damping layer the FRF for the lower and higher order models are nearly similar. However, at the natural frequencies the damping behavior of the higher order model is slightly more than the lower order model. The ratio of damping layer and top elastic layers to the base layer is assumed to be R_c and R_t, respectively. In Figure 4.4 for R_t =0.2 and different values of R_c, the effective loss factors resulted from different finite element models (mentioned in Table 4.1) are compared for the clamped-free boundary condition. It should be noted that the effective loss factor is calculated here based on considering 10 circumferential modes and their first 3 axial modes for sandwich cylindrical shell under point loading.

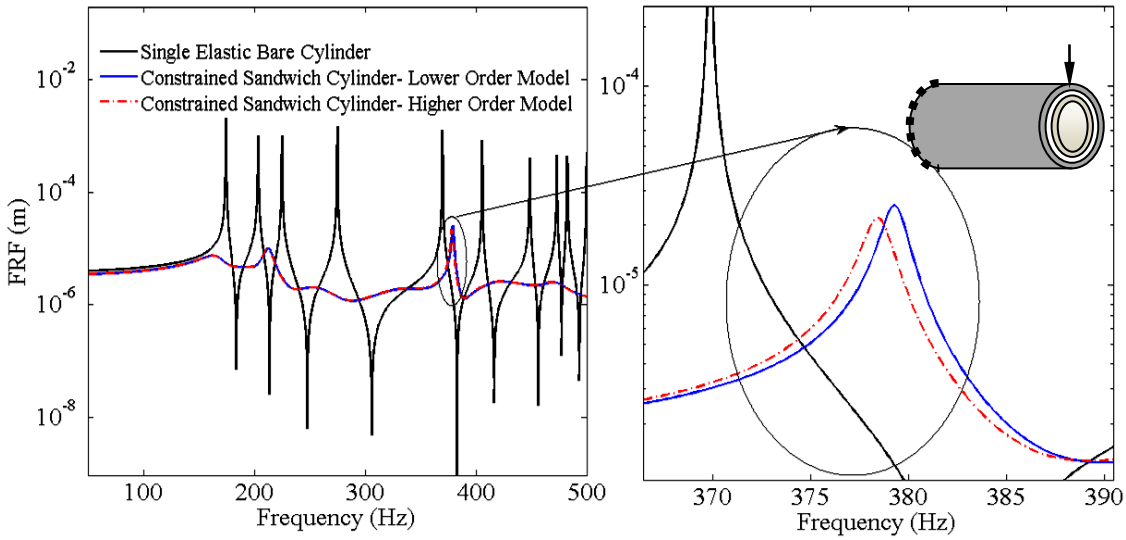

Figure 4.3 Frequency response for clamped-free constrained sandwich cylindrical shell; h_b= h_c=1.5 mm, h_t= 0.3 mm, comparison between lower and higher order models

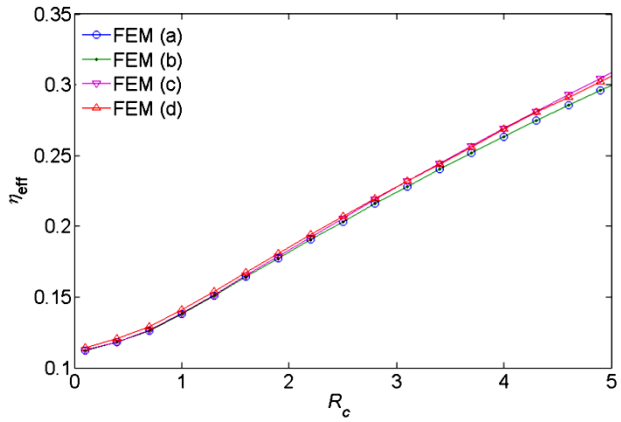

Figure 4.4 Comparison between the results of the lower and higher order models for effective loss factor in clamped-free boundary condition using, R_t = 0.2

As expected, the results from the lower and higher order models deviate as R_c becomes larger (core viscoelastic becomes thicker). One can realize that the difference between lower and higher order models are insignificant (l%) for value of R_c up to 3.

Table 4.2 Properties and dimension of the three layered sandwich cylinder- Properties of damping layer is frequency dependent

	Radius (mm)	Length (mm)	Thickness (mm)	Young modules (N m^{-2})	Density (kg m^{-3})	Poisson's ratio
Base Layer	216.2	511.2	1.5	1.83×10^{11}	7492	0.3
Viscoelastic Layer	216.2	511.2	h_c	380560 $(\omega/2\pi)^{0.475}(1+1.46i)$	1140	0.34
Constraining Layer	216.2	511.2	h_t	1.83×10^{11}	7492	0.3

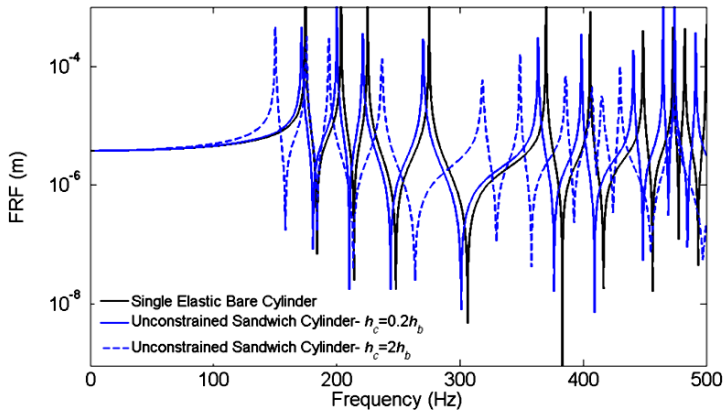

Figure 4.5 Frequency response for clamped-free unconstrained sandwich cylindrical shell; comparison between thin and thick core layers

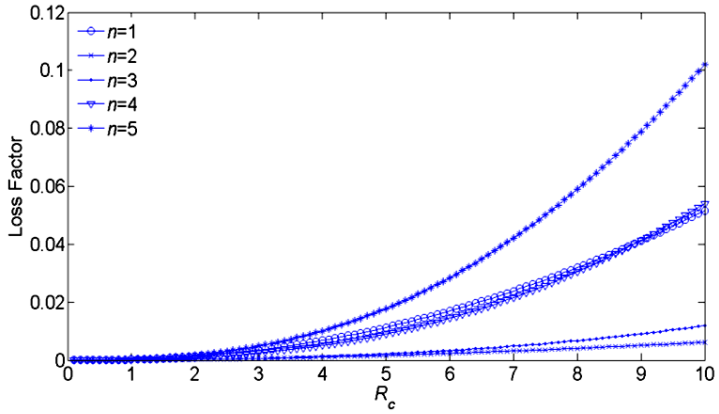

Figure 4.6 Effect of core layer thickness on the loss factor of unconstraint sandwich cylindrical shell at different fundamental circumferential mode for clamped-free boundary condition

The difference of 2.5% is observed for the thick core layer ($3 < R_c < 5$). The results also show that the method_1 and method_2 for the lower and higher order models generate similar results. The small difference (0.8%) between FEM (c) and (d) arises from neglecting the general solution in Eqs (4.30) and (4.31).

4.6.2 Unconstrained sandwich cylinder

Figure 4.5 shows frequency response of the unconstrained sandwich cylindrical shell. According to the previous discussions in section 4.4.1, the lower order model has been employed for the unconstrained treatment. The main disadvantage of unconstrained

sandwich structure is poor damping property due to small shear stress at the damping layer. Due to increase in the total mass of the structure while small change in the stiffness, the natural frequency considerably decreases as the thickness of the core layer increases. The effect of the core thickness on the loss factor of the clamped–free uncontained sandwich cylindrical shell is also demonstrated in Figure 4.6. As expected, the loss factor increases as the core layers become thicker. This is especially more pronounced for the lower modes.

4.6.3 Effect of cuts, partial treatments and their distribution on loss factor and frequency response function

First, the sandwich structure layer is assumed to be fully treated without cut at the core and top layers. The damping property using the lower and higher order models in terms of the loss factor at each fundamental circumferential mode and also in terms of the effective loss factor for R_c= 1 and R_t= 0.2 is shown in Figure 4.7. According to the results, the higher order model exhibits more damping properties than the lower order model. Effects of partial treatment on the loss factor considering the treatment configurations shown in Figure 4.1 are presented in Figure 4.8. According to these configurations, although the partial treatment process can reduce significantly total weight of the structure, an inappropriate distribution may decrease the damping properties. It will be shown further that one can optimize the partial treatment locations and thickness ratio to achieve higher loss factor compared with that of fully treated structure. The effect of cuts considering the configurations given in Figure 4.2 (b) is also shown in Figure 4.9. One can realize that cutting in the core and top layers can increase the damping property compared with the fully treated sandwich cylinder. Also increasing the total number of cuts does not guarantee increase in damping properties.

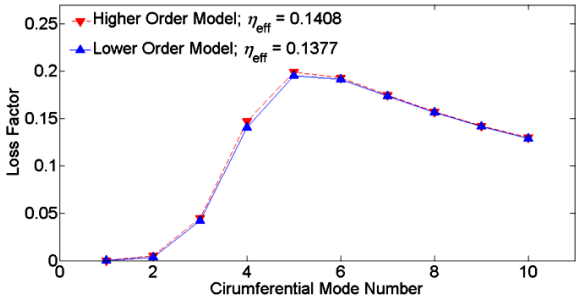

Figure 4.7 Damping properties of fully treated sandwich cylindrical shell without cutting; R_c =1, R_t = 0.2, comparison between lower and higher order models using FEM (b) and (d)

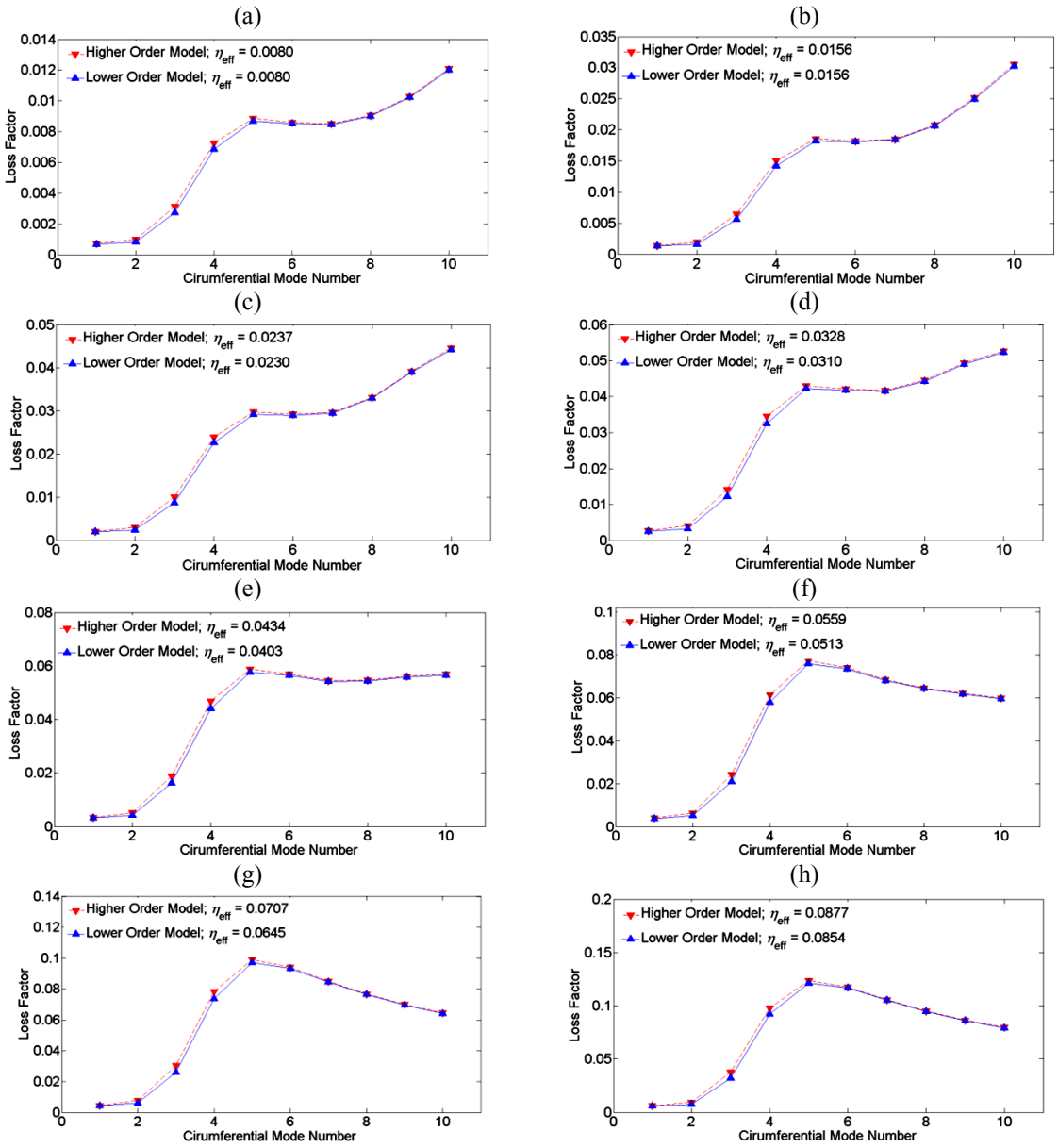

Figure 4.8 Partial treatment and its distribution effect on damping properties; R_c =1, R_t = 0.2, (a) 1 treatment, (b) 2 treatments, (c) 3 treatments, (d) 4 treatments, (e) 5 treatments, (f) 6 treatments, (g) 7 treatments, (h) 8 treatments

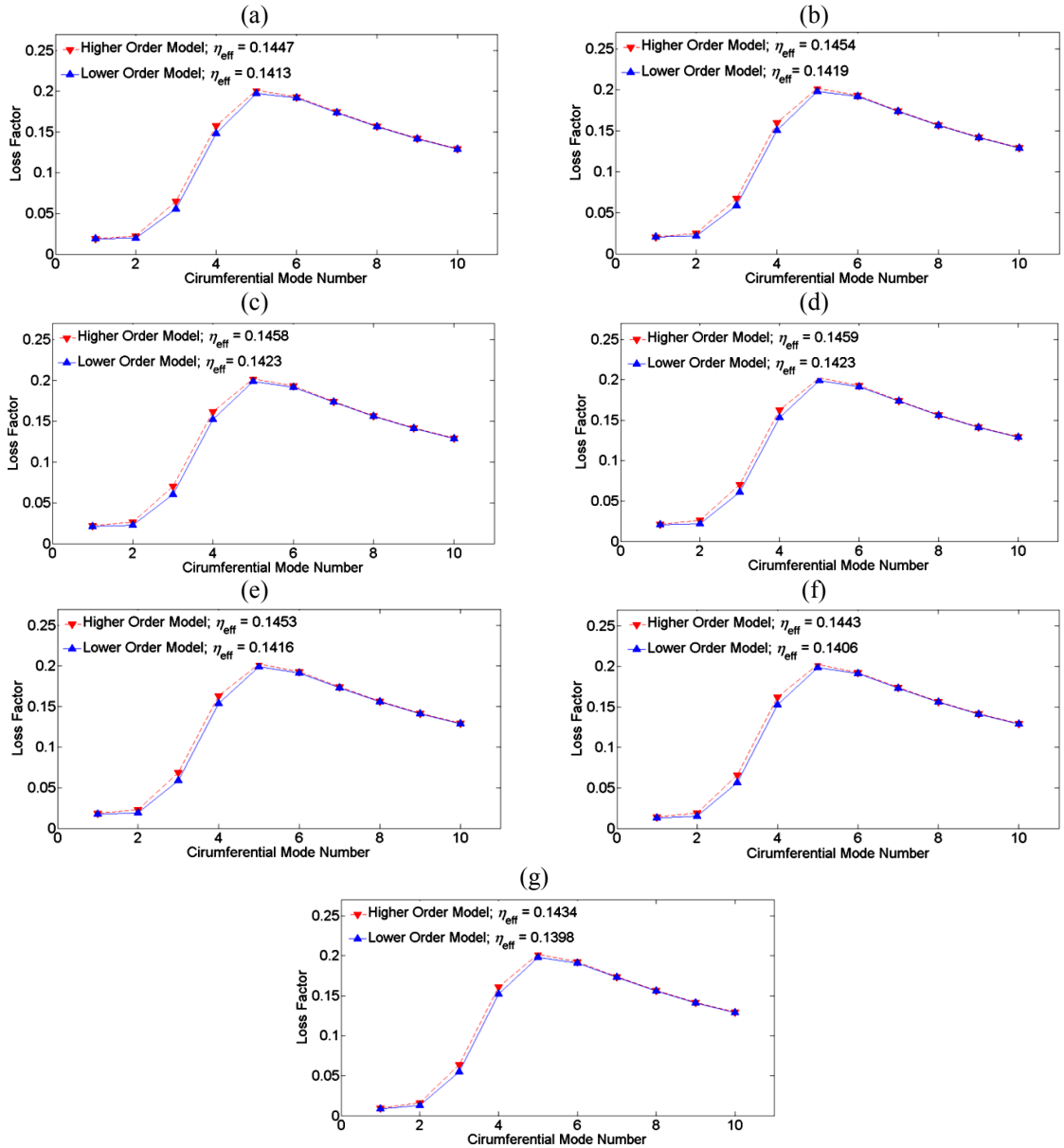

Figure 4.9 Cut and its distribution effect on damping properties; R_c =1, R_t = 0.2, (a) 2 cut, (b) 4 cuts, (c) 6 cuts, (d) 8 cuts, (e) 10 cuts, (f) 12 cuts, (g) 14 cuts

The FRFs for the sandwich cylindrical shell including 14 cuts and also for the same cylinder with 8 treatments (no cutting) are compared with FRF of the fully treated cylindrical shell in Figure 4.10. Increase in damping due to the cuts leads to smaller amplitude in the frequency response. However, less damping due to the partial treatment using the configuration of 8 elements leads to higher amplitudes at the natural frequencies.

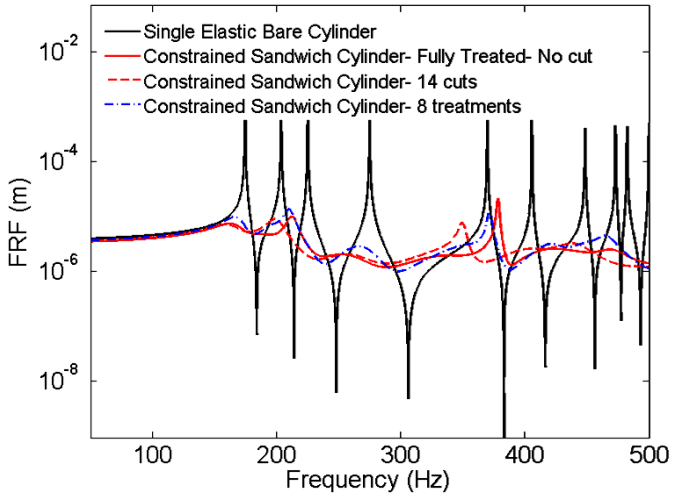

Figure 4.10 Effect of cuts and partial treatments on frequency response function; R_c =1, R_t = 0.2

4.6.4 Optimization results

The parametric studies in this chapter and the chapter 2 demonstrated that damping characteristics are highly affected by thickness ratios of the treating layers, cut/partial treatment and their distribution and slippage between layers at the interfaces. As shown in the chapter 2, in order to increase damping the slippage should be prevented. Therefore the results here are presented considering perfect bonding at the interfaces.

Table 4.3 Optimum cutting distribution on fully treated cylinder, R_t = 0.2, R_c = 1

Cut distribution for clamped-free sandwich cylinder (η_{eff} = 0.1481)	No cutting
	η_{eff} = 0.1408
Cut distribution for simply supported sandwich cylinder (η_{eff} = 0.1003)	
	η_{eff} = 0.0942
Cut distribution for clamped-clamped sandwich cylinder (η_{eff} = 0.0997)	
	η_{eff} = 0.0935

Table 4.4 Optimum partial treating and thickness ratio of top and core layers

Treatment distribution for clamped-free sandwich cylinder (η_{eff} = 0.1716)	R_t	R_c
	0.163	2.083
Treatment distribution for simply supported sandwich cylinder (η_{eff} = 0.1207)		
	0.098	1.781
Treatment distribution for clamped-clamped sandwich cylinder (η_{eff} = 0.1106)		
	0.079	1.881

As mentioned before, the displacement vector $\mathbf{X}_0$ resulted from harmonic point loading condition is considered to find the effective loss factor. The load is applied at the tip of the clamped-free and at the middle of the simply supported and clamped- clamped sandwich cylinders. Optimization results for number of cuts and their distribution along the axial direction considering different boundary conditions are shown in Table 4.3. According to the results, the effective loss factor is improved for clamped-free, simply support and clamped-clamped respectively by 5.2%, 6.5% and 6.6% with respect to that of fully treated sandwich cylinder with no cut. Symmetric distribution of cuts is observed for the clamped-clamped and simply supported boundary conditions. Since $\mathbf{X}_0$ resulted from point loading at the middle of the cylinder has similar configuration for both simply supported and clamped-clamped boundary conditions, the optimization results are similar in both cases. To observe the damping effect of the optimized cutting on the clamped-free sandwich cylinder, its frequency response is compared to the frequency response of the fully treated sandwich cylinder without cutting in Figure 4.11. One can realize that the optimum cutting can considerably decrease the amplitude in the frequency response function especially at higher frequencies.

Another optimization is performed to find optimum treatment in which a light structure exhibiting maximum damping property is achieved. The total number of treatments, distribution of treatments, and thickness of top and core layer are simultaneously optimized. It has been assumed that the total mass of the structure does not exceed 25% of the bare structure mass. The optimum treatment distribution with the optimum thickness ratio of the core and top layers for different boundary conditions are presented in Table 4.4.

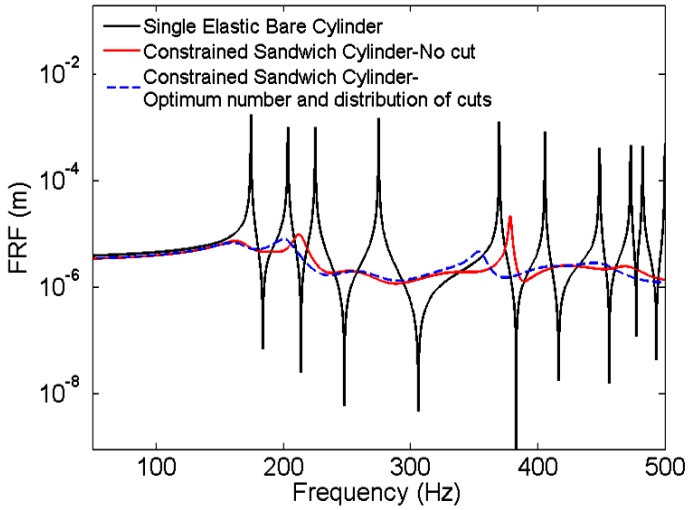

Figure 4.11 Frequency response of fully treated clamped-free sandwich cylinder; R_c =1, R_t = 0.2, comparison between optimum cutting and no cutting.

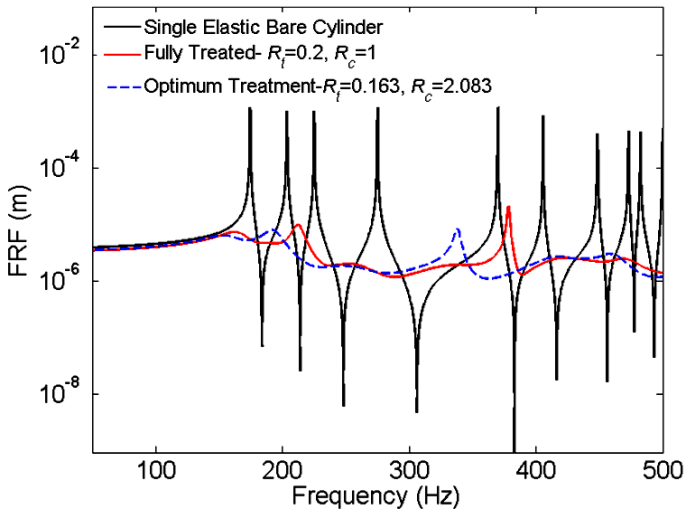

Figure 4.12 Comparison between frequency responses of optimum treating and full treating in clamped-free sandwich cylinder.

The optimum number of treatment for clamped-free boundary condition is found to be 7 and they are clustered at the free end of the shell. However for the simply-supported and clamped-clamped boundary conditions the optimum number of partial treatments is found to be 9 and they are clustered at the middle of the shell due to symmetry condition. It can be realized that for achieving maximum shear strain, the treated elements are mainly placed at the locations in which the deflection is high. The percentages of improvement of effective loss factor for the clamped-free, simply-supported and

clamped-clamped are respectively 25.1%, 28.1% and 18.3%. Therefore the damping characteristics can considerably improved whilst the total weight of the structure is decreased. In order to understand the effect of the optimum treatment on damping, the frequency responses for the optimum design and the primary design in the clamped-free sandwich cylinder are shown in Figure 4.12. It can be concluded that the optimum treatment provides better damping comparing to the initial design especially at the lower modes.

4.7 Conclusion

Considering slippage between layers at the interfaces, new higher order Taylor's expansions of displacement fields in the core layer were developed to investigate damping characteristics of sandwich cylindrical shell. The developed higher order model can compatibly describe the displacement field in the core layer in terms of displacements at the elastic faces. The higher order model was considered in the optimization problems due to the feasible displacement profile achieved by this model especially for thick constrained viscoelastic core layer. Optimization results showed that by embedding an optimum distribution of the cuts, the loss factors particularly at the higher modes are considerably increased. It was also shown that a light structure with high damping characteristics can be achieved by optimizing simultaneously partial treatment distribution and the thicknesses of treating layers.

CHAPTER 5

DYNAMIC MECHANICAL PROPERTIES OF AN ELECTRO-RHEOLOGICAL FLUID UNDER LARGE AMPLITUDE OSCILLATORY SHEAR STRAIN

5.1 Introduction

Electrorheological (ER) fluids have many applications in engineering such as shock absorption, vibration control of structures and flow control of fluids due to their ability to provide reversible and rapid response. An ER fluid consists of suspension of solid dielectric particle dispersed in an insulating oil [41]. The rheological properties of the ER fluids are immediately changed when they are subjected to external electric field. ER fluids naturally behave as Newtonian fluid and immediately transform to the plastic (semi-solid) state under electric field due to the formation of polarized particle chains in the direction of electric field. In many applications, ER and MR fluids are subjected to oscillatory shear [62]. The dynamic properties of ER and MR fluids under oscillating shear strains in both pre-yielding and post yielding regimes are investigated by many researchers [43-74] as discussed in chapter 1.

From previous studies, it can be concluded that the shear response of ER fluids and the material properties under large deformation at certain field intensity are highly nonlinear with respect to strain amplitude and frequency. In the present chapter, based on the dynamic mechanical analysis (DMA), linear and nonlinear viscoelastic properties of an ER fluid material consists of cornstarch dispersed in corn oil is systematically investigated experimentally under small and large amplitude oscillatory shear strain. The experimental data are extracted for moderate range of frequencies and different electric field strengths. However, for relatively high frequencies the device fails to capture the

properties at small shear strain amplitude. Finally, a constitutive model has been proposed to predict the experimental data and also extrapolate the mechanical behavior at the immeasurable regions. The proposed model requires less number of parameters compared with the Fourier transformation rheology for predicting the stress response and the mechanical properties for different strain amplitudes, frequencies and field intensities. This leads to simplify the parameter identification using the optimization techniques. As shown in the results, the proposed constitutive model is able to predict material response for large amplitudes and also the transition between the linear and nonlinear regimes is observable using this model.

5.2 Experiment

The ER fluid is prepared by dispersing cornstarch into corn oil with viscosity of 40 mPa s. The weight fraction of the particles is chosen to be 30 %. Figure 5.1 (a) shows the dispersed cornstarch particles in the corn oil which are distributed randomly in the absence of electric field. As the electric field is applied inside the fluid, the polarized particles form chains in the direction of the electric field as shown in Figure 5.1 (b) and (c) for the field intensity of E=0.1 KV/mm and E=0.5 KV/mm, respectively. In order to increase the accuracy and also safety of the experiment, an acrylic box is designed with number of grooves at certain height of the box. The fabricated conductive aluminum plates are then fixed inside the grooves and by applying high voltage to these plates the electric field is established in the ER fluid. With this feature, an approximate pure shear force can be generated inside the ER fluid.

(a)

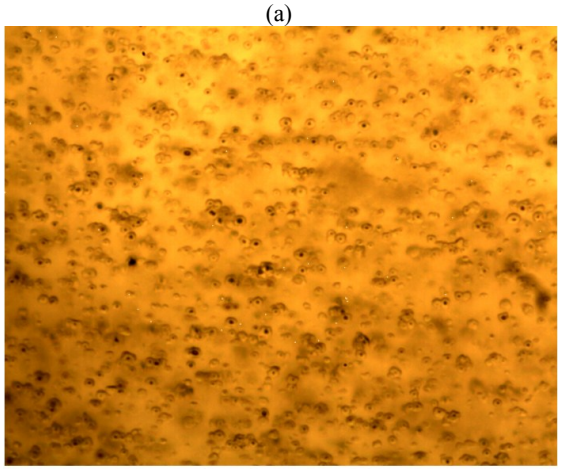

(b)

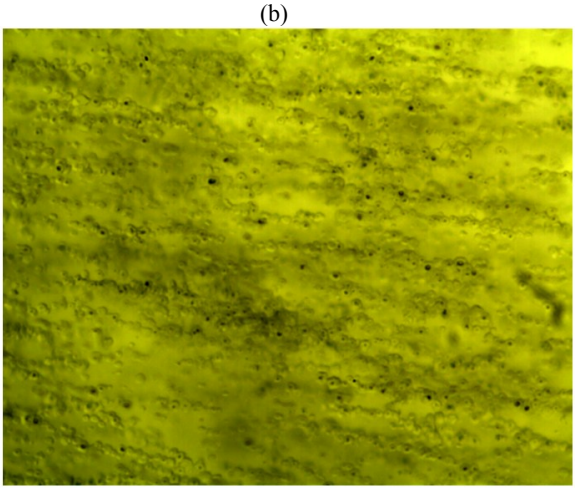

(c)

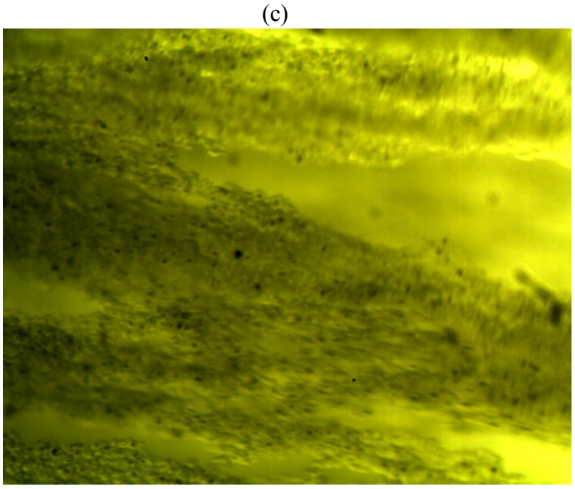

Figure 5.1 Electrorheological fluid (cornstarch suspensions in corn oil); E=0 KV/mm, (b) E= 0.1 KV/mm, (c) E= 0.5 KV/mm

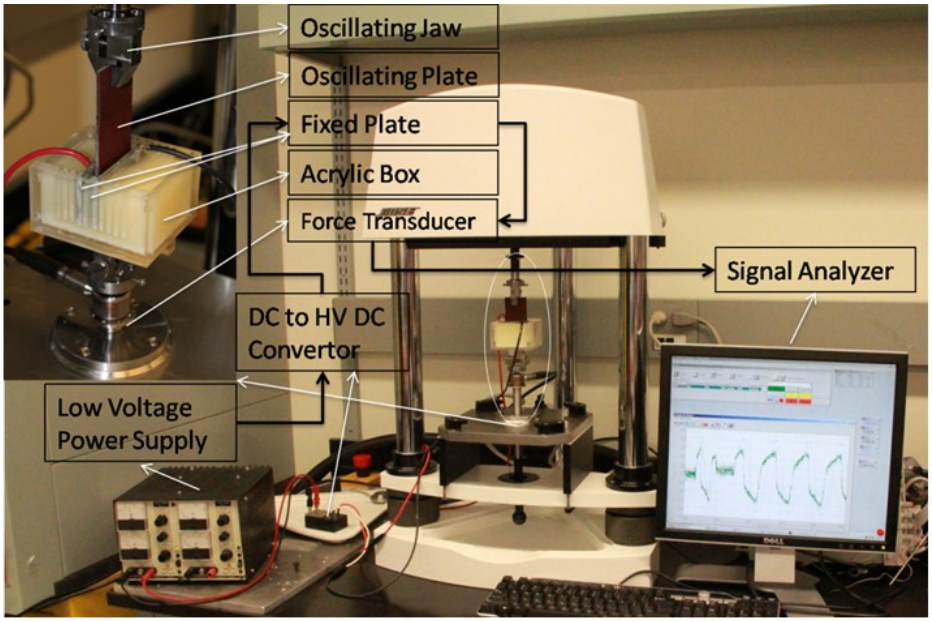

Figure 5.2 Experimental setup to measure dynamic properties of the ER fluid material

The shear area of the ER fluid contacting with the oscillating plate is 844 mm^2. The distance between the fixed aluminum plates is 5.4 mm and the thickness of the oscillating plate inserted between the fixed plates is 2.8 mm. The experiment has been carried out using Bose ElectroForce 3200 device. Figure 5.2 shows the experimental setup demonstrating the positions of the acrylic box containing the ER fluid, oscillating plate, fixed plates, low voltage power supply and DC to high voltage DC converters. The electric field is induced in the ER fluid by applying voltage between the fixed plates. Low input voltage is first generated by the low voltage power supply (o to 15 Volt) and then the DC to high voltage DC converter provides the high DC voltage (0 to 10000 Volts) inside the fixed plates. The oscillating plate generates the shear strain in the ER fluid and the resulted axial force is measured by the force transducer. The timed data of the measured force and the input displacement are analyzed by the DMA software using Fourier transform technique. The amplitude and also the phase of the fundamental frequency for the measured force and displacement are considered to calculate the complex modulus based on Eq. (1.4). In order to prevent sedimentation of the cornstarch particles, the ER fluid is carefully blended after each frequency sweep.

The experiment has been conducted to explore the material properties for frequency range of 0.1 Hz to 60 Hz and the shear strain amplitude ranging from 0.1538 % to 7.69 %. It should be noted that at higher frequencies the device could not maintain the small oscillatory displacement. Considering this, it was not possible to provide accurate properties at high frequencies and small strain amplitude.

5.3 Proposed Constitutive Model

According to the rheology analysis based on Fourier transform, the stress response of ER fluids under large amplitude oscillatory shear strain depends on many variables including amplitude, frequency and field intensity. For a given frequency, strain amplitude and electric field, too many terms and coefficients in Fourier transform relation should be determined to accurately express the stress response in the time domain. The coefficients should be also expressed in terms of these variables using appropriate functions to incorporate them in the stress response. Therefore, evaluating the stress response mathematically could be too complicated. In this study, a modified form of the Bingham-Hooke model used by Laun et al. [74] which has been shown in Eq. (1.5) has been developed. As mentioned before, according to their results the material properties obtained by the Bingham-Hooke model represented by Eq. (1.5) deviate from the experimental data at the nonlinear regime. In this chapter, this model has been considered as the starting point for developing a model to accurately describe the experimental results. The strain amplitude variable is included in the developed model to provide more accurate results particularly at the nonlinear regime. Considering this, the following relation has been proposed for the stress response under the oscillatory shear strain:

$$\tau = \begin{cases} \dfrac{\mu(\dot{\gamma} - \dot{\gamma}_R)}{\tilde{\dot{\gamma}}} + (K + \dfrac{D}{\tilde{\dot{\gamma}}})(\gamma - \gamma_R) & \tau\dot{\gamma} > 0 \\ \tilde{\tau}\,\mathrm{sgn}(\tau) + G_0(\gamma - \tilde{\gamma}) + \eta\dot{\gamma} & \tau\dot{\gamma} \le 0 \end{cases} \tag{5.1}$$

where η, μ, K, D and G_0 are the model parameters which are generally frequency and field dependent, $\tilde{\tau}$ and $\tilde{\gamma}$ represent, respectively the shear stress and strain amplitudes and $\tilde{\dot{\gamma}}$ is shear strain rate amplitude ($\tilde{\dot{\gamma}} = \omega\tilde{\gamma}$).

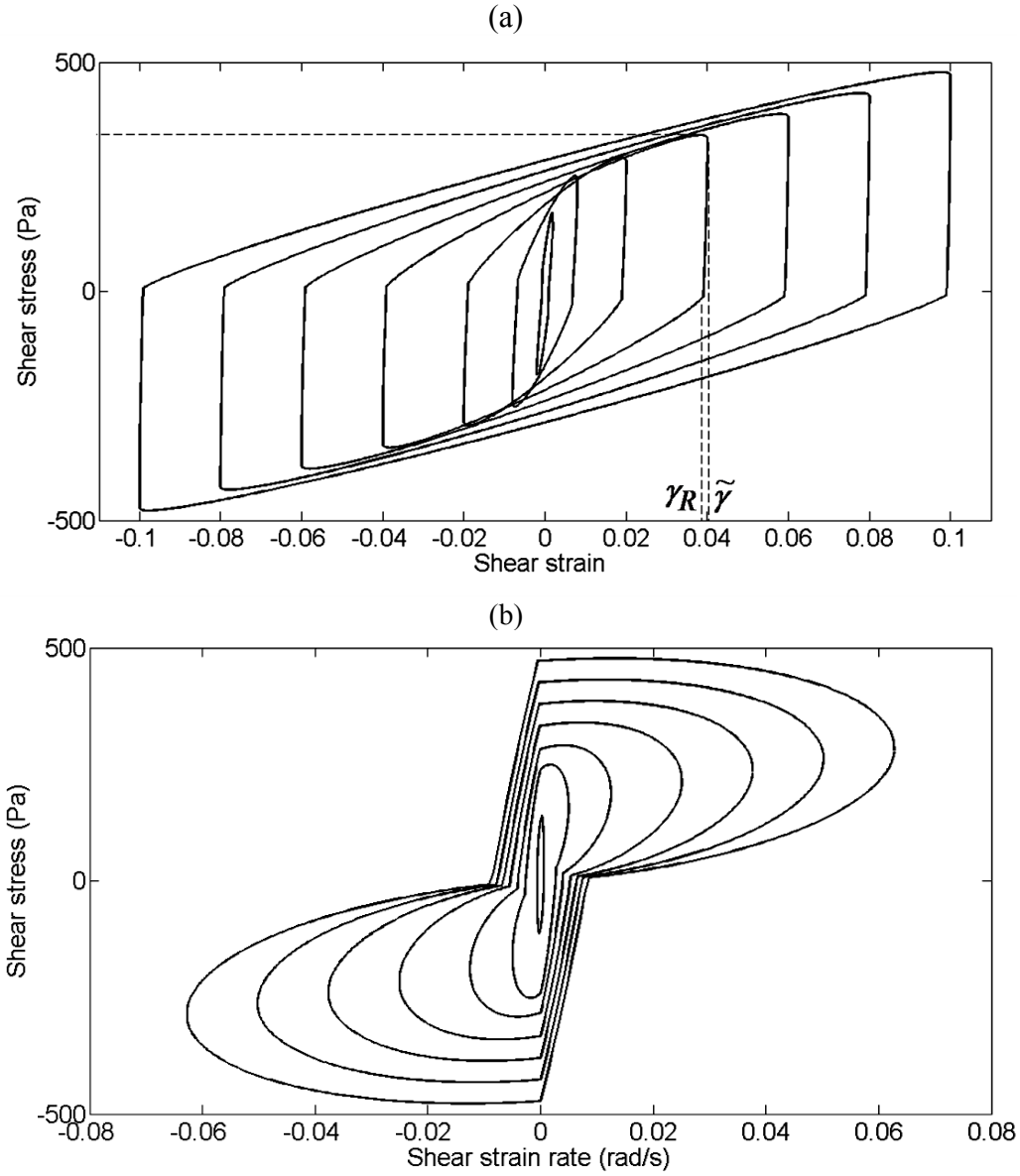

Figure 5.3 Typical hysteresis loops of the proposed model, f= 0.1 Hz, E=1.9 KV/mm, (a) stress-strain (b) stress-strain rate

For frequency of 0.1 Hz and electric field of 1.9 KV/mm, the typical hysteresis loops according to the proposed model is shown in Figure 5.3. At the unloading stage where $\tau\dot{\gamma} \le 0$, the material properties are assumed to be linear viscoelastic. In order to provide continuity in the hysteresis loop, $\tilde{\tau}\,\mathrm{sgn}(\tau)$ and $\tilde{\gamma}$ (in bottom line of Eq. (5.1)) and also shear strain γ_R and shear strain rate $\dot{\gamma}_R$ at τ=0 (in top line of Equation (5.1)) are included in the model. In the nonlinear regime where $\tau\dot{\gamma} > 0$, an amplitude dependent relation defines

the shear stress response which governs the response in the beginning of the loading stage (τ=0) up to the unloading stage. Consequently, the yielding stress is practically assumed to be negligible in this model. However as shown further in the results for stress amplitude versus strain amplitude, the proposed model is able to predict the transition between the linear and nonlinear regimes. Without considering variables $\tilde{\gamma}$ and $\dot{\tilde{\gamma}}$ in the top line of Eq. (5.1), the amplitude of shear stress significantly increases as the shear strain amplitude increases. Therefore, the rate of increase in the shear stress amplitude is reduced by dividing the viscous and elastic terms respectively over the strain rate and strain amplitudes. However, an elastic term (with parameter K) is added to the stress response in order to maintain the increase of the stress amplitude with increasing the strain amplitude. This model provides a simple relation between stress and strain which includes the variable of shear strain amplitude. Based on the results from the experiment and the parametric study of the proposed model at different amplitudes and field intensities, the following functions are chosen to describe parameters η, μ and D as:

$$\begin{aligned} \eta &= c_1 \exp(-c_2 f) + c_3 (f)^{(-c_4)} \\ \mu &= c_5 + c_6 \exp(-c_7 f) \\ D &= c_8 \exp(c_9 f) + c_{10} \exp(-c_{11} f) \end{aligned} \tag{5.2}$$

where $f=\omega/2\pi$ is frequency (Hz), the coefficients c_1, c_3, c_5, c_6, c_8 and c_{10} are assumed to be second order polynomial functions of electric field and c_2, c_4, c_7, c_9, c_{11} are assumed to be constant. The frequency independent elastic parameters K and G_0 are also assumed to be second order polynomial functions of electric field. Using the genetic algorithm (GA) combined with sequential quadratic programming (SQP) available in MATLAB, K,

D and the coefficients c_1 through c_{11} are obtained to minimize the following objective function:

$$e = \sum_{\omega}\sum_{\tilde{\gamma}}\sum_{E}\left(G'_{\text{Model}} - G'_{\text{Exp}}\right)^2 + \left(G''_{\text{Model}} - G''_{\text{Exp}}\right)^2 \tag{5.3}$$

in which the experimental mechanical properties including storage and loss modulus (G'_{Exp} and G''_{Exp}) are obtained using Eq. (1.4) based on the time data of the shear stress and strain. It should be noted that in the optimization problem, the results from GA are used as the starting point for the SQP solution in order to catch the global optimum solution as accurate as possible. The phase difference between the stress and strain at the fundamental frequency for the proposed model can be found using the first order terms in the stress response as:

$$\begin{aligned} G'_1(\omega, E, \tilde{\gamma}) &= \frac{\omega}{\pi\tilde{\gamma}}\int_T \tau(t, \omega, E, \tilde{\gamma})\sin(\omega t)\text{dt} \\ G'_2(\omega, E, \tilde{\gamma}) &= \frac{\omega}{\pi\tilde{\gamma}}\int_T \tau(t, \omega, E, \tilde{\gamma})\cos(\omega t)\text{dt} \end{aligned} \tag{5.4}$$

where T is the time period. The phase difference between the strain and stress is then calculated as:

$$\phi = \arctan\left(\frac{G'_2}{G'_1}\right) \tag{5.5}$$

The storage and loss modulus are now obtained as:

$$G'_{\text{Model}} = \frac{\tilde{\tau}}{\tilde{\gamma}}\cos(\phi) \qquad\qquad G''_{\text{Model}} = \frac{\tilde{\tau}}{\tilde{\gamma}}\sin(\phi) \tag{5.6}$$

which can be compared to the complex modulus from the experiment. The results from the optimization problem are provided in Table 5.1 which can be then substituted into Eq. (5.2) to define the model's parameters.

5.4 Results and Discussion

First, the results from the Bingham-Hooke and proposed constitutive models are compared to the experimental data. As shown by Laun et al [74], the Bingham-Hooke model given in Eq. (1.5) fails to capture loss modulus at small amplitude. Therefore they added $\eta_p\dot{\gamma}$ to the total stress component without changing the Bingham-Hooke model element. As shown in Figure 5.4, by assigning optimum value to the parameters of Eq. (1.5), the Bingham-Hooke model is not able to predict the experimental data particularly at large shear strain amplitude. The parameters $(G_0, \eta_B, \eta_p, \tau_Y)$ of the Bingham-Hooke model ($\lambda=\eta_B/G_0$) for E=0.7, 1.3 and 1.9 KV/mm are respectively (0.4 MPa, 0.28 KPa s, 10.2 KPa s, 57 Pa), (0.65 MPa, 0.31 KPa s, 20.5 KPa s, 88 Pa) and (1.3 MPa, 0.52 KPa s, 51.3 KPa s, 151 Pa). On the other hand, good agreement exists between the results from the proposed constitutive model and experiment.

In the following, the stress response and the complex modulus resulted from the proposed model are presented and compared with the experimental data. The results are presented for different amplitudes, frequencies and electric field intensities.

Table 5.1 The field dependent coefficients of the model's parameters

c_1	c_2	c_3	c_4	c_5
3064-4997E+2698E^2	0.3744	2602-2885E+2893E^2	0.7717	-3.07+15.86E-3.92E^2
c_6	c_7	c_8	c_9	c_{10}
39.71-44.76E+24.88E^2	1.7188	55.34-49.22E+53.65E^2	7.31E-05	-31.84+45.83E-24.97E^2
c_{11}		K		G_0
0.6273		288.5-231E+359.7E^2		21909-3228E+19732E^2

(a)

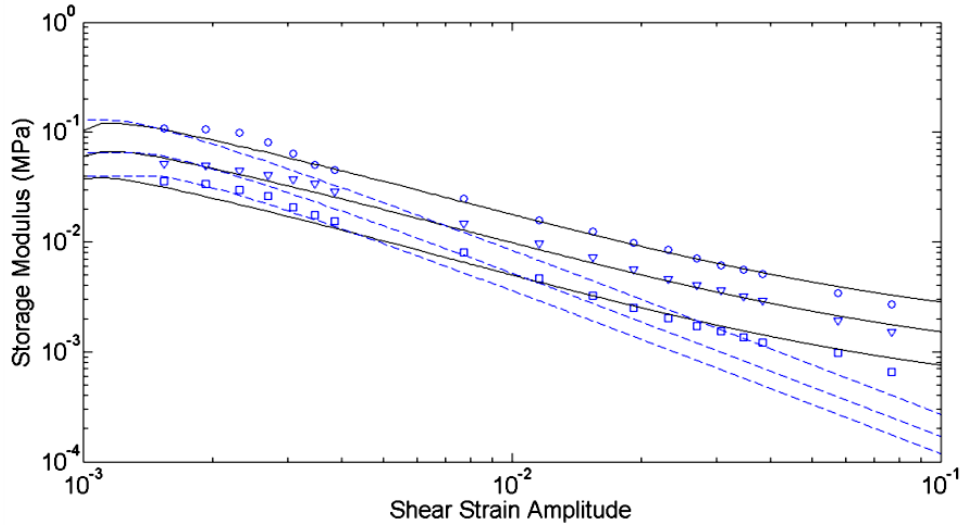

(b)

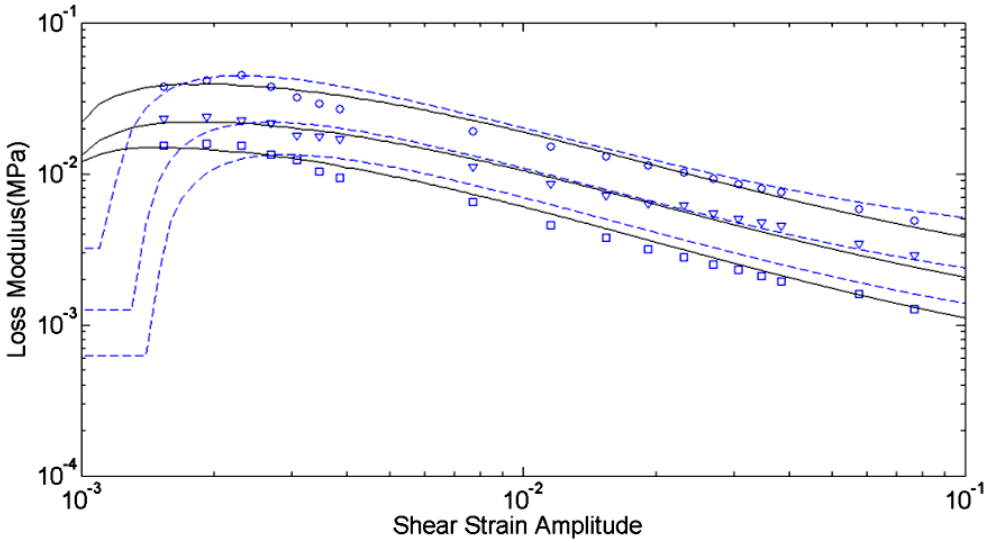

Figure 5.4 (a) Storage and (b) Loss modulus of the ER fluid versus shear strain amplitudes for f=0.1 Hz and different electric field intensities; Symbols represent the experimental results; dashed and solid lines respectively represent simulation results using the Bingham-Hooke and proposed models. □ E=0.7 KV/mm; ∇ E=1.3 KV/mm; ○ E=1.9 KV/mm

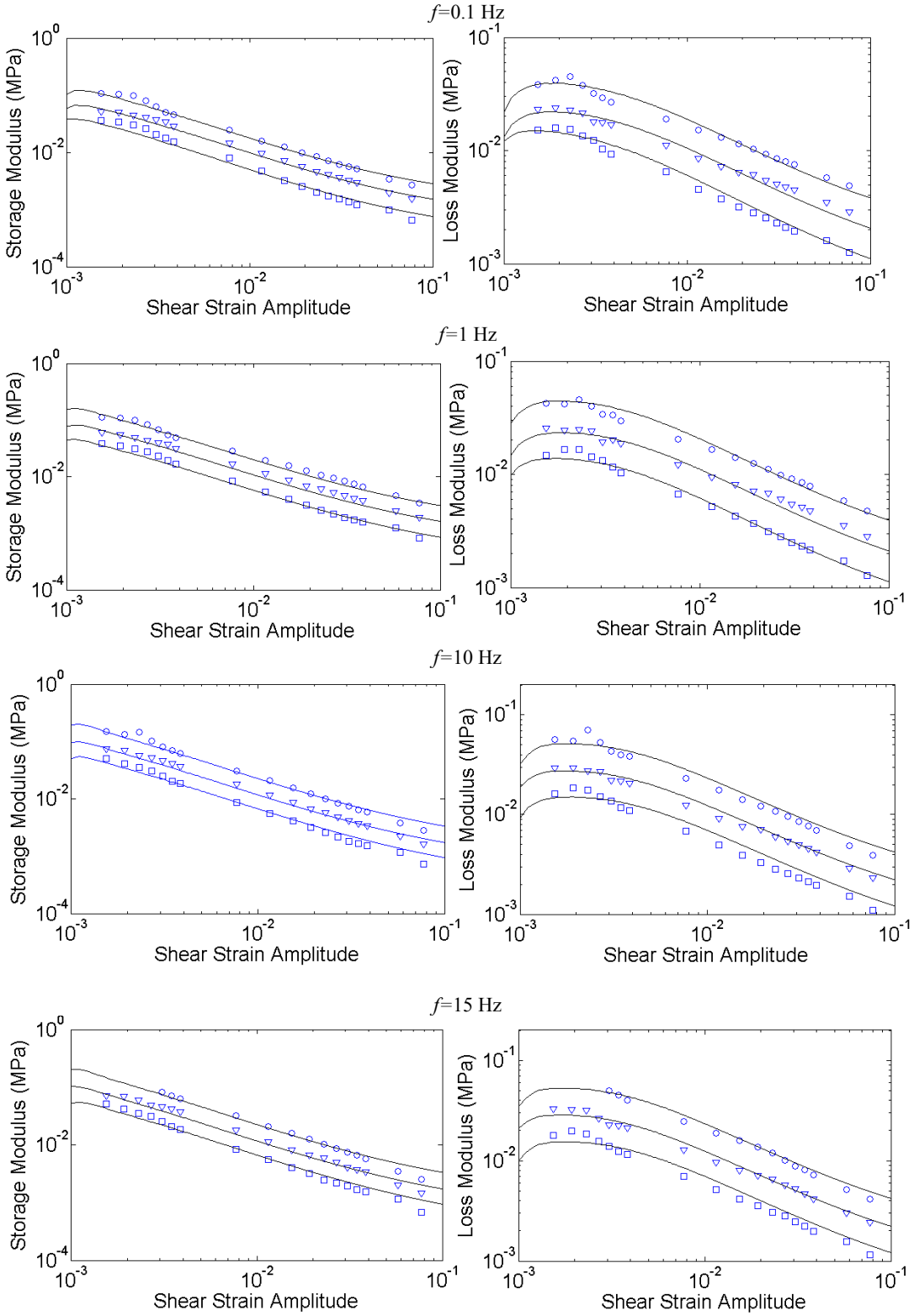

Figure 5.5 Complex modulus of the ER fluid versus shear strain amplitudes for different electric field intensities and frequencies; Symbols represent the experimental results and the solid lines represent simulation results using the proposed model. □ E=0.7 KV/mm; ∇ E=1.3 KV/mm; ○ E=1.9 KV/mm

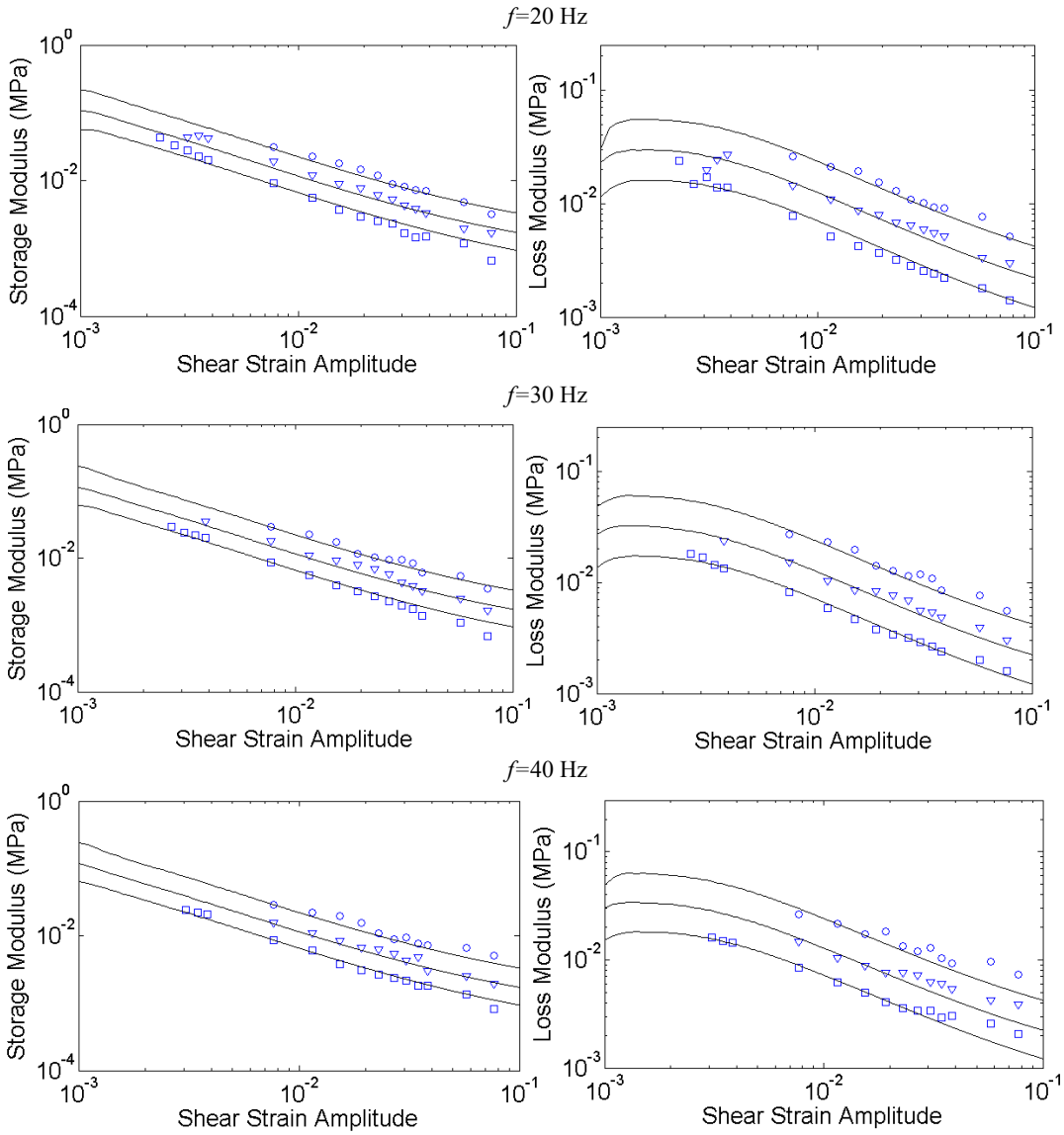

Figure 5.5 Continued

5.4.1 Complex modulus

Using the proposed model, the complex modulus including the storage and loss modulus is compared to the experimental data. Figure 5.5 shows the variation of storage and loss modulus with respect to shear strain amplitude at different frequencies varying from 0.1 Hz to 40 Hz and different electric field intensities (E=0.7 KV/mm, E=1.3 KV/mm, E=1.9 KV/mm). The symbols and solid lines represent, respectively, experimental data and the model's estimation. According to results, the storage modulus

generally decreases with increasing shear strain amplitude. On the other hand, the loss modulus first increases and then decreases. This behavior is also reported in literature such as references [65, 74, 135, 136] which is referred to "weak-strain overshoot behavior". The behavior is related to the complex structures which show resistance to strain deformation up to critical strain amplitude where the loss modulus starts to decrease [135, 136]. For the shear strain larger than the critical shear strain, the material shows "strain thinning" behavior in which both storage and loss modulus decrease with increasing the strain amplitude. As shown in Figure 5.5, the proposed model is able to catch the weak-strain overshoot and strain thinning behaviors accurately. Also, very good agreement exists between the results obtained by the experiment and the proposed model at different frequencies and field intensities. As expected, the results show that with increasing the electric field intensity, the storage and shear modulus increase. The model also reasonably predicts the material behavior for the immeasurable regions with small strain amplitude and higher frequencies.

The material behavior with respect to frequency at different strain amplitudes and field intensities is also shown in Figure 5.6. According to the results, the nonlinear behavior in the complex modulus versus frequency increases with increasing the electric field intensity. This behavior has also been reported in literature such as reference [65]. For each frequency sweep at different strain amplitudes and field intensities, the complex modulus resulted by the present model is in a good agreement with the experimental data. Furthermore, one can observe that with increasing the frequency up to 5 Hz, the storage and loss modulus first increase and then remain nearly constant with further increasing the frequency.

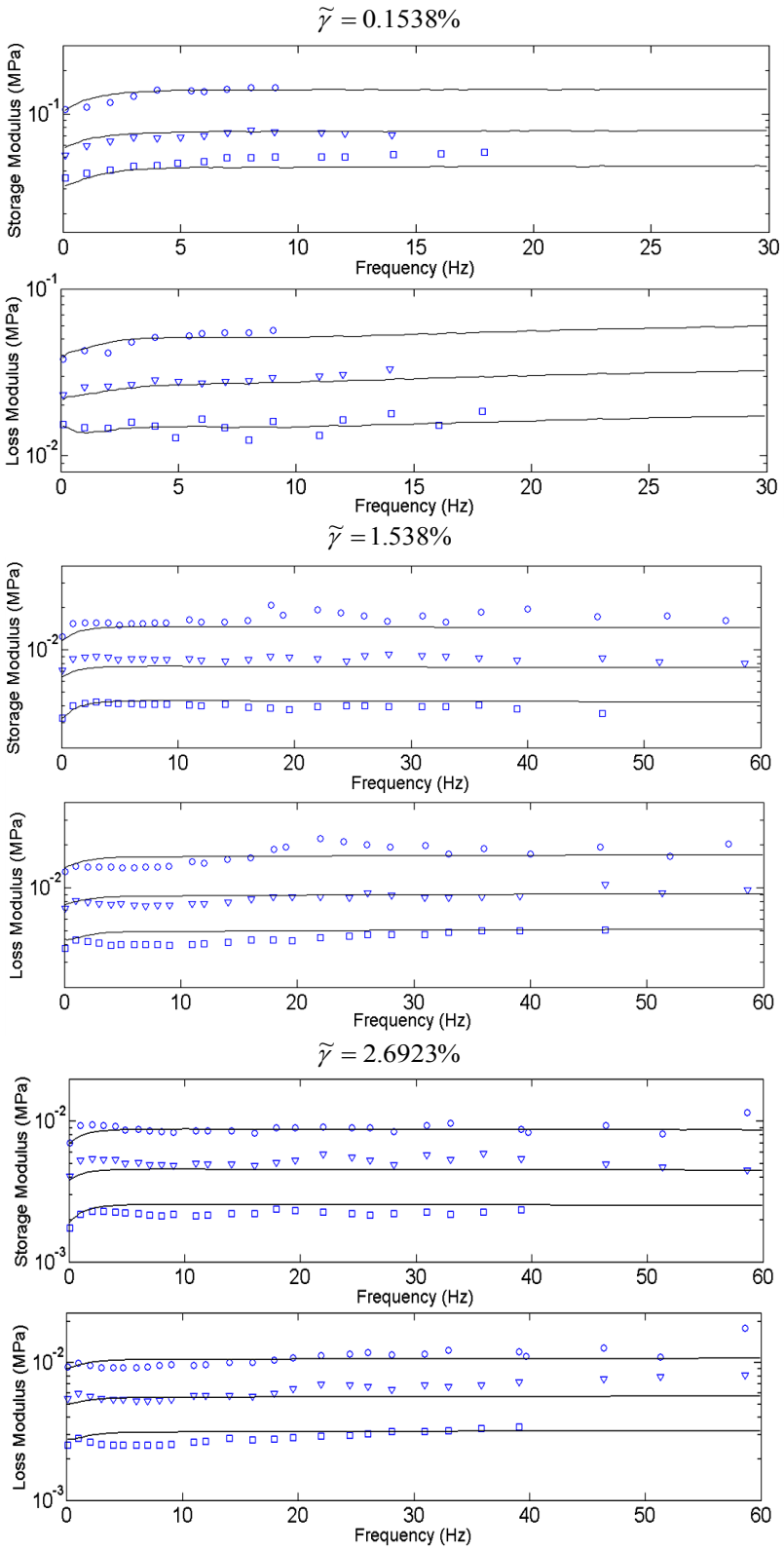

Figure 5.6 Complex modulus of the ER fluid versus frequency for different electric field intensities and shear strain amplitudes; Symbols represent the experimental results and the solid lines represent simulation results using the proposed model. . □ E=0.7 KV/mm; ∇ E=1.3 KV/mm; ○ E=1.9 KV/mm

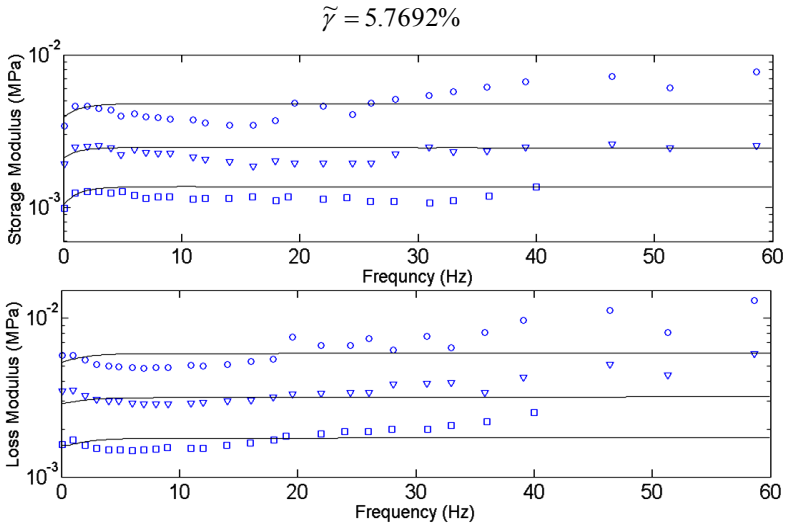

Figure 5.6 Continued

It is noted that the proposed model is capable to reasonably predict the material behavior for wide range of strain amplitudes, frequencies and electric field intensities. This is due to that fact that, the characteristic parameters of the model are obtained to consider all these variables simultaneously and provide smooth function in order to predict the data at different ranges of the input variables. Considering this, some slight deviation is expected between the results obtained by the proposed model and experiment since many variables are contributing in the stress response.

5.4.2 Stress-strain amplitude

Figure 5.7 shows the stress-strain amplitude predicted by the proposed model compared with the experimental data at different frequencies and field intensities. It is interesting to note that despite the fact that in the proposed model the yielding stress in loading stage is assumed to be negligible, nevertheless due to the strain amplitude parameters included in the model the linear regime is well predicted in which by increasing the strain amplitude the rate of increase in the stress amplitude decreases.

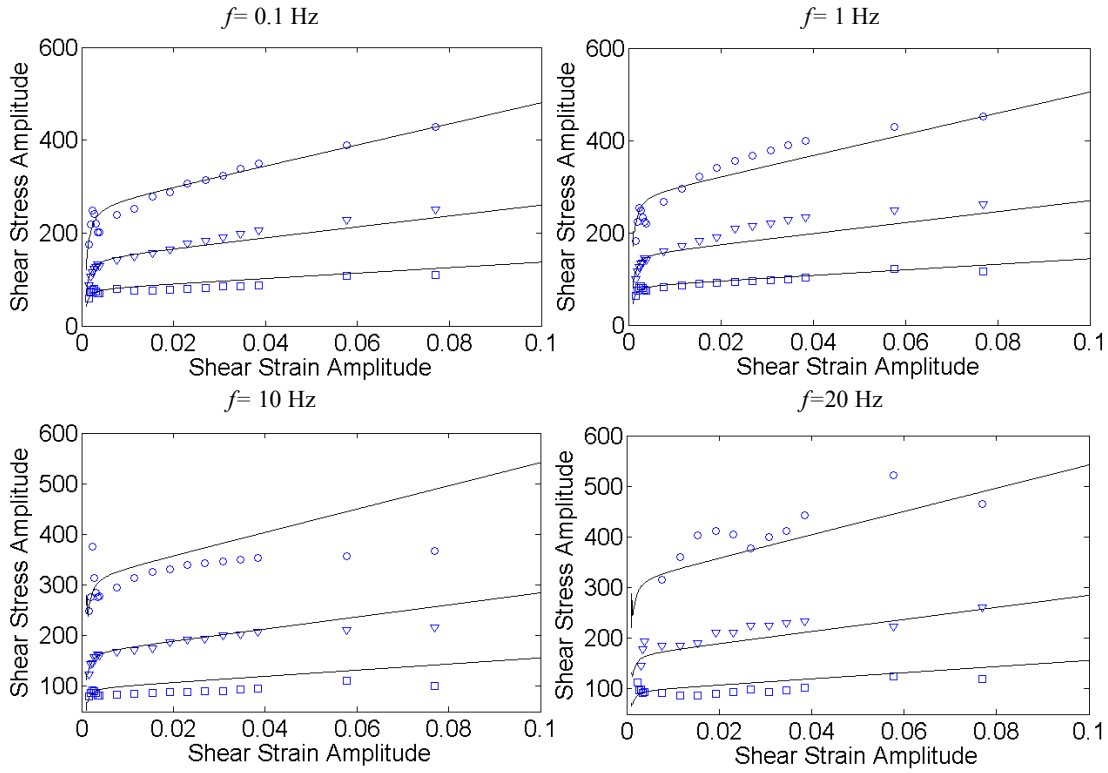

Figure 5.7 Shear stress amplitude versus shear strain amplitude for different electric field intensities and frequencies; Symbols represent the experimental results and the solid lines represent simulation results using the proposed model. □ E=0.7 KV/mm; ∇ E=1.3 KV/mm; ○ E=1.9 KV/mm

At the lower frequencies, very good agreement can be observed between the results. At the higher frequencies and high electric fields, the results obtained by the model deviates from the experimental data. However, considering the nonlinearity due to the different variables including shear amplitude, frequency and electric field, very good agreement still exists between the model and experiment. It should be noted that the slope of the stress-strain amplitude curve in the nonlinear regime depends on the elastic term in the top line of Eq. (5.1) in which with increasing K the slope increases.

5.4.3 Time history of the stress response

Figures 5.8 though 5.10 show the time history of the shear force response measured in the experiment and compare with the results predicted by the model for different field intensities at frequencies f=0.1 Hz and f=1 Hz and large strain amplitude $\tilde{\gamma} = 3.8462\%$.

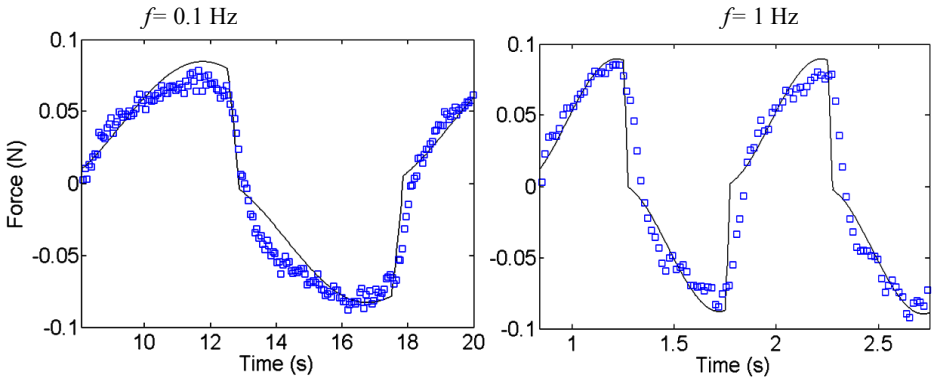

Figure 5.8 Time history of the shear force for $\tilde{\gamma} = 3.8462\%$ and E=0.7 KV/mm.

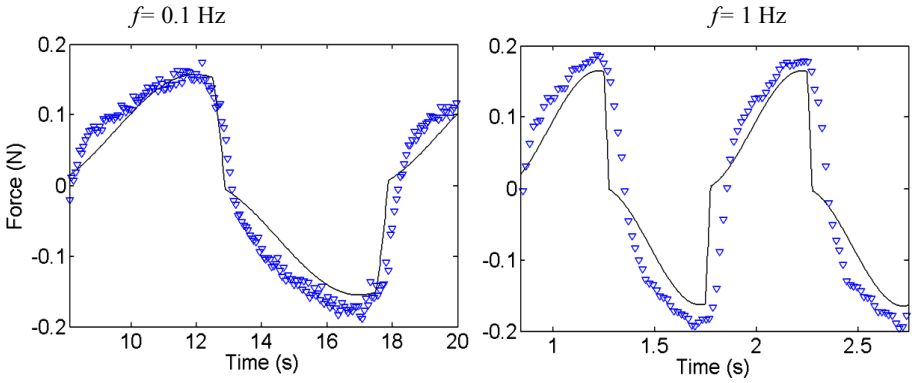

Figure 5.9 Time history of the shear force for $\tilde{\gamma} = 3.8462\%$ and E=1.3 KV/mm.

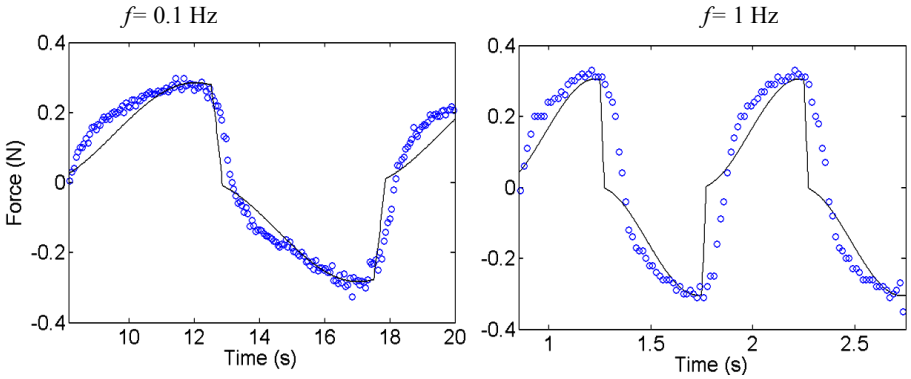

Figure 5.10 Time history of the shear force for $\tilde{\gamma} = 3.8462\%$ and E=1.9 KV/mm.

As it can be realized, a very good agreement can be observed between the proposed model and experiment for the results in both loading and unloading stages. Therefore the proposed model is able to predict the timed data of the shear stress obtained from experiment as well as the storage and loss modulus of the ER fluid.

5.5 Conclusion

Dynamic mechanical properties of an electrorheological fluid consisting of cornstarch dispersed into corn oil were investigated based on the experiment and the proposed model. The results show that the complex modulus increases with increasing the field intensity. Furthermore, as the amplitude of the shear strain increases the storage modulus decreases, however, the loss modulus first increases and then decrease. The complex modulus increases with increasing the frequency up to certain point and then remains constant for moderate range of the frequency. It has been shown that the proposed model provides good estimation of the complex modulus as well as the time history of the shear stress response. Although the yielding stress in the proposed model was assumed to be negligible, due to including the strain amplitude in the model the linear regime was discernible whereas by increasing the strain amplitude the rate of increase in the stress amplitude decreases.

CHAPTER 6

NONLINEAR FREE VIBRATION ANALYSIS OF SANDWICH SHELL STRUCTURES WITH CONSTRAINED ELECTRORHEOLOGICAL FLUID LAYER

6.1 Introduction

As mentioned in chapter 1, the studies on structural vibration damping using MR/ER semi-active treatment are mainly limited to the beam and plate type sandwich structures and also to the linear region of MR/ER fluids where the complex modulus is independent from amplitude of the shear strain [75-85]. Geometrically nonlinear vibration of bare and sandwich structure has been reported in literature [86-101] and discussed in chapter 1. Due to the small linear region in ER fluid, here the vibration analysis of the sandwich structure containing ER fluid has been investigated in nonlinear region in which the material properties depend on frequency, amplitude and electric field. Currently, there are no available studies on vibration damping of ER or MR based sandwich cylindrical shells/panels subjected to large deformation. The main objective in this chapter is to investigate the nonlinear free vibration analysis of sandwich shell/plate structure with constrained ER fluid.

In this chapter, by considering kinetic and potential energies attributed to the elastic and ER fluid layers and using Lagrange equations, nonlinear finite element formulation has been derived for the ER based sandwich shell structures. The developed nonlinear model is then used to investigate the nonlinear vibration behavior of sandwich shell structure with constrained ER fluid layer. As mentioned before, the main problem in nonlinear vibration analysis of structure using direct integration technique is the time-consuming integrations, which should be performed for several times throughout this

method. This is especially very critical for finite element modeling of sandwich shell structures where the number of degrees of freedom drastically increases compared with beam type structures. Here, a new technique is presented to represent the equations of motion in a new notation referred to as H-notation which fundamentally reduces the computational costs in nonlinear vibration damping analysis of sandwich shell structure. Finally, parametric study is conducted to show the effect of small/ large displacement, electric field intensities and core thickness ratios on damping behavior of the ER based sandwich shell structures for different boundary conditions.

6.2 Finite Element Modeling of Constrained ER Fluid Sandwich Shell Structure

Nonlinear vibration analysis of shell structures using finite element method is computationally expensive particularly for sandwich shell structures in which number of degree of freedom and integrations increases. Therefore, an efficient element is required for discretizing the shell structure in which less number of element and degrees of freedom are required. Ashwel and Sabir [124] presented a four-node shell element with 20 degrees of freedom (5 degrees of freedom per node) based on assumed strain functions. This element includes higher order displacement field without additional nodes [123]. Compared with the conventional ordinary and high-order elements, this element has shown a superior convergence using less number of elements [123, 124]. In this chapter, this element (shown in Figure 6.1) has been used to develop the finite element modeling of the sandwich shell structure. Considering the degrees of freedom associated with the top and bottom elastic layers in the three-layer sandwich structure, the element consists of 40 degrees of freedom.

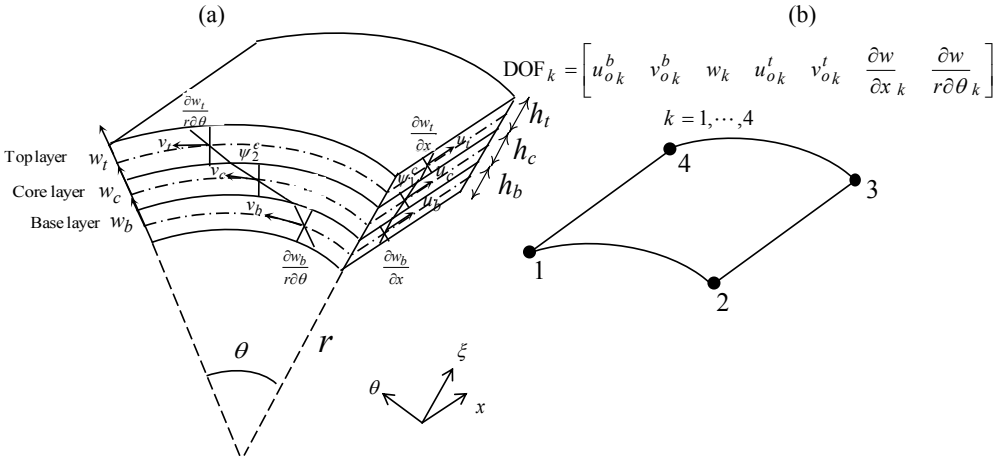

$$\text{DOF}_k = \begin{bmatrix} u^b_{ok} & v^b_{ok} & w_k & u^t_{ok} & v^t_{ok} & \dfrac{\partial w}{\partial x_k} & \dfrac{\partial w}{r\partial\theta_k} \end{bmatrix}$$

Figure 6.1 (a): Sandwich panel demonstrating displacement fields at each layer, (b) Shell element to model the panel

It should be noted that by applying boundary conditions at interfaces, degrees of freedom associated with the core layer can be obtained using those at top and bottom elastic layers as will be discussed later. If the deflection is considered to be constant through the thickness of the sandwich shell, then the total number of degrees of freedom can be reduced to 28. The displacement through the top and bottom elastic layers can be obtained using the assumed strain function based on considering rigid body motion and the compatibility equations [123, 124] as written in the following for the bottom layer:

$$\begin{aligned}
u^b_o &= \frac{1}{2}a_2 r\theta^2 + a_4 + a_6 r\theta + a_7 x + a_8 r\theta x - \frac{1}{2}a_{10} r^2\theta^2 + \frac{1}{2}a_{11} r\theta - \frac{1}{24}a_{17} r^3\theta^4 \\
&- \frac{1}{120}a_{19} r^4\theta^5 - \frac{1}{12}a_{20} r^2\theta^3 \\
v^b_o &= -a_1\theta - a_2 x\theta - \frac{1}{2}a_3 r\theta^2 + a_5 - a_6 x - \frac{1}{2}a_8 x^2 + a_9 r\theta + a_{10} xr\theta + \frac{1}{2}a_{11} x \\
&+ \frac{1}{6}a_{16} r^2\theta^3 + \frac{1}{6}a_{17} xr^2\theta^3 + \frac{1}{24}a_{18} r^3\theta^4 + \frac{1}{24}a_{19} xr^3\theta^4 + \frac{1}{4}a_{20} xr\theta^2 \\
w &= a_1 + a_2 x + a_3 r\theta - \frac{1}{2}a_{12} x^2 - \frac{1}{6}a_{13} x^3 - \frac{1}{2}a_{14} x^2 r\theta - \frac{1}{6}a_{15} x^3 r\theta \\
&- \frac{1}{2}a_{16} r^2\theta^2 - \frac{1}{2}a_{17} xr^2\theta^2 - \frac{1}{6}a_{18} r^3\theta^3 - \frac{1}{6}a_{19} xr^3\theta^3 - \frac{1}{2}a_{20} xr\theta
\end{aligned} \tag{6.1}$$

where r is the radius of the cylindrical shell element, u_o^b and v_o^b are, respectively, in-plane translations at the middle plane in axial (x) and circumferential (θ) directions of the bottom layer. w is transverse displacement which is considered to be constant with respect to the thickness coordinates in each layer and the rotations of the normals to the middle plane of the sandwich shell element in axial and circumferential directions are, respectively, denoted by $\partial w/\partial x$ and $\partial w/r\partial\theta$. The coefficients a_1 through a_{20} can be obtained using the 20 nodal displacements in the shell element where each node of the element consists of five degrees of freedom including u_b, v_b, w, $\partial w/\partial x$ and $\partial w/r\partial\theta$. After obtaining these coefficients, the displacement fields can be represented by the shape functions and the nodal displacement vector as:

$$u_o^b = N_u Q_b \quad v_o^b = N_v Q_b \quad w = N_w Q_b \tag{6.2}$$

in which N_u, N_v and N_w are row vectors of the shape functions depending on the axial and circumferential coordinates and Q_b is a column vector of the nodal displacements in the bottom layer given as:

$$Q_b^{\mathrm{T}} = \left[u_{o1}^b \quad v_{o1}^b \quad w_1 \quad \frac{\partial w}{\partial x}_1 \quad \frac{\partial w}{r\partial\theta}_1 \quad \cdots \quad u_{o4}^b \quad v_{o4}^b \quad w_4 \quad \frac{\partial w}{\partial x}_4 \quad \frac{\partial w}{r\partial\theta}_4 \right]_{1\times 20} \tag{6.3}$$

where T denotes vector transpose. Similarly, the displacement at the top layer can be represented using the same shape function and following nodal displacement vector as:

$$Q_t^{\mathrm{T}} = \left[u_{o1}^t \quad v_{o1}^t \quad w_1 \quad \frac{\partial w}{\partial x}_1 \quad \frac{\partial w}{r\partial\theta}_1 \quad \cdots \quad u_{o4}^t \quad v_{o4}^t \quad w_4 \quad \frac{\partial w}{\partial x}_4 \quad \frac{\partial w}{r\partial\theta}_4 \right]_{1\times 20} \tag{6.4}$$

Considering the element nodal displacement vector, Q, consists of all independent degrees of freedom in the sandwich shell element, the displacement fields at the top and bottom layers can be described as:

$$u_o^b = N_u^b Q \quad v_o^b = N_v^b Q \quad w = N_w Q \quad u_o^t = N_u^t Q \quad v_o^t = N_v^t Q \tag{6.5}$$

where the element nodal displacement vector, Q is written as:

$$Q^{\mathrm{T}} = \Big[u_{o1}^b \quad v_{o1}^b \quad w_1 \quad u_{o1}^t \quad v_{o1}^t \quad \frac{\partial w}{\partial x_1} \quad \frac{\partial w}{r\partial\theta_1} \quad \cdots \quad u_{o4}^b \quad v_{o4}^b \quad w_4 \quad u_{o4}^t \quad v_{o4}^t \quad \frac{\partial w}{\partial x_4} \quad \frac{\partial w}{r\partial\theta_4} \Big]_{1\times 28} \tag{6.6}$$

and N_u^b, N_v^b, N_w, N_v^t, and N_u^t are row vectors of the element shape functions which can be written as:

$$\begin{aligned}
N_u^b &= \Big[\overset{1,3}{N_u} \quad 0 \quad 0 \quad \overset{4,5}{N_u} \quad \overset{6,8}{N_u} \quad 0 \quad 0 \quad \overset{9,10}{N_u} \quad \overset{11,13}{N_u} \quad 0 \quad 0 \quad \overset{14,15}{N_u} \quad \overset{16,18}{N_u} \quad 0 \quad 0 \quad \overset{19,20}{N_u} \Big]_{1\times 28} \\
N_v^b &= \Big[\overset{1,3}{N_v} \quad 0 \quad 0 \quad \overset{4,5}{N_v} \quad \overset{6,8}{N_v} \quad 0 \quad 0 \quad \overset{9,10}{N_v} \quad \overset{11,13}{N_v} \quad 0 \quad 0 \quad \overset{14,15}{N_v} \quad \overset{16,18}{N_v} \quad 0 \quad 0 \quad \overset{19,20}{N_v} \Big]_{1\times 28} \\
N_w &= \Big[\overset{1,3}{N_w} \quad 0 \quad 0 \quad \overset{4,5}{N_w} \quad \overset{6,8}{N_w} \quad 0 \quad 0 \quad \overset{9,10}{N_w} \quad \overset{11,13}{N_w} \quad 0 \quad 0 \quad \overset{14,15}{N_w} \quad \overset{16,18}{N_w} \quad 0 \quad 0 \quad \overset{19,20}{N_w} \Big]_{1\times 28} \\
N_u^t &= \Big[0 \quad 0 \quad \overset{3}{N_u} \quad \overset{1,2}{N_u} \quad \overset{4,5}{N_u} \quad 0 \quad 0 \quad \overset{8}{N_u} \quad \overset{6,7}{N_u} \quad \overset{9,10}{N_u} \quad 0 \quad 0 \quad \overset{13}{N_u} \quad \overset{11,12}{N_u} \quad \overset{14,15}{N_u} \quad 0 \quad 0 \quad \overset{18}{N_u} \quad \overset{16,17}{N_u} \quad \overset{19,20}{N_u} \Big]_{1\times 28} \\
N_v^t &= \Big[0 \quad 0 \quad \overset{3}{N_v} \quad \overset{1,2}{N_v} \quad \overset{4,5}{N_v} \quad 0 \quad 0 \quad \overset{8}{N_v} \quad \overset{6,7}{N_v} \quad \overset{9,10}{N_v} \quad 0 \quad 0 \quad \overset{13}{N_v} \quad \overset{11,12}{N_v} \quad \overset{14,15}{N_v} \quad 0 \quad 0 \quad \overset{18}{N_v} \quad \overset{16,17}{N_v} \quad \overset{19,20}{N_v} \Big]_{1\times 28}
\end{aligned} \tag{6.7}$$

in which $\overset{j}{N_d}$ is the jth component of the vector N_d (d=u,v and w) and $\overset{i,j}{N_d}$ are the ith through jth components of vector N_d. Now, based on the classical shell theory, the displacements through the thickness of the top and bottom layers can be written as:

$$\begin{aligned}
u_t(x,\theta,\xi_1,t) &= u_o^t(x,\theta,t) - \xi_1 \frac{\partial w(x,\theta,t)}{\partial x} \\
v_t(x,\theta,\xi_1,t) &= v_o^t(x,\theta,t) - \xi_1 \frac{\partial w(x,\theta,t)}{r\partial\theta} \qquad -\frac{h_t}{2} < \xi_1 < \frac{h_t}{2} \\
w_t &= w(x,\theta,t)
\end{aligned} \tag{6.8}$$

$$
\begin{aligned}
u_b(x,\theta,\xi_2,t) &= u_o^b(x,\theta,t) - \xi_2 \frac{\partial w(x,\theta,t)}{\partial x} \\
v_b(x,\theta,\xi_2,t) &= v_o^b(x,\theta,t) - \xi_2 \frac{\partial w(x,\theta,t)}{r\partial\theta} \qquad -\frac{h_b}{2} < \xi_2 < \frac{h_b}{2} \\
w_b &= w(x,\theta,t)
\end{aligned} \tag{6.9}
$$

Using FSDT, the displacement field in the core layer can be also expressed as:

$$
\begin{aligned}
u_c(x,\theta,\xi_3,t) &= u_o^c(x,\theta,t) + \xi_3 \psi_1^c(x,\theta,t) \\
v_c(x,\theta,\xi_3,t) &= v_o^c(x,\theta,t) + \xi_3 \psi_2^c(x,\theta,t) \qquad -\frac{h_c}{2} < \xi_3 < \frac{h_c}{2} \\
w_c &= w(x,\theta,t)
\end{aligned} \tag{6.10}
$$

in which u_o^c and v_o^c are, respectively, in-plane translations at the middle plane of the core layer in axial and circumferential directions, h_t, h_b and h_c are the thicknesses of top, bottom and core layers, ψ_1^c and ψ_2^c are, respectively, the rotations of the normals to the middle plane of the core layer in axial and circumferential directions, and ξ_i (i= 1,2 and 3) are the coordinates in thickness direction at the middle of each layer. According to the boundary conditions for perfect bonding, the in-plane and transverse displacements are continuous at the interfaces. Therefore the in-plane displacements and rotations in the core layer can be described with respect to those in top and bottle layers as:

$$
\begin{aligned}
u_o^c &= \frac{u_o^t + u_o^b}{2} + \frac{h_t \dfrac{\partial w}{\partial x} - h_b \dfrac{\partial w}{\partial x}}{4} \\
v_o^c &= \frac{v_o^t + v_o^b}{2} + \frac{h_t \dfrac{\partial w}{r\partial\theta} - h_b \dfrac{\partial w}{r\partial\theta}}{4} \\
\psi_1^c &= \frac{u_o^t - u_o^b}{h_c} + \frac{h_t \dfrac{\partial w}{\partial x} + h_b \dfrac{\partial w}{\partial x}}{2h_c} \\
\psi_2^c &= \frac{v_o^t - v_o^b}{h_c} + \frac{h_t \dfrac{\partial w}{r\partial\theta} + h_b \dfrac{\partial w}{r\partial\theta}}{2h_c}
\end{aligned} \tag{6.11}
$$

Lagrange's equation has been used here to establish the governing equations of motion:

$$\frac{\mathrm{d}}{\mathrm{d}t}\left(\frac{\partial T}{\partial \dot{Q}_k}\right)-\left(\frac{\partial T}{\partial Q_k}\right)+\left(\frac{\partial U}{\partial Q_k}\right)=F_k \quad k=1,\cdots,n \tag{6.12}$$

where n is the total DOF in the sandwich panel structure, Q and F are the nodal displacements and applied external force, respectively and T and U are respectively the kinetic and potential energies in the sandwich shell structure. The kinetic and potential energies are obtained in each layer using the following equations:

$$T_i=\int_{-\frac{h_i}{2}}^{\frac{h_i}{2}}\int_0^{\theta_0}\int_0^{l_0}\frac{1}{2}\rho_i\left(\dot{u}_i{}^2+\dot{v}_i{}^2+\dot{w}_i{}^2\right)\mathrm{d}V_i \tag{6.13}$$

$$U_i=\int_{-\frac{h_i}{2}}^{\frac{h_i}{2}}\int_0^{\theta_0}\int_0^{l_0}\frac{1}{2}\left(\sigma_{xx}^i\,\varepsilon_{xx}^i+\sigma_{\theta\theta}^i\,\varepsilon_{\theta\theta}^i+\sigma_{\xi_i\xi_i}^i\,\varepsilon_{\xi_i\xi_i}^i+\tau_{x\theta}^i\,\gamma_{x\theta}^i+\tau_{\xi_i x}^i\,\gamma_{\xi_i x}^i+\tau_{\xi_i\theta}^i\,\gamma_{\xi_i\theta}^i\right)\mathrm{d}V_i \tag{16.14}$$

where i=t, b and c, respectively, represent the top, bottom and core layers, $\mathrm{d}V_i$ =$r\mathrm{d}\theta\mathrm{d}x\,\mathrm{d}\xi_i$ and $(\xi_t,\xi_b,\xi_c)=(\xi_1,\xi_2,\xi_3)$ are, respectively, thickness coordinates at top, bottom and core layers. Also l_0 and θ_0 respectively represent the length and the angle of the panel element. σ and τ are normal and shear stress, ε and γ are normal and shear strain. x, θ and ξ_i are the coordinates in axial, circumferential and transverse directions, respectively. It should be noted that in Eq. (6.14) the energy terms related to the in-plane and normal stresses of the core layer, i.e. $\tau_{x\theta}^c,\sigma_{\theta\theta}^c$ and σ_{xx}^c are neglected due to the much small modulus in the core layer compared to that in elastic faces in which the in-plane shear and normal stresses are carried. The nonlinear strain-displacement relation using non-

linear Green's Strain Tensor which is based on small strain and moderate rotation for a cylindrical shell element can be expressed as follows:

$$\varepsilon_{xx}^{i}=\left(\frac{\partial u_i}{\partial x}+\frac{1}{2}\left(\frac{\partial w}{\partial x}\right)^2\right)\qquad \varepsilon_{\theta\theta}^{i}=\left(\frac{\partial v_i}{r\partial\theta}+\frac{w}{r}+\frac{1}{2}\left(\frac{\partial w}{r\partial\theta}\right)^2\right)$$
$$\gamma_{x\theta}^{i}=\left(\frac{\partial v_i}{\partial x}\right)+\left(\frac{\partial u_i}{r\partial\theta}\right)+\frac{\partial w}{r\partial\theta}\frac{\partial w}{\partial x}\qquad \gamma_{\xi_i x}^{i}=\frac{\partial u_i}{\partial\xi_i}+\frac{\partial w}{\partial x}\qquad \gamma_{\xi_i\theta}^{i}=\frac{\partial v_i}{\partial\xi_i}+\left(\frac{\partial w}{r\partial\theta}-\frac{v_i}{r}\right) \tag{6.15}$$

The following constitutive equations give the relation between stress and strain components at the top and bottom elastic layers as follows:

$$\sigma_{xx}^{i}=\frac{E_i}{\left(1-\upsilon_i{}^2\right)}\left[\varepsilon_{xx}^{i}+\upsilon_i\varepsilon_{\theta\theta}^{i}\right]\quad \sigma_{\theta\theta}^{i}=\frac{E_i}{\left(1-\upsilon_i{}^2\right)}\left[\varepsilon_{\theta\theta}^{i}+\upsilon_i\varepsilon_{xx}^{i}\right]$$
$$\tau_{x\theta}^{i}=\frac{E_i}{2\left(1+\upsilon_i\right)}\gamma_{x\theta}^{i}\quad \tau_{\xi_i x}^{i}=\frac{E_i}{2\left(1+\upsilon_i\right)}\gamma_{\xi_i x}^{i}\quad \tau_{\xi_i\theta}^{i}=\frac{E_i}{2\left(1+\upsilon_i\right)}\gamma_{\xi_i\theta}^{i} \tag{6.16}$$

where i=t, b, and also E and υ are respectively the Young's modulus and Poisson's ratio . For the core layer, the constitutive equation will be described in the next section. In order to define the stiffness matrix, the strain components in Eq. (6.15) are rewritten in terms of the shape functions and element nodal displacement vector using Eq. (6.5) as:

$$\varepsilon_{xx}^{i}=\left(\frac{\partial N_u^i}{\partial x}-\xi_i\frac{\partial^2 N_w}{\partial x^2}\right)Q+\frac{1}{2}\left(\frac{\partial N_w}{\partial x}Q\right)\left(\frac{\partial N_w}{\partial x}Q\right)=N_1^iQ+\frac{1}{2}\left(N_2Q\right)\left(N_2Q\right)$$
$$\varepsilon_{\theta\theta}^{i}=\left(\frac{\partial N_v^i}{r\partial\theta}-\xi_i\frac{\partial^2 N_w}{r^2\partial\theta^2}+\frac{N_w}{r}\right)Q+\frac{1}{2}\left(\frac{\partial N_w}{r\partial\theta}Q\right)\left(\frac{\partial N_w}{r\partial\theta}Q\right)=N_3^iQ+\frac{1}{2}\left(N_4Q\right)\left(N_4Q\right) \tag{6.17}$$
$$\gamma_{x\theta}^{i}=\left(\frac{\partial N_v^i}{\partial x}-2\xi_i\frac{\partial^2 N_w}{r\partial x\partial\theta}+\frac{\partial N_u^i}{r\partial\theta}\right)Q+\left(\frac{\partial N_w}{r\partial\theta}Q\right)\left(\frac{\partial N_w}{\partial x}Q\right)=N_5^iQ+\left(N_4Q\right)\left(N_2Q\right)$$

$$\gamma^c_{\xi_3 x} = \psi^c_1 + \frac{\partial w_c}{\partial x} = \left(\frac{N^t_u - N^b_u}{h_c} + \frac{h_t \dfrac{\partial N_w}{\partial x} + h_b \dfrac{\partial N_w}{\partial x}}{2h_c} + \frac{\partial N_w}{\partial x} \right) Q = N^c_6 Q$$

$$\gamma^c_{\xi_3 \theta} = \psi^c_2 + \frac{\partial w_c}{r\partial \theta} = \left(\frac{N^t_v - N^b_v}{h_c} + \frac{h_t \dfrac{\partial N_w}{r\partial \theta} + h_b \dfrac{\partial N_w}{r\partial \theta}}{2h_c} + \frac{\partial N_w}{r\partial \theta} \right) Q = N^c_7 Q$$

$$\gamma^i_{\xi_i x} = 0 \qquad i = t, b$$

$$\gamma^i_{\xi_i \theta} = 0 \qquad i = t, b$$

where N_1 through N_7 are written as:

$$N^i_1 = \frac{\partial N^i_u}{\partial x} - \xi_i \frac{\partial^2 N_w}{\partial x^2} \quad N^i_2 = \frac{\partial N_w}{\partial x} \quad N^i_3 = \frac{\partial N^i_v}{r\partial \theta} - \xi_i \frac{\partial^2 N_w}{r^2 \partial \theta^2} + \frac{N_w}{r} \quad N^i_4 = \frac{\partial N_w}{r\partial \theta}$$

$$N^i_5 = \frac{\partial N^i_v}{\partial x} - 2\xi_i \frac{\partial^2 N_w}{r\partial x \partial \theta} + \frac{\partial N^i_u}{r\partial \theta} \quad N^c_6 = \frac{N^t_u - N^b_u}{h_c} + \frac{h_t \dfrac{\partial N_w}{\partial x} + h_b \dfrac{\partial N_w}{\partial x}}{2h_c} + \frac{\partial N_w}{\partial x} \tag{6.18}$$

$$N^c_7 = \frac{N^t_v - N^b_v}{h_c} + \frac{h_t \dfrac{\partial N_w}{r\partial \theta} + h_b \dfrac{\partial N_w}{r\partial \theta}}{2h_c} + \frac{\partial N_w}{r\partial \theta}$$

Eqs (6.16) and (6.17) are now substituted into Eq. (6.14) in order to obtain the strain energy in the sandwich shell element. It should be noted that the energy terms associated with transverse shear strains at the elastic top and bottom layers are zero (according to the classical shell theories). Also the kinetic energy can be found using the displacement fields given in Eqs (6.8)-(6.11) substituted in Eq. (6.13). The obtained kinetic and strain energies in Eqs (6.13) and (6.14) are then substituted into Lagrange's equation given in Eq. (6.12) to establish stiffness and mass matrices of the sandwich shell structure. These matrices are obtained by summing the stiffness matrices of different layers. In the following, the stiffness matrices associated with the top and bottom elastic layers are formulated which includes the constant, linear and quadratic displacement dependent stiffness matrices. The stiffness matrix of the ER-fluid core layer is a nonlinear matrix

depending on the displacement due to the amplitude dependent dynamic properties of ER-fluid material which is presented in the next section. It should be noted that the mass matrix of the sandwich shell structure is independent of the displacement.

After substituting the energy terms into the Lagrange equation, the nonlinear equations of motion is directly obtained in the B-notation form as:

$$\mathbf{M}\ddot{Q} + \mathbf{K}_0 Q + \mathbf{K}_1(Q)Q + \mathbf{K}_2(Q)Q + \mathbf{K}_c(Q,E,\omega)Q = \mathbf{F} \tag{6.19}$$

where $\mathbf{M}$ is the mass matrix and $\mathbf{K}_c$ is a nonlinear complex stiffness matrix of the core layer given in the next section. As shown in the following $\mathbf{K}_0$ is a symmetric matrix independent of displacement, $\mathbf{K}_1$ is asymmetric matrix linearly depends on the displacement and $\mathbf{K}_2$ is asymmetric matrix quadratically depends on the displacement. These are given in the following as:

$$\mathbf{K}_0 = \sum_{i=t,b} \frac{E_i}{(1-\upsilon_i^2)} \int_{-\frac{h_i}{2}}^{\frac{h_i}{2}} \int_0^{\theta_0} \int_0^{l_0} \left(N_1^{i\mathrm{T}} N_1^i + N_3^{i\mathrm{T}} N_3^i + \upsilon_i N_1^{i\mathrm{T}} N_3^i + \upsilon_i N_3^{i\mathrm{T}} N_1^i + \frac{1-\upsilon_i}{2} N_5^{i\mathrm{T}} N_5^i \right) \mathrm{d}V_i \tag{6.20}$$

$$\begin{aligned} \mathbf{K}_1(Q) = \sum_{i=t,b} \frac{E_i}{(1-\upsilon_i^2)} \int_{-\frac{h_i}{2}}^{\frac{h_i}{2}} \int_0^{\theta_0} \int_0^{l_0} \Bigg(& \left(\frac{1}{2} N_1^{i\mathrm{T}} N_2 + N_2^{\mathrm{T}} N_1^i + \frac{\upsilon_i}{2} N_3^{i\mathrm{T}} N_2 + \frac{1-\upsilon_i}{2} N_4^{\mathrm{T}} N_5^i + \upsilon_i N_2^{\mathrm{T}} N_3^i \right) (N_2 Q) \\ & + \left(\frac{1}{2} N_3^{i\mathrm{T}} N_4 + N_4^{\mathrm{T}} N_3^i + \frac{\upsilon_i}{2} N_1^{i\mathrm{T}} N_4 + \upsilon_i N_4^{\mathrm{T}} N_1^i + \frac{1-\upsilon_i}{2} \left(N_2^{\mathrm{T}} N_5^i + N_5^{i\mathrm{T}} N_2 \right) (N_4 Q) \right) \Bigg) \mathrm{d}V_i \end{aligned} \tag{6.21}$$

$$\begin{aligned} \mathbf{K}_2(Q) = \sum_{i=t,b} \frac{E_i}{(1-\upsilon_i^2)} \int_{-\frac{h_i}{2}}^{\frac{h_i}{2}} \int_0^{\theta_0} \int_0^{l_0} \Bigg(& \frac{1}{2} (N_2 Q) \left(N_2^{\mathrm{T}} N_2 + \upsilon_i \left(N_2^{\mathrm{T}} N_4 + N_4^{\mathrm{T}} N_2 \right) \right) (N_2 Q) \\ & + \frac{1-\upsilon_i}{2} (N_2 Q) N_4^{\mathrm{T}} N_2 (N_4 Q) + \frac{1}{2} (N_4 Q) \left((1-\upsilon_i) N_2^{\mathrm{T}} N_2 + N_4^{\mathrm{T}} N_2 \right) (N_4 Q) \Bigg) \mathrm{d}V_i \end{aligned} \tag{6.22}$$

The abovementioned displacement dependent matrices are found in B-Notations in which the nonlinear stiffness matrices are asymmetric. If the derivation is performed carefully, then a symmetric form can be obtained for the nonlinear stiffness matrices. One can observe that $\mathbf{K}_1$ and $\mathbf{K}_2$ are multiplied by nodal displacement vector Q in Eq. (6.19). Considering this and also using this fact that $N_k^i Q$ (k =1, 2..., 5) is scalar, Eqs (6.21) and (6.22) can be manipulated to find a symmetric form of the displacement dependent matrices. Consequently, Eq. (6.19) can be rewritten in the following form known as N-notation:

$$\mathbf{M}\ddot{Q} + \mathbf{K}_0 Q + \frac{1}{2}\mathbf{KN}_1(Q)Q + \frac{1}{3}\mathbf{KN}_2(Q)Q + \mathbf{K}_c(Q,E,\omega)Q = \mathbf{F} \tag{6.23}$$

where

$$\begin{aligned}\mathbf{KN}_1(Q) = \sum_{i=t,b}\frac{E_i}{(1-\upsilon_i{}^2)}\int_{-\frac{h_i}{2}}^{\frac{h_i}{2}}\int_0^{\theta_0}\int_0^{l_0}\Bigg(\Bigg(N_1^{i\mathrm{T}}N_2 + N_2^{\mathrm{T}}N_1^i + \upsilon_i\left(N_3^{i\mathrm{T}}N_2 + N_2^{\mathrm{T}}N_3^i\right)\Bigg)(N_2Q)\\ + \frac{1-\upsilon_i}{2}\left(N_4^{\mathrm{T}}N_5^i + N_5^{i\mathrm{T}}N_4\right)(N_2Q) + \left(N_3^{i\mathrm{T}}N_4 + N_4^{\mathrm{T}}N_3^i\right)(N_4Q)\\ + \left(\upsilon_i\left(N_1^{i\mathrm{T}}N_4 + N_4^{\mathrm{T}}N_1^i\right) + \frac{1-\upsilon_i}{2}\left(N_2^{\mathrm{T}}N_5^i + N_5^{i\mathrm{T}}N_2\right)\right)(N_4Q) + \left(N_2^{\mathrm{T}}N_2 + \upsilon_i N_4^{\mathrm{T}}N_4\right)(N_1^iQ)\\ + \left(N_4^{\mathrm{T}}N_4 + \upsilon_i N_2^{\mathrm{T}}N_2\right)(N_3^iQ) + \frac{1-\upsilon_i}{2}\left(N_2^{\mathrm{T}}N_4 + N_4^{\mathrm{T}}N_2\right)(N_5^iQ)\Bigg)\mathrm{d}V_i\end{aligned} \tag{6.24}$$

$$\begin{aligned}\mathbf{KN}_2(Q) = \sum_{i=t,b}\frac{E_i}{(1-\upsilon_i{}^2)}\int_{-\frac{h_i}{2}}^{\frac{h_i}{2}}\int_0^{\theta_0}\int_0^{l_0}\Bigg((N_2Q)\left(\frac{3}{2}N_2^{\mathrm{T}}N_2 + \frac{3}{2}N_4^{\mathrm{T}}N_4\right)(N_2Q)\\ + (N_4Q)\left(\frac{3}{2}N_4^{\mathrm{T}}N_4 + \frac{3}{2}N_2^{\mathrm{T}}N_2\right)(N_4Q)\Bigg)\mathrm{d}V_i\end{aligned} \tag{6.25}$$

The main problem in nonlinear vibration analysis using the abovementioned notations is the time-consuming integrations which should be performed for several times in the direct iteration method. Here, a new approach is presented to obtain the nonlinear

stiffness matrices once and use it throughout the iteration procedure. The main idea is to remove the vector Q in the nonlinear stiffness matrices $\mathbf{KN}_1$ and $\mathbf{KN}_2$. According to Eq. (6.24), one can observe that matrix $\mathbf{KN}_1$ includes the scalar terms in the form of $N_k^i Q$ which are pre-multiplied by a matrix in the form of $\mathbf{A}_{n\times n} = N_{k_1}^i N_{k_2}^i$. This can be represented in the following form:

$$\mathbf{B}_{n\times n} = \left(N_{k_1}^i N_{k_2}^i \right)\left(N_k^i Q\right) = \mathbf{A}\mathbf{I}_k \tag{6.26}$$

where $\mathbf{I}_k$ is a diagonal matrix with the size of $n\times n$ in which all the components on the main diagonal are equal to $N_k^i Q$. Also, n represents the number of degrees of freedom in an element which is 28 as discussed before. $\mathbf{I}_k$ can be written in the following form:

$$\mathbf{I}_k = \mathbf{Z}_k \mathbf{X} \tag{6.27}$$

where

$$\mathbf{Z}_k = \begin{bmatrix} N_k^i & 0_{1\times n} & 0_{1\times n} & 0_{1\times n} & \cdots & 0_{1\times n} \\ 0_{1\times n} & N_k^i & 0_{1\times n} & 0_{1\times n} & \cdots & 0_{1\times n} \\ 0_{1\times n} & 0_{1\times n} & N_k^i & 0_{1\times n} & \cdots & 0_{1\times n} \\ \vdots & \vdots & \vdots & \vdots & \vdots & \vdots \\ 0_{1\times n} & 0_{1\times n} & 0_{1\times n} & 0_{1\times n} & \cdots & N_k^i \end{bmatrix}_{n\times n^2}$$

$$\mathbf{X} = \begin{bmatrix} Q_{n\times 1} & 0_{n\times 1} & 0_{n\times 1} & \cdots & 0_{n\times 1} \\ 0_{n\times 1} & Q_{n\times 1} & 0_{n\times 1} & \cdots & 0_{n\times 1} \\ 0_{n\times 1} & 0_{n\times 1} & Q_{n\times 1} & \cdots & 0_{n\times 1} \\ 0_{n\times 1} & 0_{n\times 1} & 0_{n\times 1} & \cdots & 0_{n\times 1} \\ \vdots & \vdots & \vdots & \vdots & \vdots \\ 0_{n\times 1} & 0_{n\times 1} & 0_{n\times 1} & \cdots & Q_{n\times 1} \end{bmatrix}_{n^2\times n} \tag{6.28}$$

in which $0_{1\times n}$ is a row null vector, $0_{n\times 1}$ is a column null vector, $Q_{n\times 1}$ is the column nodal displacement vector and N_k^i is row vectors of the element shape functions given in

Eq. (6.18). $\mathbf{Z}_{n\times n^2}$ is multiplied by the matrix $\mathbf{A}_{n\times n}$ and consequently the nodal displacement vector included in matrix $\mathbf{X}_{n\times n^2}$ is separated in Eq. (6.26). The integration is now required to be performed only once over the matrix $\mathbf{AZ}_k$ with the size of $n\times n^2$ in the nonlinear matrix $\mathbf{KN}_1$. Similar formulations can be developed for $\mathbf{KN}_2$. This matrix includes the terms in the following form:

$$\mathbf{C}_{n\times n}=\left(N_{k_3}Q\right)\left(N_{k_1}N_{k_2}\right)\left(N_{k_4}Q\right)=\left(Q^{\mathrm{T}}N_{k_3}^{\mathrm{T}}\right)\left(N_{k_1}N_{k_2}\right)\left(\left(N_{k_4}Q\right)\right)=\mathbf{I}_{k_3}^{\mathrm{T}}\mathbf{A}\mathbf{I}_{k_4} \tag{6.29}$$

where

$$\begin{aligned}\mathbf{I}_{k3}&=\mathbf{Z}_{k_3}\mathbf{X}\\ \mathbf{I}_{k4}&=\mathbf{Z}_{k_4}\mathbf{X}\end{aligned} \tag{6.30}$$

in which $\mathbf{Z}_{k_3}$ and $\mathbf{Z}_{k_4}$ are the matrices with the size $n\times n^2$ which can be obtained by replacing the index k with k_3 and k_4 in Eq. (6.28), respectively. The integration is required now to be performed only once over the $\mathbf{Z}_{k3}^{\mathrm{T}}\mathbf{AZ}_{k4}$ with the size of $n^2\times n^2$ in the nonlinear matrix $\mathbf{KN}_2$. It should be noted that in these relations the k, k_1, k_2, k_3 and k_4 are integer numbers ranging from 1 to 5. Now the nonlinear equations of motion can be rewritten in the following form referred here to as H-notation:

$$\mathbf{M}\ddot{Q}+\left(\mathbf{K}_0+\frac{1}{2}\mathbf{H}_1\mathbf{X}(Q)+\frac{1}{3}\mathbf{X}(Q)^{\mathrm{T}}\mathbf{H}_2\mathbf{X}(Q)+\mathbf{K}_c(Q,e,\omega)\right)Q=\mathbf{F} \tag{6.31}$$

where $\mathbf{H}_1$ is the matrix with the size $n\times n^2$ established by summing the multiplications of $\mathbf{A}=N_{k_1}^i N_{k_2}^i$ and $\mathbf{Z}_k$ for different k, k_1 and k_2 at top and bottom layers. $\mathbf{H}_2$ is the matrix with the size $n^2\times n^2$ established by summing the multiplication of $\mathbf{Z}_{k3}^{\mathrm{T}}\mathbf{AZ}_{k4}$ for different k, k_1, k_2, k_3 and k_4. The matrix $\mathbf{X}$ including the nodal displacement vector is then substituted into Eq. (6.31) while the integration has already been performed. This

technique significantly reduces the computational costs particularly for nonlinear vibration analysis of sandwich structures. The only drawback of this method might be the computation of the large matrix $\mathbf{H}_2$. Compared with the computational time required to perform the integrations for several times using B-notation (Eq. (6.19)) or N-notation (Eq. (6.23)), the H-notation (Eq. (6.31)) is much more efficient.

6.3 Material Properties of ER Fluid and Evaluating the Stiffness Matrix of the ER Fluid Core Layer

In order to calculate the stiffness matrix $\mathbf{K}_c$, the material properties of the core layer should be determined. The dynamic mechanical properties of the ER-fluid layer have been experimentally obtained as explained in chapter 5. The experiment was carried out using Bose ElectroForce 3200 device. The ER fluid was prepared by dispersing cornstarch into corn oil with viscosity of 40 mPa s. The weight fraction of the particles was considered to be 30 %. Based on the Fourier transform technique, the timed data of the measured force and the input displacement were analyzed by the dynamic mechanical analysis (DMA) software. The dynamic material properties of the ER fluid have been explored for frequency range of 0.1 Hz to 60 Hz and for the shear strain amplitudes ranging from 0.1538 % to 7.69 %. A constitutive model has been proposed to predict the experimental data including storage/loss modulus and stress response. Here, this model has been briefly explained as it will be used to develop the stiffness matrix of the ER-core layer required for the finite element model of the ER based sandwich structure discussed in section 6.2.

For free nonlinear vibration analysis of the sandwich structure with constrained core layer, the mechanical properties under large amplitude oscillatory shear strain is desired.

As shown in Eq. (1.3), the stress response of ER fluids under large amplitude depends on many variables including amplitude, frequency and field intensity. Too many terms and coefficients in Fourier transform relation should be determined to accurately express the stress response in the time domain. Besides, appropriate functions should be assigned to the coefficients G'_{2n+1} and G''_{2n+1} to incorporate the main variables in the stress response. Therefore, evaluating the stress response based on Fourier transform could be mathematically very complicated. In this study, the Bingham-Hooke model which was used by Laun et al. [74] has been modified to represent the hysteresis loop. According to their results, the material properties obtained by the Bingham-Hooke model deviate from the experimental data in the nonlinear regime. Here, considered this model has been considered as the starting point to develop a model predicting the experimental results more accurately. The variable of strain amplitude is included in the developed model to provide more accurate results particularly at the nonlinear regime. Considering this, the following relation has been proposed for the stress response under the oscillatory shear strain:

$$\tau = \begin{cases} \dfrac{\mu(\dot{\gamma} - \dot{\gamma}_R)}{\tilde{\dot{\gamma}}} + (K + \dfrac{D}{\tilde{\dot{\gamma}}})(\gamma - \gamma_R) & \tau\dot{\gamma} > 0 \\ \tilde{\tau}\,\mathrm{sgn}(\tau) + G_0(\gamma - \tilde{\gamma}) + \eta(\dot{\gamma}) & \tau\dot{\gamma} \le 0 \end{cases} \tag{6.32}$$

where η, μ, K, D and G_0 are the model parameters which are generally frequency and electric field dependent. $\tilde{\dot{\gamma}}$ is shear strain rate amplitude ($\tilde{\dot{\gamma}} = \omega\tilde{\gamma}$) and $\tilde{\tau}$ and $\tilde{\gamma}$ are, respectively, the shear stress and strain amplitudes. At the unloading stage where $\tau\dot{\gamma} \le 0$, the material properties are assumed to be linear viscoelastic. For providing continuity in the hysteresis loop, $\tilde{\tau}\,\mathrm{sgn}(\tau)$ and $\tilde{\gamma}$ (in bottom line of Eq. (6.32)) and also shear strain γ_R and shear strain rate $\dot{\gamma}_R$ at τ=0 (in top line of Eq. (6.32)) are included in the model. In the

nonlinear regime where $\tau\dot{\gamma} > 0$, an amplitude dependent relation has been defined for the shear stress response which governs the response in the beginning of the loading stage (τ = 0) up to the unloading stage. Therefore, the yielding stress is practically assumed to be negligible in this model. However, as shown in the results in chapter 5, the proposed model is able to show the transition between the linear and nonlinear regimes accurately. Without considering variables $\tilde{\gamma}$ and $\tilde{\dot{\gamma}}$ in top line of Eq. (6.32), the amplitude of shear stress highly increases with increasing shear strain amplitude. Therefore, the rate of increase in the shear stress amplitude has been reduced by dividing the viscous and elastic terms respectively over the strain rate and strain amplitudes. However, an elastic term (with parameter *K*) is added to the stress response in order to maintain the reasonable increase of the stress amplitude with increasing the strain amplitude. The abovementioned parameters are given in Table 5.1. The material properties including the storage and loss modulus, stress-strain amplitude and the stress response in time domain for different frequencies and shear strain amplitudes are also given in chapter 5. As shown in the results good agreement exists between the results by the experiment and the proposed constitutive model. The first order terms then can be obtained using the following equations:

$$G_1'(\omega,e,\bar{\gamma}) = \frac{\omega}{\pi\tilde{\gamma}}\int_T \tau(t,\omega,e,\tilde{\gamma})\sin(\omega t)\mathrm{dt}$$
$$G_2'(\omega,e,\bar{\gamma}) = \frac{\omega}{\pi\tilde{\gamma}}\int_T \tau(t,\omega,e,\tilde{\gamma})\cos(\omega t)\mathrm{dt} \quad (6.33)$$

In nonlinear free vibration damping analysis of the sandwich shell structure, in order to quantify damping the material properties of the ER fluid material can be approximated by different first order complex modulus as shown in Figure 6.2. The loss modulus of the

complex modulus for all cases is G''_2 which leads to identical dissipated energy equal to the dissipated energy resulted by the nonlinear stress response given in Eq. (6.32). However, the slopes of the ellipses are different.

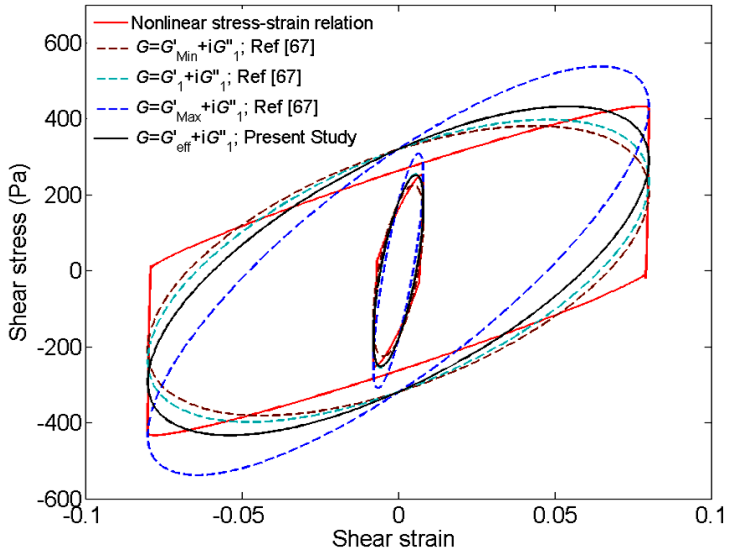

Figure 6.2 Different first order approximation of hysteresis loops versus the nonlinear hysteresis loop, f= 0.1 Hz, e =1.9 KVmm^{-1}

As shown by Ewoldt et al. [67], considering $G'_{\min} = \mathrm{d}\tau/\mathrm{d}\gamma \ \ (\mathrm{at}\,\gamma = 0)$ leads to minimum storage modulus and consequently the maximum shear stress provided by this storage modulus is smaller than that in the nonlinear stress amplitude. Considering the storage modulus as $G'_{\max}=\tau/\gamma \ \ (\mathrm{at}\,\gamma = \tilde{\gamma})$ results in larger amplitude for the stress response. G''_1 can averagely show the stress response in the nonlinear regime however, the stress amplitude is smaller compared to that from the exact nonlinear stress.

Here, a complex modulus has been considered which shows the same dissipated energy as well as the stress amplitude. Employing G''_2 for the loss modulus, the storage modulus is defined in a way that amplitude of the stress response is equal to the amplitude of the nonlinear stress response. Considering this, the effective storage modulus $G'_{\mathrm{eff}} = \sqrt{\tilde{G}^2 - G''^2_1}$ is defined for the storage modulus of the complex modulus in

which $\widetilde{G} = \widetilde{\tau} / \widetilde{\gamma}$ is the amplitude of the complex modulus. The stress response using the effective storage modulus is shown by black solid line in Figure 6.2 for small/large amplitudes and compared to the other first order complex modulus. Compared with the nonlinear response, the complex modulus based on the G'_{eff} can effectively describes the stress response. The effective storage modulus depends on the amplitude, electric field and frequency. Now based on finite element formulation discussed in section 6.2, the stiffness matrix due to the ER fluid core layer is now expressed as follows:

$$\mathbf{K}_c(Q,E,\omega) = \int_{-\frac{h_c}{2}}^{\frac{h_c}{2}} \int_0^{\theta_0} \int_0^{l_0} \left(\left(G'_{\text{eff}} + \text{iG}''_1\right)_{x\xi_3} N_6^{c\,\text{T}} N_6^c + \left(G'_{\text{eff}} + \text{iG}''_1\right)_{\theta\xi_3} N_7^{c\,\text{T}} N_7^c \right) \text{d}V_c \tag{6.34}$$

Since the transverse shear strain components are different in axial and circumferential directions, the complex modulus should be calculated according to shear strain associated with those directions. As shown in the results presented in chapter 5, the frequency dependency in the complex modulus of ER fluid is negligible. Otherwise, an iteration procedure should be performed to evaluate the material properties at the natural frequencies. It should be noted that since shear strain components are linear in von Karman hypothesis, the integrations in Eq. (6.34) can be performed symbolically once in terms of the material properties which can be afterward evaluated by substituting the shear strain amplitude in the complex modulus of the core layer.

6.4 Nonlinear Free Vibration Analysis

Now, for the free vibration analysis, governing equations of motion given in Eq. (6.31) can be written as follows:

$$-\lambda \mathbf{M}\widetilde{Q} + \left(\mathbf{K}_0 + \frac{1}{2}\mathbf{H}_1\mathbf{X}(\widetilde{Q}) + \frac{1}{3}\mathbf{X}(\widetilde{Q})^{\text{T}}\mathbf{H}_2\mathbf{X}(\widetilde{Q}) + \mathbf{K}_c(\widetilde{Q},e,\omega) \right)\widetilde{Q} = 0 \tag{6.35}$$

where $\widetilde{Q}$ is the amplitude of the displacement (eigenvector) and λ is the eigenvalue. Based on the direct iteration method given in Reference [101], the linear eigenvalue problem of Eq. (6.35) is solved by setting the nonlinear terms to zero. Then, the fundamental frequency and the mode shape are calculated using the standard algorithms for extracting the eigenvalue and eigenvector. The mode shape is normalized and scaled up in way that the deflection at the center point of the shell element is proportional to the thickness of shell structure with the desired amplitude. The scaled up eigenvector is then used to calculate the matrix **X** and $\mathbf{K}_{c.}$ After calculating the nonlinear terms in Eq. (6.35), the eigenvalue problem is again solved and the scaled up eigenvector is used to update the nonlinear terms in the eigenvalue problem. The iteration continues until the desired convergence is provided for the frequency in which the two sequential frequencies are very close considering a pre-determined tolerance ($<10^{-4}$). The frequency and loss factor are obtained at each iteration using the real and imaginary parts of the complex eigenvalue. As shown by Rikards [132], for the eigenvalue of $\lambda = \lambda_1 + \mathrm{i}\lambda_2$ the angular frequency is $\omega = \sqrt{\lambda_1}$ and loss factor is $\eta = \lambda_1 / \lambda_2$.

6.5 Results and Discussions

In the following, the developed finite element model has been validated by comparing the results to the experiments and the results available in the literatures. Finally, the parametric studies are presented for the nonlinear vibration damping analysis of sandwich shell structure for different boundary conditions including CCCC (all edges are clamped) SSSS (all edges are simply-supported) CFCF (the two edges in circumferential direction are clamped while the other two edges are free) and SFSF (the two edges in circumferential direction are simply-supported while the other two edges are free).

6.5.1 Validation of the finite element model

The developed approach has been validated in this chapter by comparing the results to those in the literature. Table 6.1 shows the natural frequencies associated to the first two modes of bare cylindrical panel structure for clamped-clamped and simply-supported boundary conditions on the edges. The numbers of elements in axial and circumferential directions are considered here to be 10. It should be noted that the material properties and the dimensions are given in the caption of each table in which L represents the length of the panel or complete cylinders in axial direction and $b=r\theta$ represents the edge length in circumferential direction. Compared to the results presented by Djoudi and Bahai [123], excellent agreement exists between the results since the exact same higher order expansion of displacement fields are considered in axial and circumferential directions. Similar comparison has been provided in Table 6.2 for bare clamped-free complete cylinder in which the results using the developed finite element modeling have been compared with other approach including semi-analytical finite element and analytical methods. One can observe a very good agreement between the results. Also, the damping behavior of sandwich plate structure including loss factor and natural frequency for clamped-free and simply supported boundary conditions resulted from this study have been compared to the results given by Bilasse et al. [137] in Tables 6.3 and 6.4 .

Table 6.1 Comparing the results obtained by the developed approach and those in the literature for linear vibration analysis of bare panel; L=1 m, r = 2 m; h= 0.005 m, θ = 0.5 rad, E =208 $\times 10^9$ N m^{-2}, ρ= 7833 kgm^{-3}; υ= 0.29

Clamped-Clamped	Present study	Ref. [123]	ABAQUS [123]
First Mode	**173.91**	173.61	175.11
Second Mode	**180.5**	180.37	181.6
Simply Supported	Present study	Ref. [123]	ABAQUS [123]
First Mode	**101.22**	100.96	104.28
Second Mode	**127.78**	127.33	135.3

The material and structural loss factors are respectively represented by η_c and η_l. As it can be realized excellent agreement exists between the results obtained by the developed finite element and the analytical methods. Similar comparison between the finite element and semi-analytical finite element methods is shown in Figure 6.3 for vibration damping of the complete sandwich viscoelastic cylinder which shows a very good agreement between the results.

Table 6.2 Comparing the results obtained by the developed approach and those in the literature for linear vibration analysis of clamped-free complete cylinder; L=0.5112 m, r = 0.2162 m; h= 0.0015 m, E =1.83 $\times 10^{11}$ N m^{-2}, ρ=7492 kg m^{-3}, υ=0.29

m	***n***	Present study-FEM	Semi Analytical FEM [138]	Reference [123]	Nastran [125]	Analytical [125]
1	1	**855.5**	857.5	-	-	-
	2	**400.8**	405.6	403.91	410.1	403.72
	3	**221.96**	225.1	224.79	232.2	223.34
	4	**175.2**	174.6	172.4	180.5	171.77
	5	**207.8**	203.6	203.37	206.2	199.16
	6	**279.0**	274.9	274.04	275.5	268.86
	7	**376.2**	369.8	369.8	370.1	361.92
	8	**489.6**	482.5	482.96	483.5	472.54
	9	**618.2**	611.1	611.42	614	599.03
	10	**763.1**	755.4	755.14	—	740
2	2	**1439.8**	1440.5	1446.56	—	1437.11
	3	**922.9**	932.9	940.2	943.2	928.28
	4	**639.1**	649.4	647.25	671.4	644.48
	5	**491.3**	500.0	509.11	529.3	494.69
	6	**443.3**	448.6	442.16	478	442
	7	**470.8**	473.1	477.32	496.9	464.59
	8	**549.1**	550.0	542.69	567.2	539.45
	9	**659.9**	661.2	656.06	673.2	648.34
	10	**793.7**	796.5	788.39	—	781.15
3	2	**2481.1**	2491.3	2530.79	—	2487.6
	3	**1839.7**	1841.5	1876.8	—	1834.82
	4	**1388.0**	1376.1	1412.72	—	1367.64
	5	**1072.1**	1066.3	1103.56	—	1057.12
	6	**878.8**	874.7	875.29	—	864.82
	7	**782.1**	795.97	789.5	—	767.65
	8	**764.1**	763.3	748.35	—	750.67
	9	**808.4**	812.9	809.48	—	798.18
	10	**899.4**	910.8	884.6	—	893.6

Table 6.3 Comparing the results using the developed analysis and those in literature for linear vibration analysis of sandwich SFSF plate; L=0.1778 m, h_i= 0.001524 m, b = 12.7 mm E_i = 6.9 ×10^{10} N m^{-2}, ρ_i= 2766 kg m^{-3}, υ_i= 0.3, h_c= 0.00127 m, E_c = 1794 × 10^3 N m^{-2}, ρ_c= 968.1 kg m^{-3}, υ_c= 0.3

	SFSF Plate – Present study		SFSF Plate – Ref. [137]		Analytical SS beam Ref. [8]	
η_c	f (Hz)	η_i/η_c	f (Hz)	η_i/η_c	f (Hz)	η_i/η_c
0.1	**148.570**	**0.350**	148.56	0.35	148.51	0.3502
	489.06	**0.196**	489.28	0.1954	488.47	0.1958
	1037.48	**0.107**	1038.74	0.1066	1034.69	0.1071
	1803.52	**0.0649**	1807.57	0.0647	1795.13	0.0653
0.6	**151.488**	**0.3328**	150.75	0.3327	150.71	0.3329
	491.144	**0.1941**	490.56	0.194	489.75	0.1944
	1038.69	**0.1066**	1039.43	0.1064	1035.38	0.1069
	1804.27	**0.0649**	1807.99	0.0646	1795.54	0.0652
1	**156.21**	**0.305**	154.47	0.3051	154.42	0.3052
	494.86	**0.192**	492.87	0.1914	492.06	0.1918
	1040.87	**0.106**	1040.69	0.106	1036.63	0.1065
	1805.63	**0.0648**	1808.75	0.0646	1796.3	0.0651
1.5	**163.741**	**0.2626**	160.77	0.2625	160.72	0.2626
	501.823	**0.1868**	497.3	0.1867	496.49	0.1871
	1045.09	**0.1056**	1043.13	0.1054	1039.07	0.1059
	1808.29	**0.0646**	1810.23	0.0644	1797.78	0.065

Table 6.4 Comparing the results using the developed analysis and those in literature for linear vibration analysis of sandwich CFFF plate, material properties are given in the caption of Table 6.3

	CFFF Plate – Present study		CFFF Plate – Ref. [137]		FE method CF beam Ref. [139]	
η_c	f (Hz)	η_i/η_c	f (Hz)	η_i/η_c	f (Hz)	η_i/η_c
0.1	**64.3656**	**0.2810**	64.3	0.281	64.1	0.281
	297.926	**0.2417**	298.1	0.242	296.7	0.242
	748.074	**0.1533**	749	0.153	744.5	0.154
	1403.88	**0.0882**	1406.9	0.088	1395.7	0.089
0.6	**65.9498**	**0.2456**	65.7	0.245	65.5	0.246
	301.118	**0.2316**	300.6	0.232	299.2	0.232
	750.605	**0.1519**	750.7	0.152	746.3	0.153
	1405.31	**0.0879**	1407.8	0.088	1396.6	0.089
1	**68.0419**	**0.2018**	67.7	0.202	67.5	0.202
	306.057	**0.2171**	304.5	0.217	303.1	0.218
	755.056	**0.1495**	753.9	0.149	749.4	0.15
	1407.84	**0.0874**	1409.5	0.087	1398.3	0.088
1.5	**70.6342**	**0.1527**	70.2	0.153	69.9	0.153
	313.668	**0.1970**	310.6	0.197	309.1	0.198
	763.233	**0.1452**	759.7	0.145	755.2	0.146
	1412.56	**0.0866**	1412.6	0.086	1401.4	0.087

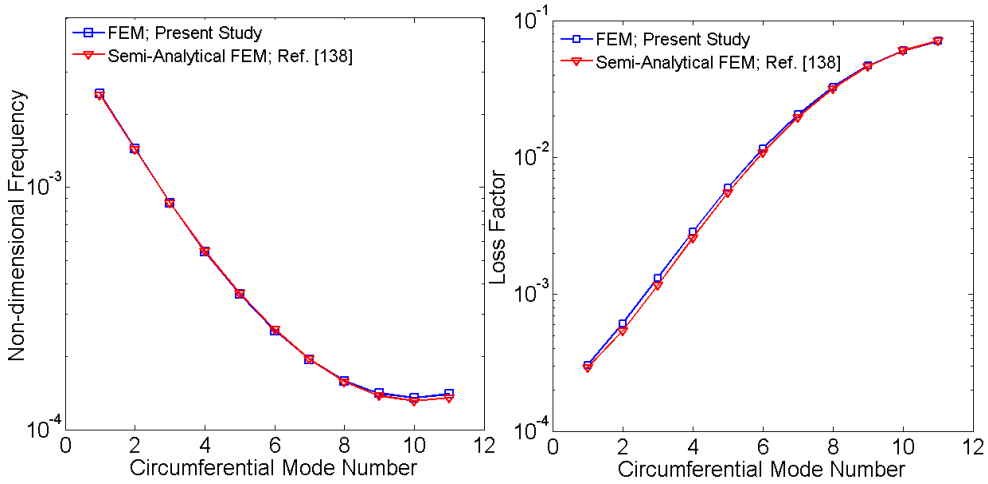

Figure 6.3 Comparing the Non-dimensional frequency ($\Omega = \rho_b h_b r\omega^2/E_b$) and loss factor using the developed approach and those in the literature for clamped-clamped complete sandwich cylinder; L=0.18 m, r = 0.1 m, h_i= 0.001 m, E_i = 2.1 × 10^{11} Nm^{-2}, ρ_i= 7850 kgm^{-3}, υ_i= 0.3, h_c= 0.001 m, E_c = (2.3+0.8i) ×10^7 Nm^{-2}, ρ_c= 1340 kgm^{-3}, υ_c= 0.34

The ratios of nonlinear and linear angular frequency (ω_{NL}/ω_L) for various curvatures are compared to those reported by Shin [140]. The results are shown for different ratios of maximum amplitude at the center of the panel to the thickness of the bare layer (w_{max}/h_b) which are provided in Table 6.5.

Table 6.5 Frequency ratios ω_{NL}/ω_L for square isotropic cylindrical shells; b/L = 1, L/h = 10; simply-supported boundary condition; u=0, v=0, w=0, $\partial w/\partial x$=0 at the top and bottom edges; u=0, v=0, w=0, $\partial w/r\partial\theta$=0 at the left and right edges

		r/h					
	w_{max}/h	25	50	100	200	500	∞
Ref. [140]	0.2	1.0191	1.029	1.0331	1.0342	1.0342	1.0305
	0.4	1.0673	1.1024	1.114	1.1163	1.1159	1.1128
	0.6	1.1549	1.2201	1.2392	1.2417	1.2407	1.2365
	0.8	1.2723	1.3682	1.3945	1.3978	1.3961	1.3903
	1	1.4095	1.5355	1.5699	1.5749	1.5725	1.5649
Present study	**0.2**	**1.0442**	**1.0563**	**1.0542**	**1.0409**	**1.0324**	**1.0266**
	0.4	**1.1027**	**1.1498**	**1.1527**	**1.129**	**1.1135**	**1.1027**
	0.6	**1.2157**	**1.3016**	**1.2857**	**1.255**	**1.2342**	**1.2196**
	0.8	**1.3745**	**1.4542**	**1.4445**	**1.4093**	**1.385**	**1.3675**
	1	**1.5523**	**1.6523**	**1.6223**	**1.5844**	**1.5577**	**1.5384**
Ref. [140]	-0.2	1.0176	1.0273	1.0319	1.0334	1.0339	1.0305
	-0.4	1.0532	1.088	1.1054	1.1116	1.1142	1.1128
	-0.6	1.1137	1.1845	1.2182	1.231	1.2361	1.2365
	-0.8	1.1977	1.3093	1.3611	1.3801	1.3885	1.3903
	-1	1.3012	1.456	1.5258	1.5513	1.5624	1.5649
Present study	**-0.2**	**0.9357**	**0.9891**	**0.9968**	**1.0117**	**1.0206**	**1.0266**
	-0.4	**0.9615**	**0.9979**	**1.0451**	**1.0744**	**1.0915**	**1.1027**
	-0.6	**1.0291**	**1.0841**	**1.139**	**1.1805**	**1.2043**	**1.2196**
	-0.8	**1.0873**	**1.1803**	**1.269**	**1.3203**	**1.3493**	**1.3675**
	-1	**1.2041**	**1.3274**	**1.426**	**1.4851**	**1.5179**	**1.5384**

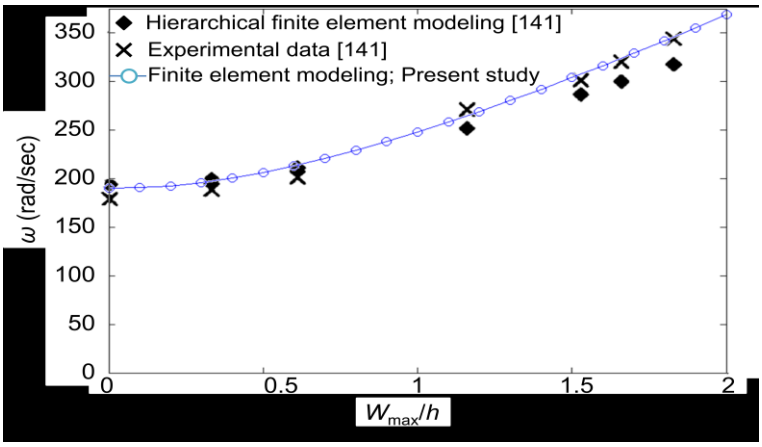

Figure 6.4 Nonlinear natural frequency of CFCF plate; comparison between hierarchical finite element method, the developed finite element modeling and experiment; L=0.58 m, b = 0.02 m; h= 0.002 m, E = 70 × 10^9 Nm^{-2}, ρ= 2778 kgm^{-3}; υ = 0.3

It should be noted that Shin [140] considered von Karman type nonlinear and FSDT in the nonlinear vibration analysis of panel structures in which fourth-order Runge-Kutta time integration method was used to solve the nonlinear equation. As it can be realized good agreement exists between the results. The deviation between the results which increases with decreasing the radius of curvature is reasonable since different frameworks including FSDT and CT have been used in these studies. Similar deviation between the results using HSDT and FSDT has been also addressed by Panda and Singh [104]. It should be noted that the negative and positive signs for transverse displacement w_{max} indicate that the shell structure begins to vibrate in the inward or outward directions, respectively [140]. In the inward direction, the equations of motion for free vibration of the bare shell structure can be easily formulated by changing the positive sign of the linearly displacement dependent matrix ($\mathbf{K}_1$ in B-notation, $\mathbf{KN}_1$ in N-notation and $\mathbf{H}_1$ in H-notation) to the negative sign since the other terms are the same odd functions with respect to the displacement. The developed methodology is also validated by comparing the results to experiment and hierarchical finite element method reported by Ribeiro [141] as shown in Figure 6.4. Compared with the hierarchical finite element method, the

developed finite element modeling is more close to the experimental results particularly at larger amplitude, which indicates the accuracy of the developed finite element modeling.

6.5.2 Parametric study

The main parameters which influence the damping behavior of the sandwich shell structure with constrained ER fluid layer is the thickness ratios of the layers, boundary condition, electric field intensity and amplitude of the displacement. The material properties and the dimensions of the top and bottom layers are chosen in order to achieve moderate values of natural frequency for different boundary conditions. The elastic top and bottom layers of the sandwich shell structure are aluminum sheets in which E_i= 68 GPa, ρ_i=2766 kg/m^3 and υ_i=0.3. The dimensions of the sandwich panel are chosen so that b/L=1, r/L=10, h_b/L=0.01, h_c/L=0.003 and h_t/L=0.002.

Figure 6.5 shows the effect of the electric field and amplitude on the natural frequency of the sandwich panel with ER-fluid core layer for different boundary conditions. According to the results, the natural frequency increases with increasing the amplitude indicating that the nonlinear behavior has hardening effect and stiffen the structure. As shown by Amabili [142], rotation constraints (in clamped boundary conditions) reduce the hardening type nonlinearity and consequently the frequency ratio ω_{NL}/ω_L. Therefore, as shown in Figure 6.5, the rate of increase in frequency ratio for simply supported boundary conditions is higher than the clamped boundary conditions. As can be observed, the electric field has a negligible effect on the frequency ratio so that with increasing the electric field intensity, the frequency ratio slightly decreases for different boundary conditions.

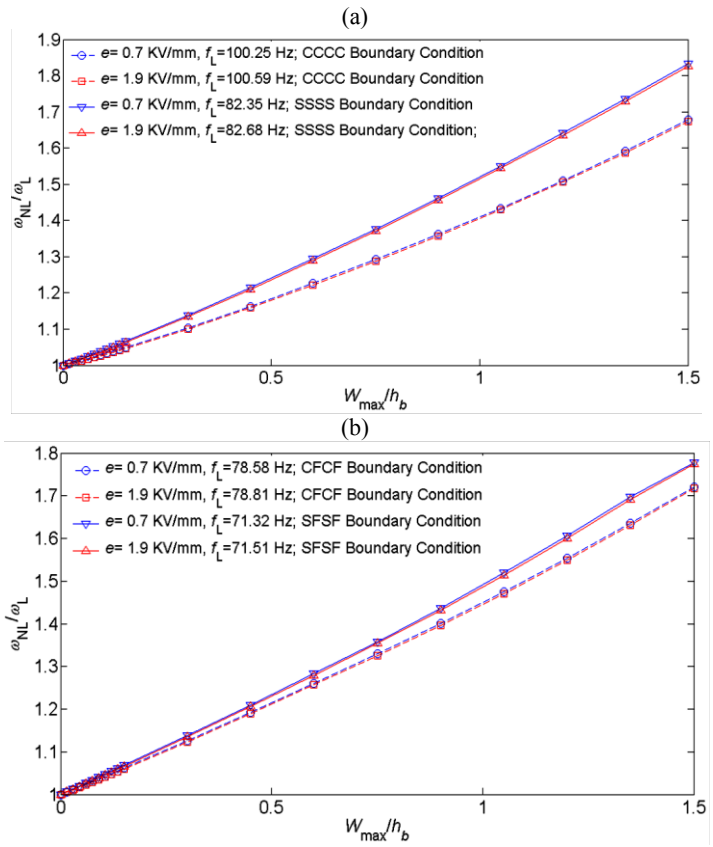

Figure 6.5 Effect of displacement and electric field intensity on the frequency ratio ω_{NL}/ω_L of sandwich cylindrical panel, (a) CCCC and SSSS boundary conditions, (b) CFCF and SFSF boundary conditions

On the other hand, both the displacement and electric field intensity have significant effect on the loss factor ratio η_{NL}/η_L which is shown in Figure 6.6. As the displacement increases the loss factor ratio first increases and then decreases. Due to hardening type of the nonlinearity, it is expected that the loss factor ratio decreases. However, according to the experimental data and the results from the constitutive model shown in chapter 5, with small increase in the shear strain amplitude, the loss modulus of the ER fluid initially increases. This leads to increase in the structural loss factor ratio up to certain value as the amplitude increases. With more increase in amplitude, effects of decrease in loss modulus and the hardening of the structure considerably reduce the structural loss factor ratio. The loss modulus of the ER fluid material increases with increasing the electric field intensity, and consequently the structural loss factor increases.

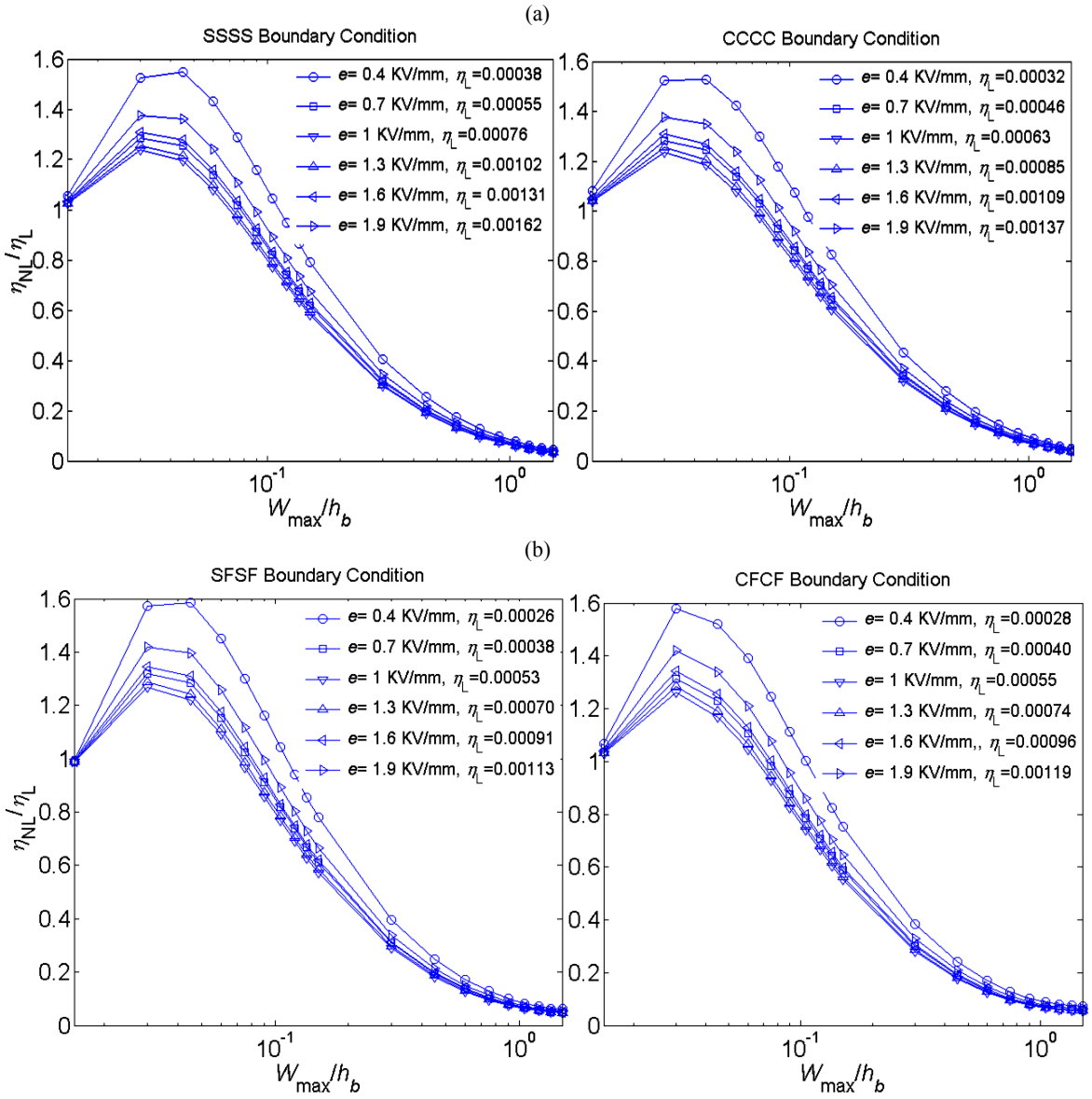

Figure 6.6 Effect of displacement and electric field intensity on the loss factor ratio η_{NL}/η_L of sandwich cylindrical panel; (a) CCCC and SSSS boundary conditions, (b) CFCF and SFSF boundary conditions

On the other hand, as shown in Figure 6.6, with increasing electric field intensity, the loss factor ratio first decreases and then increases. This indicates that for low and high values of field intensity, the nonlinearity due to the relatively small amplitude can desirably increase the structural loss factor. The transverse shear strain contours generated in the ER fluid core layer due to the displacement (shown in Figure 6.7) determines the structural loss factor.

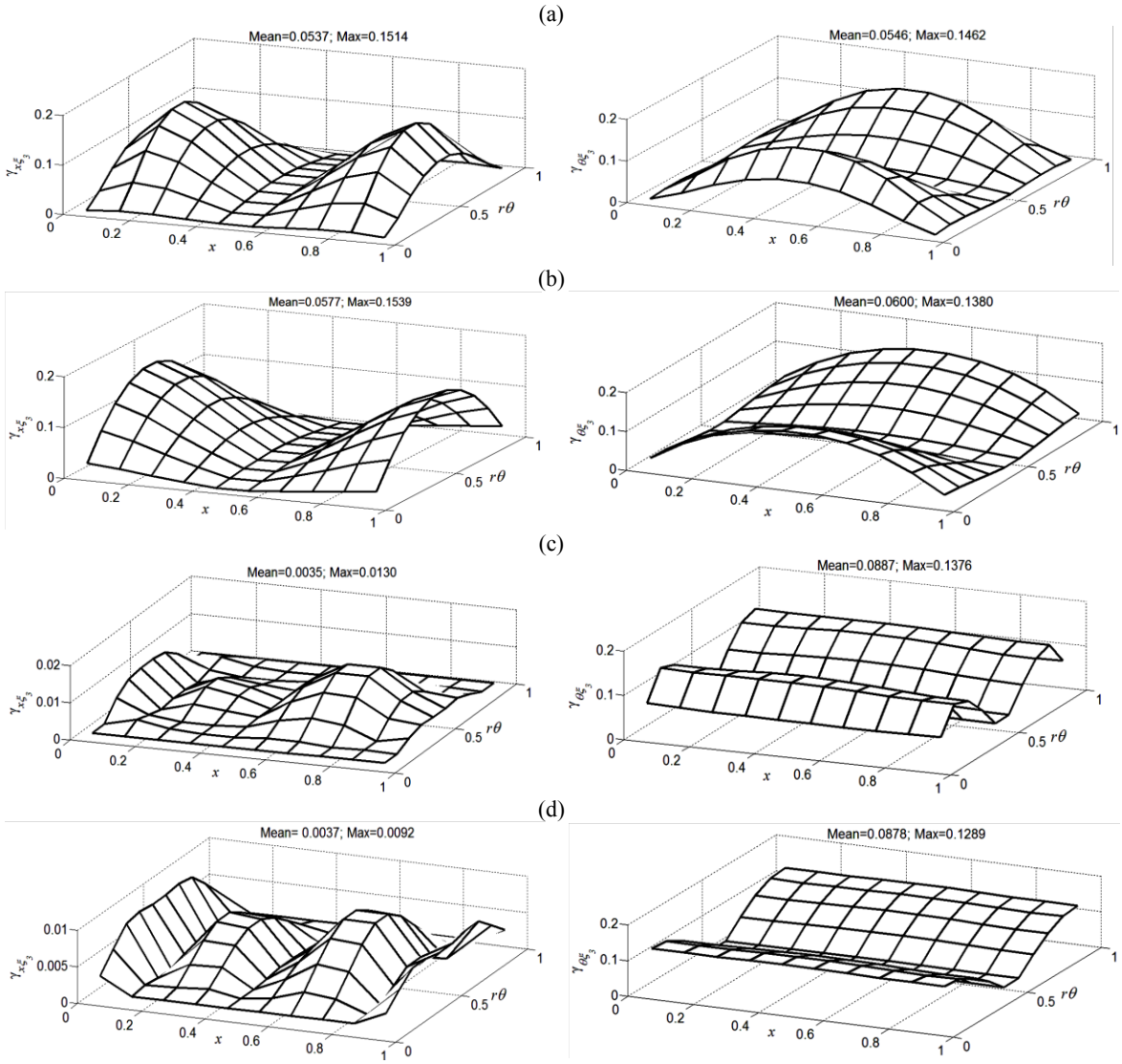

Figure 6.7 Distribution of transverse shear strains of the ER fluid core layer in axial and circumferential directions of the sandwich shell structure for different boundary conditions; W_{max}/h_b=1.5, e =1.3 KVmm^{-1}; (a) CCCC boundary condition, (b) SSSS boundary condition, (c) CFCF boundary condition (d) SFSF boundary condition

However, due to the larger shear strain amplitude in CFCF boundary condition compared with the SFSF boundary condition, the structural loss factor is slightly greater in CFCF boundary condition. The structural loss factor for different displacements and core thickness ratios at e =1.3 KV/mm and h_t/L=0.002 is shown in Figure 6.8 for different boundary conditions. According to results shown in Figure 6.6, the structural loss factor for SSSS boundary condition is greater than that for CCCC boundary

condition since the transverse shear strains in the core layer are greater in SSSS boundary condition indicating more energy dissipating in the structure.

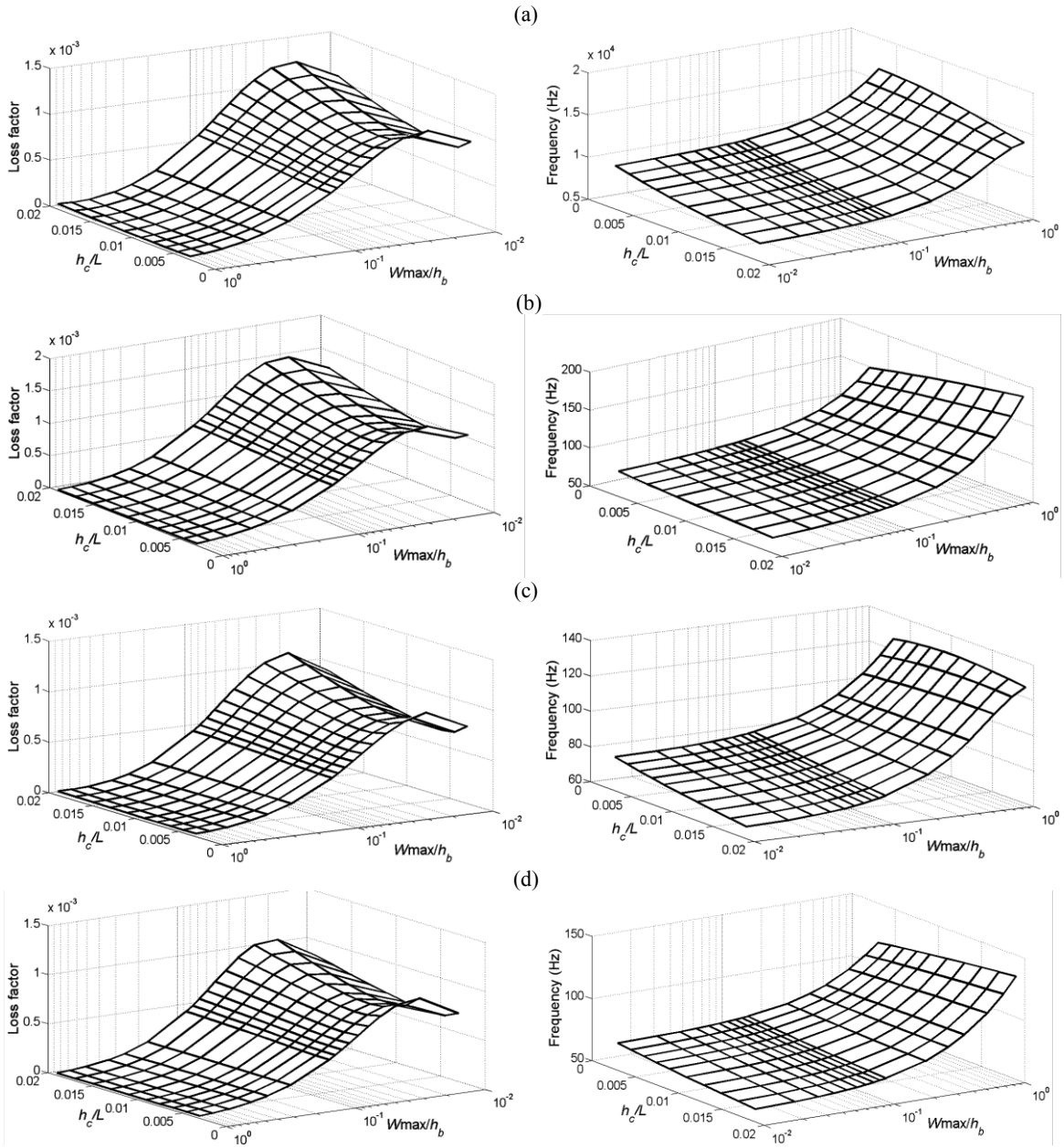

Figure 6.8 Effect of core thickness ratio and displacement on structural loss factor for different boundary conditions; e =1.3 KVmm^{-1}; (a) CCCC boundary condition, (b) SSSS boundary condition, (c) CFCF boundary condition (d) SFSF boundary condition

The loss factor initially decreases with increasing the core thickness for small displacements, and then increases with more increasing the core thickness. This behavior is also shown in reference [138] at the fundamental mode for small amplitudes. With

increasing the displacement, the variation rate of loss factor with respect to core thickness amplitude decreases and for large displacements the loss factor is almost constant with respect to core thickness ratio. For the clamped (CCCC and CFCF) boundary conditions, at large displacements the natural frequency initially increases and then slightly decreases with increasing the core thickness ratio while at small displacements the natural frequency decreases as the core thickness ratio increases. Similarly, for the simply supported (SSSS and SFSF) boundary conditions, at small displacements the natural frequency decreases as the core thickness ratio increases. However, at large displacements the natural frequency increases with increasing the core thickness ratio.

6.6 Conclusion

The nonlinear vibration analysis of sandwich shell structure with constrained ER fluid core layer was presented in this chapter. The finite element modeling based on assumed strain functions was efficiently used for discretizing the sandwich shell structure. A new notation referred to as H-notation for nonlinear stiffness matrices in equations of motion was developed in which the integrations are performed only once before implementing the direct iteration procedure and consequently the repeatedly time consuming integrations has been avoided in the direct iteration technique. According to the experimental data available in literature, the results show that the developed finite element modeling leads to more accurate results compared with the hierarchical finite element modeling for large displacements. Parametric studies on nonlinear vibration damping behavior for different boundary conditions showed the hardening type in the nonlinear behavior of sandwich panel in which the natural frequency increases with increasing the amplitude. The structural loss factor also depends on the shear strain

distribution in the shell structure. Similar to displacement, the electric field has significant effect on the structural loss factor while it has negligible effect on nonlinear frequency. The results also showed that the core thickness ratio can affect the loss factor and natural frequency, depending on the boundary conditions.

CHAPTER 7

VIBRATION ANALYSIS AND DESIGN OPTIMIZATION OF SANDWICH CYLINDRICAL PANELS FULLY AND PARTIALLY TREATED WITH ELECTRORHEOLOGICAL FLUID MATERIALS

7.1 Introduction

Compared with viscoelastic materials, ER fluids can be effectively used to suppress the vibration over a broad frequency and temperature range. In current chapter, the design optimization is carried out to maximize damping in sandwich cylindrical panel using both unconstrained viscoelastic material and constrained ER fluid damping layers. The damping in sandwich structure is mainly due to constrained damping layer in which large amount of shear deformation is generated compared with the unconstrained damping layer. At lower temperatures, the treatment may be performed using only constrained viscoelastic patches since the complex modulus of the viscoelastic material is generally greater than that of the ER fluid material. However, at higher temperatures the complex modulus of the viscoelastic material considerably reduces and the passive treatment is not reliable [30-35]. Reliable treatment can be achieved using ER fluid treatment for wide range of frequency in which the material property of the damping layer can be tuned using the electric field. Here the unconstrained viscoelastic and constrained ER fluid patches are considered to treat the bare panel structure. The constrained ER fluid has considerable contribution in the damping of the structure since large deformation is generated in the constrained layer. The unconstrained viscoelastic layer is mainly used to seal the ER fluid. Also it can provide the possibility if the partial treatment of constrained ER fluid is required in order to achieve better damping. The optimization problem is then

conducted to find simultaneously the optimum number and distribution of unconstrained viscoelastic and constrained ER fluid patches, electric field intensity and thickness ratios of treating layers. An efficient shell element is employed to discretize the sandwich structure. An accurate design optimization algorithm has been developed in which the finite element model of the smart sandwich cylindrical has been combined with the genetic algorithm (GA) to approximately obtain optimum global variables. These optimum values are then used as the starting point for sequential quadratic programming (SQP) algorithm in order to obtain accurate optimum results.

7.2 Finite Element Modeling

The optimization process of cylindrical panel structure may be computationally very expensive since the higher order elements with additional nodes are required for discretizing the structure that leads to increase in number of degrees of freedom (DOF). This is even more critical for multi-layer sandwich panel structure with larger number of DOF compared with the bare structure. Therefore, an efficient element is required for discretizing the panel structure in a way that less number of elements/nodes and consequently less number of DOF are used in the finite element modeling. In this chapter the shell element developed by Ashwel and Sabir [124] is employed and generalized to discretize sandwich panel structure as shown in Figure 6.1. This element has been developed based on the assumed strain functions using compatibility equations and considering rigid body motion. Higher order displacement fields are obtained in this element without additional nodes in which each element contains four nodes with 20 degrees of freedom. Using the higher order displacement fields, the element has shown excellent convergence [123, 124]. Considering this, the element can be efficiently used

for discretizing sandwich shell structure in the optimization problem in which large number of computations are performed. The element in this chapter is now generalized for three-layer sandwich panel structure and consequently the number of DOF increases to 40 which are associated with the top and bottom layers. It is noted that degrees of freedom associated with core layer, as it will be shown later, can be obtained with respect to those at the top and bottom layers. However, by assuming the constant transverse displacement through the thickness of the panel structure, the number of DOF in sandwich panel element reduces to 28. Using the compatibility equation and considering rigid body motion in the panel element, the displacement field at the bottom layer (base layer) can be described as [124]:

$$
\begin{aligned}
u_o^b &= \frac{1}{2}a_2 r\theta^2 + a_4 + a_6 r\theta + a_7 x + a_8 r\theta x - \frac{1}{2}a_{10} r^2\theta^2 + \frac{1}{2}a_{11} r\theta - \frac{1}{24}a_{17} r^3\theta^4 \\
&- \frac{1}{120}a_{19} r^4\theta^5 - \frac{1}{12}a_{20} r^2\theta^3 \\
v_o^b &= -a_1\theta - a_2 x\theta - \frac{1}{2}a_3 r\theta^2 + a_5 - a_6 x - \frac{1}{2}a_8 x^2 + a_9 r\theta + a_{10} xr\theta + \frac{1}{2}a_{11} x \\
&+ \frac{1}{6}a_{16} r^2\theta^3 + \frac{1}{6}a_{17} xr^2\theta^3 + \frac{1}{24}a_{18} r^3\theta^4 + \frac{1}{24}a_{19} xr^3\theta^4 + \frac{1}{4}a_{20} xr\theta^2 \\
w &= a_1 + a_2 x + a_3 r\theta - \frac{1}{2}a_{12} x^2 - \frac{1}{6}a_{13} x^3 - \frac{1}{2}a_{14} x^2 r\theta - \frac{1}{6}a_{15} x^3 r\theta \\
&- \frac{1}{2}a_{16} r^2\theta^2 - \frac{1}{2}a_{17} xr^2\theta^2 - \frac{1}{6}a_{18} r^3\theta^3 - \frac{1}{6}a_{19} xr^3\theta^3 - \frac{1}{2}a_{20} xr\theta
\end{aligned}
\tag{7.1}
$$

in which u_o^b and v_o^b are respectively in-plane translations at the middle plane in axial (x) and circumferential (θ) directions of the bottom layer, w is transverse displacement which is considered to be constant with respect to the thickness coordinates in each layer, and r is the radius of the cylindrical panel element. The rotations of the normals to the middle plane of the sandwich panel element in axial and circumferential directions are respectively represented by $\partial w/\partial x$ and $\partial w/r\partial\theta$. Each node of the element consists of five

degrees of freedom including u_b, v_b, w, $\partial w/\partial x$ and $\partial w/r\partial\theta$ and consequently the coefficients a_1 through a_{20} can be obtained using the 20 nodal displacements in the panel element. The displacement fields then can be represented by the shape functions and the nodal displacement as:

$$u_o^b = N_u Q_b \quad v_o^b = N_v Q_b \quad w = N_w Q_b \tag{7.2}$$

where N_u, N_v and N_w are row vectors of the shape functions depending on the axial, circumferential coordinates x and θ, and Q_b is a column vector of the nodal displacements of the bottom layer given in the following:

$$Q_b^{\mathrm{T}} = \left[u_{o1}^b \quad v_{o1}^b \quad w_1 \quad \frac{\partial w}{\partial x}_1 \quad \frac{\partial w}{r\partial\theta}_1 \quad \cdots \quad u_{o4}^b \quad v_{o4}^b \quad w_4 \quad \frac{\partial w}{\partial x}_4 \quad \frac{\partial w}{r\partial\theta}_4 \right]_{1\times 20} \tag{7.3}$$

in which the symbol T denotes vector transpose. The displacement field at the top layer can be similarly represented using the same shape functions and the nodal displacement at the top layer given in the following:

$$Q_t^{\mathrm{T}} = \left[u_{o1}^t \quad v_{o1}^t \quad w_1 \quad \frac{\partial w}{\partial x}_1 \quad \frac{\partial w}{r\partial\theta}_1 \quad \cdots \quad u_{o4}^t \quad v_{o4}^t \quad w_4 \quad \frac{\partial w}{\partial x}_4 \quad \frac{\partial w}{r\partial\theta}_4 \right]_{1\times 20} \tag{7.4}$$

The displacement field at the top and bottom layers can be expressed in terms of element nodal displacements in the sandwich panel element as follows:

$$u_o^b = N_u^b Q \quad v_o^b = N_v^b Q \quad w = N_w Q \quad u_o^t = N_u^t Q \quad v_o^t = N_v^t Q \tag{7.5}$$

in which the element nodal displacement vector is written as:

$$\begin{aligned} Q^{\mathrm{T}} = \Big[& u_{o1}^b \quad v_{o1}^b \quad w_1 \quad u_{o1}^t \quad v_{o1}^t \quad \frac{\partial w}{\partial x}_1 \quad \frac{\partial w}{r\partial\theta}_1 \quad \cdots \\ & u_{o4}^b \quad v_{o4}^b \quad w_4 \quad u_{o4}^t \quad v_{o4}^t \quad \frac{\partial w}{\partial x}_4 \quad \frac{\partial w}{r\partial\theta}_4 \Big]_{1\times 28} \end{aligned} \tag{7.6}$$

N_u^b, N_v^b, N_w, N_v^t, and N_u^t are row vectors of the element shape functions which are given in the following:

$$
\begin{aligned}
N_u^b &= \begin{bmatrix} \overset{1,3}{N_u} & 0 & 0 & \overset{4,5}{N_u} & \overset{6,8}{N_u} & 0 & 0 & \overset{9,10}{N_u} & \overset{11,13}{N_u} & 0 & 0 & \overset{14,15}{N_u} & \overset{16,18}{N_u} & 0 & 0 & \overset{19,20}{N_u} \end{bmatrix}_{1\times 28} \\
N_v^b &= \begin{bmatrix} \overset{1,3}{N_v} & 0 & 0 & \overset{4,5}{N_v} & \overset{6,8}{N_v} & 0 & 0 & \overset{9,10}{N_v} & \overset{11,13}{N_v} & 0 & 0 & \overset{14,15}{N_v} & \overset{16,18}{N_v} & 0 & 0 & \overset{19,20}{N_v} \end{bmatrix}_{1\times 28} \\
N_w &= \begin{bmatrix} \overset{1,3}{N_w} & 0 & 0 & \overset{4,5}{N_w} & \overset{6,8}{N_w} & 0 & 0 & \overset{9,10}{N_w} & \overset{11,13}{N_w} & 0 & 0 & \overset{14,15}{N_w} & \overset{16,18}{N_w} & 0 & 0 & \overset{19,20}{N_w} \end{bmatrix}_{1\times 28} \\
N_u^t &= \begin{bmatrix} 0 & 0 & \overset{3}{N_u} & \overset{1,2}{N_u} & \overset{4,5}{N_u} & 0 & 0 & \overset{8}{N_u} & \overset{6,7}{N_u} & \overset{9,10}{N_u} & 0 & 0 & \overset{13}{N_u} & \overset{11,12}{N_u} & \overset{14,15}{N_u} & 0 & 0 & \overset{18}{N_u} & \overset{16,17}{N_u} & \overset{19,20}{N_u} \end{bmatrix}_{1\times 28} \\
N_v^t &= \begin{bmatrix} 0 & 0 & \overset{3}{N_v} & \overset{1,2}{N_v} & \overset{4,5}{N_v} & 0 & 0 & \overset{8}{N_v} & \overset{6,7}{N_v} & \overset{9,10}{N_v} & 0 & 0 & \overset{13}{N_v} & \overset{11,12}{N_v} & \overset{14,15}{N_v} & 0 & 0 & \overset{18}{N_v} & \overset{16,17}{N_v} & \overset{19,20}{N_v} \end{bmatrix}_{1\times 28}
\end{aligned}
\tag{7.7}
$$

in which $\overset{j}{N}_d$ is the jth component of the vector N_d (d=u,v and w) and $\overset{i,j}{N}_d$ are the ith through jth components of vector N_d. Using the classical shell theory, the displacement through the thickness of the top and bottom layers can be represented as:

$$
\begin{aligned}
u_t(x,\theta,\xi_1,t) &= u_o^t(x,\theta,t) - \xi_1 \frac{\partial w(x,\theta,t)}{\partial x} \\
v_t(x,\theta,\xi_1,t) &= v_o^t(x,\theta,t) - \xi_1 \frac{\partial w(x,\theta,t)}{r\partial \theta} \qquad -\frac{h_t}{2} < \xi_1 < \frac{h_t}{2} \\
w_t &= w(x,\theta,t)
\end{aligned}
\tag{7.8}
$$

$$
\begin{aligned}
u_b(x,\theta,\xi_2,t) &= u_o^b(x,\theta,t) - \xi_2 \frac{\partial w(x,\theta,t)}{\partial x} \\
v_b(x,\theta,\xi_2,t) &= v_o^b(x,\theta,t) - \xi_2 \frac{\partial w(x,\theta,t)}{r\partial \theta} \qquad -\frac{h_b}{2} < \xi_2 < \frac{h_b}{2} \\
w_b &= w(x,\theta,t)
\end{aligned}
\tag{7.9}
$$

For the core layer, the first order shear deformation theory (FSDT) has been used to define the displacement field through its thickness as follows:

$$
\begin{aligned}
u_c(x,\theta,\xi_3,t) &= u_o^c(x,\theta,t) + \xi_3 \psi_1^c(x,\theta,t) \\
v_c(x,\theta,\xi_3,t) &= v_o^c(x,\theta,t) + \xi_3 \psi_2^c(x,\theta,t) \qquad -\frac{h_c}{2} < \xi_3 < \frac{h_c}{2} \\
w_c &= w(x,\theta,t)
\end{aligned}
\tag{7.10}
$$

where u_o^c and v_o^c are respectively the in-plane translations at the middle plane of the ER fluid core layer in axial and circumferential directions. Also h_t, h_b and h_c are the thicknesses of top, bottom and ER fluid core layers, and ψ_1^c and ψ_2^c are respectively the rotations of the normals to the middle plane in axial and circumferential directions. ξ_i (i= 1, 2 and 3) represent the coordinates in thickness direction at the middle of each layer. Perfect bonding or slippage between layers at the interfaces can be considered for the boundary conditions. However, as shown in chapter 4, the slippage should be avoided in order to increase the structural loss factor. According to the boundary conditions for perfect bonding, the in-plane and transverse displacements are continuous at the interfaces and consequently the in-plane displacements and the rotations are obtained as:

$$
\begin{aligned}
u_o^c &= \frac{u_o^t + u_o^b}{2} + \frac{h_t \dfrac{\partial w}{\partial x} - h_b \dfrac{\partial w}{\partial x}}{4} \\
v_o^c &= \frac{v_o^t + v_o^b}{2} + \frac{h_t \dfrac{\partial w}{r\partial \theta} - h_b \dfrac{\partial w}{r\partial \theta}}{4} \\
\psi_1^c &= \frac{u_o^t - u_o^b}{h_c} + \frac{h_t \dfrac{\partial w}{\partial x} + h_b \dfrac{\partial w}{\partial x}}{2h_c} \\
\psi_2^c &= \frac{v_o^t - v_o^b}{h_c} + \frac{h_t \dfrac{\partial w}{r\partial \theta} + h_b \dfrac{\partial w}{r\partial \theta}}{2h_c}
\end{aligned}
\tag{7.11}
$$

It should be noted that in order to achieve a perfect sealing, the thickness of unconstrained viscoelastic layer has been considered to be equal to the thickness of constrained ER fluid core and its constraining layers. The unconstrained viscoelastic layer has been modeled by discretizing the layer into two layers in which the outer layer has the same thickness as the elastic face and the inner layer has the thickness of the ER fluid core layer. This allows providing the continuity in the displacement field of the

unconstrained viscoelastic layer, the ER fluid core layer, and its constraining layer. The equations of motion have been established using Lagrange's equation written in the following:

$$\frac{\mathrm{d}}{\mathrm{d}t}\left(\frac{\partial T}{\partial \dot{Q}_k}\right)-\left(\frac{\partial T}{\partial Q_k}\right)+\left(\frac{\partial U}{\partial Q_k}\right)=F_k \quad k=1,\cdots,n \tag{7.12}$$

where n is the total DOF in the sandwich panel structure, Q and F are the nodal displacements and applied external force, respectively and T and U are respectively the kinetic and potential energies in the sandwich panel structure which can be written for each layer as follows:

$$T_i=\int_{-\frac{h_i}{2}}^{\frac{h_i}{2}}\int_0^{\theta_0}\int_0^{l_0}\frac{1}{2}\rho_i\left(\dot{u}_i{}^2+\dot{v}_i{}^2+\dot{w}_i{}^2\right)\mathrm{d}V_i \tag{7.13}$$

$$U_i=\int_{-\frac{h_i}{2}}^{\frac{h_i}{2}}\int_0^{\theta_0}\int_0^{l_0}\frac{1}{2}\left(\sigma_{xx}^i\,\varepsilon_{xx}^i+\sigma_{\theta\theta}^i\,\varepsilon_{\theta\theta}^i+\tau_{x\theta}^i\,\gamma_{x\theta}^i+\tau_{x\xi_i}^i\,\gamma_{x\xi_i}^i+\tau_{\theta\xi_i}^i\,\gamma_{\theta\xi_i}^i\right)\mathrm{d}V_i \tag{7.14}$$

In Eqs (7.13) and (7.14), i=t, b and c respectively denotes the top, bottom and core layers and $\mathrm{d}V_i = r\mathrm{d}\theta\mathrm{d}s\,\mathrm{d}\xi_i$. Also l_0 and θ_0 respectively represent the length and the angle of the panel element. σ and τ are normal and shear stress components, and ε and γ are normal and shear strain components. x, θ and ξ_i are the coordinates in axial, circumferential and transverse directions, respectively. It should be noted that in Eq. (7.14) the energy terms related to the in-plane and normal stresses of the constrained ER core layer, i.e. $\tau_{s\theta}^c$, $\sigma_{\theta\theta}^c$ and σ_{ss}^c can be neglected due to the much small modulus in the core layer compared with the elastic faces so that the in-plane shear and normal stresses are carried only by the elastic faces.

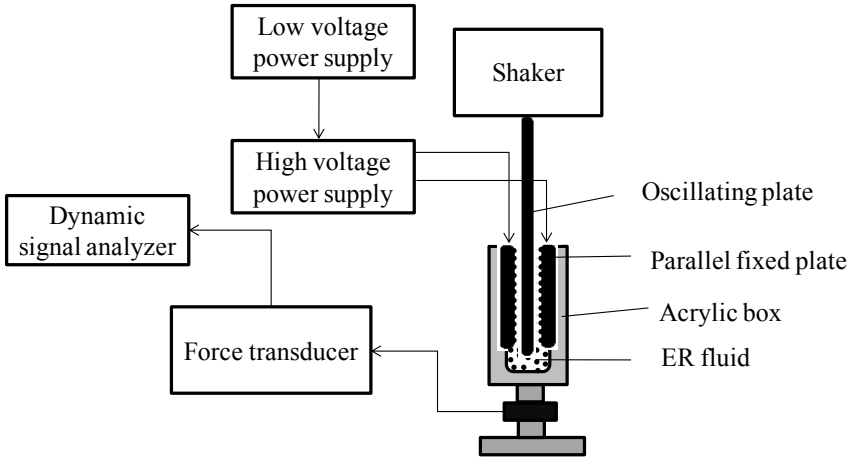

Figure 7.1 Sketch of the experimental setup in order to measure dynamic properties of the ER fluid material

However, they have been incorporated in the total strain energy in the sandwich panel structure to achieve more accuracy. The strain–displacement relation for a cylindrical panel element can be expressed as follows:

$$\varepsilon_{xx}^{i}=\frac{\partial u_i}{\partial x}\qquad \varepsilon_{\theta\theta}^{i}=\frac{\partial v_i}{r\partial\theta}+\frac{w}{r}$$
$$\gamma_{x\theta}^{i}=\left(\frac{\partial v_i}{\partial x}\right)+\left(\frac{\partial u_i}{r\partial\theta}\right)\qquad \gamma_{\xi_i x}^{i}=\frac{\partial u_i}{\partial \xi_i}+\frac{\partial w}{\partial x}\qquad \gamma_{\xi_i\theta}^{i}=\frac{\partial v_i}{\partial \xi_i}+\left(\frac{\partial w}{r\partial\theta}-\frac{v_i}{r}\right) \tag{7.15}$$

The following constitutive equations give the relationship between the stress and strain components at different layers:

$$\sigma_{xx}^{i}=\frac{E_i}{\left(1-\upsilon_i{}^2\right)}\left[\varepsilon_{xx}^{i}+\upsilon_i\varepsilon_{\theta\theta}^{i}\right]\quad \sigma_{\theta\theta}^{i}=\frac{E_i}{\left(1-\upsilon_i{}^2\right)}\left[\varepsilon_{\theta\theta}^{i}+\upsilon_i\varepsilon_{xx}^{i}\right]$$
$$\tau_{x\theta}^{i}=G_i\gamma_{x\theta}^{i}\quad \tau_{x\xi_i}^{i}=G_i\gamma_{\xi_i x}^{i}\quad \tau_{\theta\xi_i}^{i}=G_i\gamma_{\xi_i\theta}^{i} \tag{7.16}$$

where E, G and υ are respectively the Young's modulus, shear modulus and Poisson's ratio. The experimental study has been extensively explained in chapter 5 in order to determine the material properties of the ER fluid and an efficient constitutive model has been also proposed to predict the experimental data including complex modulus and

stress response. The ER fluid has been prepared by dispersing cornstarch into corn oil with viscosity of 40 mPa s. The weight fraction of the particles has been chosen to be 30 %. The sketch of the experimental setup is shown in Figure 7.1. The electric field is applied between the aluminum plates inside an acrylic box. First, low input voltage is generated using the low voltage power supply (o to 15 Volt) and then a DC to high voltage DC converter generates the high DC voltage (0 to 10000 Volts) between the fixed plates. The shear area of the oscillating plate contacting with the ER fluid is 844 mm^2. The distance between the fixed aluminum plates and the thickness of the oscillating plate are, respectively, 5.4 mm and 2.8 mm. The complex modulus including storage and loss modulus are shown chapter 5 for different frequencies, shear strain amplitude and electric field intensities. The results show that proposed modulus given in chapter 5 reasonably predicts the experimental data. The details of the experiment and the proposed constitutive model have been extensively illustrated in chapter 5. The model is now used for small shear amplitudes, different frequencies and field intensities. The constitutive equations for ER fluid core layer regarding the transverse shear stress components can be generally written as:

$$\tau^{c}_{\xi_3 x} = \left(G'(e,\omega) + \mathrm{i}G''(e,\omega)\right)\gamma^{c}_{\xi_3 x} \qquad \tau^{c}_{\xi_3 \theta} = \left(G'(e,\omega) + \mathrm{i}G''(e,\omega)\right)\gamma^{c}_{\xi_3 \theta} \tag{7.17}$$

where the material properties of the ER fluid depend on electric field intensity e and frequency ω. The density of the ER fluid material is ρ_c = 970 kg/m^3 and Poisson's ratio is considered to be 0.4. The material properties of the viscoelastic patches are frequency dependent with the real part of the complex shear modulus of $799700(\omega/2\pi)^{0.026}$ Pa, material loss factor of $0.0669(\omega/2\pi)^{0.17}$, density of 1104 kg/$m^3$ and Poisson's ratio of 0.34. The other components of the strain including in-plane normal and shear strains of

the ER fluid and viscoelastic layers can be obtained using the Eq. (7.16). As mentioned before strain energies associated with these components in ER fluid layer can be neglected due to its much small modulus compared with that of the elastic faces.

In order to define the stiffness matrix, the strain components in Eq. (7.15) are rewritten in terms of the shape functions and the element nodal displacements as:

$$\varepsilon_{xx}^{i} = \left(\frac{\partial N_u^i}{\partial x} - \xi_i \frac{\partial^2 N_w}{\partial x^2} \right) Q = N_1^i Q$$

$$\varepsilon_{\theta\theta}^{i} = \left(\frac{\partial N_v^i}{r\partial \theta} - \xi_i \frac{\partial^2 N_w}{r^2 \partial \theta^2} + \frac{N_w}{r} \right) Q = N_2^i Q$$

$$\gamma_{x\theta}^{i} = \left(\frac{\partial N_v^i}{\partial x} - 2\xi_i \frac{\partial^2 N_w}{r\partial x \partial \theta} + \frac{\partial N_u^i}{r\partial \theta} \right) Q = N_3^i Q$$

$$\gamma_{\xi_3 x}^{c} = \psi_1^c + \frac{\partial w_c}{\partial x} = \left(\frac{N_u^t - N_u^b}{h_c} + \frac{h_t \dfrac{\partial N_w}{\partial x} + h_b \dfrac{\partial N_w}{\partial x}}{2h_c} + \frac{\partial N_w}{\partial x} \right) Q = N_4^c Q \tag{7.18}$$

$$\gamma_{\xi_3 \theta}^{c} = \psi_2^c + \frac{\partial w_c}{r\partial \theta} = \left(\frac{N_v^t - N_v^b}{h_c} + \frac{h_t \dfrac{\partial N_w}{r\partial \theta} + h_b \dfrac{\partial N_w}{r\partial \theta}}{2h_c} + \frac{\partial N_w}{r\partial \theta} \right) Q = N_5^c Q$$

$$\gamma_{\xi_i x}^{i} = 0 \quad i = b, t$$

$$\gamma_{\xi_i \theta}^{i} = 0 \quad i = b, t$$

where N_1 through N_7 are:

$$N_1^i = \frac{\partial N_u^i}{\partial x} - \xi_i \frac{\partial^2 N_w}{\partial x^2} \qquad N_2^i = \frac{\partial N_v^i}{r\partial \theta} - \xi_i \frac{\partial^2 N_w}{r^2 \partial \theta^2} + \frac{N_w}{r}$$

$$N_3^i = \frac{\partial N_v^i}{\partial x} - 2\xi_i \frac{\partial^2 N_w}{r\partial x \partial \theta} + \frac{\partial N_u^i}{r\partial \theta} \quad N_4^c = \frac{N_u^t - N_u^b}{h_c} + \frac{h_t \dfrac{\partial N_w}{\partial x} + h_b \dfrac{\partial N_w}{\partial x}}{2h_c} + \frac{\partial N_w}{\partial x} \tag{7.19}$$

$$N_5^c = \frac{N_v^t - N_v^b}{h_c} + \frac{h_t \dfrac{\partial N_w}{r\partial \theta} + h_b \dfrac{\partial N_w}{r\partial \theta}}{2h_c} + \frac{\partial N_w}{r\partial \theta}$$

The Eqs (7.16) and (7.18) should be substituted into Eq. (7.14) in order to obtain the strain energy in the sandwich panel element. Based on the classical shell theory, the energy terms associated with transverse shear strains at the top and bottom layers are zero. Similarly, substituting displacement fields given in Eqs (7.8)-(7.11) into Eq. (7.13) gives the total kinetic energy. The obtained kinetic and strain energies are then substituted into the Lagrange's equation given in Eq. (7.12) which leads to establishing the stiffness and mass matrices of the sandwich panel structure. These matrices are obtained by assembling systematically the stiffness matrices of the different layers. After substituting the energy terms into the Lagrange equation, the equations of motion under harmonic external loading can be written as:

$$\mathbf{M}\ddot{Q} + \mathbf{K}(e,\omega)Q = F(t) \tag{7.23}$$

where $\mathbf{M}$ is the mass matrix, $\mathbf{K}= \mathbf{K}'(e,\omega)+\mathrm{i}\mathbf{K}''(e,\omega)$ is a complex stiffness matrix depending on frequency and electric field intensity, and F is the equivalent nodal force. The stiffness matrix is established based on the assembling the following matrices:

$$\mathbf{K}_i(e,\omega) = \frac{E_i}{(1-\upsilon_i{}^2)} \int_{-\frac{h_i}{2}}^{\frac{h_i}{2}} \int_0^{\theta_0} \int_0^{l_0} \left(N_1^{i\mathrm{T}} N_1^i + N_2^{i\mathrm{T}} N_2^i + \upsilon_i N_1^{i\mathrm{T}} N_2^i + \upsilon_i N_2^{i\mathrm{T}} N_1^i + \frac{1-\upsilon_i}{2} N_3^{i\mathrm{T}} N_3^i \right) \mathrm{d}V_i \tag{7.24}$$

$$\mathbf{K}_c(e,\omega) = \int_{-\frac{h_c}{2}}^{\frac{h_c}{2}} \int_0^{\theta_0} \int_0^{l_0} (G_c) \left(N_4^{c\mathrm{T}} N_4^c + N_5^{c\mathrm{T}} N_5^c \right) \mathrm{d}V_c \tag{7.25}$$

where $\mathbf{K}_i$ is the stiffness matrices associated with the strain energy of the in-plane normal and shear strain components at different layers and i represents the top, bottom and core layers. $\mathbf{K}_c$ is the stiffness matrix associated with the strain energy of the transverse shear strain components at the core layer for viscoelastic and ER fluids

material. G_c is the complex shear modulus of either viscoelastic or ER fluid materials. The stiffness matrix is nonlinear with respect to frequency since the material properties of the core layer is frequency dependent. For free vibration analysis, Eq. (7.23) can be represented as:

$$\left(-\omega^2\mathbf{M}+\mathbf{K}(e,\omega)\right)Q=0 \tag{7.26}$$

Due to the nonlinearity in the stiffness matrix, Eq. (7.26) cannot be directly solved. Although the natural frequency can be directly obtained according to the frequency response function under harmonic force $\mathbf{F}=\mathbf{F}_0 e^{i\omega t}$ for a certain range of frequency, but this methodology is computationally expensive since the solution strongly depends on the resolution of the frequency axis. Alternatively, the eigenvalue problem of Eq. (7.26) can be solved iteratively using the evaluated stiffness matrix at the natural frequencies. The best starting point could be the natural frequency of the bare shell structure for each mode in the iteration procedure. The loss factor associated with each mode can be evaluated using the ratio of the dissipated energy per radian and the maximum potential energy at natural frequency as follows:

$$\eta_i=\frac{\Phi_i^{\mathrm{T}}\mathbf{K}''\Phi_i}{\Phi_i^{\mathrm{T}}\mathbf{K}'\Phi_i} \tag{7.27}$$

where Φ_i is the normalized eigenvector in free vibration and η_i is the loss factor related to the ith mode.

7.3 Optimization Problem

The objective of the optimization problem can be defined as the loss factor at different mode shapes in which the panel structure is subjected to the excitation with the frequency related to that mode shape. Here, the objective is to maximize damping at the first two

modes of the transverse vibration. In the optimization problem the distribution of viscoelastic and constrained ER fluid patches, electric field intensity and the thicknesses of the treating layers are simultaneously optimized to achieve maximum damping in the panel structure. Noteworthy, for achieving perfect sealing it has been assumed that the core layer thickness is equal to total thickness of the ER fluid core and elastic constraining layers. The constraint of the optimization problem is the total mass of the sandwich structure in which the treating layers should not increase the mass of the host structure more than 50%. First, the genetic algorithm is used in an attempt to find approximate global optimum results. Then, to accurately capture the optimum results, the GA results are, in turn, fed as initial values into the powerful sequential quadratic programming technique available in MATLAB. The binary numbers [0 1] are employed to define the location of the viscoelastic and constrained ER fluid in the sandwich panel structure. Therefore the initial population is created using random binary vectors in a way that 0 is assigned to a place where there is a constrained ER fluid patch and 1 is assigned to the place where there is an unconstrained viscoelastic patch. The length of the vector depends on the number of the element. Here, the panel structure has been discretized using 8 by 8 elements in circumferential and axial directions. Also the edge of the panel structure has been treated using the viscoelastic patches in order to achieve sealing. Therefore, the binary numbers are assigned to the 6 by 6 elements to define the configuration of the treatments. Considering the other continuous variables including the thickness ratios of the treating layers and electric field intensity, the vector of design variables has 39 components. Since two types of variable are included in the genetic algorithm, the functions in the genetic algorithm should be customized to incorporate

both binary numbers and continuous values in the optimization process. In genetic algorithm for the individuals which include only binary numbers, the useful "Scattered" function is employed for creating the Crossover Children which merges the parents by choosing randomly from the variables of the first and second parent. The crossover function is also customized to create the children. Considering this, the "Intermediate" function is used to create the thicknesses of the treating layers and electric field intensity in which weighted average of the thicknesses and field intensities from the parents are evaluated. The Mutation function has been also customized in a way that with probability less than 10%, random numbers of the variables are switched from 0 to 1 and vice versa. For the elements of an individual representing the thickness ratios and electric field intensity, the Gaussian function is used to add random values to these elements. The optimum thicknesses and electric field intensity can be further improved using sequential quadratic programming subjected to the constraint on the total mass. The result obtained by genetic algorithm is used as the starting point for the sequential quadratic programming procedure. In summary, the optimization problem can be represented as:

$$\begin{cases} \text{Maximize} \quad \eta_i(\chi) \quad i=1,2 \\ \text{s. t.} \quad m_{\text{tot}}(\chi) - \left(1+\dfrac{\beta}{100}\right) m_b \le 0 \end{cases} \tag{7.28}$$

in which m_{tot} is the total mass of the sandwich panel structure, m_b is the mass of the bare layer, and χ is vector of design variable including binary numbers and continuous values, and β is the percentage of increase in the mass of the host structure which is assumed to be β=50 in present work. In the optimization problem, the electric field intensity has been constrained to not exceed 2kV/mm. In general, with increasing the electric field the material loss factor and consequently structural loss factor increases.

The reason to include the electric field intensity in design variable is to check if for all boundary conditions the electric field should be chosen as high as possible.

7.4 Results and Discussion

In the following the parametric study are presented to show the effect of electric field intensity and thickness ratios of the treating layers on damping characteristics of the sandwich panel structure including the natural frequency, loss factor and frequency response function for different boundary conditions. The boundary conditions include CCCC (all edges are clamped) SSSS (all edges are simply-supported) CFCF (the two edges along circumferential direction are clamped while the other two edges are free) and SFSF (the two edges along circumferential direction are simply-supported while the other two edges are free). Finally the optimization results have been presented for these boundary conditions.

7.4.1 Effects of electric field intensity and thickness of the top layer on damping characteristics

In linear regime, the main parameters which influence the damping behavior of the sandwich panel structure with constrained ER fluid layer is the thickness ratios of the layers, boundary condition and electric field intensity. The material properties and the dimensions of the top and bottom layers are chosen in order to achieve moderate values of natural frequency for different boundary conditions since the experimental data are extracted for moderate frequencies. The elastic top and bottom layers of the sandwich panel structure are aluminum sheets in which E_i= 68 GPa, ρ_i=2766 kg/m^3 and υ_i=0.3. The dimensions of the sandwich bare panel are chosen so that b/L=1, r/L=3, h_b/L=0.0025. The material properties of the viscoelastic and ER fluid materials have been

explained in finite element modeling section and also given in chapter 5. Here parametric study has been conducted to realize the effect of electric field intensity, e, and the thickness ratio of the elastic face to base layer, R_t, on the vibration damping behavior at the first two natural frequencies of the ER based sandwich cylinder. The thickness ratio of the ER core layer to base layer, R_c, has been assume to be 0.5.

The effect of electric field intensity and thickness of constraining face on natural frequency for first two modes is shown in Figure 7.2 for different boundary conditions. It has been assumed that the bare structure is treated with constrained ER fluid core layer and the unconstrained viscoelastic patches cover the elements along the edges. For SSSS and CCCC boundary conditions, the natural frequencies associated with the first two modes initially decrease with increasing the thickness of the elastic face indicating that the total mass of the structure increases rather than its stiffness. However, with more increasing the thickness of elastic face, the increase in the stiffness of the structure leads to increase in the natural frequencies. Similar behavior can be observed for the second natural frequency of the CFCF and SFSF boundary conditions. On the other hand, for the CFCF and SFSF boundary conditions, with increasing the thickness of the elastic face the first natural frequency slightly increases initially and then decreases until certain value which afterward starts increasing. Also, as the electric field intensity increases, the stiffness of the structure and consequently the natural frequencies increase for different boundary conditions.

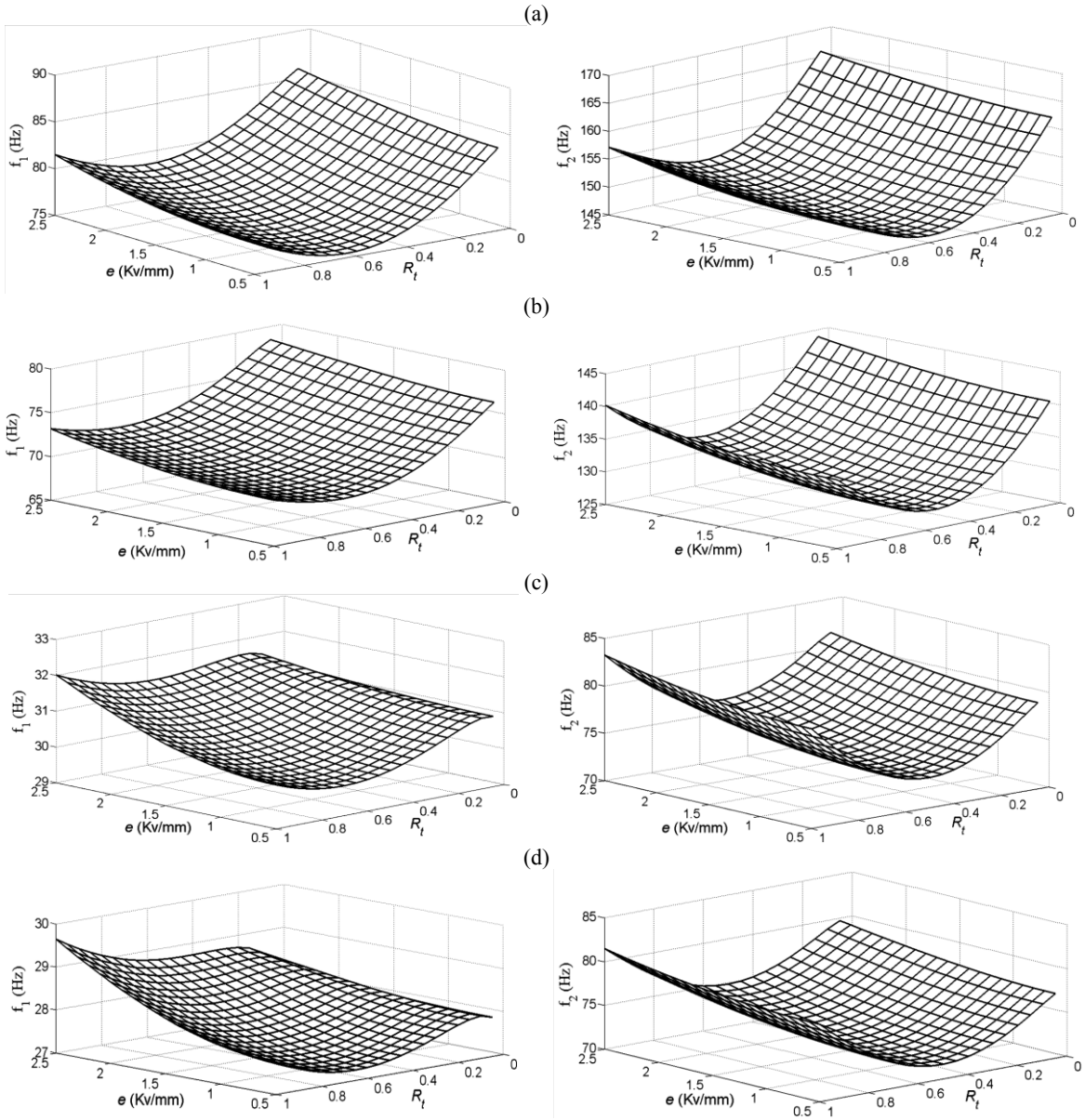

Figure 7.2 Effect of electric field intensity and thickness ratio of the top layer on the first two natural frequencies in transverse vibration of sandwich panel structure; (a) CCCC, (b) SSSS, (c) CFCF, (d) SFSF boundary conditions; R_c=0.5.

The effect of the electric field intensity and thickness ratio of the elastic face on the loss factor associated with the first two modes is also shown in Figure 7.3. For the CCCC and SSSS boundary conditions, the structural loss factors increases as the thickness of elastic top layer increases, however, the rate of increase decreases at the larger thicknesses.

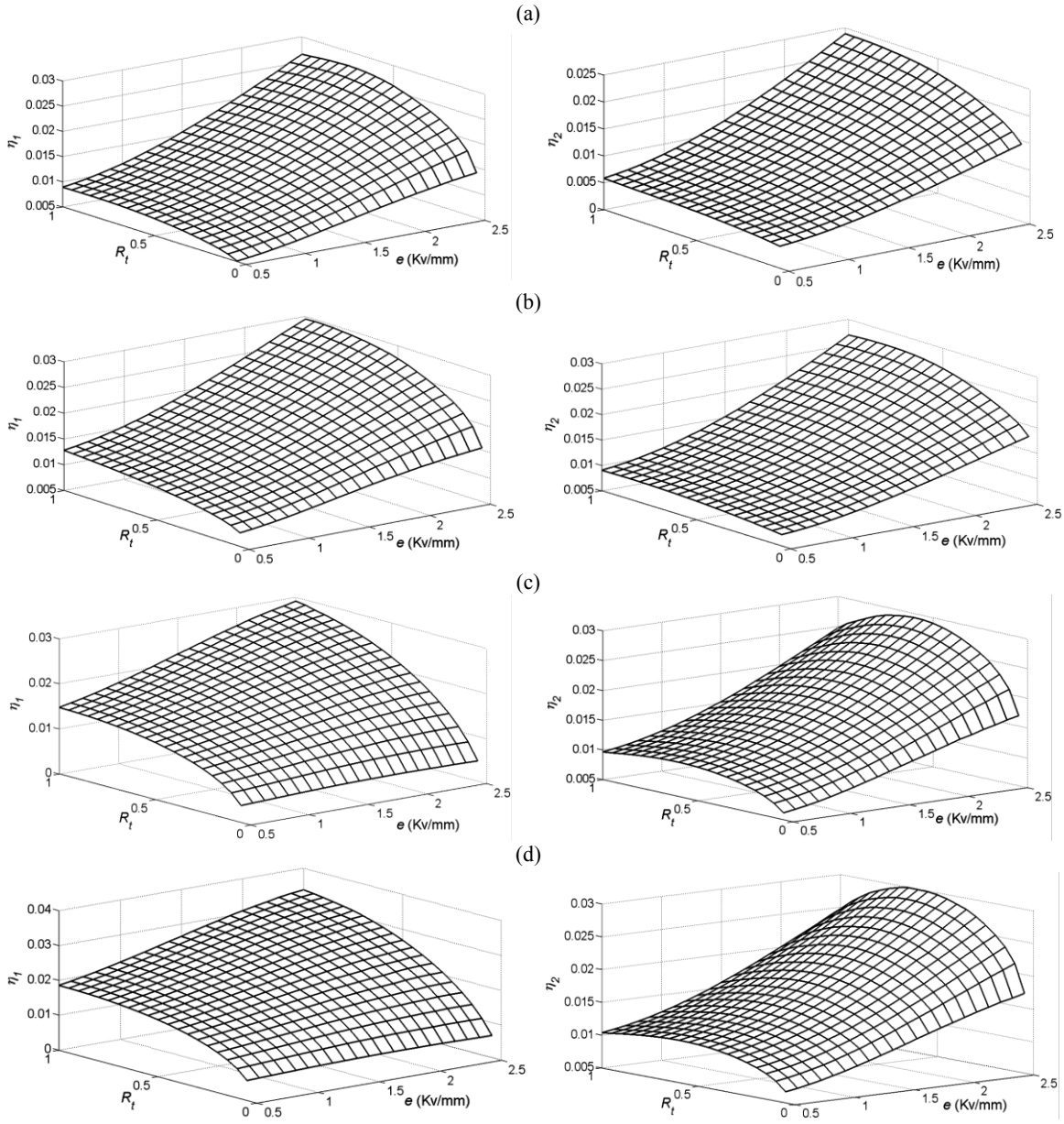

Figure 7.3 Effect of electric field intensity and thickness ratio of the top layer on the first two loss factors in transverse vibration of sandwich panel structure; (a) CCCC, (b) SSSS, (c) CFCF, (d) SFSF boundary conditions; R_c=0.5

The thickness of the top layer has greater effect at higher electric field intensities. Similar behavior can be observed for CFCF and SFSF at the fundamental frequency. However, for the second transverse mode of vibration at high electric field intensity the structural loss factor initially increases and then decreases.

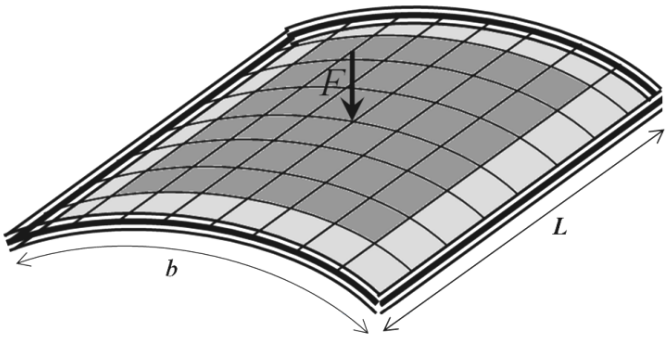

Figure 7.4 Sandwich panel structure under point load exerted at the middle of the panel. The unconstrained viscoelastic and constrained ER fluid patches are respectively identified by light and dark grey squares

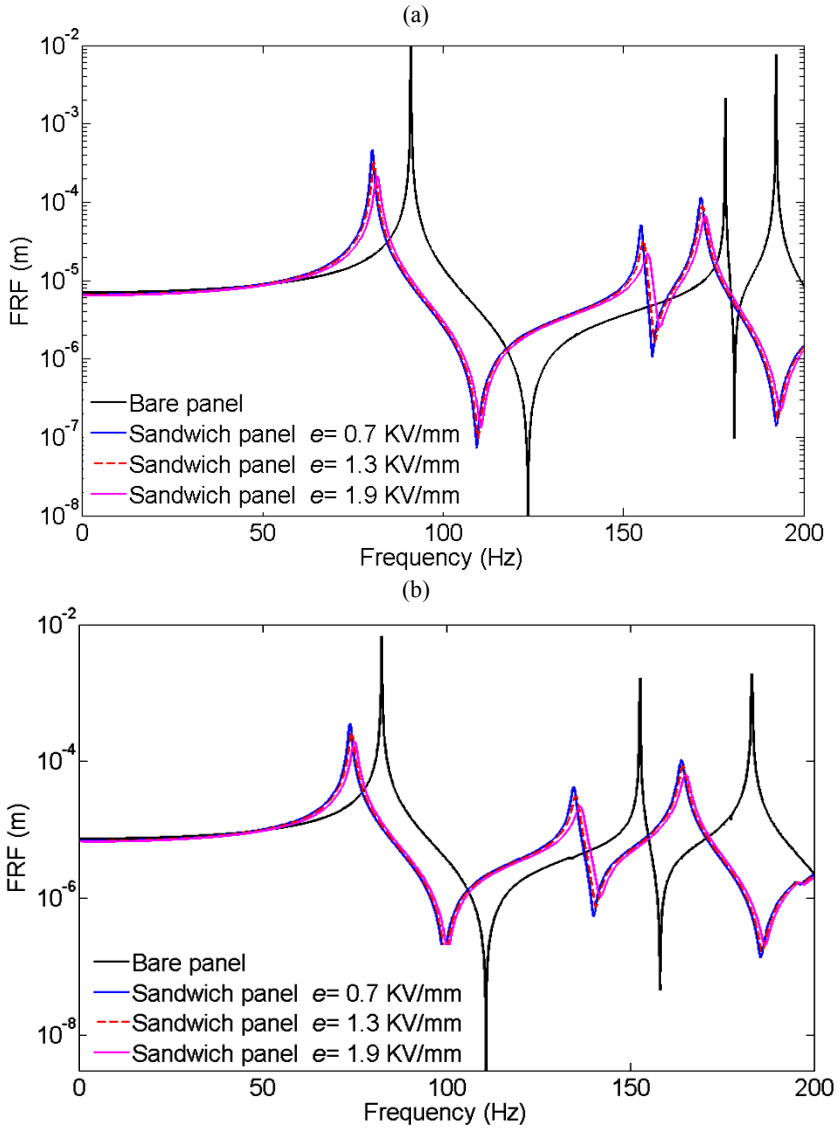

Figure 7.5 Effect of electric field intensity on the frequency response function of sandwich panel structure fully treated with ER fluid patches; (a) CCCC, (b) SSSS boundary conditions; R_t=0.2, R_c=0.5

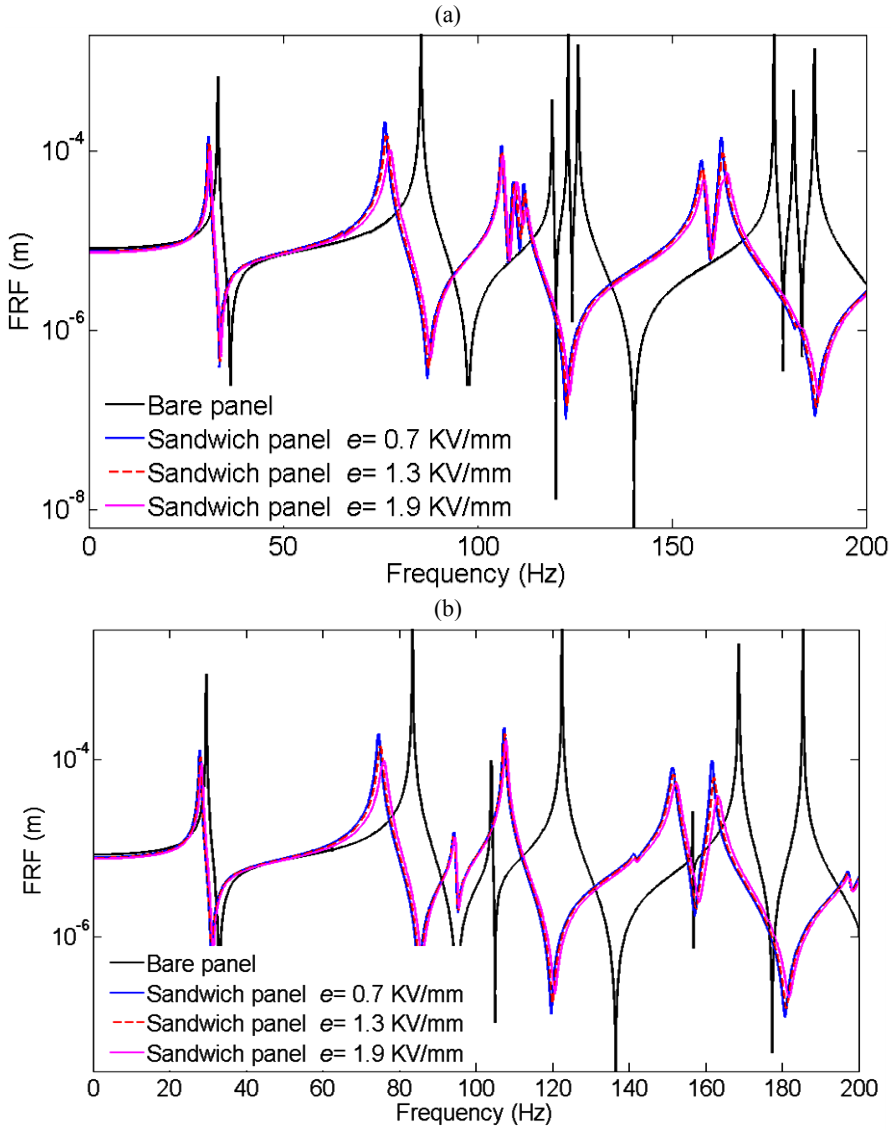

Figure 7.6 Effect of electric field intensity on the frequency response function of sandwich panel structure fully treated with ER fluid patches; (a) CFCF, (b) SFSF boundary conditions; R_t=0.2, R_c=0.5

This indicates that the for large electric field intensity, moderate value of thickness should be assigned to the elastic top layer. The structural loss factors for all types of boundary conditions increase with increasing the electric field intensity. In order to observe the effect of electric field intensity on structural loss factor, the frequency response function (FRF) under a point load exerted in the middle of the sandwich panel shown in Figure 7.4 is investigated for different boundary conditions. As expected from the results shown in Figures 7.2 and 7.3, with increasing the electric field intensity the

natural frequencies increase and response amplitudes decrease for the sandwich panel as can be realized from Figures 7.5 and 7.6 for different boundary conditions.

7.4.2 Optimization Results

Using the optimization methodology described before, the optimal configurations of treating viscoelastic and ER patches for the first two modes in transverse vibration of the sandwich panel structure under different boundary conditions have been obtained.

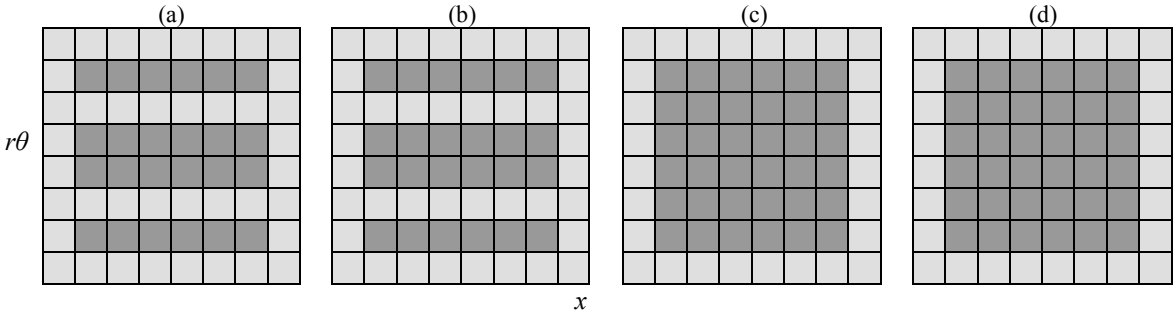

Figure 7.7 Distribution of unconstrained viscoelastic and constrained ER fluid patches for different boundary conditions to optimally suppress vibration in the first mode; (a) CCCC, (b) SSSS, (c) CFCF, (d) SFSF boundary conditions. The unconstrained viscoelastic and constrained ER fluid patches are respectively identified by light and dark grey squares

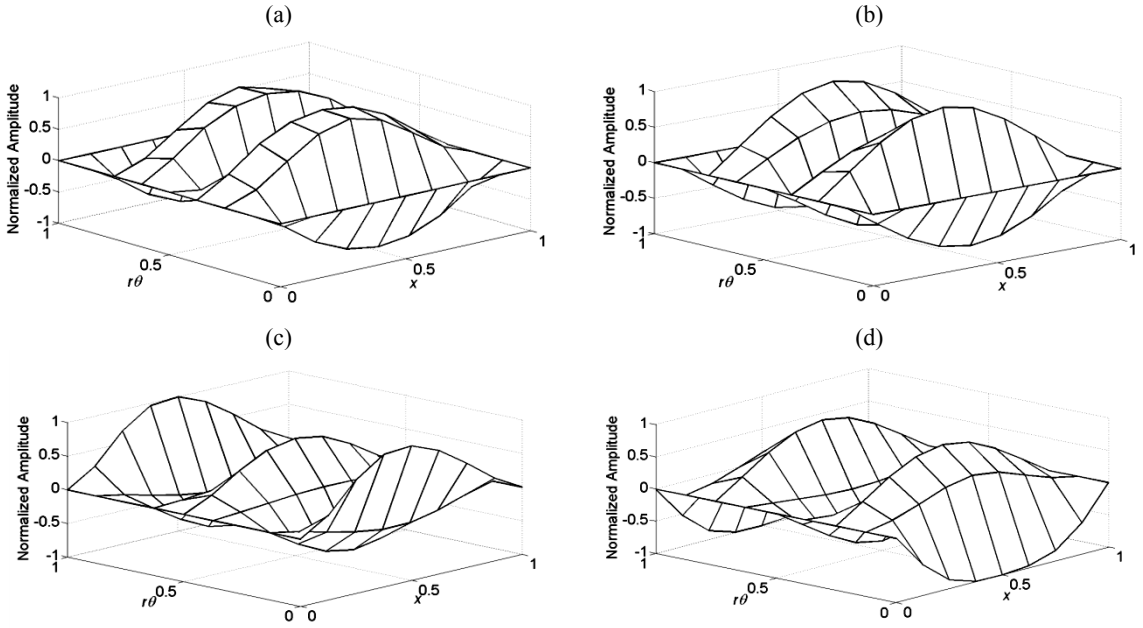

Figure 7.8 Mode shapes associated with the first transverse mode, (a) CCCC, (b) SSSS, (c) CFCF, (d) SFSF boundary conditions

The geometrical and material characteristics of the sandwich panel are the same as those used in paramedic study in previous sub-section. The results for the first mode are shown in Figure 7.7. It should be noted that the unconstrained viscoelastic and constrained ER fluid patches are respectively identified by light and dark grey squares. As mentioned before, in order to achieve perfect sealing, the regions on the boundaries should be treated by the unconstrained viscoelastic patches.

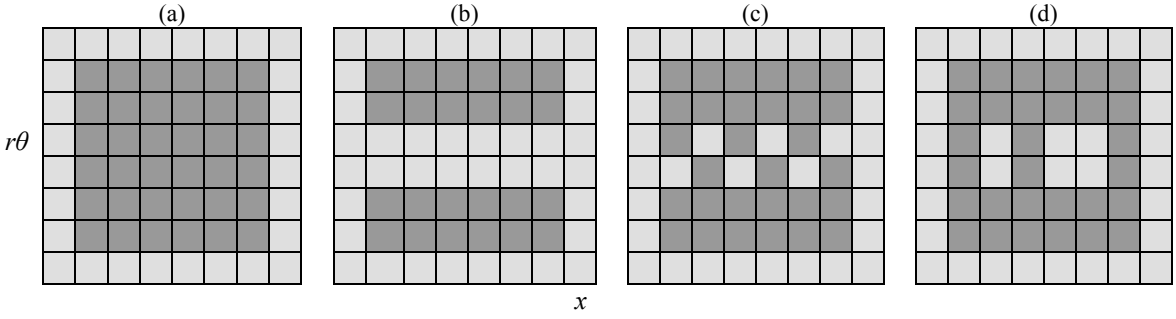

Figure 7.9 Distribution of unconstrained viscoelastic and constrained ER fluid patches for different boundary conditions to optimally suppress vibration in the second mode; (a) CCCC, (b) SSSS, (c) CFCF, (d) SFSF boundary conditions. The unconstrained viscoelastic and constrained ER fluid patches are respectively identified by light and dark grey squares.

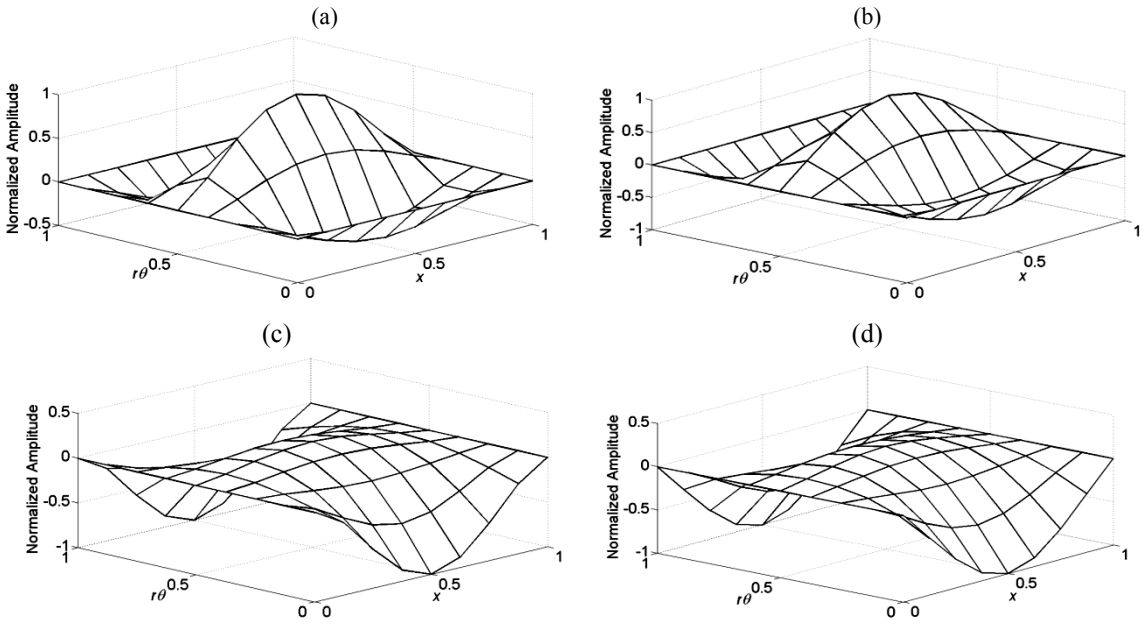

Figure 7.10 Mode shapes associated with the second transverse mode, (a) CCCC, (b) SSSS, (c) CFCF, (d) SFSF boundary conditions.

According to the optimization results, the regions near to the edges next to the region treated by unconstrained viscoelastic patches along the axial directions should be treated by the constrained ER fluid patches for CCCC and SSSS boundary conditions. The mode shapes associated to the first mode of the CCCC and SSSS boundary conditions are respectively shown in Figures 7.8 (a) and (b). One can observe that the constrained ER fluid patches are located on the elements with larger variation of transverse displacements which provide larger shear deformation energy and consequently more energy dissipation. On the other hand, the unconstrained viscoelastic patches are located on the elements with less variation in their transverse nodal displacements. For CFCF and SFSF boundary conditions, the optimization problem results in fully treated sandwich panel with constrained ER fluid patches. According to the mode shapes shown in Figures 7.8 (c) and (d), the panel structure is under large variation of transverse nodal displacement at the first mode. Therefore the panel structure should be fully treated with the constrained ER fluid patches in which higher damping is resulted. Similar studies are presented for the second mode of the transverse vibration. The optimal configurations of the treatments for the second mode under different boundary conditions are shown in Figure 7.9. The mode shapes associated to the second natural frequency for different boundary conditions are also shown in Figure 7.10. According to the results, for the CCCC boundary condition the panel structure should be fully treated by the constrained ER fluid patches while for the SSSS boundary condition, unconstrained viscoelastic patches should be used to treat the elements located in the middle of the panel structure where there is less variation in transverse nodal displacement.

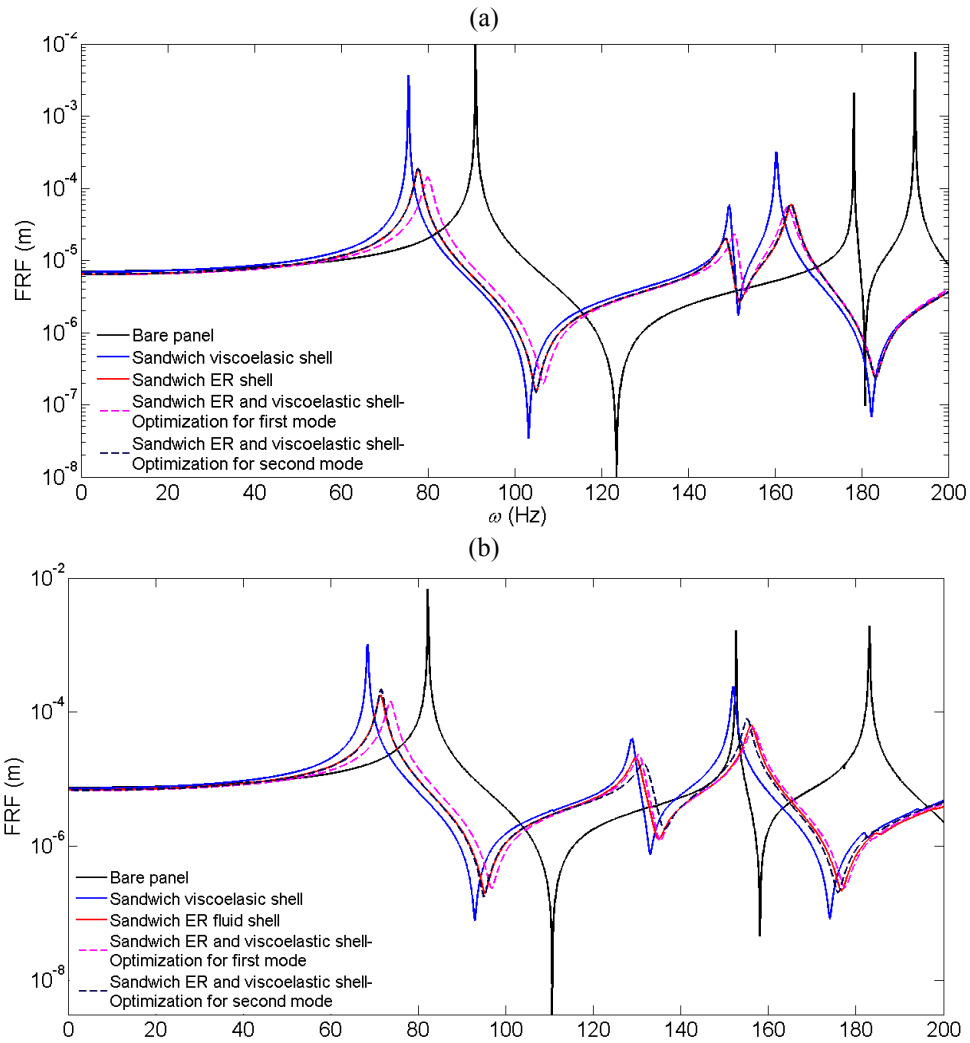

Figure 7.11 Frequency response functions due the different types of treatments; (a) CCCC, (b) SSSS boundary conditions

For the CFCF and SFSF boundary conditions the configurations shown in Figures 7.9 (c) and (d) give the maximum damping in the panel structure. In these configurations, the unconstrained viscoelastic treatments are distributed on the elements located in the middle region of the panel structure. The optimal thickness ratios of the constraining layers resulted from optimization problem for different boundary conditions associated with the first and second modes are provided in Table 7.1. It should be noted that the thickness of the unconstrained viscoelastic layer is equal to the summation of thickness of the outer elastic and ER core layers.

Table 7.1 The optimum thickness ratios of the treating layers for different boundary conditions and mode shapes

Boundary condition	Mode number	R_t	R_c	Loss factor
CCCC	Mode 1	0.212	0.951	0.0229
	Mode 2	0.186	0.973	0.0139
SSSS	Mode 1	0.148	1.068	0.0240
	Mode 2	0.165	1.040	0.0214
CFCF	Mode 1	0.168	1.010	0.0168
	Mode 2	0.125	1.085	0.0226
SFSF	Mode 1	0.227	0.891	0.0218
	Mode 2	0.145	0.911	0.0230

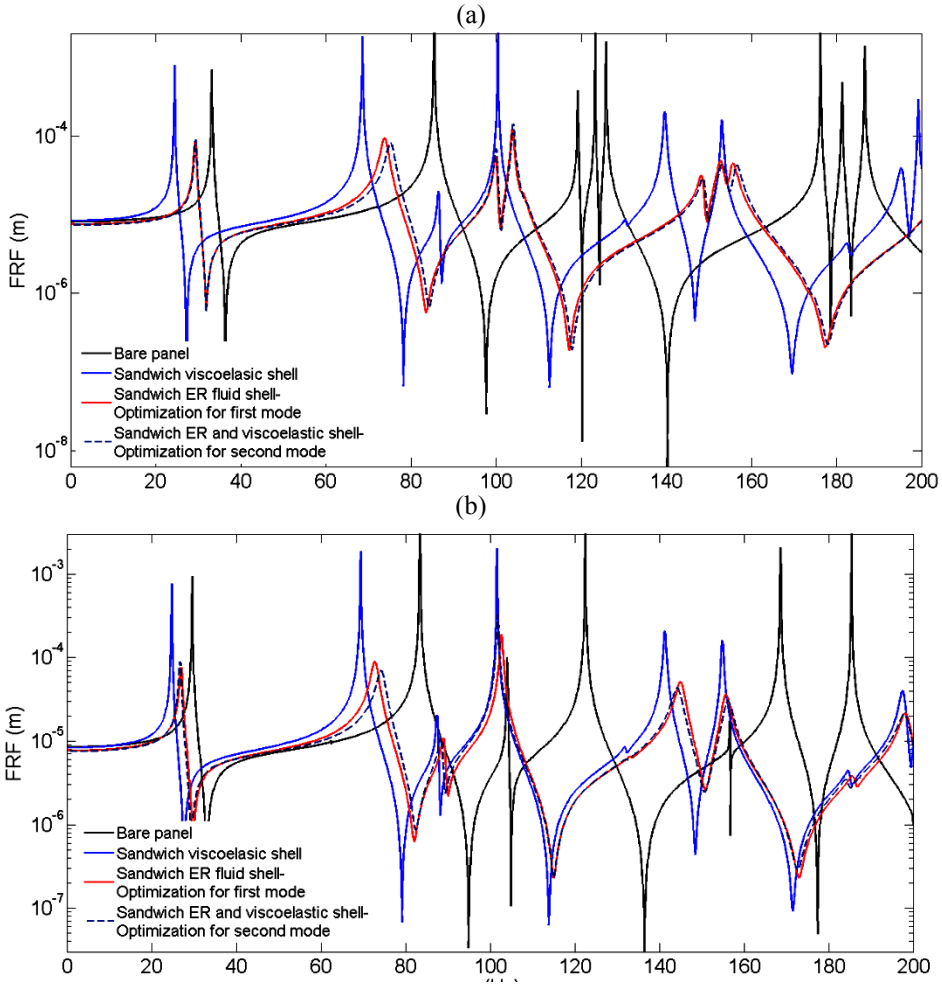

Figure 7.12 Frequency response functions due the different types of treatments; (a) CFCF, (b) SFSF boundary conditions

It is interesting to note that the optimization problem for different boundary conditions and modes results in the maximum electric field intensity (e≈2 KV/mm). This indicates that with increasing the electric field intensity the structural loss factors increase as

shown in Figure 7.3. In order to observe the damping effect of different types of treatments, the FRF of the sandwich panel structure based on the optimum treatments for the first and second modes are compared with the FRF of the bare panel structure and fully treated sandwich panel structure using the unconstrained viscoelastic or constrained ER fluid patches. It is assumed that the structure is subjected to a point force in transverse direction at the middle point of the panel structure as shown in Figure 7.4. Figures 7.11 and 7.12 show the FRFs for different boundary conditions. It should be noted that the thickness ratios in fully treated configurations are based on the results from the optimization problem for the first mode. The results show that fully treated sandwich panel using the unconstrained viscoelastic patches exhibits less damping compared with other types of treatments. This can represent the damping behavior of constrained viscoelastic sandwich structures at high temperature which significantly affects the damping property. As shown before, for some boundary conditions the damping behavior based on the fully treated sandwich panel with constrained ER fluid patches can be improved by embedding the unconstrained viscoelastic patches. The results show that optimization problem for CCCC and SSSS boundary conditions based on the first mode leads to more damping at the higher modes (except at the second mode). However, the optimization based on the second mode provides more damping at the higher modes of sandwich panel structure for CFCF and SFSF boundary conditions.

7.5 Conclusion

A design optimization methodology has been presented in this chapter to increase the damping behavior of sandwich panel structure using both unconstrained viscoelastic and constrained ER fluid patches. The unconstrained viscoelastic layer was mainly used to

seal the constrained ER fluid patches. An efficient element was employed to discretize sandwich panel structure. The finite element modeling was combined with the optimization algorithm including genetic algorithm and sequential quadratic programming to conduct the design optimization problem. The parameters of optimization including the configuration of the treating patches, thickness ratios of elastic faces and ER fluid core layer and also electric field intensity were effectively considered in the optimization problem using the vector of binary numbers and continuous values. The optimization problem for different boundary conditions and modes resulted in the maximum electric field intensity. At the first mode, fully treated configuration using ER fluid patches was resulted for CFCF and SFSF boundary conditions. On the other hand, the configurations including both unconstrained viscoelastic and constrained ER fluid patches were resulted for CCCC and SSSS boundary conditions. It was shown that only for the CCCC boundary condition at the second mode the treatment should be fully performed using the constraint ER fluid patches.

CHAPTER 8

CONCLUSION, CONTRIBUTION AND FUTURE WORK

8.1 Major Contributions and Achievements

Vibration damping analysis of sandwich cylindrical shell/panel structure using passive and semi-active damping was investigated in this dissertation. The passive damping using viscoelastic material was studied based on the semi-analytical finite element modeling. In order to achieve more accuracy, a higher order expansion of displacement fields was developed for representing displacement field of the core layer. The higher order displacement field was then used to model cut and partial treatment since the displacement fields of the core layer can be represented in terms of those at the top and bottom layers. Also the formulations have been derived considering the slippage between the layers at the interfaces. The effect of the main parameters on damping behavior of viscoelastic based sandwich shell structure was also investigated. In order to realize the effect of temperature, the transient heat transfer equation was formulated and solved for axisymmetric cylindrical structure using the finite difference method for irregular grid. Furthermore the effect of temperature and the resulted thermal stress on damping behavior of viscoelastic sandwich cylinder was investigated using the higher order expansion of the displacement field in the core layer. Using combined genetic algorithm and sequential quadratic programming technique, the design optimization was conducted to simultaneously optimize thickness ratios of treating layers, number of cuts and partial treatments and their distribution to achieve the highest damping for different boundary conditions. Considering semi-active damping treatment, the material properties of an ER fluid consisting suspension of cornstarch into corn oil were experimentally explored

systematically for small/large shear strain amplitude, moderate range of frequencies and different electric field intensities. A new constitutive model was also presented to predict the experimental data. The constitutive model was able to predict the stress response and the mechanical properties including loss modulus and shear modulus. Using the proposed constitutive model, the nonlinear vibration analysis of sandwich ER based panel structure was investigated for different boundary conditions. An efficient shell element was used to discretize the sandwich structure. Also, a new notation referred to as H-notation was presented over the two well-known notations referred to as B and N notations to represent the nonlinear equations of motion. This notation considerably reduced the computational costs associated with the time consuming integrations in the nonlinear vibration analysis of structure using conventional direct iterating technique since the integrations was only performed once throughout this technique. Finally the optimization problem was conducted in order to achieve the highest damping in sandwich panel structure using both passive and semi-active damping treatment patches. In the following the major conclusions regarding the results presented in this dissertation have been summarized.

8.2 Major Conclusions

I. The finite element model which considers the continuity in transverse shear stresses at the interfaces provides more accurate results for the three-layered structure with stiff core layer. For viscoelastic sandwich structures in which the material of the core layer is compliant, the continuity in transverse shear stresses should not be considered.

II. The higher order model exhibits more damping properties than the lower order model which leads to less time required to reach the steady state response in the transient vibration. Both models almost result in identical natural frequencies. Also, the results from the lower and higher order models deviate for thick core layer considerably at higher natural frequencies.

III. Slippage between layers at the interfaces reduces the damping characteristic and must be prevented in order to achieve higher damping in sandwich cylindrical shell structure.

IV. In order to increase the damping of sandwich cylindrical shell with thin viscoelastic core layer, the thickness of the constraining layer should increase. For thick viscoelastic core layer, increase in top layer thickness leads to decrease in loss factor. Where the constraining layer is thin, thick viscoelastic core layer show higher damping property than the thin viscoelastic core layer. On the other hand, for thick constraining layer, by increasing the thickness of viscoelastic core layer, loss factor first decreases and then increases.

V. Increase in external pressure of viscoelastic sandwich cylindrical shell leads to increase in the flexibility. Consequently, the natural frequencies decrease and the corresponding loss factors increase. On the other hand, in the sandwich cylinder under internal pressure the natural frequencies increase and accordingly the corresponding loss factors decrease because of higher stiffness introduced in the sandwich structure.

VI. With increasing the temperature, loss factor and real part of the viscoelastic layer decrease. This leads to decrease in damping behavior and natural frequencies of viscoelastic sandwich cylinder. Also, the resulted pre-stresses in the sandwich shell structure due to the thermal loads increase the stiffness of the structure. Consequently, the natural frequencies almost remain unchanged except at higher natural frequencies. However, reduction in damping performance of the viscoelastic material and the developed thermal stresses considerably decrease the loss factor of the structure.

VII. The generated heat in the viscoelastic layer under oscillatory loading will be transferred to constraining layer after long time due to low conductivity in the viscoelastic material. Therefore the temperature keeps on increasing at the viscoelastic layer which leads to decrease in loss factor and shear modulus, and consequently larger amplitude of displacement is resulted. Also, the amplitude reaches its steady state faster under forced convection. According to the shapes and slopes of the hysteresis trajectories, the area of the ellipse that represents dissipated energy is changing during time. Thus, the definition of loss factor is not unique even at the natural frequencies.

VIII. Unconstrained viscoelastic sandwich structure exhibits poor damping property since small shear stress at the damping layer is generated. Due to increase in the total mass of the structure while small change in the stiffness, the natural frequency considerably decreases with increasing the thickness of the viscoelastic layer. The loss factor increases as the unconstrained viscoelastic layer becomes thicker which is especially more pronounced for the lower modes.

IX. Although the partial treatment process can reduce significantly total weight of the structure, an inappropriate distribution can reduce the damping properties. Thus a design optimization strategy is required to identify the optimal configuration. However, cutting in the core and top layers increases the damping property compared with the fully treated sandwich cylinder. Also increasing the total number of cuts does not guarantee to increase the damping properties.

X. A systematic experimental study has been conducted to characterize the created in-house ER fluid and the proposed constitutive model was able to accurately predict the experimental results. The results show that the complex modulus of the ER fluid increases with increasing the field intensity. Furthermore, as the amplitude of the shear strain increases the storage modulus decreases, however, the loss modulus first increases and then decrease. Also, the complex modulus increases with increasing the frequency up to certain point and then remains constant for moderate range of the frequency.

XI. Although the yielding stress in the proposed constitutive model for the ER fluid was assumed to be negligible, due to including the strain amplitude in the proposed model the linear regime was discernible whereas by increasing the strain amplitude the rate of increase in the stress amplitude decreases.

XII. The new notation referred to as H-notation developed for nonlinear stiffness matrices in equations of motion considerably reduced the computational costs since the integrations were performed only once before implementing the direct iteration procedure and consequently the repeatedly time consuming integrations

has been avoided. According to the experimental data available in literature, the results showed that the developed finite element modeling leads to more accurate results compared with the hierarchical finite element modeling particularly at large displacements.

XIII. According to the results, in ER based sandwich panel the natural frequency increases with increasing the displacement of vibration indicating that the nonlinear behavior has hardening effect and stiffen the structure. The rate of increase in frequency ratio for simply supported boundary conditions is higher than the clamped boundary conditions.

XIV. The electric field has a negligible effect on the frequency ratio (ω_{NL}/ω_{L}) of the ER sandwich panel so that with increasing the electric field intensity, the frequency ratio slightly decreases for different boundary conditions.

XV. With small increase in the shear strain amplitude, the loss modulus of the ER fluid initially increases. This leads to increase in the structural loss factor ratio up to certain value as the amplitude increases. With more increase in displacement, effects of decrease in material loss modulus and the hardening of the structure considerably reduce the structural loss factor ratio.

XVI. With increasing the electric field intensity, the loss modulus of the ER fluid material increases and consequently the structural loss factor increases. On the other hand, with increasing electric field intensity, the loss factor ratio (η_{NL}/η_{L}) first decreases and then increases.

XVII. The structural loss factor for SSSS boundary condition of ER based sandwich panel structure is greater than that for CCCC boundary condition since the transverse shear strains in the core layer are greater in SSSS boundary condition indicating more energy dissipation in the structure. However, due to the larger shear strain amplitude in CFCF boundary condition compared with the SFSF boundary condition, the structural loss factor is slightly greater in CFCF boundary condition.

XVIII. For ER based sandwich structure, with increasing the amplitude of vibration, the variation rate of loss factor with respect to core thickness amplitude decreases and for large amplitudes the loss factor is almost constant with respect to core thickness ratio. For the clamped (CCCC and CFCF) boundary conditions, at large displacements with increasing the core thickness ratio the natural frequency initially increases and then slightly decreases while at small displacements the natural frequency increases as the core thickness ratio increases. Similarly, for the simply supported (SSSS and SFSF) boundary conditions, at small displacements the natural frequency increases as the core thickness ratio increases. However, at large displacements the natural frequency decreases with increasing the core thickness ratio.

XIX. For SSSS and CCCC boundary conditions, the natural frequencies associated with the first two modes of ER fluid sandwich panel initially decrease with increasing the thickness of the elastic face. However, with more increasing the thickness of elastic face, the increase in the stiffness of the structure leads to increase in the natural frequencies. Similar behavior can be observed for the second natural

frequency of the CFCF and SFSF boundary conditions. However, for the CFCF and SFSF boundary conditions, with increasing the thickness of the elastic face the first natural frequency slightly increases initially and then decreases until certain value which afterward starts increasing. As the electric field intensity increases, the stiffness of the structure and consequently the natural frequencies increase for different boundary conditions.

XX. For the CCCC and SSSS boundary conditions of the ER based sandwich panel, the structural loss factors increases as the thickness of elastic top layer increases, however, the rate of increase decreases at the larger thicknesses. The thickness of the top layer has greater effect at higher electric field intensities. Similar behavior can be observed for CFCF and SFSF at the fundamental frequency. However, for the second transverse mode of vibration at high electric field intensity the structural loss factor initially increases and then decreases. Therefore for large electric field intensity, moderate value of thickness should be assigned to the elastic top layer. However, for the second transverse mode of vibration at high electric field intensity the structural loss factor initially increases and then decreases.

XXI. From the optimization results it can be concluded that the constrained ER fluid patches are located on the elements with larger variation of transverse displacements which provide larger shear deformation energy and consequently more energy dissipation. On the other hand, the unconstrained viscoelastic patches are located on the elements with less variation in their transverse nodal displacements. The optimization problem for different boundary conditions and

modes results in the maximum electric field intensity ($e \approx 2$ KV/mm). This indicates that with increasing the electric field intensity the structural loss factors increase.

XXII. At the first mode, fully treated configuration using ER fluid patches was resulted in the optimization problem for CFCF and SFSF boundary conditions. On the other hand, the configurations including both unconstrained viscoelastic and constrained ER fluid patches were resulted for CCCC and SSSS boundary conditions. It was shown that only for the CCCC boundary condition at the second mode, the treatment should be fully performed using the constrained ER fluid patches.

XXIII. Finally, the optimization results showed that for some boundary conditions the damping behavior of the partially treated ER based sandwich panel is higher than that of fully treated ER based sandwich panel. The optimization problem for CCCC and SSSS boundary conditions based on the first mode leads to more damping at the higher modes (except at the second mode). However, the optimization based on the second mode provides more damping at the higher modes of sandwich panel structure for CFCF and SFSF boundary conditions.

8.3 Recommendation for the future works

In this dissertation the vibration damping analysis and optimization of sandwich shell/panel structure using both passive and semi-active damping treatments were systematically investigated. The developed models, analysis and design optimization formulations provide a unique platform to fundamentally design passive and adaptive

sandwich shell structures for optimal vibration suppression. Although the developed analytical, computational and experimental techniques have significantly advanced the state-of-the-art in the field of viscoelastic and smart fluid based multilayered structures, nevertheless, the following interesting aspects which are natural extension of the current work have been identified:

i. The developed finite element and semi-analytical finite element modeling can be extended to analyze vibration damping of more complicated structures such as other type of shell of revolution including sandwich conical and spherical structures.

ii. Semi-active control strategies based on different control techniques such as observer-based linear quadratic regulator (LQR), optimal control or fuzzy logic-based control can be developed to enhance vibration damping of the ER based sandwich structure in a closed-loop system under different loading conditions.

iii. Experimental study can be conducted to observe the vibration damping and the effect of the main parameters on the damping behavior of the viscoelastic based, ER based sandwich shell structure and their combinations for different range of temperature. The results from the optimization can be employed and compared with the fully treated structure based on ER and viscoelastic based sandwich structure

iv. The design optimization can be conducted in a way that the constrained ER fluid patches are induced with different field intensities. This can be

practically expensive or infeasible; however, the damping characteristics may increase.

Appendix

Six linear equations to be solved for finding the coefficients of the polynomials in the particular solution.

$$\frac{1}{12}K^*{h_c}^3{L_e}^2(2aa_2+nb_1)-\left(2aE_c{L_e}^2+2K^*h_caL_e{}^2(1+\upsilon_C)\right)a_0+K^*aL_e{}^2\left(u_2^t-u_2^b\right)$$
$$-\frac{1}{2}K^*h_caL_e\left(w_1^b+w_1^t-w_3^b-w_3^t\right)-\frac{1}{2}K^*aL^2\left(h_t\psi_{21}^t+h_b\psi_{21}^b\right)=0$$
$$\frac{1}{6}K^*{h_c}^3{L_e}^2nb_2-\left(2aE_c{L_e}^2+2K^*h_caL_e{}^2(1+\nu_C)\right)a_1+K^*h_ca\left(2w_1^t+2w_3^t+2w_1^b+2w_3^b-4w_2^t-4w_2^b\right)$$
$$+K^*aL_e\left(\frac{\left(\psi_{11}^t-\psi_{31}^t\right)}{2}h_t+\frac{\left(\psi_{11}^b-\psi_{31}^b\right)}{2}h_b+u_3^t-u_3^b+u_1^b-u_1^t\right)=0$$

$$-\left(2aE_c{L_e}^2+2K^*h_caL_e{}^2(1+\upsilon_c)\right)a_2+$$
$$K^*a\left(2u_3^t+4u_2^b+2u_1^t-4u_2^t-2u_1^b-2u_3^b+\left(2\psi_{21}^t-\psi_{11}^t-\psi_{31}^t\right)h_t+\left(2\psi_{21}^b-\psi_{11}^b-\psi_{31}^b\right)h_b\right)=0$$

$$-\frac{1}{12}K^*{h_c}^3{L_e}^2n(nb_0+aa_1)-\left(2a^2E_c{L_e}^2+2K^*h_ca^2{L_e}^2(1+\upsilon_c)\right)b_0-\frac{K^*h_caL_e{}^2n}{2}\left(w_2^t+w_2^b\right)$$
$$-K^*a^2{L_e}^2\left(\frac{h_t\psi_{22}^t+h_b\psi_{22}^b}{2}-v_2^t+v_2^b\right)=0$$

$$-\frac{1}{6}K^*{h_c}^3{L_e}^2n(aa_2+2nb_1)-\left(2a^2E_c{L_e}^2+2K^*h_ca^2{L_e}^2(1+\upsilon_c)\right)b_1+\frac{K^*h_canL_e}{2}\left(2w_1^b-w_3^b+w_1^t-w_3^t\right)$$
$$+K^*a^2L_e\left(\frac{\left(\psi_{12}^t-\psi_{32}^t\right)}{2}h_t+\frac{\left(\psi_{12}^b-\psi_{32}^b\right)}{2}h_b+v_3^t-v_3^b+v_1^b-v_1^t\right)=0$$

$$\frac{1}{12}K^*{h_c}^3{L_e}^2n^2b_2+\left(2a^2E_c{L_e}^2+2K^*h_ca^2{L_e}^2(1+\upsilon_c)\right)b_2$$
$$+K^*h_can\left(w_1^t-2w_2^t+w_3^t+w_1^b-2w_2^b+w_3^b\right)+$$
$$K^*a^2\left(\left(\psi_{12}^t-2\psi_{22}^t+\psi_{32}^t\right)h_t+\left(\psi_{12}^b-2\psi_{22}^b+\psi_{32}^b\right)h_b-2v_3^t+4v_2^t-2v_1^t+2v_3^b-4v_2^b+2v_1^b\right)=0$$

References

[1] D. Ross, U. Ungar, and U. Kerwin, "Damping of plate flexural vibrations by means of viscoelastic laminae," *Structural Damping* (*ASME*)*,* section (3), 1959.

[2] E. Ungar and E. Kerwin, "Loss factors of viscoelastic systems in terms of energy concepts," *Journal of the Acoustical Society of America,* vol. 34, pp. 954–957, 1962.

[3] D. J. Mead and S. Markus, "The forced vibration of a three-layer, damped sandwich beam with arbitrary boundary conditions," *Journal of Sound and Vibration,* vol. 10, pp. 163-175, 1969.

[4] R. A. DiTaranto and W. Blasingame, "Composite damping of vibrating sandwich beams," *Trans ASME* vol. Series B, pp. 633–638, 1967.

[5] M. J. Yan and E. H. Dowell, "Governing equations for vibrating constrained-layer damping sandwich plates and beams," *Journal of Applied Mechanics,* vol. 39, pp. 1041–1046, 1972.

[6] V. Oravský, Š. Markuš, and O. Šimková, "A new approximate method of finding the loss factors of a sandwich cantilever," *Journal of Sound and Vibration,* vol. 33, pp. 335-352, 1974.

[7] D. K. Rao, "Vibration of short sandwich beams," *Journal of Sound and Vibration,* vol. 52, pp. 253-263, 1977.

[8] D. K. Rao, "Frequency and loss factor of sandwich beams under various boundary conditions," *Journal of Mechanical Engineering Science,* vol. 20, pp. 271–282, 1978.

[9] G. Wang and N. M. Wereley, "Spectral finite element analysis of sandwich beams with passive constrained layer damping," *ASME Journal of Vibration and Acoustics,* vol. 124, pp. 376-386, 2002.

[10] G. Wang, S. Veeramani, and N. M. Wereley, "Analysis of sandwich plates with isotropic face plates and viscoelastic cores," *ASME Journal of Vibration and Acoustics,* vol. 122, pp. 305-312, 2000.

[11] T. C. Ramesh and N. Ganesan, "Finite element analysis of conical shells with a constrained viscoelastic layer," *Journal of Sound and Vibration,* vol. 171, pp. 577-601, 1994.

[12] M. G. Sainsbury and R. S. Masti, "Vibration damping of cylindrical shells using strain-energy-based distribution of an add-on viscoelastic treatment," *Finite Element in Analysis and Design,* vol. 43 pp. 175 –192, 2007.

[13] T. C. Ramesh and N. Ganesan, "Vibration and damping analysis of cylindrical shells with constrained damping treatment---A comparison of three theories," *Journal of Vibration and Acoustics,* vol. 117, pp. 213-219, 1995.

[14] J. M. Bai and C. T. Sun, "The effect of viscoelastic adhesive layers on structural damping of sandwich beams," *Mechanics of Structures and Machines,* vol. 23, pp. 1-16, 1995.

[15] D. McLean and B. E. Read, "Storage and loss moduli in discontinuous composites," *Journal of Materials Science,* vol. 10, pp. 481-492, 1975.

[16] D. J. Nelson and J. W. Hancock, "Interfacial slip and damping in fibre reinforced composites," *Journal of Materials Science,* vol. 13, pp. 2429-2440, 1978.

[17] T. T. Baber, R. A. Maddox, and C. E. Orozco, "A finite element model for harmonically excited viscoelastic sandwich beams," *Computers & Structures,* vol. 66, pp. 105-113, 1998.

[18] A. L. Araújo, C. M. Mota Soares, C. A. Mota Soares, and J. Herskovits, "Optimal design and parameter estimation of frequency dependent viscoelastic laminated sandwich composite plates," *Composite Structures,* vol. 92, pp. 2321-2327, 2010.

[19] D. I. G. Jones, "Temperature-frequency dependence of dynamic properties of damping materials," *Journal of Sound and Vibration,* vol. 33, pp. 451-470, 1974.

[20] G. A. Lesieutre and K. Govindswamy, "Finite element modeling of frequency dependent and temperature-dependent dynamic behavior of viscoelastic materials in simple shear," *International Journal of Solids and Structures,* vol. 33, pp. 419-432, 1996.

[21] T.-L. Teng and N.-K. Hu, "Analysis of damping characteristics for viscoelastic laminated beams," *Computer Methods in Applied Mechanics and Engineering,* vol. 190, pp. 3881-3892, 2001.

[22] M. Hao and M. D. Rao, "Vibration and damping analysis of a sandwich beam containing a viscoelastic constraining layer," *Journal of Composite Materials,* vol. 39, pp. 1621-1643, 2005.

[23] R. A. S. Moreira, J. D. Corte-Real, and J. D. Rodrigues, "A generalized frequency-temperature viscoelastic model," *Shock and Vibration,* vol. 17, pp. 407-418, 2010.

[24] A. Gupta and L. Kumar, "Thermal effect on vibration of non-homogenous visco-elastic rectangular plate of linearly varying thickness," *Meccanica,* vol. 43, pp. 47-54, 2008.

[25] C. T. F. Ross and T. Johns, "Vibration of circular cylinders containing water," *Thin-Walled Structures,* vol. 12, pp. 177-196, 1991.

[26] C. T. F. Ross, P. Haynes, and W. D. Richards, "Vibration of ring-stiffened circular cylinders under external water pressure," *Computers Structures,* vol. 60, pp. 1013-1019, 1996.

[27] C. T. F. Ross, "Finite elements for the vibration of cones and cylinders," *International Journal for Numerical Methods in Engineering,* vol. 9, pp. 833-845, 1975.

[28] F. Sabri and A. A. Lakis, "Hydroelastic vibration of partially liquid-filled circular cylindrical shells under combined internal pressure and axial compression," *Aerospace Science and Technology,* vol. 15, pp. 237-248, 2011.

[29] N. Ganesan and V. Pradeep, "Buckling and vibration of circular cylindrical shells containing hot liquid," *Journal of Sound and Vibration,* vol. 287, pp. 845-863, 2005.

[30] Z. Q. Xia and S. Lukasiewicz, "Effect of temperature changes on damping properties of sandwich cylindrical panels," *International Journal of Solids and Structures,* vol. 33, pp. 835-849, 1996.

[31] N. Ganesan and R. Kadoli, "Buckling and dynamic analysis of piezothermoelastic composite cylindrical shell," *Composite Structures,* vol. 59, pp. 45-60, 2003.

[32] V. Pradeep, N. Ganesan, and K. Bhaskar, "Vibration and thermal buckling of composite sandwich beams with viscoelastic core," *Composite Structures,* vol. 81, pp. 60-69, 2007.

[33] V. Pradeep and N. Ganesan, "Thermal buckling and vibration behavior of multi-layer rectangular viscoelastic sandwich plates," *Journal of Sound and Vibration,* vol. 310, pp. 169-183, 2008.

[34] G. Hausmann and P. Gergely, "Approximate methods for thermoviscoelastic characterization and analysis of elastomeric lead–lag dampers," *Proc. 18th European Rotorcraft Forum ,Avignon, France.,* 1992.

[35] P. Brahmananda, M. Evhen, and J. T. Frank, "Application of passive dampers to modern helicopters," *Smart Materials and Structures,* vol. 5, p. 509, 1996.

[36] S. Marathe, F. Gandhi, and K. W. Wang, "Helicopter blade response aeromechanical stability with a magnetorheological fluid based lag damper," *Journal of Intelligent Material Systems and Structures,* vol. 9, pp. 272-282, 1998.

[37] J. H. Yoo and N. M. Wereley, "Design of high efficiency magnetorheological valve," *Journal of Intelligent Material Systems and Structures,* vol. 13, pp. 679-685, 2002.

[38] H. Yoshoka, J. C. Ramallao, and B. F. Spencer, "Smart base isolation strategies employing magnetorheological dampers," *Journal of Engineering Mechanics,* vol. 128, pp. 540-551, 2002.

[39] Y. T. Choi and N. M. Wereley, "Vibration control of landing gear system featuring electrorheological/magnetorheological fluids," *Journal of Aircraft,* vol. 40, pp. 432-439, 2003.

[40] W. Hu and N. M. Wereley, "Hybrid magnetorheological fluid–elastomeric lag dampers for helicopter stability augmentation," *Smart Materials and Structures,* vol. 17, p. 045021 (16pp), 2008.

[41] P. M. Taylor, D. M. Pollet, A. Hosseini-Sianaki, and C. J. Varley, "Advances in an electrorheological fluid based tactile array," *Displays,* vol. 18, pp. 135-141, 1998.

[42] M. Mohebi and N. Jamasbi, "Simulation of the formation of nonequilibrium structures in magnetorheological fluids subject to an external magnetic field," *Physical Review E,* vol. 54, pp. 5407–5413, 1996.

[43] W. M. Winslow, "US Patent Specification 2417850," 1947.

[44] Y. Tian, Y. Meng, and S. Wen, "ER fluid based on zeolite and silicone oil with high strength," *Materials Letters,* vol. 50, pp. 120-123, 2001.

[45] J. P. Coulter, K. D. Weiss, and J. D. Carlson, "Electrorheological materials and their usage in intelligent material systems and structures, Part II: Applications,," *Recent Advances in Adaptive and Sensory Materials and Their Applications,*

eds., C. Rogers and R. Rogers, Technomic Publishing Company, Lancaster, PA,, pp. 507–523, 1992.

[46] T. G. Duclos, " . , pp: 2.532–2.536, "Design of devices using electrorheological fluids," *SAE Technical Paper 881134, doi:10.4271/881134,* 1988.

[47] D. A. Brooks, "Design and development of flow based electro-rheological devices," *nternational Journal of Modern Physics B,* vol. 6, pp. 2705–2730, 1992.

[48] H. Block, J. P. Kelly, A. Qin, and T. Watson, "Materials and mechanisms in electrorheology," *Langmuir,* vol. 6, pp. 6-14, 1990.

[49] M. S. Cho, H. J. Choi, and M. S. Jhon, "Shear stress analysis of a semiconducting polymer based electrorheological fluid system," *Polymer,* vol. 46, pp. 11484-11488, 2005.

[50] W. L. Zhang, Y. D. Liu, and H. J. Choi, "Graphene oxide coated core-shell structured polystyrene microspheres and their electrorheological characteristics under applied electric field," *Journal of Materials Chemistry,* vol. 21, 2011.

[51] M. Parthasarathy, K. H. Ahn, B. M. Belongia, and D. J. Klingenberg, "The role of suspension structure in the dynamic response of electrorheological suspensions," *International Journal of Modern Physics B,* vol. 8, pp. 2789–2809, 1994.

[52] M. Parthasarathy and D. J. Klingenberg, "Large amplitude oscillatory shear of ER suspensions," *Journal of Non-Newtonian Fluid Mechanics,* vol. 81, pp. 83-104, 1999.

[53] M. Parthasarathy and D. J. Klingenberg, "A microstructural investigation of the nonlinear response of electrorheological suspensions," *Rheologica Acta,* vol. 34, pp. 417-429, 1995.

[54] J. Claracq, J. Sarrazin, and J. P. Montfort, "Viscoelastic properties of magnetorheological fluids," *Rheologica Acta,* vol. 43, pp. 38–49, 2004.

[55] D. R. Gamota and F. E. Filisko, "Dynamic mechanical studies of electrorheological materials: Moderate frequencies," *J. Rheol.,* vol. 35, pp. 399-425, 1991.

[56] D. R. Gamota and F. E. Filisko, "High frequency dynamic mechanical study of an aluminosilicate electrorheological material," *J. Rheol.,* vol. 35, pp. 1411-1425, 1991.

[57] D. R. Gamota and F. E. Filisko, *Linear/non-linear mechanical properties of electrorheological materials*, 1991.

[58] D. R. Gamota, A. S. Wineman, and F. F.E., "Fourier transform analysis: non-linear dynamic response of an ER material," *Journal of Rheology,* vol. 37, pp. 919–933, 1993.

[59] W. H. Li, H. Du, G. Chen, S. H. Yeo, and N. Guo, "Nonlinear viscoelastic properties of MR fluids under large-amplitude-oscillatory-shear," *Rheologica Acta,* vol. 42, pp. 280–286, 2003.

[60] Y. Choi, A. F. Sprecher, and H. Conrad, "Vibration characteristics of a composite beam containing an electrorheological fluid," *Journal of Intelligent Material Systems and Structures,* vol. 1, pp. 91-104, 1990.

[61] C. Y. Lee and C. C.C., "Complex moduli of electrorheological material under oscillatory shear," *International Journal of Mechanical Sciences,* vol. 42, pp. 561-573, 2000.

[62] W. H. Li, G. Z. Yao, G. Chen, S. H. Yeo, and F. F. Yap, "Testing and steady state modeling of a linear MR damper under sinusoidal loading," *Smart Materials and Structures,* vol. 9, pp. 95-102, 2000.

[63] M. Wilhelm, "Fourier-transform rheology," *Macromolecular Materials and Engineering,* vol. 287, pp. 83–105, 2002.

[64] R. B. Bird, R. Armstrong, and O. Hassager, "Dynamics of polymeric liquids vol. 1 fluid mechanics," *John Wiley & Sons, New York,* 1987.

[65] K. D. Weiss, J. D. Carlson, and D. A. Nixon, "Viscoelastic properties of magneto and electro-rheological fluids," *Journal of Intelligent Material Systems and Structures,* vol. 5, pp. 772-775, 1994.

[66] K. Cho, K. Hyun, K. Ahn, and S. Lee, "A geometrical interpretation of large amplitude oscillatory shear response," *Journal of Rheology,* vol. 49, pp. 747-758, 2005.

[67] R. Ewoldt, A. E. Hosoi, and G. McKinley, "New measures for characterizing nonlinear viscoelasticity in large amplitude oscillatory shear," *Journal of Rheology,* vol. 52, p. 1427, 2008.

[68] C. Malcolm M, "Rheology of non-Newtonian fluids: A new flow equation for pseudoplastic systems," *Journal of Colloid Science,* vol. 20, pp. 417-437, 1965.

[69] T. C. Papanastasiou, "Flows of materials with yield," *Journal of Rheology,* vol. 3, pp. 385–404, 1987.

[70] M. K. Gopalakrishna and M. W. Norman, "A nonlinear viscoelastic-plastic model for electrorheological fluids," *Smart Materials and Structures,* vol. 6, pp. 351-359, 1997.

[71] R. C. Ehrgott and S. F. Masri, "Modeling the oscillatory dynamic behaviour of electrorheological materials in shear," *Smart Materials and Structures,* vol. 1, pp. 275-285, 1992.

[72] C. Lee, "Finite Element Formulation of a Sandwich Beam with Embedded Electro-Rheological Fluids," *Journal of Intelligent Material Systems and Structures,* vol. 6, pp. 718-728, 1995.

[73] C.-Y. Lee and C.-C. Cheng, "Complex moduli of electrorheological material under oscillatory shear," *International Journal of Mechanical Sciences,* vol. 42, pp. 561-573, 2000.

[74] H. M. Laun, C. Gabriel, and C. Kieburg, "Magnetorheological fluid in oscillatory shear and parameterization with regard to MR device properties," *Journal of Intelligent Material Systems and Structures,* vol. 21, pp. 1479-1489, 2010.

[75] M. Yalcintas and J. P. Coulter, "Electrorheological material based adaptive beams subjected to various boundary conditions," *Journal of Intelligent Material Systems and Structures,* vol. 6, pp. 700-717, 1995.

[76] M. Yalcintas and J. P. Coulter, "Analytical modeling of electrorheological material based adaptive beams," *Journal of Intelligent Material Systems and Structures,* vol. 6, pp. 488-497, 1995.

[77] Y. Choi, A. F. Sprecher, and H. Conrad, "Response of electrorheological fluid-filled laminate composites to forced vibration," *Journal of Intelligent Material Systems and Structures,* vol. 3, pp. 17-29, 1992.

[78] Y. Jia-Yi, "Finite element analysis of the cylindrical shells subjected to ER damping treatment," *Smart Materials and Structures,* vol. 17, pp. 1–7 2008.

[79] Y. K. Kang, J. Kim, and S. B. Choi, "Passive and active damping characteristics of smart electro-rheological composite beams," *Smart Materials and Structures,* vol. 10, pp. 724–729, 2001.

[80] Q. Sun, J.-X. Zhou, and L. Zhang, "An adaptive beam model and dynamic characteristics of magnetorheological materials," *Journal of Sound and Vibration,* vol. 261, pp. 465-481, 2003.

[81] G. Y. Zhou and Q. Wang, "Magnetorheological elastomer-based smart sandwich beams with nonconductive skins," *Smart Materials and Structures,* vol. 14, p. 1001, 2005.

[82] S. K. Dwivedy, N. Mahendra, and K. C. Sahu, "Parametric instability regions of a soft and magnetorheological elastomer cored sandwich beam," *Journal of Sound and Vibration,* vol. 325, pp. 686-704, 2009.

[83] V. Rajamohan, S. Rakheja, and R. Sedaghati, "Vibration analysis of a partially treated multi-layer beam with magnetorheological fluid," *Journal of Sound and Vibration,* vol. 329, pp. 3451-3469, 2010.

[84] V. Rajamohan, R. Sedaghati, and S. Rakheja, "Vibration analysis of a multi-layer beam containing magnetorheological fluid," *Smart Materials and Structures,* vol. 19, p. 015013 (12 p), 2010.

[85] A. Dominguez, R. Sedaghati, and I. Stiharu, "Modeling and application of MR dampers in semi-adaptive structures," *Computers & Structures,* vol. 86, pp. 407–415, 2008.

[86] M. Amabili and M. P. Paidoussis, "Review of studies on geometrically nonlinear vibrations and dynamics of circular cylindrical shells and panels, with and without fluid-structure interaction," *Applied Mechanics Reviews,* vol. 56, pp. 349-381, 2003.

[87] C.-Y. Chia, "Geometrically nonlinear behavior of composite plates: A Review," *Applied Mechanics Reviews,* vol. 41, pp. 439-451, 1988.

[88] K. A. Alhazza and A. A. Alhazza, "A review of vibrations of plates and shells " *The Shock and Vibration Digest,* vol. 36, pp. 377-395, 2004

[89] F. Moussaoui and R. Benamar, "Non-linear vibrations of shell-type structures: a review with bibliography," *Journal of Sound and Vibration,* vol. 255, pp. 161-184, 2002.

[90] L. H. Donnell, "Stability of thin walled tubes under torsion," *NACA Report. 479,* 1933

[91] J. H. Ginsberg, "Large amplitude forced vibrations of simply supported thin cylindrical shells," *Journal of Applied Mechanics,* vol. 40, pp. 471-477, 1973.

[92] V. V. Novozhilov, "Foundations of the nonlinear theory of elasticity," *Rochester, NY, USA Graylock Press,* 1953.

[93] J. L. Sanders, "Nonlinear theories of thin shells," *Quarterly of Applied Mathematics,* vol. 21, pp. 21–36, 1963

[94] M. Amabili, "Nonlinear vibrations and stability of shells and plate," *New York, Cambridge University Press,* 2008

[95] Z. Q. Xia and S. Lukasiewicz, "Nonlinear free damped vibrations of sandwich plates," *Journal of Sound and Vibration,* vol. 175, pp. 219–232, 1994.

[96] Z. Q. .Xia and S. Lukasiewicz, "Nonlinear analysis of damping properties of cylindrical sandwich panels," *Journal of Sound and Vibration,* vol. 186 pp. 55–69, 1995.

[97] E. M. Daya, L. Azrar, and M. Potier-Ferry, "An amplitude equation for the non-linear vibration of viscoelastically damped sandwich beams," *Journal of Sound and Vibration,* vol. 271, pp. 789-813, 2004.

[98] L. Azrar, E. H. Boutyour, and M. Potier-Ferry, "Non-linear forced vibrations of plates by an asymptotic–numerical method," *Journal of Sound and Vibration,* vol. 252, pp. 657-674, 2002.

[99] W. Han and M. Petyt, "Geometrically nonlinear vibration analysis of thin, rectangular plates using the hierarchical finite element method—I: The fundamental mode of isotropic plates," *Computers & Structures* vol. 63, pp. 295-308, 1997.

[100] M. K. Prabhakara and C. Y. Chia, "Non-linear flexural vibrations of orthotropic rectangular plates," *Journal of Sound and Vibration,* vol. 52, pp. 511-518, 1977.

[101] C.-F. Liu and C.-H. Huang, "Free vibration of composite laminated plates subjected to temperature changes," *Computers & Structures,* vol. 60, pp. 95-101, 1996.

[102] N. Nanda and J. N. Bandyopadhyay, "Nonlinear free vibration analysis of laminated composite cylindrical shells with cutouts," *Journal of Reinforced Plastics and Composites,* vol. 26 pp. 1413–1427, 2007.

[103] S. K. Panda and B. N. Singh, "Non-linear free vibration analysis of laminated composite cylindrical/hyperboloid shell panels based on higher-order shear deformation theory using non-linear finite-element method," *Proceedings of the Institution of Mechanical Engineers, Part G: Journal of Aerospace Engineering,* vol. 222, pp. 993-1006, 2008.

[104] S. K. Panda and B. N. Singh, "Nonlinear free vibration of spherical shell panel using higher order shear deformation theory– a finite element approach International " *Journal of Pressure Vessels and Piping,* vol. 86, pp. 373–383, 2009

[105] M. K. Singha and R. Daripa, "Nonlinear vibration of symmetrically laminated composite skew plates by finite element method," *International Journal of Non-Linear Mechanics,* vol. 42, pp. 1144-1152, 2007.

[106] R. Mallet and P. Marcal, "Finite element analysis of non-linear structures," *Journal of structural division,* vol. 94, pp. 2081-2105, 1968

[107] S. Rajasekaran and D. W. Murray, "On incremental finite element matrices," *Journal of structural division,* vol. 99, pp. 2423–2438, 1973

[108] R. D. Wood and B. Schrefler, "Geometrically nonlinear analysis–a correlation of finite element notations," *International Journal for Numerical Methods in Engineering,* vol. 12, pp. 635–642, 1978

[109] T. C. Ramesh and N. Ganesan, "Orthotropic cylindrical shells with a viscoelastic core: a vibration and damping analysis," *Journal of Sound and Vibration,* vol. 175, pp. 535-555, 1994.

[110] R. Plunkett and C. T. Lee, "Length optimization of constrained viscoelastic layer damping," *Journal of the Acoustical Society of America,* vol. 48, pp. 150-161, 1970.

[111] P. R. Mantena, R. F. Gibson, and S. J. Hwang, "Optimal constrained viscoelastic taped lengths for maximizing damping in laminated composites," *American Institute of Aeronautics and Astronautics Journal,* vol. 29, pp. 1678–1685, 1991.

[112] S. C. Huang, D. J. Inman, and E. M. Austin, "Some design considerations for active and passive constrained layer damping treatments," *Smart Materials and Structures* vol. 5, pp. 301–313, 1996.

[113] P. Trompette and J. Fatemi, "Damping of beams. Optimal distribution of cuts in the viscoelastic constrained layer," *Structural and Multidisciplinary Optimization,* vol. 13, pp. 167-171, 1997.

[114] M. A. Al-Ajmi and R. I. Bourisli, "Optimum design of segmented passive-constrained layer damping treatment through genetic algorithms," *Mechanics of Advanced Materials and Structures,* vol. 15, pp. 250-257, 2008.

[115] G. Lepoittevin and G. Kress, "Optimization of segmented constrained layer damping with mathematical programming using strain energy analysis and modal data," *Materials and Design,* vol. 31, pp. 14–24, 2010.

[116] V. Rajamohan, R. Sedaghati, and S. Rakheja, "Optimum design of a multilayer beam partially treated with magnetorheological fluid," *Smart Materials and Structures,* vol. 19, p. 065002 (15pp), 2010.

[117] Ü. Lepik, "Shape optimization of dynamically loaded viscoelastic cylindrical shells," *Structural and Multidisciplinary Optimization,* vol. 15, pp. 57-62, 1998.

[118] H. Zheng, C. Cai, G. S. H. Pau, and G. R. Liu, "Minimizing vibration response of cylindrical shells through layout optimization of passive constrained layer damping treatments," *Journal of Sound and Vibration,* vol. 279, pp. 739-756, 2005.

[119] Y. B. Chang, T. Y. Yang, and W. Soedel, "Linear dynamic analysis of revolutional shells using finite elements and modal expansion," *Journal of Sound and Vibration,* vol. 86 pp. 523–538, 1983.

[120] E. Barkanov, R. Rikards, C. Holste, and O. Täger, "Transient response of sandwich viscoelastic beams, plates, and shells under impulse loading" *Mechanics of Composite Materials* vol. 36, pp. 215–222 2000.

[121] D. Granger and A. Ross, " Effects of partial constrained viscoelastic layer damping parameters on the initial transient response of impacted cantilever beams: Experimental and numerical results," vol. 321, pp. 45–64, 2009.

[122] E. Barkanov, "Transient response analysis of structures made from viscoelastic materials," *The International Journal for Numerical Methods in Engineering,* vol. 44, pp. 393–403, 1999.

[123] M. S. Djoudi and H. Bahai, "A cylindrical strain-based shell element for vibration analysis of shell structures," *Finite Element in Analysis and Design* vol. 40, pp. 1947-1961, 2004.

[124] D. G. Ashwell and A. B. Sabir, "A new cylindrical shell finite element based on simple independent strain functions," *International Journal of Mechanical Sciences,* vol. 14 pp. 171–183 1972

[125] H. Chung, "Free vibration analysis of circular cylindrical shells," *Journal of Sound and Vibration,* vol. 74, pp. 331–350, 1981.

[126] J. L. Nowinski, "Nonlinear transverse vibrations of orthotropic cylindrical shells," *American Institute of Aeronautics and Astronautics Journal* vol. 1, pp. 617–620, 1963.

[127] K. R. Kanaka and R. G. Venkateswara, "Large amplitude asymmetric vibration of some thin shells of revolution," *Journal of Sound and Vibration* vol. 44, pp. 327-333., 1976.

[128] A. D. Nashif, D. I. G. Johnes, and J. P. Henderson, "Vibration damping," *Wiley, New York,* 1985.

[129] W. Soedel, " Vibrations of shells and plates," *Third Edition, Marcel Dekker Inc. New York,* 2004.

[130] R. C. David and G. L. David, "Heat Transfer calculations using finite difference equations," *Applied Science Publishers LTD, London,* 1977.

[131] T. T. Soong and D. a. G.F., "Passive Energy Dissipation Systems in Structural Engineering," *John Wiley & Sons, Chichester,* 1997.

[132] R. Rikards, A. Chate, and E. Barkanov, "Finite element analysis of damping the vibrations of laminated composites," *Computers & Structures* vol. 47, pp. 1005–1015, 1993.

[133] T.-W. Kim and J.-H. Kim, "Eigensensitivity based optimal distribution of a viscoelastic damping layer for a flexible beam," *Journal of Sound and Vibration,* vol. 273 pp. 201–218, 2004.

[134] W. T. Thomson and M. D. Dahleh, "Theory of vibration with applications," *5th edition. Prentice Hall, Englewood Cliffs NJ,* 1997.

[135] K. Hyun, S. H. Kim, K. H. Ahn, and S. J. Lee, "Large amplitude oscillatory shear as a way to classify the complex fluids," *Journal of Non-Newtonian Fluid Mechanics,* vol. 107, pp. 51-65, 2002.

[136] M. A. Greenfield, J. A. Hoffman, M. O. Cruz, and S. I. Stupp, "Tunable mechanics of peptide nanofiber gels," *Langmuir,* vol. 26 pp. 3641–3647, 2010.

[137] M. Bilasse, L. Azrar, and E. M. Daya, "Complex modes based numerical analysis of viscoelastic sandwich plates vibrations," *Computers & Structures,* vol. 89, pp. 539–555, 2011

[138] F. Mohammadi and R. Sedaghati, "Linear and nonlinear vibration analysis of sandwich cylindrical shell with constrained viscoelastic core layer " *International Journal of Mechanical Sciences,* vol. 54, pp. 156–171, 2012

[139] M. Bilasse, I. Charpentier, E. M. Daya, and Y. Koutsawa, " A generic approach for the solution of nonlinear residual equations. Part II: Homotopy and complex nonlinear eigenvalue method " *Computer Methods in Applied Mechanics and Engineering,* vol. 198 pp. 3999–4004, 2009

[140] D. K. Shin, "Large amplitude free vibration behavior of doubly curved shallow open shells with simply-supported edges," *Computers & Structures,* vol. 62, pp. 35–49, 1997

[141] P. Ribeiro, "Non-linear vibration of beams with internal resonance by the hierarchical finite-element method," *Journal of Sound and vibration,* vol. 224, pp. 591–624, 1999

[142] M. Amabili, "Nonlinear vibrations of rectangular plates with different boundary conditions: theory and experiments," *Computers & Structures,* vol. 82 pp. 2587–2605, 2004.